RESPONSE OF RC FRAMED STRUCTURES SUBJECT TO POST - EARTHQUAKE FIRE

Ph.D. THESIS

by

PRAVEEN KAMATH

DEPARTMENT OF CIVIL ENGINEERING
INDIAN INSTITUTE OF TECHNOLOGY ROORKEE
ROORKEE - 247667, INDIA
MARCH, 2014

RESPONSE OF RC FRAMED STRUCTURES SUBJECT TO POST - EARTHQUAKE FIRE

A THESIS
Submitted in partial fulfilment of the
requirements for the award of the degree
of
DOCTOR OF PHILOSOPHY
in
CIVIL ENGINEERING

by

PRAVEEN KAMATH

DEPARTMENT OF CIVIL ENGINEERING
INDIAN INSTITUTE OF TECHNOLOGY ROORKEE
ROORKEE - 247667, INDIA
MARCH, 2014

INDIAN INSTITUTE OF TECHNOLOGY ROORKEE
ROORKEE

CANDIDATE’S DECLARATION

I hereby certify that the work which is being presented in the thesis entitled **“RESPONSE OF RC FRAMED STRUCTURES SUBJECT TO POST EARTHQUAKE FIRE”** in partial fulfilment of the requirements for the award of the Degree of **Doctor of Philosophy** and submitted in the **Department of Civil Engineering** of the **Indian Institute of Technology Roorkee**, Roorkee is an authentic record of my own work carried out during a period from **December 31, 2009 to March, 2014** under the supervision of **Dr.Pradeep Bhargava, Professor** and **Dr.N. M. Bhandari, Professor Emeritus**, Department of Civil Engineering, Indian Institute of Technology Roorkee, Roorkee - 247667, **INDIA**.

The matter presented in this thesis has not been submitted by me for the award of any other degree of this or any other institute.

(Praveen Kamath)

This is to certify that the above statement made by the candidate is correct to the best of our knowledge.

(N. M. Bhandari) Supervisor	(Pradeep Bhargava) Supervisor

Date:..................

The Ph.D Viva Voce Examination of **Mr.Praveen Kamath**, Research Scholar, has been held on ....

Signature of Supervisors **Chairman, SRC** **Signature of External Examiner**

Head of the Deptt. / Chairman, ODC

Abstract

Fires can sometimes be regarded as collateral damage consequent to earthquakes in extremely inhabited areas and in general are an integral part of the emergency response strategies focused on life safety in most developed economies. As a mitigation strategy, the design guidelines proposed by different agencies in many countries across the globe considers the effect of seismic and fire loading on the structures as two separate entities. Adequate level of resistance to these hazards is specified considering one hazard at a time. Although they have a unique significance in an occurrence of such events individually, a sequential occurrence cannot be pretermitted. Fire following earthquakes, also termed as post-earthquake fire events manifests a greater deal of credible threat to built environment when it behaves as a single damage causing agent. There are no regulations specifying the design for required resistance for these hazards occurring in a sequential manner. The compound effect of two different hazards makes the structure more vulnerable to permanent structural damages either leading to stark failure or leaving it unfit to be put to structural use upon retrofitting.

The risk of fire consequent to earthquake is enhanced by mass urbanization. The havoc caused by the fire following earthquakes in the past is widely known from the timeline of events in the retrospect for almost a century till now. Two such largest events that history has seen were the fires followed by 1906 San Francisco earthquake and 1923 Tokyo earthquake. In both these events, fire was the dominating factor that led to a major loss in life and property than the earthquake. Reports of multiple fire events and a few large conflagrations after earthquakes have been quite common in most of the major earthquakes: 1971 San Fernando, 1994 Northridge, 1995 Hanshin earthquakes. World most densely populated cities located on the fault lines; San Francisco and Tokyo are highly vulnerable to fire following earthquake events. However, no outbreak of major fire has been reported following earthquakes in developing economies like India and China. Nevertheless, rapid urbanization in major cities calls in for consideration of such events as a measure of earthquake preparedness.

Response of buildings and structures to preceding extreme loading conditions is extremely useful in development of design guidelines. No research attempt has been made in the past for assessment of structures under fire following earthquake. A critical literature review mandates consideration of such loading conditions under performance based design techniques. Since fire following earthquake falls out of scope of practising professionals in earthquake and fire service fields, it has stimulated the interest amongst various groups of researchers in the structural engineering community to carry out a rigorous investigation in this front. Substantial research efforts required in the investigation may be identified at two different levels: Structural and Material. Structural level represents the holistic behaviour of a framed structure consisting of beams, columns, slabs and joints, whereas, material level constitutes the studies on the behaviour of constituent materials such as steel and concrete. In light of the above discussion, the principal objective of the current research was to investigate the response of a full-scale framed structure under post earthquake fire scenario, both experimentally and analytically and behaviour of pre-loaded / damaged steel / confined concrete at elevated temperatures. Material

level investigations at elevated temperature find its applications in development of constitutive models that aid analytical studies. A pre-load or a damage induced in the materials simulates the loading conditions experienced by the materials during earthquakes. Material level tests helps in establishing type-specific stress-strain relationships that can be utilized in the non-linear analysis of reinforced concrete structures using computer software application packages. This ensures a far more accurate analysis of structural members induced with earthquake and fire damage.

Firstly, tests were carried out on steel reinforcing bars under elevated temperatures as a part of material level test. Mechanical properties of steel reinforcing bars of varying diameter at elevated temperature with and without pre-load were investigated to work out their stress-strain relationships. Steel reinforcing bars of category TMT EQR (Earthquake resistant, soft-core enhanced ductility) having diameter 8ϕ, 10ϕ, 16ϕ and 20ϕ were considered in the investigation. Bars under no pre-load category were exposed to three target temperatures, 250 °C, 500 °C and 750 °C and tested in tension under steady state. Bars under the pre-load category were initially stressed to a certain known limit ($0.58fy$) to simulate the prevailing conditions caused by an earthquake. The bars were then exposed to the target temperatures and tested in tension at elevated temperature. Stress-strain behaviour for rebars of different diameter were plotted and compared. Stress-strain curve of rebars under no pre-load category shows a degradation in peak stress and modulus of elasticity at high temperatures. Specimens in pre-load category showed further degradation in peak stress upto 500 °C. Thereafter, the specimen failed to retain sufficient strength and stiffness before attaining the next level of target temperature, 750 °C.

Secondly, under material level test category, confined concrete specimens were examined at elevated temperatures. Undamaged and damaged confined concrete specimens, with two different levels of confinement (42 *mm* and 68 *mm*) were investigated at elevated temperatures. The specimens under undamaged category were directly exposed to the target temperature and the target temperature was maintained constant to attain a steady state. Thereafter, the specimens were loaded to failure in heated state. The specimens under damaged category were initially stressed by applying a load corresponding to a desired level of strain (0.0033, 0.0056 and 0.008), representing three different levels of damage to simulate the condition imparted by an earthquake. The specimen was then unloaded and exposed to the target temperature (250 °C, 500 °C and 750 °C) and upon attaining the steady state, it was loaded to failure. Mechanical properties like stress-strain relationship, peak stress, modulus of elasticity, strain at peak stress and ultimate strain were extracted from the data and the influence of damage and confinement were studied rigorously. Reduction in peak stress and modulus of elasticity at elevated temperatures was evident from the results analysed.

Following the material level tests, a full-scale test was conducted on a single storey reinforced concrete (RC) frame representing an intermediate portion of a $G + 3$ storey building. The main scope of conducting the test was to evaluate the response of the RC frame under simulated fire following earthquake. The test frame sub-assemblage consisted of four floor beams, four columns, four roof beams and a slab. The dead load from the storeys above was superimposed evenly on the four columns by using hydraulic jacks. A rigorous instrumentation was devised on the frame to reckon its structural response. The test frame was imparted with quasi-static simulated earthquake loading by two double-acting hydraulic jacks. A bi-directional loading was achieved in eleven displacement cycles with a combination of 10 mm and 20 mm displacement per cycle. A maximum displacement of 150 mm that corresponds to the *"Collapse Prevention"* level of structural safety as per FEMA 366 was achieved. Thereafter, the structure was enclosed in a $3m \times 3m \times 3m$ compartment and it was exposed to one hour pool fire. Ultimately, the fire damaged RC frame was pushed to reckon its residual capacity. Response of the frame was measured in terms of load-displacement hysteresis, strains at rebar level, temperature experienced in various structural entities and displacement during fire. The reinforced concrete frame was inferred to be intact without collapse. However, the frame underwent a degradation in strength and stiffness following the simulated earthquake and fire.

With a rigorous experimental work under structural and material level, focus was finally laid on analytical work on reinforced concrete frame. A finite element model was developed using commercial software suite, ABAQUS version 6.9. Modelling was achieved using solid homogeneous element, $C3D8$ for concrete and truss element, $T3D2$ for steel reinforcement. Different structural elements such as beams, columns and slab were discretized using octahedral elements. A detailed heat transfer analysis was carried out on the frame to generate temperature profiles, which were then compared with the experimentally assessed temperature profiles. Thereafter, a cyclic analysis was carried out to simulate the earthquake damage on the frame model. The load-displacement hysteresis obtained was compared with the experimental results.

Acknowledgements

As I approach the ultimatum, it is my sincere pleasure to express gratitude to all those who incessantly helped me accomplish an arduous journey called thesis. I owe thanks to a great many people who have made this thesis possible through their encouragement, friendship, wisdom, and patience. It is because of them my graduate experience has been one that I will cherish forever.

I would like to express my sincerest gratitude to my supervisors Pradeep Bhargava, Professor and NM Bhandari, Professor Emeritus, Department of Civil Engineering, Indian Institute of Technology Roorkee for their eminent guidance in my Ph.D research. Their patience, motivation, encouragement and immense knowledge is greatly appreciated. Their esteemed guidance helped me at every stage of research and writing of this thesis. I have been astoundingly fortunate to have an advisor like Prof. Bhargava, who gave me the freedom to explore on my own and at the same time, the guidance to recoup whenever I needed the most. Prof. Bhargava encouraged me to accomplish a quality research with extreme meticulousness. His immense support in academic and personal fronts helped me overcome many crisis situations and complete the thesis. Equally supportive, Prof. Bhandari has always been a vital part of all my technical discussions, enlightening my intellect with his adept advices. His constructive criticisms at different stages of my research and insightful comments have been thought-provoking and helped me focus my research. I also extend my sincere appreciation to my supervisors for their conscientious effort in scrutinizing my thesis and providing invaluable inputs. I could never imagine a successful accomplishment of my thesis without supervisors like Prof. Bhargava and Prof. Bhandari.

Besides my supervisors, I would like to Thank Dr.Umesh Kumar Sharma, Associate Professor, Department of Civil Engineering, IIT Roorkee. Dr. Sharma has been more than a co-supervisor to me. He has been always there to listen and give advice on various domains. I am deeply grateful to him for the long discussions that helped me sort out the technical issues related my experimental work.

I extend my sincere thanks to Prof. Asif Usmani, Professor & Chair, Institute for Infrastructure and Environment, The University of Edinburgh and Dr. Martin Gillie, Reader in Structural Engineering, School of Mechanical, Aerospace and Civil Engineering, The University of Manchester, UK for giving me valuable opportunities in their research groups and leading me working on diverse, exciting projects during my tenure as a visiting researcher at Edinburgh under the UKIERI Project.

Further, I would like to thank rest of my thesis committee: Prof. Yogendra Singh, Department of Earthquake Engineering and Dr. Anupam Chakrabarti, Associate Professor, Department of Civil Engineering, IIT Roorkee for their invaluable support, comments and questions during comprehensive examination, interim review and pre-synopses.

I am grateful to the head of the department and faculties in the Structural Engineering Group, Civil Engineering Department, IIT Roorkee, for making the state-of-the-art laboratory facilities available to me. I am thankful to the staff members of the concrete technology and structural engineering laboratory for their timely support and co-operation. I extend my thanks to the laboratory technicians and helpers for assisting me in carrying out the experimental work.

I express my warm appreciation to the British Council, India for funding my research project under United Kingdom - India Education and Research Initiative (UKIERI) program. I am also thankful to the Ministry of Human Resources, Government of India for providing me the fellowship all though the course of my Ph.D.

I appreciate the help delivered in the initial stages of modelling and simulation by the former graduate students Mr. Hitesh Lakhani, Mr. Sahil Aggarwal and Mr. Ankit Agrawal, and the current graduate student Mr. M. Jayakrishna.

I appreciate the support and care provided by my fellow Ph.D scholars, Mr. Heaven Singh and Dr. Virendra Kumar. Without their help, overcoming the setbacks and hard times would have been extremely onerous. I also extend my thanks to my fellow researchers at The University of Edinburgh, Dr. Panagiotis Kotsovinos and Dr. Yaqiang Jiang for their collaborative research activities, interminable technical discussions and interesting conversation on world economy, globalization and multiculturalism. I greatly value their companionship.

Good friends who can share your joys, carry your burdens and counsel you the right things are priceless. I express a great pleasure in acknowledging the many friends who have helped me while dealing with tough times.

Above all, none of this would have been possible without the unconditional support provided by my parents, to whom this thesis is dedicated to. Their patience, encouragement, emotional support, understanding and endless love throughout my degree is greatly appreciated.

Lastly, I thank Almighty God for endowing me with apt skills and providing me an opportunity to achieve one of the most significant accomplishments in Life.

To my parents

Contents

Abstract . . . i
Acknowledgements . . . iv
Dedication . . . vi
Table of Contents . . . viii
List of Figures . . . xii
List of Tables . . . xviii
List of Symbols . . . xix

1. Introduction **2**
1.1 GENERAL . . . 2
1.1.1 Post-Earthquake Fire . . . 2
1.1.2 Fire as a Disaster . . . 3
1.1.3 Fire Response of Reinforced Concrete . . . 3
1.2 OBJECTIVES OF THE RESEARCH . . . 4
1.3 SCOPE OF THE RESEARCH . . . 4
1.4 OVERVIEW OF THESIS . . . 6

2. Behaviour of UnLoaded and Pre-Loaded Steel Rebars at Elevated Temperatures **8**
2.1 INTRODUCTION . . . 8
2.2 ELEVATED TEMPERATURE PROPERTIES OF STEEL REBARS . . . 9
2.3 EXPERIMENTAL EVALUATION . . . 11
2.3.1 General . . . 11
2.3.2 Specimens for Elevated Temperature Tensile Test . . . 13
2.3.3 Test Setup . . . 13
2.3.4 Instrumentation . . . 13
2.3.5 Tensile Test of Rebar Specimens . . . 14
2.4 RESULTS AND DISCUSSION . . . 16
2.4.1 Stress-Strain Relationships . . . 17
2.4.2 Influence of Pre-loading . . . 19
2.4.3 Variation of Plastic Strain . . . 24
2.5 FAILURE MODES . . . 26
2.6 SCOPE FOR FURTHER RESEARCH . . . 27
2.7 CONCLUDING REMARKS . . . 27

3. Undamaged and Damaged Confined Concrete at Elevated Temperatures 28
3.1 INTRODUCTION 28
3.2 CONCRETE AT ELEVATED TEMPERATURES: MATERIAL BEHAVIOUR 29
3.2.1 Phase Transformations Occurring in the Cement Paste 29
3.2.2 Phase Transformations Occurring in the Aggregates 29
3.2.3 Incompatibility Between Aggregates and Cement Paste: 29
3.3 TESTING OF CONCRETE AT ELEVATED TEMPERATURES 31
3.3.1 Damaged Concrete at Elevated Temperatures 32
3.4 EXPERIMENTAL PROGRAMME 33
3.4.1 General 33
3.4.2 Specimens 33
3.4.3 Instrumentation 35
3.4.4 Test Setup 35
3.4.5 Testing Methodology 36
3.5 RESULTS AND DISCUSSION 39
3.5.1 Stress-Strain Curves 39
3.5.2 Modulus of Elasticity 43
3.5.3 Peak Stress and Corresponding strain 46
3.5.4 Damage Induced in Confined Concrete Specimens 51
3.5.5 Specimen Behaviour at Elevated Temperatures 52
3.5.6 Failure Modes 52
3.6 CONCLUDING REMARKS 59

4. Structural Response of RC Frame Under Fire Following Earthquake 62
4.1 INTRODUCTION 62
4.2 CONSTRUCTION OF REINFORCED CONCRETE TEST FRAME 63
4.3 INSTRUMENTATION 69
4.4 FRAME TEST STAGE I: SIMULATED EARTHQUAKE LOAD TEST 72
4.4.1 Gravity and Seismic Loads 72
4.4.2 Simulated Earthquake Load 73
4.4.3 Strain Data 78
4.5 FRAME TEST STAGE II: FIRE TEST 92
4.5.1 Compartment Fire 92
4.5.2 Fire Design 95
4.5.3 Mock Fire Tests 96
4.5.4 Compartment Fire for the RC Frame 99
4.6 FRAME TEST STAGE III: RESIDUAL CAPACITY TEST 120
4.7 CONCLUDING REMARKS 121

5. Numerical Analysis of RC Frame Under Fire Following Earthquake 122

5.1 INTRODUCTION 122
5.2 MODELLING OF REINFORCED CONCRETE FRAME 122
5.2.1 Geometric Modelling of RC Frame on ABAQUS 122
5.2.2 Material Modelling: CDP Model for Tension and Compression 123
5.2.3 Meshing the Model 127
5.3 SIMULATED EARTHQUAKE LOADING IN ABAQUS 128
5.3.1 Comparison of Simulated Earthquake Loading Test Results 128
5.4 HEAT TRANSFER ANALYSIS ON THE RC FRAME 131
5.5 THERMAL STRESS ANALYSIS 176
5.5.1 Material Constitutive Models for Thermal Stress Analysis 177
5.5.2 Results of Thermal Stress Analysis 178
5.6 RESIDUAL TEST ON FIRE DAMAGED FRAME 181
5.7 CONCLUDING REMARKS 182

6. Conclusions and Scope for Further Research 184
6.1 CONCLUSIONS 184
6.2 SCOPE FOR FURTHER RESEARCH 188
References 190
List of Publications 198

List of Figures

2.1 Stressstrain for reinforcing bars at elevated temperature per Eurocode 2 10
2.2 Testing arrangement for steel rebars at elevated temperature 14
2.3 Tensile test setup for steel rebars at elevated temperature 15
2.4 Typical input temperature time curves 16
2.5 Stress-Strain plot for steel rebars without pre-load (a) 8 *mm* (b) 10 *mm* (c) 16 *mm* (d) 20 *mm* 18
2.6 Variation of peak stress for: (a) fe 500 (b) fe 500D reinforcing bars at elevated temperatures 20
2.7 Variation of Modulus of Elasticity for (a) fe500 (b) fe 500D reinforcing bars at elevated temperatures 21
2.8 Stress-Strain plot for pre-loaded steel rebars (a) 8 *mm* (b) 10 *mm* (c) 16 *mm* (d) 20 *mm* 22
2.9 Variation of Plastic Strain for steel rebars without pre-load(a) 8 *mm* (b) 10 *mm* (c) 16 *mm* (d) 20 *mm* 25
2.10 Failure modes of reinforcing bars at different elevated temperatures 27

3.1 Phase transformations in cement paste at elevated temperatures 30
3.2 Schematics of different test methods (a) Stressed Test (b) Unstressed Test (c) Residual Test 31
3.3 Schematics of damaged unstressed tests (a) Temperature-time (b) Stress-time 33
3.4 3D schematics of: (a) Confined concrete reinforcement (b) Split-type mould 34
3.5 Strain gauges (a) Surface preparation (b) Bondable strain gauge (c) Spot welding (d) High-temperature resistant, weldable strain gauge 36
3.6 3D Schematic of the split-vertical furnace with the confined concrete specimen 37
3.7 3D Schematic of the test setup 37
3.8 Actual test setup with elevated temperature testing in progress 39
3.9 Stress-strain plots for confinement C1 at elevated temperatures (a) 250 °C (b) 500 °C (c) 750 °C 41
3.10 Stress-strain plots for confinement C2 at elevated temperatures (a) 250 °C (b) 500 °C (c) 750 °C 42
3.11 Initial modulus of elasticity at elevated temperature for confined concrete with confinement C1 44
3.12 Initial modulus of elasticity at elevated temperature for confined concrete with confinement C2 44
3.13 Comparison of initial modulus of elasticity for confined concrete with existing models 45

3.14 Peak stress at elevated temperature for confined concrete with confinement C1 48
3.15 Peak stress at elevated temperature for confined concrete with confinement C2 48
3.16 Cracks induced in damage cycle 51
3.17 Thermal Gradient evident from color change 53
3.18 Failure of Strain Gauges 53
3.19 Failure of confined concrete specimens by: (a) Buckling of longitudinal reinforcement (b) Opening of lateral ties 54
3.20 Aggregate-mortar separation 55
3.21 Loss of cover concrete 55
3.22 Failure of specimens with confinement C1 under damage category D1 56
3.23 Failure of specimens with confinement C1 under damage category D2 56
3.24 Failure of specimens with confinement C1 under damage category D3 57
3.25 Failure of specimens with confinement C2 under damage category D1 57
3.26 Failure of specimens with confinement C2 under damage category D2 58
3.27 Failure of specimens with confinement C2 under damage category D3 58
3.28 Confinement failure at 750 °C 59

4.1 RC structure layout (a) In plan (b) In elevation 63
4.2 Frame test strategy 64
4.3 Schematic diagram of the test setup (a)Plan (b)Elevation 66
4.4 Detailing of a column reinforcement 67
4.5 Detailing of beam reinforcement 68
4.6 Detailing of slab (a) Plan showing bottom reinforcement (b) Plan showing top reinforcement (c) Section though the slab 69
4.7 Member nomenclature and location of strain gauges in the frame sub-assemblage . . . 70
4.8 Location of thermocouples (a) Floor beam (b) Roof beam (c) Column (d) Slab (e) Compartment 71
4.9 Simulated earthquake cycles (a) Displacement (b) Load 75
4.10 Damage induced at floor beam column joints 76
4.11 Damage induced at roof beam column joints 77
4.12 Load-Displacement hysteresis for simulated earthquake loading 77
4.13 Strain profile in beam B1 (a) Left section, bottom rebar (b) Left section, top rebar (c) Mid-span section, top rebar (d) Right section, bottom rebar 80
4.14 Strain profile in beam B2 (a) Mid-span section, bottom rebar (b) Mid-span section, top rebar (c) Right section, bottom rebar (d) Right section, top rebar 81
4.15 Strain profile in beam B3 (a) Left section, bottom rebar (b) Left section, top rebar (c) Mid-span section, bottom rebar (d) Right section, top rebar 82
4.16 Strain profile in beam B4 (a) Left section, bottom rebar (b) Left section, top rebar (c) Mid-span section, top rebar (d) Right section, top rebar 83

4.17 Strain profile in beam B5 (a) Left section, bottom rebar (b) Mid-span section, bottom rebar (c) Mid-span section, top rebar (d) Right section, bottom rebar 84

4.18 Strain profile in beam B6 (a) Left section, bottom rebar (b) Left section, top rebar (c) Right section, bottom rebar (d) Right section, top rebar 85

4.19 Strain profile in beam B7 (a) Left section, bottom rebar (b) Mid-span section, bottom rebar (c) Right section, bottom rebar (d) Right section, top rebar 86

4.20 Strain profile in beam B8 (a) Left section, bottom rebar (b) Left section, top rebar (c) Mid-span section, top rebar 87

4.21 Strain profile in column C1 (a) Bottom section, exposed face (b) Bottom section, unexposed face (c) Mid-Height section, exposed face (d) Top section, unexposed face . 88

4.22 Strain profile in Column C2 (a) Bottom section, exposed face (b) Bottom section, unexposed face (c) Mid-Height section, exposed face (d) Mid-Height section, unexposed face 89

4.23 Strain profile in Column C3 (a) Bottom section, unexposed face (b) Mid-Height section, exposed face (c) Mid-Height section, unexposed face 90

4.24 Strain profile in Column C4 (a) Mid-Height section, exposed face (b) Mid-Height section, unexposed face (c) Top section, exposed face (d) Top section, unexposed face 91

4.25 Comparison of different parametric fire curves 93

4.26 Generic temperature-time *(Swedish Fire)* curves for different ventilation factors and fuel loads (from Table 10.2, Drysdale [29]) 94

4.27 Desired constant temperature fire curve 95

4.28 Compartment temperature - compartment shape relationships (from Purkiss [69], pp. 59) 96

4.29 Proposed shape of the compartment 97

4.30 Rate of burning vs. time from laboratory scale experiment by Friedman 1975(from Figure 9.2, Drysdale [29], pp 353) 98

4.31 Mock fire test (a) Brick masonry compartment (b) Temperature-time curve for the compartment 99

4.32 Flashover 100

4.33 Compartment temperature-time history at (a)Location A (b)Location B (c)Location C *(ref. Fig. 8(e))* 101

4.34 Compartment temperature history for 90 minutes at location C 102

4.35 Slab vertical deflections during and after the fire 102

4.36 Lateral deflections at roof level during and after the fire 103

4.37 Slab vertical and lateral deflections (a) After 1 hour fire (b) Max. Obtained 104

4.38 Temperature profile for floor beams (a) Beam B1 (b) Beam B2 (c) Beam B3 (d) Beam B4 106

4.39 Temperature profile for roof beam B5 at (a) Left section (b) Mid-span section (c) Right section 107

4.40 Temperature profile for roof beam B6 at (a) Left section (b) Mid-span section (c) Right section 108
4.41 Temperature profile for roof beam B7 at (a) Left section (b) Mid-span section (c) Right section 109
4.42 Temperature profile for roof beam B8 at (a) Left section (b) Mid-span section (c) Right section 110
4.43 Temperature profile for column C1 at (a) Bottom section (b) Mid-height section (c) Top section 111
4.44 Temperature profile for column C2 at (a) Bottom section (b) Mid-height section (c) Top section 112
4.45 Temperature profile for column C3 at (a) Bottom section (b) Mid-height section (c) Top section 113
4.46 Temperature profile for column C4 at (a) Bottom section (b) Mid-height section (c) Top section 114
4.47 Temperature profile for slab (a) Location A (b) Location B (c) Location C 115
4.48 Temperature profile for slab (d) Location D (e) Location O 116
4.49 Temperature gradient column (C1, top) 117
4.50 Structural damage in Fire (a) Spalling during fire (b) Surface microcracks (c) Spalling of cover concrete in cooling regime (d) Debonding of reinforcement 118
4.51 Concrete spalling (a) Beam-column joints (b) Corners of the column 119
4.52 Load-Displacement plot from residual capacity test 120

5.1 Sequence of analysis 123
5.2 Geometric model of Reinforced Concrete frame generated in ABAQUS 124
5.3 Behaviour of Concrete in (a) Uniaxial Tension (b) Uniaxial Compression 126
5.4 Meshing of the model 129
5.5 Load-Displacement hysteresis under pushover loading for RC frame model generated in ABAQUS 130
5.6 Comparison of load vs. time plot 131
5.7 Comparison of loading envelope (a) Push Cycle (b) Pull cycle 132
5.8 Surface temperatures considered for heat transfer analysis (a) Columns (b) Floor beams (c) Roof beams (d) Slab 137
5.9 Comparison of thermal profile for beam B1 (a) Left, D1 (b) Left, D2 (c) Left, D3 (d) Mid-Span, D1 (e) Mid-Span, D2 (f) Mid-Span, D3 (g) Right, D1 (h) Right, D2 (i) Right, D3 141
5.10 Comparison of thermal profile for beam B2 (a) Left, D1 (b) Left, D2 (c) Left, D3 (d) Mid-Span, D1 (e) Mid-Span, D2 (f) Mid-Span, D3 (g) Right, D1 (h) Right, D2 (i) Right, D3 142

5.11 Comparison of thermal profile for beam B3 (a) Left, D1 (b) Left, D2 (c) Left, D3 (d) Mid-Span, D1 (e) Mid-Span, D2 (f) Mid-Span, D3 (g) Right, D1 (h) Right, D2 (i) Right, D3 . . . 143
5.12 Comparison of thermal profile for beam B4 (a) Left, D1 (b) Left, D2 (c) Left, D3 (d) Mid-Span, D1 (e) Mid-Span, D2 (f) Mid-Span, D3 (g) Right, D1 (h) Right, D2 (i) Right, D3 . . . 144
5.13 Comparison of thermal profile for beam B5 (a) Left, B1 (b) Left, B2 (c) Left, D1 (d) Left, D2 (e) Left, D3 . . . 147
5.14 Comparison of thermal profile for beam B5 (a) Mid-Span, B1 (b) Mid-Span, B2 (c) Mid-Span, D1 (d) Mid-Span, D2 (e) Mid-Span, D3 . . . 148
5.15 Comparison of thermal profile for beam B5 (a) Right, B1 (b) Right, B2 (c) Right, D1 (d) Right, D2 (e) Right, D3 . . . 149
5.16 Comparison of thermal profile for beam B6 (a) Left, B1 (b) Left, B2 (c) Left, D1 (d) Left, D2 (e) Left, D3 . . . 150
5.17 Comparison of thermal profile for beam B6 (a) Mid-Span, B1 (b) Mid-Span, B2 (c) Mid-Span, D1 (d) Mid-Span, D2 (e) Mid-Span, D3 . . . 151
5.18 Comparison of thermal profile for beam B6 (a) Right, B1 (b) Right, B2 (c) Right, D1 (d) Right, D2 (e) Right, D3 . . . 152
5.19 Comparison of thermal profile for beam B7 (a) Left, B1 (b) Left, B2 (c) Left, D1 (d) Left, D2 (e) Left, D3 . . . 155
5.20 Comparison of thermal profile for beam B7 (a) Mid-Span, B1 (b) Mid-Span, B2 (c) Mid-Span, D1 (d) Mid-Span, D2 (e) Mid-Span, D3 . . . 156
5.21 Comparison of thermal profile for beam B7 (a) Right, B1 (b) Right, B2 (c) Right, D1 (d) Right, D2 (e) Right, D3 . . . 157
5.22 Comparison of thermal profile for beam B8 (a) Left, B1 (b) Left, B2 (c) Left, D1 (d) Left, D2 (e) Left, D3 . . . 158
5.23 Comparison of thermal profile for beam B8 (a) Mid-Span, B1 (b) Mid-Span, B2 (c) Mid-Span, D1 (d) Mid-Span, D2 (e) Mid-Span, D3 . . . 159
5.24 Comparison of thermal profile for beam B8 (a) Right, B1 (b) Right, B2 (c) Right, D1 (d) Right, D2 (e) Right, D3 . . . 160
5.25 Comparison of thermal profile for column C1 (a) Bottom, L1 (b) Bottom, L2 (c) Bottom, P1 (d) Bottom, P2 (e) Bottom, P3 . . . 163
5.26 Comparison of thermal profile for column C1 (a) Mid-Height, L1 (b) Mid-Height, L2 (c) Mid-Height, P1 (d) Mid-Height, P2 (e) Mid-Height, P3 . . . 164
5.27 Comparison of thermal profile for column C1 (a) Top, L1 (b) Top, L2 (c) Top, P1 (d) Top, P2 (e) Top, P3 . . . 165
5.28 Comparison of thermal profile for column C2 (a) Bottom, L1 (b) Bottom, L2 (c) Bottom, P1 (d) Bottom, P2 (e) Bottom, P3 . . . 166
5.29 Comparison of thermal profile for column C2 (a) Mid-Height, L1 (b) Mid-Height, L2 (c) Mid-Height, P1 (d) Mid-Height, P2 (e) Mid-Height, P3 . . . 167

5.30 Comparison of thermal profile for column C2 (a) Top, L1 (b) Top, L2 (c) Top, P1 (d) Top, P2 (e) Top, P3 168
5.31 Comparison of thermal profile for column C3 (a) Bottom, L1 (b) Bottom, L2 (c) Bottom, P1 (d) Bottom, P2 (e) Bottom, P3 171
5.32 Comparison of thermal profile for column C3 (a) Mid-Height, L1 (b) Mid-Height, L2 (c) Mid-Height, P1 (d) Mid-Height, P2 (e) Mid-Height, P3 172
5.33 Comparison of thermal profile for column C3 (a) Top, L1 (b) Top, L2 (c) Top, P1 (d) Top, P2 (e) Top, P3 173
5.34 Comparison of thermal profile for column C4 (a) Bottom, L1 (b) Bottom, L2 (c) Bottom, P1 (d) Bottom, P2 (e) Bottom, P3 174
5.35 Comparison of thermal profile for column C4 (a) Mid-Height, L1 (b) Mid-Height, L2 (c) Mid-Height, P1 (d) Mid-Height, P2 (e) Mid-Height, P3 175
5.36 Comparison of thermal profile for column C4 (a) Top, L1 (b) Top, L2 (c) Top, P1 (d) Top, P2 (e) Top, P3 176
5.37 Mathematical model for concrete at elevated temperature *(from Eurocode 2 [34])* . . . 178
5.38 Comparison of vertical displacement for VLVDT1 179
5.39 Comparison of vertical displacement for VLVDT2 179
5.40 Comparison of vertical displacement for VLVDT3 180
5.41 Comparison of vertical displacement for VLVDT4 180
5.42 Comparison of vertical displacement for VLVDT5 181
5.43 Comparison of residual capacity plots 182

List of Tables

2.1 Mathematical model for stress strain relationships of reinforcing steel at elevated temperatures 11
2.2 Values for the parameters of the stress-strain relationship of hot rolled and cold worked reinforcing steel at elevated temperatures (a) Class X (b) Class N 12
2.3 Testing plan for elevated temperature tensile tests 15
2.4 Mechanical properties of reinforcing bars at elevated temperatures without pre-load . 23
2.5 Mechanical properties of pre-loaded reinforcing bars at elevated temperatures 24
2.6 Coefficients α_i and β_i for Fe500 TMT Bars 26
2.7 Coefficients α_i and β_i for Fe500D TMT Bars 26

3.1 Damage levels 38
3.2 Mechanical properties for confined concrete at elevated temperatures: C1 43
3.3 Mechanical properties for confined concrete at elevated temperature: C2 43
3.4 Confined peak stress: Experimental vs. Predicted 49
3.5 Strain at confined peak stress: Experimental vs. Predicted (Damage D0 / Confinement C1) 50
3.6 Strain at confined peak stress: Experimental vs. Predicted (Damage D0 / Confinement C2) 50

5.1 Mesh details 128
5.2 Input displacements for earthquake loading simulation 129
5.3 Comparison of load values obtained in ABAQUS results with respect to experimental results *(+ indicates a push cycle and - indicates a pull cycle)* 133
5.4 Comparison of peak temperatures in the floor beams B1, B2, B3 and B4 140
5.5 Comparison of peak temperatures in the roof beams B5 and B6 146
5.6 Comparison of peak temperatures in the roof beams B7 and B8 154
5.7 Comparison of peak temperatures in the columns C1 and C2 162
5.8 Comparison of peak temperatures in the columns C3 and C4 170
5.9 Values for the stress-strain relationships of normal weight concrete at elevated temperatures 177

List of Symbols

α	Emissivity coefficient
$\bar{\sigma}_c$	Effective compressive cohesion stress
$\bar{\sigma}_t$	Effective tensile cohesion stress
$\frac{S_a}{g}$	Response reduction factor
ϵ	Emissivity coefficient relating the radiation of the surface concrete surface (gray) to that of an ideal black body ($0 \leq \epsilon \leq 1$)
ϵ'_{ccT}	Strain at maximum stress of confined concrete at elevated temperature
ϵ'_{cT}	Concrete strain at elevated temperature
ϵ'_{cT}	Temperature dependent strain at peak stress for unconfined concrete
ϵ^{el}	Total elastic strain or log strain in finite strain problems
ϵ_{cT}	Strain at maximum stress of unconfined concrete at elevated temperature
ϵ_{tr}	Transient creep strain
$\hat{\bar{\sigma}}_{max}$	The maximum principal effective stress
$[C]$	Global heat capacity matrix
$[C^e]$	The heat capacity matrix
$[K]$	Global heat conduction matrix
$\left\{\dot{T}^e\right\}$	The element conductivity matrix
$\{F\}$	Thermal load vector at the structural level

$\{F^e\}$	The thermal load vector
$\psi(\theta, f_i)$	Dilation angle measured in the p-q plane at high confining pressure
ρ	Density of solid in kg/m^3
σ	Total stress: True or Cauchy stress in finite-strain problems
σ'_{c0}	Unconfined concrete compressive strength at ambient temperature
σ'_{cc0}	Confined concrete compressive strength at ambient temperature
σ'_{ccT}	Compressive strength of confined concrete at elevated temperature
σ'_{cT}	Compressive strength of concrete at elevated temperature
σ'_{cT}	Concrete compressive strength at elevated temperature
σ'_{lT}	Effective lateral confining stress at elevated temperature
σ'_{l}	Effective lateral confining stress on concrete at ambient temperature
$\sigma_{t0}(\theta, f_i)$	Uniaxial tensile stress at failure, taken from the user-specified tension stiffening
σ_{yT}	Temperature dependent yield strength of rebars
A	Total internal area of the compartment
A_0	Area of the opening
A_s	Cross-sectional area of transverse reinforcement
c	Specific heat of solid in $J/kg.\,^{\circ}\mathrm{C}$
C_s	Stephen Boltzman's constant equal to $5.667 \times 10^{-8} W/m^2\ ^{\circ}\mathrm{C}\ K^4$
d	Base dimension in the considered direction
d	Scalar stiffness degradation variable
$D^{el} = (1-d)D^{el}_0$	Degraded elastic stiffness
D^{el}	Fourth order elasticity tensor
D^{el}_0	Initial / undamaged elastic stiffness of the material
D^{el}_0	Initial / undamaged elasticity matrix
d_s	Diameter of transverse rebars
E_0	Initial / Undamaged elastic stiffness of the material

E_{c0}	Initial elastic modulus of confined concrete at ambient temperature
E_{cT}	Initial elastic modulus of confined concrete at elevated temperature
g	Function to calculate the elastic modulus variations due to application of external loads
h	Height of the Building
H_0	Height of the opening
I	Importance factor
k	Thermal conductivity components expressed in $W/m.$ °C
K_e	Confinement effectiveness coefficient
K_e	Confinement effectiveness coefficient
n	Unit normal vector to the surface
Q	Time rate of heat generated per unit volume by hydration of cement paste in concrete within the body (W/m^3)
q	Time rate of heat transferred between the environment and concrete surface per unit area, expressed in W/m^2
q_c	Loss of heat flux due to convection
q_r	Loss of heat flux due to radiation
q_{T_o}	Compartment temperature
R	Response reduction factor
S_h	Spacing between transverse hoop rebars
$sigma_{cT}$	Concrete compressive stress at elevated temperature
t	Time (minutes)
T^*	Constant equal to 273 which is used to convert the temperature from degree Celsius °C to °CK
T_0	Ambient temperature °C
t_h	Time (hours)
T_s	Fundamental natural time period
Z	Zone factor

Introduction

1

1.1 GENERAL

Fire following earthquake events, although less frequent in occurrence, is a complex task involving sequential and situational components [86] The possibilities of fire consequent to earthquakes in urban locations and in general are an integral part of the emergency response strategies focused on life safety in most developed economies [27]. Building regulations in most countries require engineers to consider the effect of seismic and fire loading on the structures to provide an adequate level of resistance to these hazards however only on a separate basis. There are no current regulations that require buildings to consider these hazards in a sequential manner to quantify the adequacy of structures for combined loading and design for the required resistance.

1.1.1 Post-Earthquake Fire

Post-earthquake fires are rather a scarce phenomenon that structures experience in their lifetime. But literatures [27] [44] suggest that many of the earthquakes often accompany with them after effects such as fault rupture, shaking, liquefaction, landslides, fires, release of hazardous materials, tsunami, etc. [27]. Fire is one such phenomenon which ignites and propagates at a rapid rate yielding to post-earthquake conflagrations. The main reason for the ignition is attributed to rupture of underground gas lines and fuel lines, electric short-circuiting and improper storage and disposal of hazmats. Occasionally, building characteristics and metrological conditions combine to create a situation in which post-earthquake fire is the predominant cause of damage. Large fires, despite their low probability of occurrence after an earthquake, have been very severe. History has produced two largest urban fires following earthquakes, which have caused tremendous devastation of life and property - San Francisco (1906) and Tokyo (1923). More than 600 km region was incinerated in San Francisco and Kanto earthquake in Tokyo claimed more than 140000 lives. Apart from these major events, various incidents of fire were reported in 1989 Loma Prieta earthquake in California, 1994 Northridge, earthquake in California, 1995 Hanshin (Kobe) earthquake in Japan, 1999 Marmara earthquake in Turkey. The intensity of fire in these earthquakes varied from few hours to three days. [27]. An occurrence of earthquake and tsunami in Fukushima, Japan, 2011 also reported fire in a nuclear reactor turbine building.

1.1.2 Fire as a Disaster

Fires in general, earthquake triggered or otherwise, are considered hazardous to the life of concrete structures. Major fires caused in USCE Building, Yugoslavia (Mar 1999) World Trade Center, NYC (Sep 2001), Carlton Towers in Bangalore (Feb 2010) and Shanghai apartment building (Nov 2010) can cause a great deal of damage to structures. More than 950 deaths have been reported in major building and industry fires over 10 years in India. These events of fire calls for upgrading the existing building fire safety measures, which successively depends on an extensive study of structures subjected to fire attaining elevated temperatures. Apart from the building fires, Reinforced Concrete is expected to achieve higher temperatures in Air craft launch pads, turbo jet runways, rocket and missile launch pads and nuclear installations.

1.1.3 Fire Response of Reinforced Concrete

Reinforced Concrete (RC) structures in general remain passive in fires. Fire-damaged RC structures can be repaired and put back to use even after severe fires. Certainly, the damaged structural members must be repaired to regain the minimum strength, stiffness and ductility they ought to possess before the fires. Elevated temperature in concrete triggers physical and chemical changes, such as loss of moisture, dehydration of cement paste and decomposition of aggregate. These changes will cause deterioration in the microstructure of concrete, affecting its mechanical properties. Therefore, concrete members without visible damage may have reduced strength due to elevated temperatures. To evaluate and repair the fire-damaged concrete members, it is essential to understand the effect of temperature on the mechanical properties of concrete, particularly the stress-strain relationships used to predict the behaviour in a strong earthquake. Many studies have been made on the residual mechanical properties of concrete after exposure to elevated temperatures such as compressive strength, splitting tensile strength and elastic modulus [26]. Scarce information is available on the compressive stress-strain relationships of concrete after exposure to elevated temperatures. Wu et al. [89] have tested 44 prismatic concrete specimens after heating to temperatures up to 600 °C and proposed a stress-strain equation for unheated and heated concrete with the same shape of the non-dimensional curves for different temperatures. The purposes of this research is to establish a database of the mechanical properties of concrete after heating to temperatures up to 800 °C and to propose a single equation of the complete stress-strain curve applicable to unheated and heated concrete for different temperatures. Chang et al. [26] conducted compression and split-cylinder tests are to examine the validity of the relationships of temperature with the residual compressive strength, corresponding peak strain, elastic modulus, splitting tensile strength and stress-strain curves. They also considered the stress-strain relationship proposed by Tsai and modified it for ascending and descending branches and made their experimental results fit better with existing models [89].

1.2 OBJECTIVES OF THE RESEARCH

Experimental investigations on behaviour of building materials in fire till date are primarily based on the assessment of the material properties of steel and concrete separately at elevated temperatures. Besides, the lack of understanding full-scale behaviour of structural elements triggers a demand for full scale testing of structures. It is also imperative to study the effect of multiple loading on structures since they cause a compounding level of distress. Limited studies exist on damaged structural elements and full-scale reinforced concrete framed structures at elevated temperature due to complexities involved in finance, experimentation and instrumentation at high temperatures. These issues help to define objectives of the current research as enumerated below:

1. To evaluate the mechanical properties of unloaded and pre-loaded steel reinforcing bars at elevated temperatures.
   Researchers in the past have performed tensile tests on locally available steel rebars used in construction . However, no studies exist on pre-loaded steel rebars at elevated temperatures. Tests were devised on commercially available rebars of four different diameters: 8 *mm*, 10 *mm*, 16 *mm* and 20 *mm* at 250 °C, 500 °C and 750 °C in tension.

2. To evaluate the mechanical properties of confined concrete specimens with no damage and with pre-damage at elevated temperatures. Work till date has been limited to experiments involving assessment of residual properties and some elevated temperature properties without the consideration of pre-damage. This study aims at the assessment of the mechanical properties of confined concrete with two levels of confinement and three levels of damage *(mild, moderate and severe)*.

3. Full-scale testing of reinforced concrete structure subjected to fire following earthquake. No studies exist prior to the current work on full-scale testing of RC frame under post-earthquake fire. Besides, the integral behaviour of structural elements in fire is best reckoned by full-scale tests. Current study aims at evaluating the performance of an RC frame exposed to simulated earthquake and fire. The results obtained in terms of temperature profiles, strains and load-displacem hysteresis were then aimed to be compared with an analytical model built in the finite element package Abaqus Version 6.9.

1.3 SCOPE OF THE RESEARCH

With a broad objective of the work outlined in the previous section, the scope of the work is enumerated as follows.

1. Mechanical properties of steel reinforcing bars with and without pre-load finds its applications in development of constitutive material model for steel that aids the numerical analysis of reinforced concrete structures. Structures which are subjected to multiple loads require different material properties to simulate the actual distress conditions in materials after every step of loading. Steel

reinforcing bars of four different diameters *(8 mm, 10 mm, 16 mm and 20 mm)* were considered for testing in tension at target temperatures 250 °C, 500 °C and 750 °C. The reinforcing bars were selected from the same lot used in the construction of reinforced concrete frame subjected to post-earthquake fire. The material properties at elevated temperatures obtained in testing of pre-loaded rebars finds its implications in the numerical analysis of the earthquake damaged frame, where they are subjected to fire following a pre-load imparted by cyclic loading.

2. Assessment of mechanical properties of confined concrete specimens at elevated temperatures is imperative in numerical modelling of reinforced concrete structures. Investigations on confined concrete specimens of two different levels of confinement *(lateral tie spacing = 42 mm and 68 mm)* under three different target temperatures: 250 °C, 500 °C and 750 °C were planned. Cylindrical specimens of size 150 mm × 600 mm were categorized as specimens without damage and specimens with damage. The specimens under damage category were contrived to impart three different conceptual damage levels in terms of displacements deduced from pre-defined strains. The strain levels were defined in three zones: one at the yield point and two others in plastic zones. The key parameters for evaluation were temperature, damage level and confinement level.

3. Full-scale testing of reinforced concrete framed structure was planned to evaluate its performance under post-earthquake fire. This test targets the response of a framed structure under extreme loading (simulated earthquake and fire) in terms of temperature profiles, displacements and strains. Construction of a reinforced concrete frame of dimensions 3 m × 3 m × 3 m consisting of 4 columns, 4 roof beams, 4 plinth beams and a roof slab was outlined in a outdoor test facility. Simulated earthquake loading was worked out on the frame by double-acting hydraulic jacks in eleven displacement cycles. A maximum target displacement of 150 mm was imparted to the frame. The damage induced frame, susceptible to a greater extent of spalling, was then exposed to a one hour designed compartment fire determined by conducting mock tests prior to construction of the frame. Thereafter, the fire damaged frame was retested and pushed to the ultimate capacity to assess its residual capacity. As a scope, this study confirms the holistic behaviour of structural elements forming the skeleton of reinforced concrete buildings.

4. Analysis of the reinforced concrete frame modelled using the finite element package ABAQUS version 6.8 is the final scope of the study. Validation of experimental results is a vital part of any research. Hence, numerical modelling of the reinforced concrete frame was achieved using solid elements for concrete and truss element for steel. The constitutive material properties were assigned as per Eurocode [34]. The thermal profiles and load-displacement hysteresis plots obtained were compared with the experimental results to demonstrate the validity of the analytical approach in the simulation of RC frame behaviour.

1.4 OVERVIEW OF THESIS

Following the objectives and scope of the research summarized in the previous sections, this section focusses on defining the outline of the thesis. The thesis was broadly divided into six chapters consisting of two general chapters of introduction and conclusions *(Chapters 1 and 6)*, three chapters based on experimental work *(Chapters 2, 3 and 4)* and one chapter based on analytical work *(Chapter 5)*.

Chapter 2 is based on the element-level laboratory testing of commercially available steel reinforcing bars at elevated temperatures. This chapter summarises the testing and assessment of mechanical properties of steel reinforcing bars subjected to elevated temperatures. An explicit study was carried out to study the effect of tensile pre-load on the steel rebars at elevated temperatures, which defines the uniqueness of work.

Chapter 3 sums up the details on experimental evaluation of mechanical properties of undamaged and damaged confined concrete at elevated temperatures. In this chapter, an extensive experimental investigation conducted on confined concrete at different elevated temperatures is outlined. Also, the effect of pre-damage on the mechanical properties of confined concrete has been studied and discussed. The material behavioural changes observed at elevated temperature evident by degradation in strength and stiffness have been presented.

Chapter 4 focuses on the structural response of a full-scale reinforced concrete frame subjected to post-earthquake fire. A panoptic study conducted on structural elements such as beams and columns as an integral part of the building frame has been presented. A reinforced concrete frame assembly consisting of 4 No. floor beams, 4 No. roof beams, 4 No. columns and a roof slab was constructed in a unique outdoor testing facility, which was subjected to a quasi-static push-pull loading using two double-acting hydraulic jacks followed by a one-hour compartment fire. Novel set of results on the building performance has also been summarized. This chapter is based on one of the three full-scale tests on reinforced concrete frame performed as a part of UK-India Education and Research Initiative (UKIERI) sponsored project *"Fire resistance and repair of earthquake damaged structure"*.

Chapter 5 presents the analytical work carried out on reinforced concrete (RC) frame model. The reinforced concrete frame described in Chapter 4 is modelled using the commercial software suite for finite element analysis and computer aided engineering, ABAQUS version 6.9. RC frame was modelled using the inbuilt solid element *(C3D8)* for concrete and truss element *(T3D2)* for steel reinforcement. Constitutive models for concrete and steel were chosen from the Eurocode [34]. A pushover analysis was conducted on the frame by specifying the displacements analogous to those given in the experiment to impart quasi-static earthquake loading. This was followed by heat transfer analysis was and the results obtained were compared with the experimental results given in Chapter 4 *(Subsection 4.4.1.3)*. Key results from the comparison are also discussed.

Chapter 6 gives the conclusions, summing up the complete work discussed and presented in detail in the previous chapters *(2, 3, 4 and 5)*. Presenting the work, findings and remarks, author also recommends the scope of future work in the area of fire following earthquake in this chapter.

Behaviour of UnLoaded and Pre-Loaded Steel Rebars at Elevated Temperatures

2

2.1 INTRODUCTION

Behaviour of reinforced concrete framed structures in fire has been a domain of prime importance over the past decade [32]. Performance based fire design has mandated the investigation of concrete and steel at an elemental level to understand the composite effect of constituent materials in a reinforced concrete member subjected to fire. A number of full scale tests have been performed in the past on composite steel structures [6, 7], which have evaluated the structural response of composite steel structures in fire. However, reinforced concrete has evolved as the primary construction material in some of the countries like India, where most of the multi-storeyed buildings that are exist or are being constructed. Response of steel reinforcing bars at elevated temperatures in reinforced concrete members need in-depth study since the concrete spalling in fire may expose the bars to direct fire scenario, deteriorating its strength and stiffness. Evaluating mechanical properties of rebars at elevated temperatures is also helpful in reckoning the behavioural characteristics of reinforced concrete structures in fire. Unifying the characteristics of steel rebars at elevated temperatures is a complex task due to several reasons. Performance based design practices and research in construction material industry has brought about a wide variety of steel rebars in the commercial market, the elevated temperature behaviour of which is highly non-uniform. This evinces a need to evaluate the mechanical properties and characteristics of commercially available steel rebars at elevated temperatures. Steel rebars inside the concrete can be exposed to temperatures ranging from 100 °C to 900 °C based on a variety of aspects such as location of the rebar, clear cover, number of exposed face, duration of fire and concrete spalling (if occurred). However, predicting the behaviour of RC members with respect to the reinforcement failure is a complex phenomenon that involves certain material and geometric parameters. [32]. A number of numerical approaches have been developed in the past decade which reports the prediction of the level of deformation and load corresponding to failure by reinforcement fracture at elevated temperature [24, 31, 42, 63, 64]. Nevertheless, these predictions need an experimental evaluation of reinforcing bars at desired levels of temperature. Evaluation of mechanical properties of steel rebars with and without pre-load at elevated temperature at elevated temperature finds its applications in development of steel material models likely to be used in reinforced concrete structural members subjected to earthquake triggered fire. Fairly good literature [32, 62, 81, 83] is available on tensile testing and mechanical properties of steel rebars at elevated temperatures whereas the information available on pre-loaded steel rebars is scanty. Pre-loaded rebars simulate the stressed conditions of rebars in concrete members damaged in a natural hazard, particularly earthquakes. An attempt was made to simulate the condition before heating the rebar specimens to target temperature and loading it to failure. A quantitative comparison of results reported by various authors is not feasible due to the differences in materials used and testing conditions. Analysis of reinforced concrete structures in context of fire following earthquake requires properties of pre-loaded and damaged (due to pre-load) steel rebars at elevated temperatures. The damage induced by the earthquake is simulated in lab conditions by applying a pre-load in tension on rebars before subjecting them to elevated temperatures. Behaviour of concrete and steel rebars at high temperature is important for predicting the response of reinforced concrete structures at elevated temperatures [81]. The deterioration of the mechanical properties such as peak stress and modulus of elasticity is considered as the primary element affecting the performance of steel structures under fire [83]. In the present experimental investigation, 72 ribbed rebar specimens of different type and diameters were tested in tension at elevated temperatures. Test specimens were prepared from the materials used in construction of full-scale reinforced concrete frame subjected to simulated earthquake and fire. First set of specimens were tested at desired elevated temperature without any pre-load. i.e., the bars were heated to the target temperature and tested in tension to failure under uniaxial steady state conditions. Second set of specimens were initially stressed to a certain known limit (0.58 fy) to simulate damage caused by an earthquake. After inducing the damage, they were exposed to a desired temperature level in a circular furnace arrangement coupled with a 400 kN universal testing machine. The bars were then tested in tension to failure under uniaxial steady state conditions. The elongation was recorded using two LVDTs fixed between gauge lengths of 270 mm at the mid-height. Results obtained in the tests will be utilized to draw various relationships: Tensile Strength, peak stress, strain at peak stress, ultimate strain and initial elastic modulus vs. Temperature, Stress vs. Strain at elevated temperatures.

2.2 ELEVATED TEMPERATURE PROPERTIES OF STEEL REBARS

Commercially available steel rebars utilized for construction possess different characteristics and mechanical properties based on their type. The behaviour of these steel rebars at elevated temperature, their reduction in strength and stiffness is greatly influenced by their manufacturing process. [4, 5, 24, 34]

Eurocode 2 [34] establishes an idealized stress-strain relationship, which gives the strength and deformation properties for the steel reinforcing bars at elevated temperatures. The stress-strain curve per EC 2 is defined by three parameters: the slope of the linear elastic range, $E_{s,\theta}$, the proportional limit $f_{sp,\theta}$ - the maximum stress level $f_{sy,\theta}$. Figure 2.1 shows the idealized stress strain cure for steel rebars at elevated temperatures.

Mathematical model for stress strain relationship of steel rebars at elevated temperatures is depicted

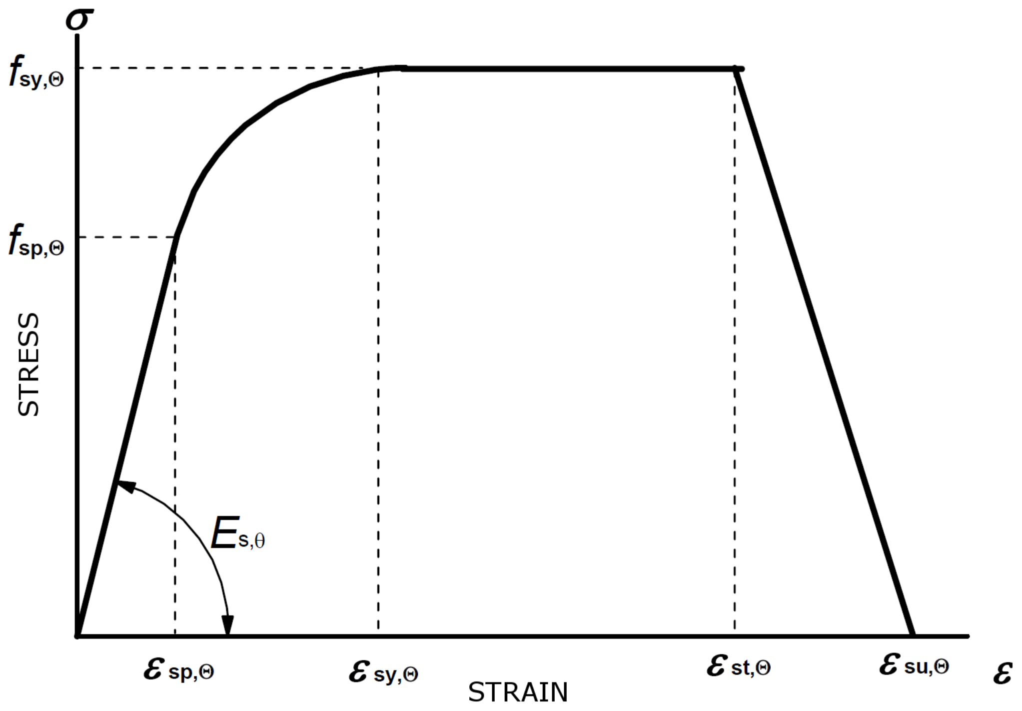

Fig. 2.1: Stressstrain for reinforcing bars at elevated temperature per Eurocode 2

in Table 2.1.The parametric values have been defined for both hot rolled and cold worked steel rebars. Table 2.2 and Table 2.2 show the three parameters for hot rolled and cold worked steel reinforcing bars at elevated temperatures.

The stress-strain relationship given in Eurocode 2 [34], as shown in Figure 2.1 follows a linear trend initially, followed by an elliptical representation until the maximum stress is achieved at a strain of $\epsilon_{sy,y}$, after which a constant strength is assumed between $\epsilon_{sy,y}$ and $\epsilon_{st,y}$. $E_{s,y}$, $f_{sp,y}$ and $f_{sy,y}$ are the main parameters related to strength and stiffness, for which reduction factors are assigned at elevated temperatures. Eurocode approach assigns a constant value for parameters related to ductility $\epsilon_{sy,y}$, $\epsilon_{sy,y}$ and $\epsilon_{su,y}$: 0.02, 0.15 and 0.2, respectively (for Class B and C reinforcement) and 0.02, 0.05 and 0.1, respectively (for Class A reinforcement) and considers them as temperature independent. The code thus considers ductility of reinforcement as temperature independent.
Elghazouli et al., [32] have investigated the accuracy of this assumption. The code recommends a constant value for coefficient of thermal expansion: $14 \times 10^{-6} / {}^{\circ}\mathrm{C}$ for convenience in calculation of simple models. Steel is expected to exhibit the creep strain effects when exposed to elevated temperatures and time dependent stresses, which is shown to be insignificant up to temperatures around 400 - 500 °C [24]. The expansion at higher temperature increases with time at constant temperature and stresses, although the process proceeds more rapidly. Creep- related strain calculations are tedious and thus it tends to be implicitly accounted for in the stressstrain idealisations used in analysis. However, it has been shown [84] that within a realistic range of heating rates that are representative of real fires (i.e. between $5\,{}^{\circ}\mathrm{C}/min$ for a member with heavy insulation to $50\,{}^{\circ}\mathrm{C}/min$

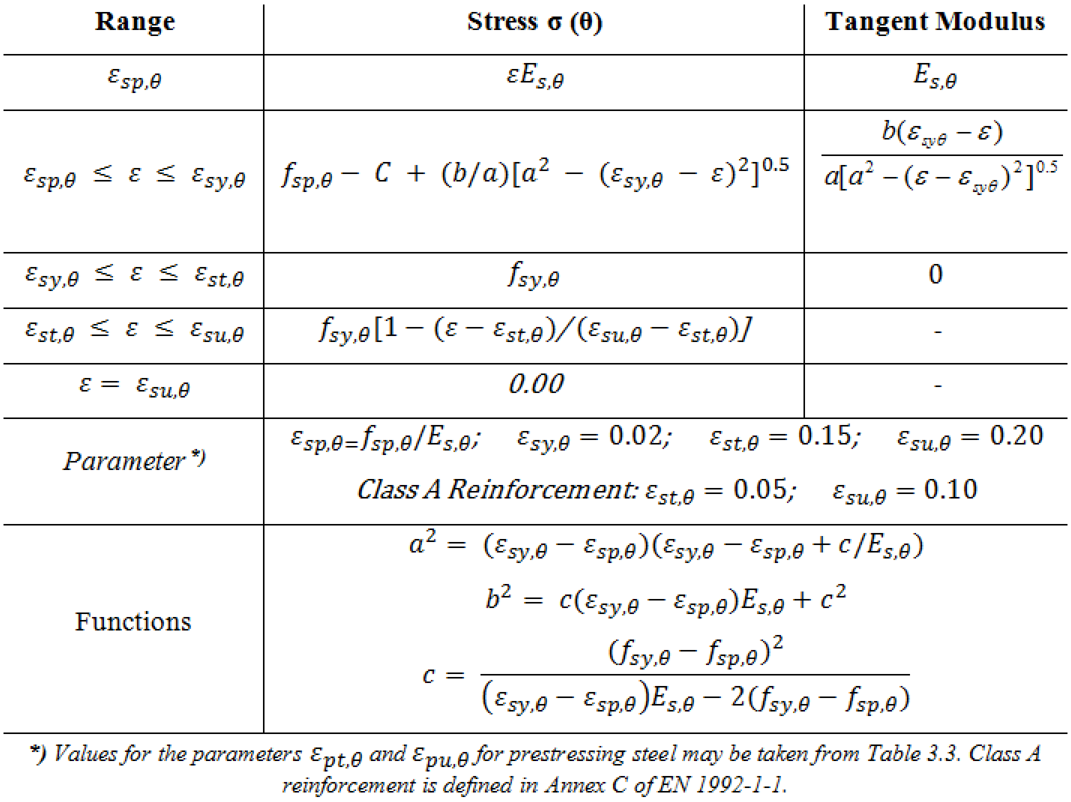

Range	**Stress σ (θ)**	**Tangent Modulus**
$\varepsilon_{sp,\theta}$	$\varepsilon E_{s,\theta}$	$E_{s,\theta}$
$\varepsilon_{sp,\theta} \le \varepsilon \le \varepsilon_{sy,\theta}$	$f_{sp,\theta} - C + (b/a)[a^2 - (\varepsilon_{sy,\theta} - \varepsilon)^2]^{0.5}$	$\frac{b(\varepsilon_{sy\theta} - \varepsilon)}{a[a^2 - (\varepsilon - \varepsilon_{sy\theta})^2]^{0.5}}$
$\varepsilon_{sy,\theta} \le \varepsilon \le \varepsilon_{st,\theta}$	$f_{sy,\theta}$	0
$\varepsilon_{st,\theta} \le \varepsilon \le \varepsilon_{su,\theta}$	$f_{sy,\theta}[1 - (\varepsilon - \varepsilon_{st,\theta})/(\varepsilon_{su,\theta} - \varepsilon_{st,\theta})]$	-
$\varepsilon = \varepsilon_{su,\theta}$	*0.00*	-
*Parameter *)*	$\varepsilon_{sp,\theta} = f_{sp,\theta}/E_{s,\theta}$; $\varepsilon_{sy,\theta} = 0.02$; $\varepsilon_{st,\theta} = 0.15$; $\varepsilon_{su,\theta} = 0.20$ *Class A Reinforcement:* $\varepsilon_{st,\theta} = 0.05$; $\varepsilon_{su,\theta} = 0.10$	
Functions	$a^2 = (\varepsilon_{sy,\theta} - \varepsilon_{sp,\theta})(\varepsilon_{sy,\theta} - \varepsilon_{sp,\theta} + c/E_{s,\theta})$ $b^2 = c(\varepsilon_{sy,\theta} - \varepsilon_{sp,\theta})E_{s,\theta} + c^2$ $c = \frac{(f_{sy,\theta} - f_{sp,\theta})^2}{(\varepsilon_{sy,\theta} - \varepsilon_{sp,\theta})E_{s,\theta} - 2(f_{sy,\theta} - f_{sp,\theta})}$	

**) Values for the parameters $\varepsilon_{pt,\theta}$ and $\varepsilon_{pu,\theta}$ for prestressing steel may be taken from Table 3.3. Class A reinforcement is defined in Annex C of EN 1992-1-1.*

Tab. 2.1: Mathematical model for stress strain relationships of reinforcing steel at elevated temperatures

for a non-insulated member), the development of creep strain is insignificant.

The experimental study by Elghazouli et al., [32] focuses on assessing the stressstrain behaviour of deformed and plain bars of relatively small diameters that may be typically employed in composite slabs. The tests consider the behaviour at temperature levels that may be reached by the reinforcement within the cross-section of composite slabs, as well as the residual properties after cooling. Influence of elevated temperature on ductility of steel rebars (in terms of ultimate strain at fracture) has been emphasized in the investigation. This is regarded as critical for reliable assessment of the performance of structural members in fire.

Eurocode 2 [34] neglects the strain-hardening effect of steel at elevated temperatures. However, in case of accurate analysis, Eurocode 4 [35] proposes a secondary model in which strain hardening is considered up to 400 °C, where significant hardening is generally observed.

2.3 EXPERIMENTAL EVALUATION

2.3.1 General

As noted before, the current chapter is focused on experimentally determining the mechanical properties of various commercially available special purpose reinforcing bars used in construction. SAIL TMT EQR deformed bars were used for the experimental investigation. EQR stands for earthquake

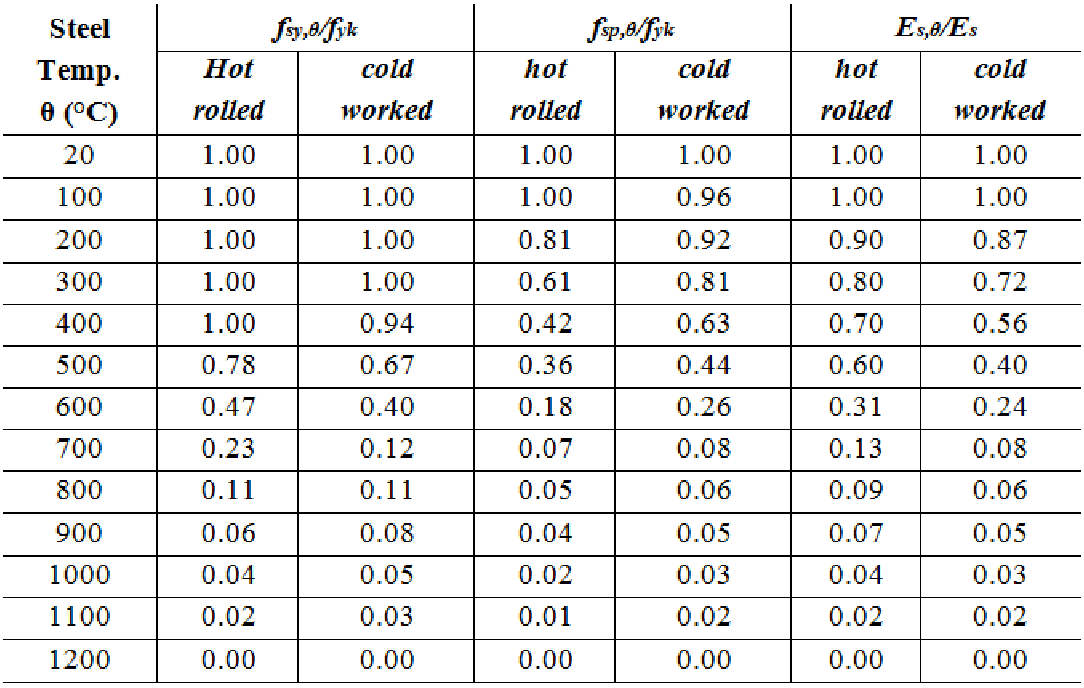

Steel Temp. θ (°C)	$f_{sy,\theta}/f_{yk}$		$f_{sp,\theta}/f_{yk}$		$E_{s,\theta}/E_s$	
	Hot rolled	***cold worked***	***hot rolled***	***cold worked***	***hot rolled***	***cold worked***
20	1.00	1.00	1.00	1.00	1.00	1.00
100	1.00	1.00	1.00	0.96	1.00	1.00
200	1.00	1.00	0.81	0.92	0.90	0.87
300	1.00	1.00	0.61	0.81	0.80	0.72
400	1.00	0.94	0.42	0.63	0.70	0.56
500	0.78	0.67	0.36	0.44	0.60	0.40
600	0.47	0.40	0.18	0.26	0.31	0.24
700	0.23	0.12	0.07	0.08	0.13	0.08
800	0.11	0.11	0.05	0.06	0.09	0.06
900	0.06	0.08	0.04	0.05	0.07	0.05
1000	0.04	0.05	0.02	0.03	0.04	0.03
1100	0.02	0.03	0.01	0.02	0.02	0.02
1200	0.00	0.00	0.00	0.00	0.00	0.00

(a)

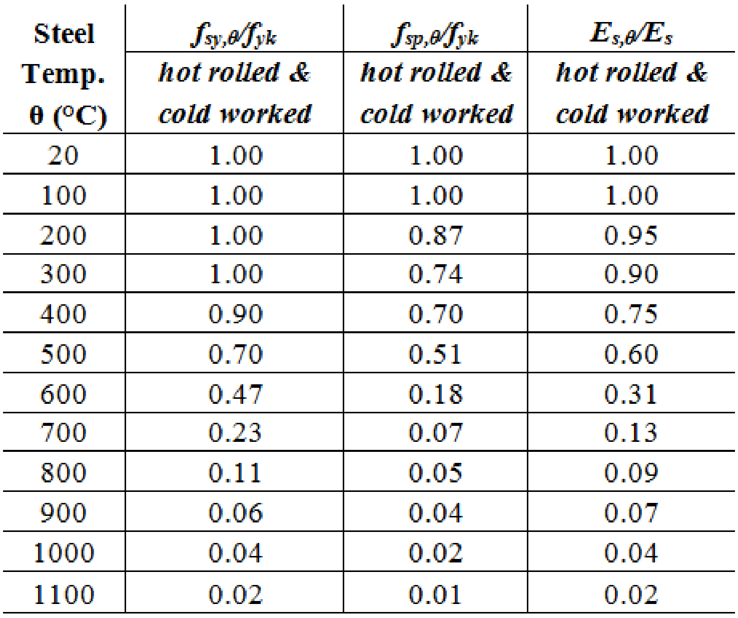

Steel Temp. θ (°C)	$f_{sy,\theta}/f_{yk}$	$f_{sp,\theta}/f_{yk}$	$E_{s,\theta}/E_s$
	hot rolled & cold worked	***hot rolled & cold worked***	***hot rolled & cold worked***
20	1.00	1.00	1.00
100	1.00	1.00	1.00
200	1.00	0.87	0.95
300	1.00	0.74	0.90
400	0.90	0.70	0.75
500	0.70	0.51	0.60
600	0.47	0.18	0.31
700	0.23	0.07	0.13
800	0.11	0.05	0.09
900	0.06	0.04	0.07
1000	0.04	0.02	0.04
1100	0.02	0.01	0.02

(b)

Tab. 2.2: Values for the parameters of the stress-strain relationship of hot rolled and cold worked reinforcing steel at elevated temperatures (a) Class X (b) Class N resistance. These bars are thermo-mechanically treated, high plastic and elastic energy absorbing and most suitable for construction in seismic zones. The bars are in compliance with IS 1786: 2008 norms. Their capability of being ductile makes them more energy absorbent when loaded beyond yield point, which is the condition expected in natural hazards such as earthquakes and tsunamis. Apart from ductility, they possess better weldability, bond strength, bendability, fire resistance when embedded in concrete and exposed upto 600 °C and corrosion resistance. The bars also have a pre-defined ultimate tensile strength to yield strength ratio accounting for additional safety. Two types of bars: fe-500D and fe-500 categorized based on IS 1786:2008 were considered for investigation. The bars were chosen from the same lot used in the construction of a full-scale reinforced concrete frame tested for earthquake triggered fire, described in CHAPTER 4.

2.3.2 Specimens for Elevated Temperature Tensile Test

Steel reinforcing bars of four different diameters, 8 mm, 10 mm, 16 mm and 20 mm were considered for performing tensile test at elevated temperatures. 16 mm and 8 mm dia bars (fe-500) were used as main and secondary reinforcements for beams in the RC frame respectively, whereas 20 mm and 10 mm diameter bars (fe-500D) were used as main and secondary reinforcements in columns of RC frame respectively. A specimen of length 700 mm was chosen in order to ensure proper grip in the jaws of a tension testing machine outside the furnace. A total gauge length of 270 mm was considered for the measurement of expansion since the length of bar inside the furnace, exposed to elevated temperature was 265 mm. Table 2.3 shows the specimen data and testing plan.

2.3.3 Test Setup

A unique testing arrangement facilitated the application of mechanical and thermal loads on the rebar specimens simultaneously. The rebar specimens were subjected to tensile loading at ambient temperature in the same arrangement as that of elevated temperature tests, to facilitate identical testing conditions. Figure 2.2 shows the schematic of the testing arrangement for steel rebars at ambient and elevated temperatures. A round electric furnace with a 50 mm diameter and 260 mm long heating zone encapsulated the test specimen. Two rods were clamped to the specimen just outside the furnace to mark the gauge length. Linear variable differential transformers (LVDT) / displacement transducers mounted on these rods between the gauge lengths facilitated in monitoring the deflection of the specimen under uniaxial tension. Measures were taken to insulate the arrangement from getting affected by heat. Figure 2.3 shows the actual test setup for rebars at elevated temperature.

2.3.4 Instrumentation

The test setup shown in Figure 2.3 was facilitated with automatic data acquisition scheme. Two K-type sheathed thermocouples were positioned at the openings of the circular furnace to record the temperature throughout the test. The furnace was attached to a microcontroller unit. This unit aided the elaborate programming of heating and cooling cycles of the test. A pressure sensor, fitted at the

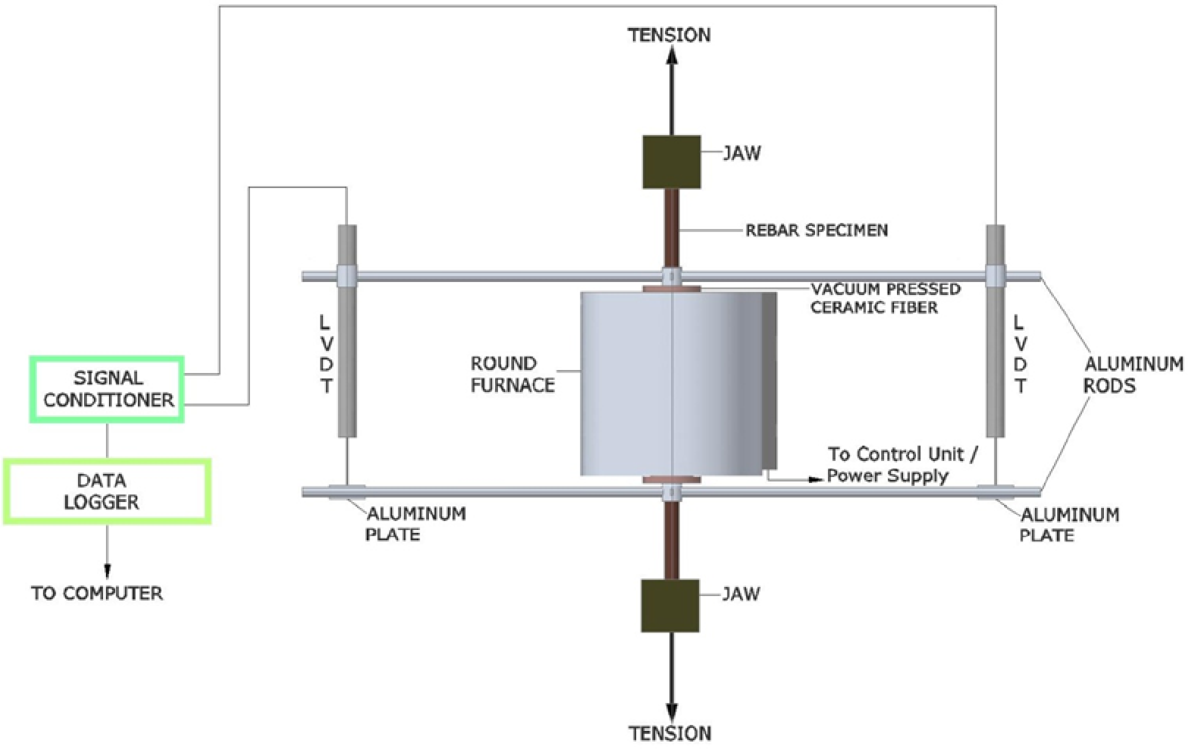

Fig. 2.2: Testing arrangement for steel rebars at elevated temperature

inlet of hydraulic supply unit of the universal testing machine helped in monitoring the oil pressure and hence the load. As mentioned in the previous sub-section, deflection was measured using two AC LVDTs positioned on either side across a fixed gauge length of 270 mm. These LVDTs were capable of measuring deflections upto 100 mm. Temperature, load and deflection data were collected at a frequency of 1 second using automated data acquisition system connected to a laptop computer. Real time data was monitored throughout the test.

2.3.5 Tensile Test of Rebar Specimens

The experimental investigation was primarily aimed at performing 3 types of tensile test on reinforcing bar specimens (a) Ambient temperature tensile test (b) Steady state elevated temperature tensile test (c) Steady state elevated temperature tensile test at a pre-defined load. Table 2.3 shows the specimen details and testing plan. In ambient temperature tensile test, the rebar specimens were subjected to tensile loading in the same arrangement as that of elevated temperature tensile tests, to maintain identical testing conditions. At least 3 specimens of each diameter were tested in tension. A length of 260 mm at the center of the specimen was enclosed in a round furnace. 50 mm at each ends were gripped between the top and bottom jaws of the 400 kN universal testing machine set to perform a tensile test. Attempts were made to maintain a constant loading rate throughout the test. The rebar was loaded to failure at ambient temperature.

In steady state elevated temperature tensile test, the rebar specimen was initially exposed to three different temperatures: 250 °C, 500 °C and 750 °C. A heating rate of 5 °C/$minute$ was employed to achieve the target temperature. Figure 2.4 shows typical input temperature-time curves, to which

Fig. 2.3: Tensile test setup for steel rebars at elevated temperature

Diameter (mm)	**Ambient Temperature Tensile Test**	**Steady State Elevated Temperature Tensile Test**			**Steady State Elevated Temp. Tensile Test with Pre-Load**		
		Temperature			**Temperature**		
	20°C	**250°C**	**500°C**	**750°C**	**250°C**	**500°C**	**750°C**
8	3	3	3	3	3	3	3
10	3	3	3	3	3	3	3
16	3	3	3	3	3	3	3
20	3	3	3	3	3	3	3

Tab. 2.3: Testing plan for elevated temperature tensile tests

the rebar specimens were exposed. The target temperature was maintained constant for duration of 30 minutes in order to achieve a steady state in rebars. The target temperature was also maintained during the mechanical loading to ensure the steady state condition.

In steady state elevated temperature tensile test at a pre-defined load, the rebar specimen was initially loaded to a certain stress-level before exposing them to elevated temperature. The stress level identified was in the range of $0.4 - 0.6$ times the yield stress i.e., $0.4 - 0.6\sigma_y$. The assumed pre-loading level has been chosen by considering the fact that the design yield stress in the reinforcing bar $0.87\sigma_y$ and its corresponding partial load factor if 1.5, used in the limit state design. Under service conditions, the initial stress level, assumed as the pre-load level, is considered to be the ratio of design yield stress and partial load factor i.e., $0.4 - 0.6\sigma_y$. The defined pre-load was induced in the specimen before the heating was started. The rebar specimen was then exposed to the target temperature and upon reaching the steady state; the specimen was loaded to failure. Under all circumstances, the specimen was loaded uniaxially in tension with a very low and constant loading rate ($< 10 ton/min$). Care was taken to ensure a proper grip of clamps onto the rods during the test, especially at elevated temperatures since elevated temperature tests were subjected to the risk of reduction in cross-section due to softening. The openings of the furnace were thoroughly insulated with glass wool to prevent the escape of heat outside the furnace and maintain a uniform temperature.

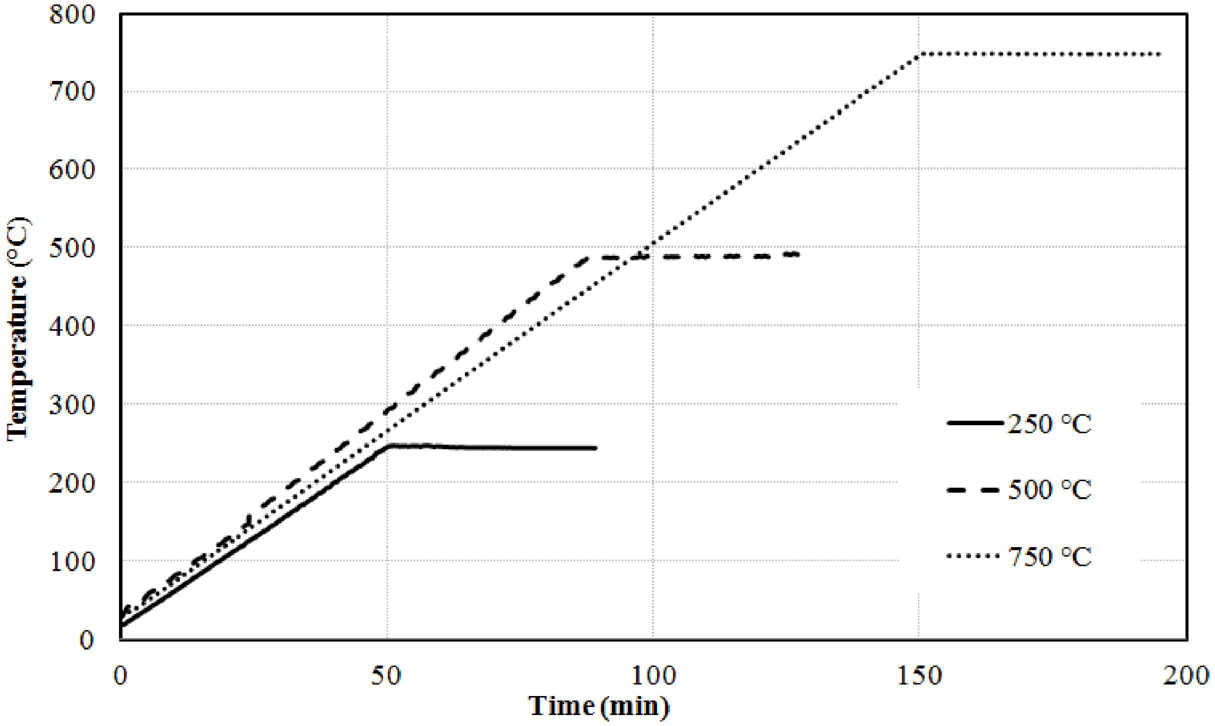

Fig. 2.4: Typical input temperature time curves

2.4 RESULTS AND DISCUSSION

Results obtained from the tests exhibit a reduction in tensile strength, modulus of elasticity and strain at peak stress at elevated temperatures as it is more pronounced from available literature [32,34,38,62].

The test is ultimately aimed at generating stress-strain relationships of steel reinforcing bars with and without pre-load at elevated temperatures. Also, emphasis is laid on development of mechanical strains, transient plastic strains during pre-loading and variation of modulus of elasticity at elevated temperatures.

2.4.1 Stress-Strain Relationships

It should be noted that the ‘stress-induced strain or ‘mechanical strain is accompanied by the thermal strains at elevated temperature. The total displacement exhibited by the reinforcement at elevated temperature also includes the influence of strain arising from thermal expansion. The strains reported in this investigation are a combination of both mechanical and thermal strains. However, the thermal strain is expected to recover on cooling. Figures 2.5(a), 2.5(b), 2.5(c) and 2.5(d) show the stress-strain plots for 8, 10, 16 and 20 mm diameter rebars subjected to 20, 250, 500 and 750 °C without any pre-load respectively. From these plots, it can be clearly observed that 8 mm and 16 mm diameter bars exhibited a similar trend and 10 mm and 20 mm bars exhibited a similar trend. This is attributed to the fact that 8 mm and 16 mm diameter bars belonged to the fe 500 category of bars that have higher yield and ultimate strengths ($> 800\ Mpa$) with a fairly average ductility. On the other hand, 10 mm and 20 mm diameter bars fall under fe500D category possessing high ductility and slightly lower ultimate strength ($< 600\ Mpa$). The peak stress in the rebars does not show much degradation upto a temperature of 250 °C. Further, the peak stress in rebars of all diameters exhibited an enormous degradation in peak stress at elevated temperatures.

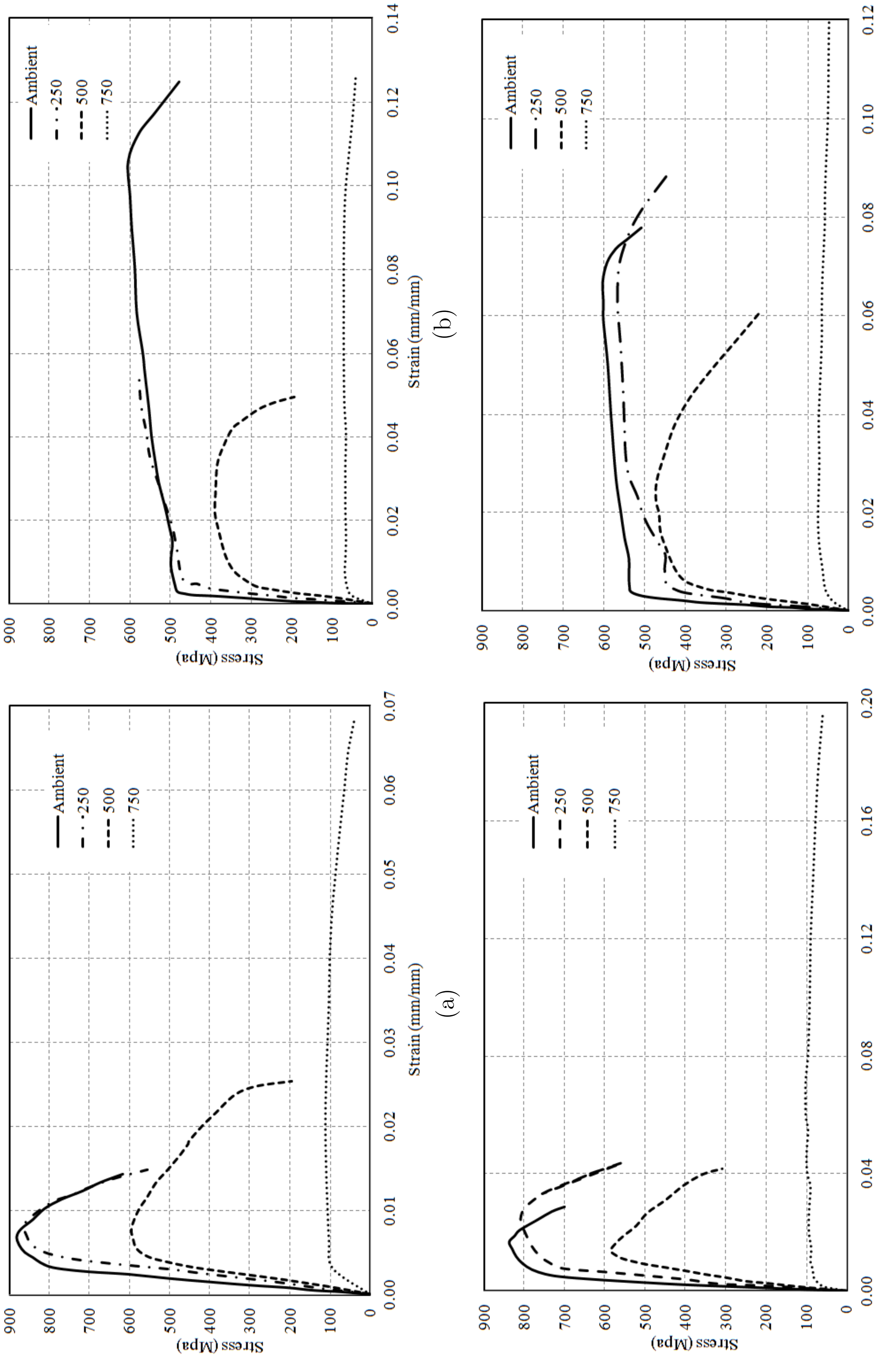

Fig. 2.5: Stress-Strain plot for steel rebars without pre-load (a) 8 *mm* (b) 10 *mm* (c) 16 *mm* (d) 20 *mm*

Figures 2.6(a) and (b) show the normalized peak stress, ($\sigma'_{sT}/\sigma'_{s0}$) plotted against the temperature. Figure 2.6 (a) shows the variation of peak stress for fe 500 reinforcing bars, i.e., 8 *mm* and 16 *mm* diameter bars at elevated temperatures. A percentage degradation of 3%, 31% and 88% in peak stress was registered at 250 °C, 500 °C and 750 °C. Figure 2.6 (b) shows the variation of peak stress (normalized) for fe 500D (10 *mm* and 20 *mm* diameter) reinforcing bars at elevated temperatures. A percentage degradation of 5%, 28% and 88% in peak stress was registered at 250 °C, 500 °C and 750 °C. No specific pattern was observed in strain at peak stress and ultimate strain at elevated temperatures. This is attributed to the type of rebars (fe 500 / fe 500D) and efficiency of load-controlled testing machine in maintaining a constant loading rate. In the figures, 2.7 (a) and (b), normalized modulus of elasticity (E_{sT}/E_{s0}) is plotted against the temperature . Figure 2.7 (a) shows the variation in modulus of elasticity of fe 500 reinforcing bars (8 *mm* and 16 *mm* diameter) at elevated temperatures. Modulus of elasticity registered a reduction by 15%, 52% and 88% at 250 °C, 500 °C and 750 °C. Figure 2.7 (b) depicts the comparison of fe 500D (10 *mm* and 20 *mm*) reinforcing bars at elevated temperatures. Similar to fe 500 bars, a degradation of 16%, 55% and 89% was observed at a temperature of 250 °C, 500 °C and 750 °C respectively.

2.4.2 Influence of Pre-loading

In practice during a fire scenario, weakening of the structural concrete transfers the loading on steel rebars. Literature [40] shows that the steel under the combined actions of applied stress and elevated temperature results in inducing a creep. Creep strains occur at a temperature of about 400 °C at a constant stress rate. In a case where high stress and temperature varies with time, creep in steel becomes evident even at 300 °C [49].

Figure 2.8 (a), Figure 2.8 (b), Figure 2.8 (c) and Figure 2.8 (d) shows the stress-strain plots for 8, 10, 16 and 20 *mm* diameter pre-loaded rebars subjected to 250, 500 and 750 °C respectively. From the plots, it is evident that peak stress and strain at peak stress decreases with increase in temperature. Analogous to rebars tested without pre-load, the peak stress increases slightly at 250 °C. Table 2.4 and Table 2.5 summarize the results from the test. Peak stress, ultimate strain and strain at peak stress, modulus of elasticity and transient plastic strain (pre-loaded bars) for each diameter rebar at a particular temperature for steel rebars without pre-load and pre-loaded steel rebars at elevated temperatures.

For rebar specimens without preload, marginal or no change in material behaviour is observed around 250 °C. About 95% - 97% of original strength is retained 250 °C. This phenomenon is attributed to the fact that no degradation in strength occurs until re-crystallization temperature of 450 °C is reached. At 500 °C, 65% - 75% of original strength is retained. At temperatures beyond 500 °C, rapid degradation of strength is observed due to material softening. Only about 12% of peak stress is retained at 750 °C. The fact is also attributed to maximum reduction in dislocation density by re-crystallization process coupled with grain growth [72].

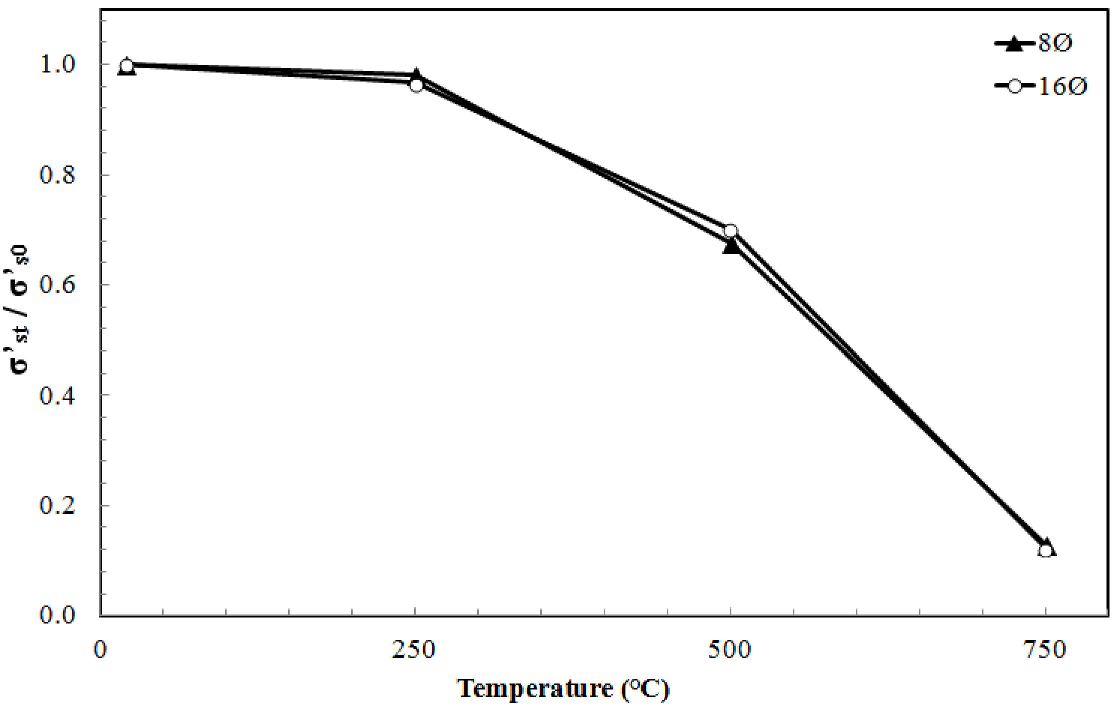

(a)

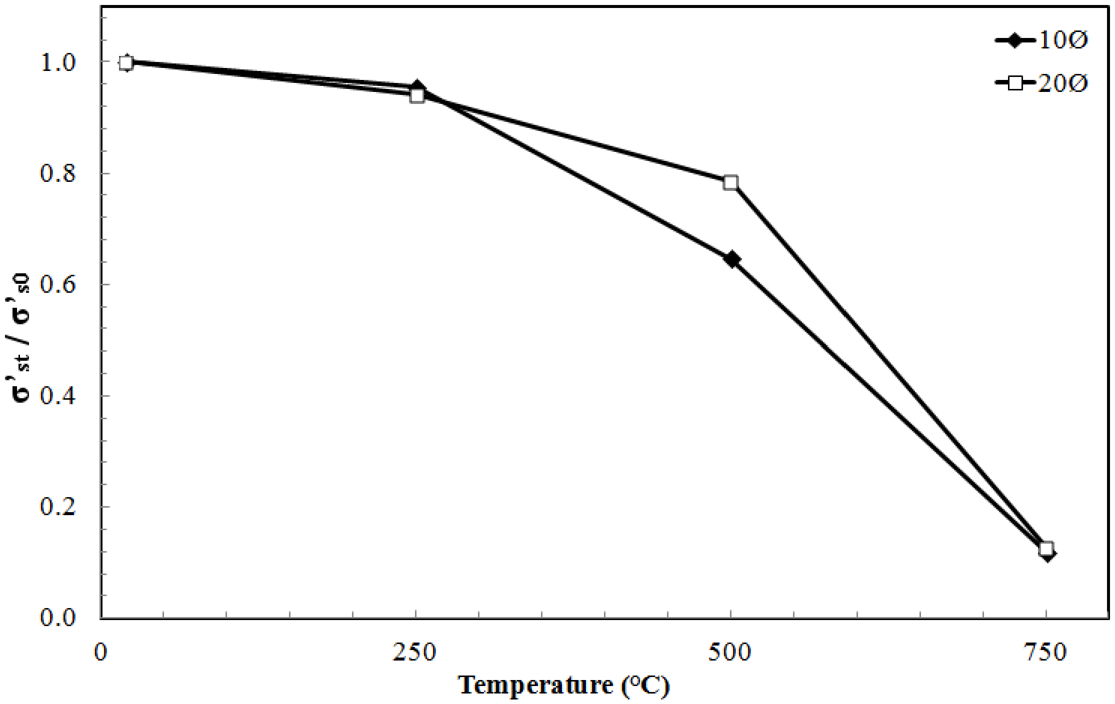

(b)

Fig. 2.6: Variation of peak stress for: (a) fe 500 (b) fe 500D reinforcing bars at elevated temperatures

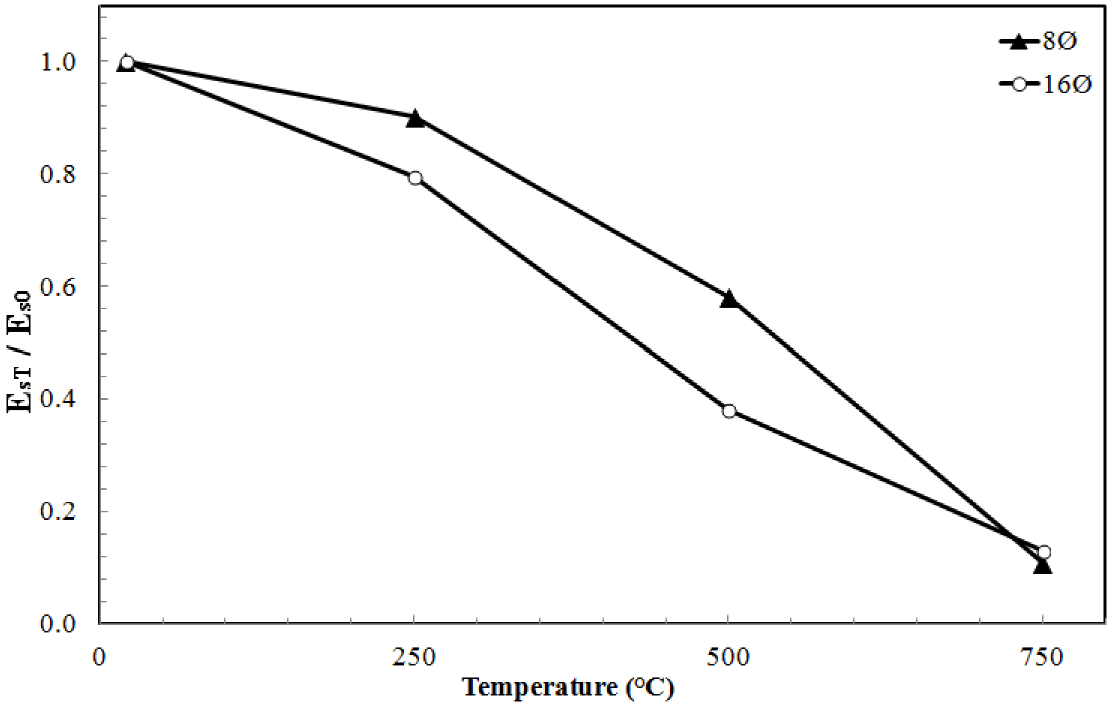

(a)

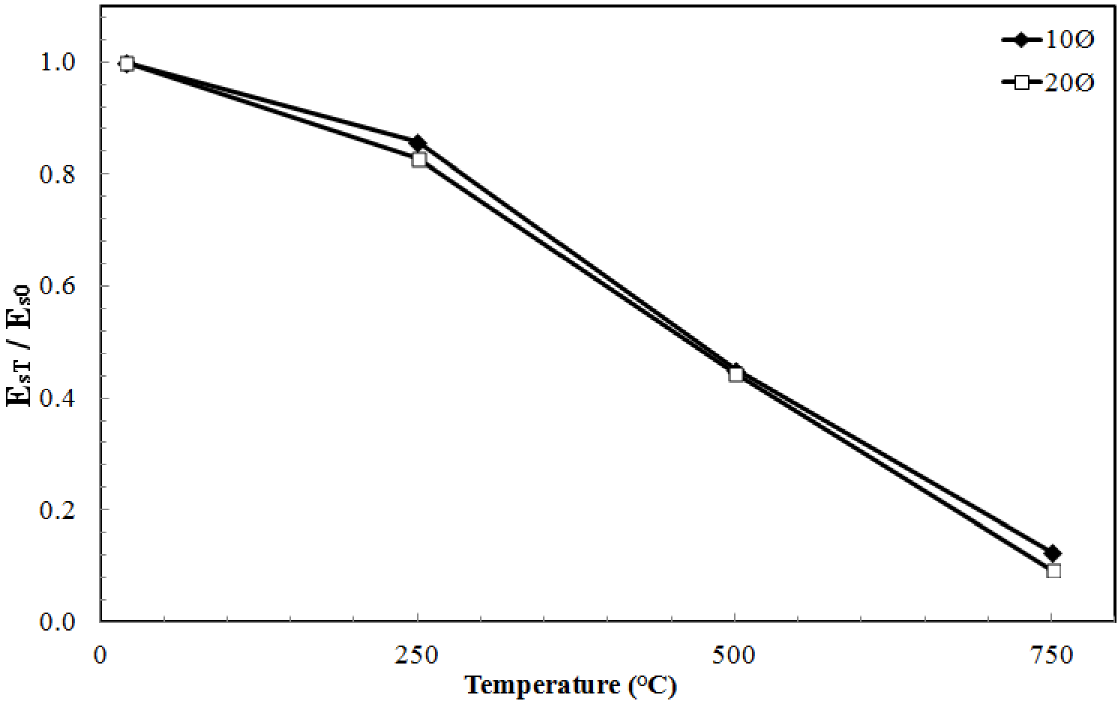

(b)

Fig. 2.7: Variation of Modulus of Elasticity for (a) fe500 (b) fe 500D reinforcing bars at elevated temperatures

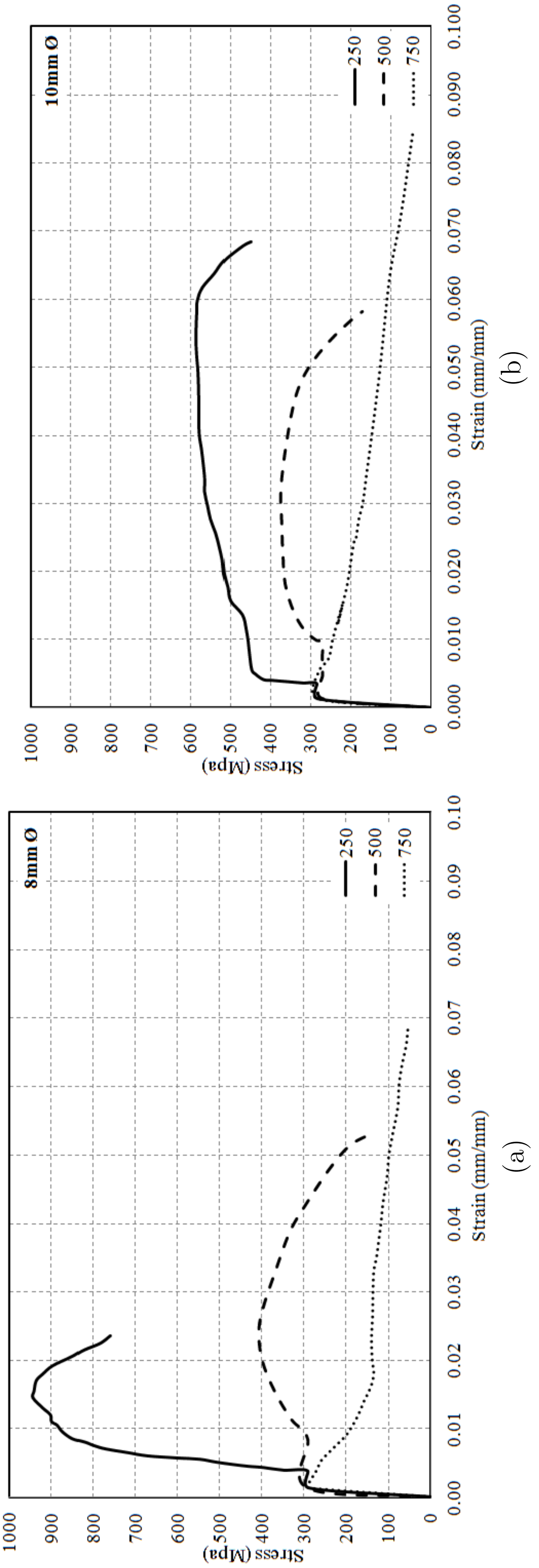

(a) (b) (c) (d)

Fig. 2.8: Stress-Strain plot for pre-loaded steel rebars (a) 8 mm (b) 10 mm (c) 16 mm (d) 20 mm

Ambient

Dia of the Bar (mm)	Proportionality Limit (Mpa)	Elastic Modulus (Mpa)	Peak Stress (Mpa)	Strain at Peak Stress	Ultimate Strain
20	503.00	2.15E+05	602.61	0.0668	0.0734
16	703.85	2.18E+05	837.25	0.0166	0.0285
10	438.87	2.10E+05	605.37	0.1057	0.1247
8	802.13	2.00E+05	881.78	0.0069	0.0143

250 °C

Dia of the Bar (mm)	Proportionality Limit (Mpa)	Elastic Modulus (Mpa)	Peak Stress (Mpa)	Strain at Peak Stress	Ultimate Strain
20	402.78	1.78E+05	567.61	0.0637	0.0893
16	532.69	1.74E+05	809.04	0.0236	0.0433
10	402.63	1.80E+05	578.31	0.0528	0.0554
8	702.35	1.80E+05	865.68	0.0080	0.0148

500 °C

Dia of the Bar (mm)	Proportionality Limit (Mpa)	Elastic Modulus (Mpa)	Peak Stress (Mpa)	Strain at Peak Stress	Ultimate Strain
20	306.42	9.57E+04	473.26	0.0223	0.0606
16	355.77	8.36E+04	586.92	0.0138	0.0416
10	283.48	9.47E+04	391.32	0.0218	0.0495
8	447.12	1.16E+05	596.82	0.0079	0.0254

750 °C

Dia of the Bar (mm)	Proportionality Limit (Mpa)	Elastic Modulus (Mpa)	Peak Stress (Mpa)	Strain at Peak Stress	Ultimate Strain
20	*Indistinct*	2.01E+04	76.09	0.0190	0.1471
16	*Indistinct*	2.85E+04	101.96	0.0600	0.1967
10	*Indistinct*	2.66E+04	71.50	0.0607	0.1263
8	*Indistinct*	2.17E+04	112.96	0.0202	0.0202

Tab. 2.4: Mechanical properties of reinforcing bars at elevated temperatures without pre-load

250 °C

Dia of the Bar (mm)	**Transient Creep Strain**	**Proportionality Limit (Mpa)**	**Reloading Modulus (Mpa)**	**Peak Stress (Mpa)**	**Strain at Peak Stress**	**Ultimate Strain**
20	3.90E-03	478.81	1.49E+05	625.65	0.0636	0.0925
16	2.70E-03	605.10	1.36E+05	841.97	0.0270	0.0394
10	2,20E-03	414.53	1.99E+05	587.56	0.0526	0.0683
8	2.50E-03	786.32	1.94E+05	943.01	0.0145	0.0236

500 °C

Dia of the Bar (mm)	**Transient Creep Strain**	**Proportionality Limit (Mpa)**	**Reloading Modulus (Mpa)**	**Peak Stress (Mpa)**	**Strain at Peak Stress**	**Ultimate Strain**
20	6.50E-03	334.75	6.75E+04	439.12	0.0220	0.0635
16	6.22E-03	494.69	6.10E+04	540.93	0.0140	0.0420
10	8.23E-03	301.28	5.15E+04	376.32	0.0321	0.0580
8	7.10E-03	368.89	1.65E+04	407.37	0.0244	0.0528

750 °C

Mechanical Properties Indistinctive at this Temperature

Tab. 2.5: Mechanical properties of pre-loaded reinforcing bars at elevated temperatures

For specimens with induced pre-load, slightly better performance was observed with increasing temperature upto 500 °C. 20 *mm*, 16 *mm* and 10 *mm* diameter rebars were found to sustain the pre-load until the target temperature of 500 °C. 8 *mm* diameter rebars were unable to sustain the temperature for a long time and yielded very soon. No pre-loaded rebars could sustain the pre-load until they reached the target temperature of 750 °C. They yielded in tension and failed due to increasing temperature. It was observed that a temperature beyond 600 °C proved to be fatal to rebars that were pre-loaded. An increase in strength of about 2% was observed at 250 °C in pre-load. This is again attributed to the effect of rebars below re-crystallization temperature. 61% of original peak stress was retained at a temperature of 500 °C, which is 12% less than the peak stress retained by the rebars at the same temperature without pre-load. Overall, compared with the results of rebars tested without the pre-load, an increase in yield strength and decrease in ductility were observed in the specimens tested at elevated temperature with pre-loading.

2.4.3 Variation of Plastic Strain

Figures 2.9 (a), (b), (c) and (d) show the variation of plastic strain vs. stress w.r.t temperature in reinforcing bars of diameter 8 *mm*, 10 *mm*, 16 *mm* and 20 *mm* respectively. Regression analysis was carried out on the plastic strain data and a normalized expression was proposed to calculate the plastic strains knowing the stress and vice-versa. The normalized expression is as shown in Equation

2.1. Equation 2.1 can be expanded into Equation 2.2. The equation contains temperature dependent coefficients, which can be calculated by the expression given in Equation 2.3. The two coefficients, i and i can be obtained from Table 2.6 and 2.7 respectively. Table 2.6 gives the value of the coefficients for Fe500 rebars, i.e., 8 mm and 16 mm whereas Table 2.7 gives the coefficients for Fe500D rebars, i.e., 10 mm and 20 mm.

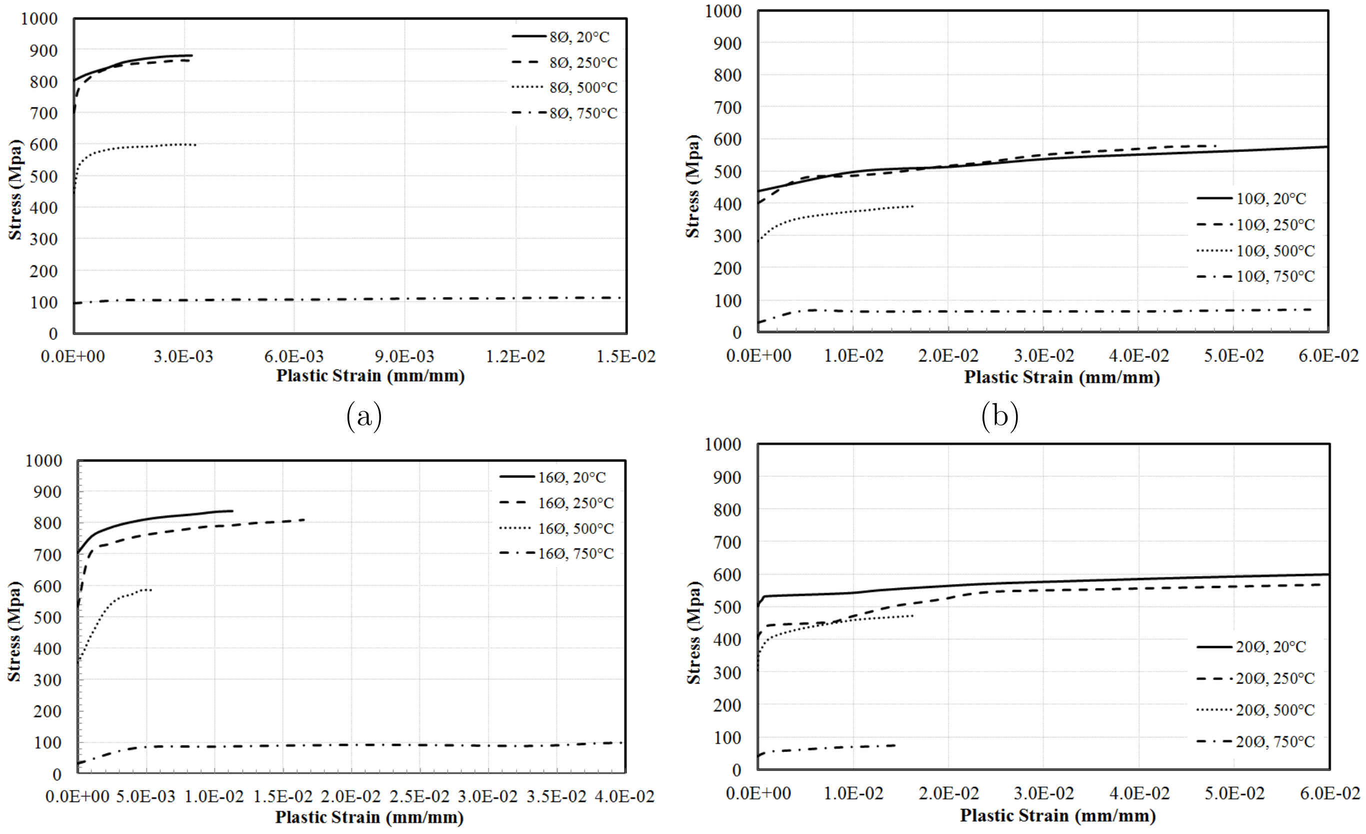

(a) (b) (c) (d)

Fig. 2.9: Variation of Plastic Strain for steel rebars without pre-load(a) 8 mm (b) 10 mm (c) 16 mm (d) 20 mm

$$\sigma = \sum_{i=1}^{n} a_i(T)\epsilon_p^{n-1}; \qquad (n = 1 - 5) \tag{2.1}$$

$$\sigma = a_1(T)\epsilon_p^4 + a_2(T)\epsilon_p^3 + a_3(T)\epsilon_p^2 + a_4(T)\epsilon_p + a_5(T) \tag{2.2}$$

$$a_i(T) = \alpha_i T + \beta_i \tag{2.3}$$

where,

α_i and β_i $\longrightarrow$ coefficients given in Table 2.6 and Table 2.7 Observations recorded with regard to the prediction of the stress-strain behaviour of steel at elevated temperatures suggests erroneous predictions. These erroneous predictions were more pronounced while tracing the post-peak (or descending) branch of the stress-strain curve. All rebars show a low-ductile and the ultimate strain values. However, the proportionality limit and initial elastic modulus variation with respect to temperature conforms the Eurocode 2 [34] recommendations.

The fact may be attributed to instrumentation issues arising because of furnace size/type and the

		Coefficient a				
		i = 1	i = 2	i = 3	i = 4	i = 5
		$(\times 10^{13})$	$(\times 10^{11})$	$(\times 10^{8})$	$(\times 10^{5})$	$(\times 10^{3})$
α_i	$T < 250\,^\circ\mathrm{C}$	-0.0043	0.0043	-0.0126	0.0117	0.0001
	$T > 250\,^\circ\mathrm{C}$	0.0042	-0.0042	0.0122	-0.0092	-0.0015
β_i	$T < 250\,^\circ\mathrm{C}$	0.0826	-0.0761	0.1522	0.3201	0.7050
	$T > 250\,^\circ\mathrm{C}$	-2.0600	2.0600	-6.0400	5.5463	1.0843

Tab. 2.6: Coefficients α_i and β_i for Fe500 TMT Bars

		Coefficient a				
		i = 1	i = 2	i = 3	i = 4	i = 5
		$(\times 10^{9})$	$(\times 10^{8})$	$(\times 10^{6})$	$(\times 10^{5})$	$(\times 10^{3})$
α_i	$T < 250\,^\circ\mathrm{C}$	-0.0030	0.0022	-0.0052	0.0004	-0.0001
	$T > 250\,^\circ\mathrm{C}$	-0.0240	0.0088	-0.0080	0.0003	-0.0005
β_i	$T < 250\,^\circ\mathrm{C}$	-0.2391	0.2565	-0.6953	0.1078	-0.0005
	$T > 250\,^\circ\mathrm{C}$	5.0000	-1.4000	-0.0080	0.1364	0.5255

Tab. 2.7: Coefficients α_i and β_i for Fe500D TMT Bars

condition of testing equipment. In view of this, additional checks have been performed by testing the rebars at ambient temperature using the code specified test length and gauge length recommendations. The results obtained by this approach are satisfactory.

2.5 FAILURE MODES

Failure in steel rebars typically occurs in a cup and cone failure mode. At 20 °C, the rebar specimens failed just outside the furnace either near the top jaw or the bottom jaw. At 250 °C, failure occurred usually at the junction of furnace opening, normally just outside the furnace. This fact can be attributed to strengthening of the thermo-mechanically treated rebars at temperatures around 250 °C. Due to this, a stress concentration is developed at the portion of rebar just outside the furnace. At 500 °C, rebar becomes more ductile and a plastic softening is observed. Cross-sectional dimensions of the rebar inside the furnace show a decrement and failure normally occurs at the middle third of the specimen inside the furnace. However, the cup and cone mode of failure is still observed. Failure at 750 °C follows a different trend. The rebar becomes very soft and continues elongating until it fails. Essentially the bar loses almost 80-90% of its strength and fails with a pointed tip at the centre inside the furnace. Figure 2.10 shows typical failure modes of rebars at 20 °C, 250 °C, 500 °C and 750 °C. No difference in failure modes were observed between steel rebar specimens tested with and without pre-load.

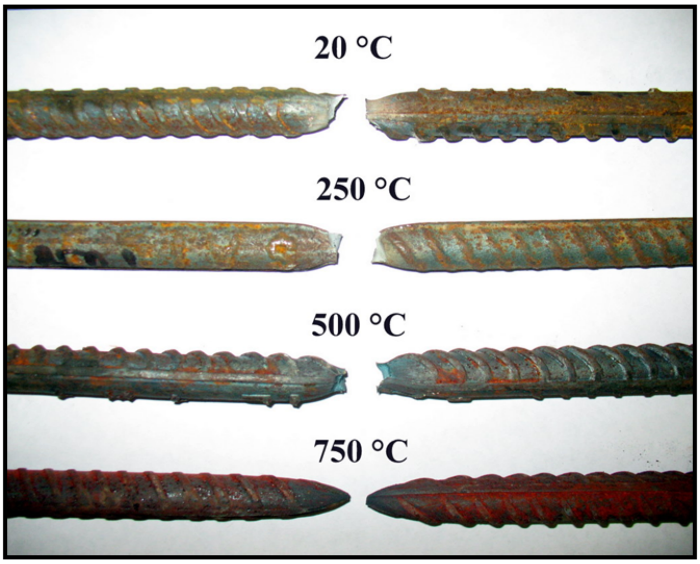

Fig. 2.10: Failure modes of reinforcing bars at different elevated temperatures

2.6 SCOPE FOR FURTHER RESEARCH

A series of tests on steel rebars with and without pre-load at elevated temperatures aims at capturing the changes in mechanical properties of steel rebars at elevated temperatures. Rebars of different diameter in the first phase of the series were tested without applying any pre-load. The experimentally obtained stress-strain data obtained shall be used to carry out multiple linear regression analysis and build material constitutive models for steel rebars at elevated temperatures with and without pre-load. Also, assessing the residual properties in the cooling regime when rebars are subjected to elevated temperatures is of significant importance in case the structures need to be retrofitted.

2.7 CONCLUDING REMARKS

As predicted by previous studies in the literature [32, 34, 62, 83], degradation in strength of fe 500 and fe500D TMT EQR steel rebars at elevated temperatures is conspicuously seen from the obtained results. In the current study, mechanical properties of steel rebars with and without pre-load at elevated temperatures have been evaluated experimentally. 8 *mm*, 10 *mm*, 16 *mm* and 20 *mm* diameter TMT reinforcing bars with no pre-load exhibited a brittle mode of failure under elevated temperature upto 250 °C. At 500 °C, the mode of failure was in transition from brittle to ductile. However, at 750 °C, the mode of failure was purely ductile. Loss of strength was in the order of 3%, 31% and 88% for rebars exposed to 250 °C, 500 °C and 750 °C respectively. Stress-strain relationships were plotted for each diameter at a particular temperature. Unlike steel rebars without pre-load, pre-loaded steel rebars exhibited brittle mode of failure only at 250 °C. Beyond this temperature, the behaviour of rebars changed from brittle to ductile. For a target temperature of 750 °C, the pre-loaded rebar failed in tension before reaching the target temperature. A strength reduction of 0%, 32% and 100% was observed in at 250 °C, 500 °C and 750 °C.

Undamaged and Damaged Confined Concrete at Elevated Temperatures

3

3.1 INTRODUCTION

Concrete is a heterogeneous material ubiquitously used in construction of high-rise buildings, bridges and roads. It is a vital component in structural design [47]. Modeling of mechanical behaviour of concrete at temperatures above ambient is necessary in assessing the performance of concrete structures in fire events. The design of fire resistant structural elements requires a realistic knowledge on the behaviour of concrete at high temperature [10]. At present, prescriptive approaches are established and are generally used to calculate the fire resistance of reinforced concrete members, which are based on either empirical methods or standard fire resistance tests. These approaches do not provide rational and realistic fire safety assessment and have major drawbacks. New codes are moving towards performance based design, and temperature dependent calculations are expected to be required to satisfy certain performance based criteria. There is an increased focus on the use of numerical methods for evaluating the fire performance of the structural members, which depends on the property of the constituent materials. Knowledge of the high temperature properties of concrete is critical for fire resistance assessment under performance based codes [50]. The constitutive laws of concrete materials under fire are complicated, and knowledge of currently known thermal properties is based on very limited material properties. There exists either limited test data for elevated temperature concrete properties, or there are considerable differences and inconsistencies in the elevated temperature test data for other properties of concrete [61, 67, 68]. Thus there are no well founded constitutive relationships in codes and standards for elevated temperature properties of concrete.Confined concrete subjected to elevated temperature still remains an area that requires experimental evidences to be precisely understood. A mismatch in the thermal properties of steel and concrete is responsible for the bond deterioration in reinforced concrete members and the reduction of yield stress in transverse reinforcing bars at elevated temperatures. [4, 46, 55, 58, 59, 69]

3.2 *CONCRETE AT ELEVATED TEMPERATURES: MATERIAL BEHAVIOUR*

Concrete, when exposed to elevated temperatures deteriorates under the influence of various physical and chemical changes which are identified as damage causing mechanisms. These damage causing mechanisms are broadly classified into four types: (a) Phase transformations occurring in the cement paste, (b) Phase transformations occurring in the aggregates, (c) Incompatibility between aggregates and cement paste at elevated temperatures and (d) Thermal Spalling. First three damage mechanisms cause a reduction in strength and stiffness whereas the last damage mechanism is regarded as a complex phenomenon causing a reduction in material affecting the integrity of the structure.

3.2.1 *Phase Transformations Occurring in the Cement Paste*

Elevated temperatures are found to influence all the three major products of concrete hydration process, namely Calcium Silicate Hydrates ($C_2S_2H_3/C-S-H$), Calcium Hydroxide (CH), and Ettringite ($C_6AS_3H_{32}$. The products further decompose and bring about a reduction in the strength and stiffness. Figure 3.1 shows the transformations taking place in the cement paste at elevated temperatures. The following chemical equations represent the decomposition reactions taking place in the cement paste at elevated temperatures. At elevated temperatures, $CaCO_3$ decomposes and evaporation of water takes place.
Decomposition of $C-S-H$:
$3.4CaO \cdot 2SiO_2 \cdot 3H_2O \longrightarrow 2.4CaO \cdot 2SiO_2 + 3H_2O$
Decomposition of CH:
$Ca(OH)_2 \longrightarrow CaO + H_2O$
Accelerated carbonation reaction of CH:
$Ca(OH)_2 + CO_2 + H_2O \longrightarrow CaO + H_2O$
Chemical reactions such as decomposition of CH cause shrinkage in the cement paste causing voids and cracks, thus proving to be detrimental for concrete. The newly formed phases exhibit a change in stiffness, which further causes the stiffness degradation in concrete.

3.2.2 *Phase Transformations Occurring in the Aggregates*

Two major types of aggregates normally used in normal strength concrete are silicious aggregates and calcarious aggregates. Silicious aggregates such as quartzite undergoes a phase transformation at about 570 °C.from α state to β state. The reaction is endothermic and it involves a heat of transformation of $5.9kJ/kg$. Assuming the participation of about 75% of quartzitic aggregates in concrete, a high heat of transformation of $8.8MJ/m^3$ may be observed.

3.2.3 *Incompatibility Between Aggregates and Cement Paste:*

Concrete, being a composite material with aggregates as inclusion and cement paste as matrix, exhibits different thermal properties following a temperature rise. Aggregates expand with increase in

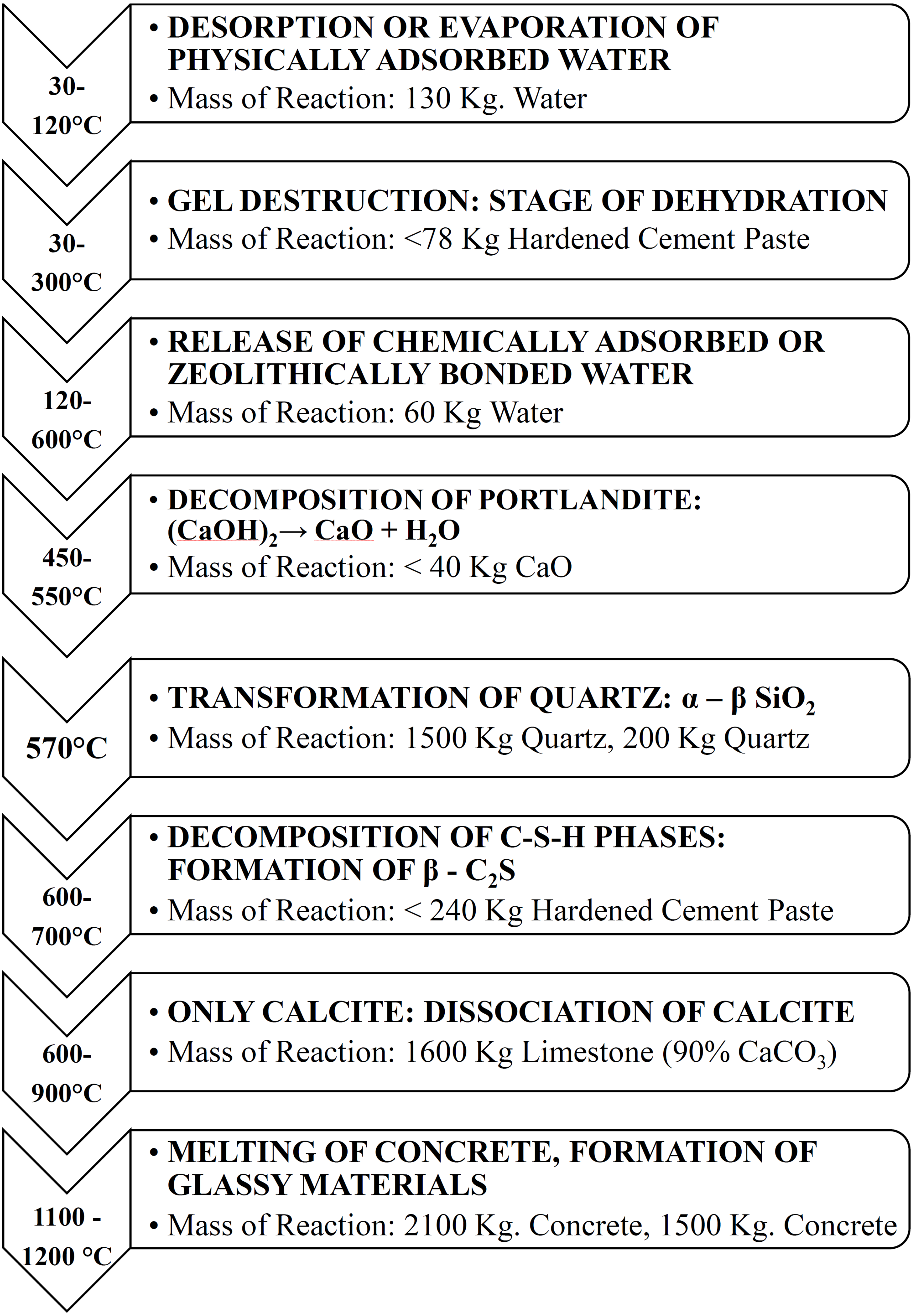

Fig. 3.1: Phase transformations in cement paste at elevated temperatures

temperature whereas the cement paste matrix has a tendency to shrink at high temperature due to loss of moisture. These changes may be governed by rate of heating, duration of exposure and composition of concrete. This thermal incompatibility leads to formation of cracks in the interface transition zone around the aggregate. Also, alternate heating and cooling of concrete results in widening of these cracks, inducing spalling that ultimately leads to failure of concrete structures.

Thermal Spalling:

Thermal spalling is one of the major damage causing agents affecting the structure by reducing the cross-sectional area of the members hence reducing its integrity. Spalling, although not much pronounced in normal strength concrete, becomes the most cause for the failure of structures constructed using high strength concrete. With a growing usage of contemporary concrete demanding a higher strength, durability and performance, it is equally important to understand the cause and effect of concrete spalling. The major causes for spalling have been identified as thermal stresses and pore pressure in concrete exposed to elevated temperatures. However, the exact mechanism of spalling has been an important area of study over the past decade.

3.3 TESTING OF CONCRETE AT ELEVATED TEMPERATURES

Testing of concrete specimens at elevated temperatures can be performed using three different methods: stressed test, unstressed test and residual test, based on the loading scenario [66,87] Figures 3.2 (a), (b) and (c) show the schematic of the three test methods. In stressed tests, a pre-load (20 – 40% of ultimate compressive strength) is imparted to the specimen, prior to heating, and the load is sustained during the heating period. Upon attaining the steady state, further load is applied till the specimen fails. Such tests are most desirable to assess the fire performance of concrete in a

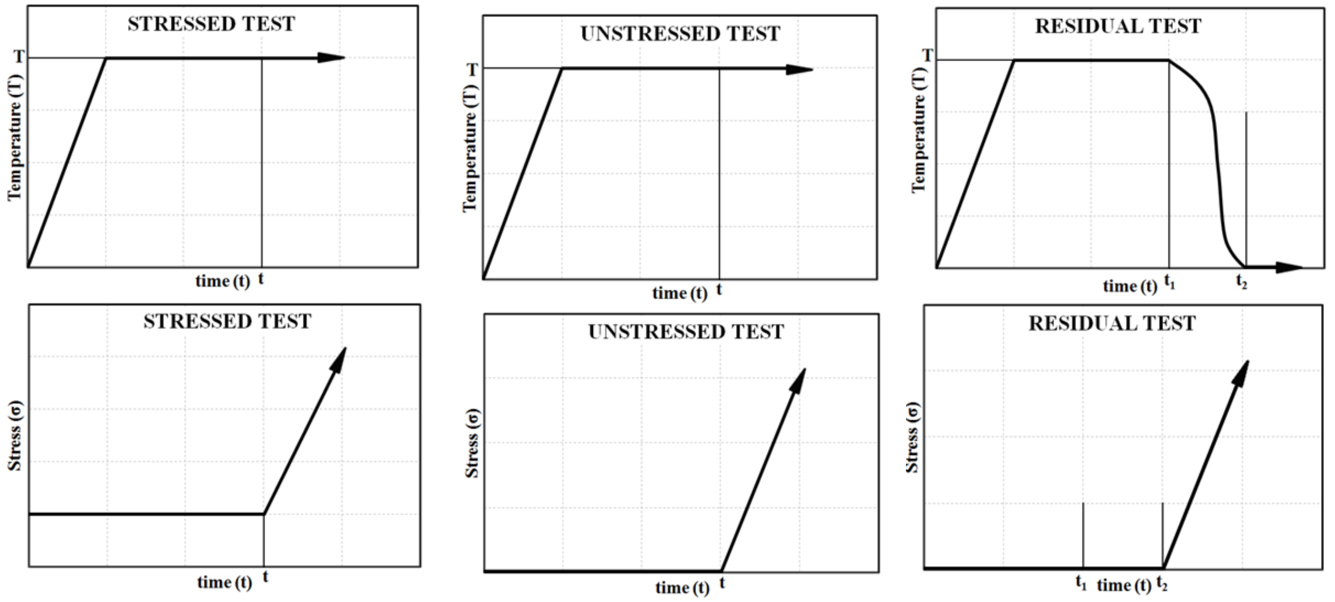

(a) (b) (c)

Fig. 3.2: Schematics of different test methods (a) Stressed Test (b) Unstressed Test (c) Residual Test

compression member such as a column and compression zones of a flexural members like beams and slabs, where excessive stresses are anticipated during fire due to instability in the structural system following the failure of a structural member. In unstressed tests, unlike stressed tests, no pre-load is imparted prior to heating. The specimens are generally exposed to a desired level and maintained until it reaches the steady state. It is then loaded to failure in the heated condition. Unstressed tests prove to be advantageous for evaluating the performance of concrete members with low stress levels under service conditions and loaded under high temperatures. In unstressed residual strength tests, the specimen is heated to the desired target temperature and maintained until it reaches the steady state after which it is cooled to ambient temperature. It is then loaded to failure under ambient conditions. Such tests are normally carried out to reckon the post-fire / residual properties of concrete. All three test methods can be used to determine the peak stress, the modulus of elasticity, the strain at peak stress and the dissipated mechanical energy as function of temperatures.

A general stressstrain relationship for concrete when subjected to fire is needed, as it allows designing concrete structures to specific fire performance criteria and improves the understanding of the behaviour of these structures under fire events. Existing relationships are developed based on fire tests of unconfined concrete specimens. They provide significantly different predictions because of uniqueness of each relationship and the existence of numerous formulations for calculating the governing parameters [90]. The effect of elevated temperatures on the stressstrain relationship of confined concrete is not fully understood. Confinement is expected to be affected by the deterioration of the bond between the reinforcing bars and the surrounding concrete [67,68] and the reduction in the yield stress of transverse reinforcing bars during fire [61, 67, 68]. Youssef and Moftah [90] considered available formulations for estimating the parameters based on well-established relationships for unconfined and confined concrete at ambient temperature and proposed suitable stressstrain relationships for concrete in compression and tension at elevated temperatures. The paper emphasized the fact that additional tests at different temperatures are needed to investigate the role of initial compressive and tensile stresses on the concrete compressive strength, concrete strain at peak stress, and initial modulus of elasticity of concrete. Further investigation is also proposed to evaluate the effect of elevated temperatures on the maximum concrete compressive stress, tensile behaviour of concrete, bond strength of reinforcing bars, and stressstrain relationships for confined initially stressed concrete.

3.3.1 Damaged Concrete at Elevated Temperatures

A detailed study on mechanical properties of damaged *(Damage induced by pre-loading)* confined concrete at elevated temperatures is of a significant interest in evaluating the performance of earthquake wrecked structures subjected to fire accidents. Also, the damage induced in existing structures due to several unforeseen activities: change in usage of structures, construction of more storeys, installation of heavy machinery etc. tend to impart a load-induced damage in structures. No literature exists on damaged concrete behaviour at elevated temperature. However, limited literature [10] exists on constitutive models and relationships for pre-loaded concrete at elevated temperature. In the current study, a combination of stressed and unstressed test has been adopted to carry out a different method of testing confined concrete. In this test, the specimens are basically pre-loaded to the load corresponding to a desired level of strain (0.0033, 0.0056 and 0.008) to simulate the damage caused either by earthquake or any other external factors acting on it. After inducing the desired level of damage, the specimen is heated to the target temperature and the temperature is maintained until the steady state is reached. The specimen is then re-loaded to failure in heated state. Such tests find the application of their results in reinforced concrete members damaged in earthquake. Figures 3.3 (a) and (b) show the schematics of the damaged unstressed tests, which is carried out at elevated temperatures.

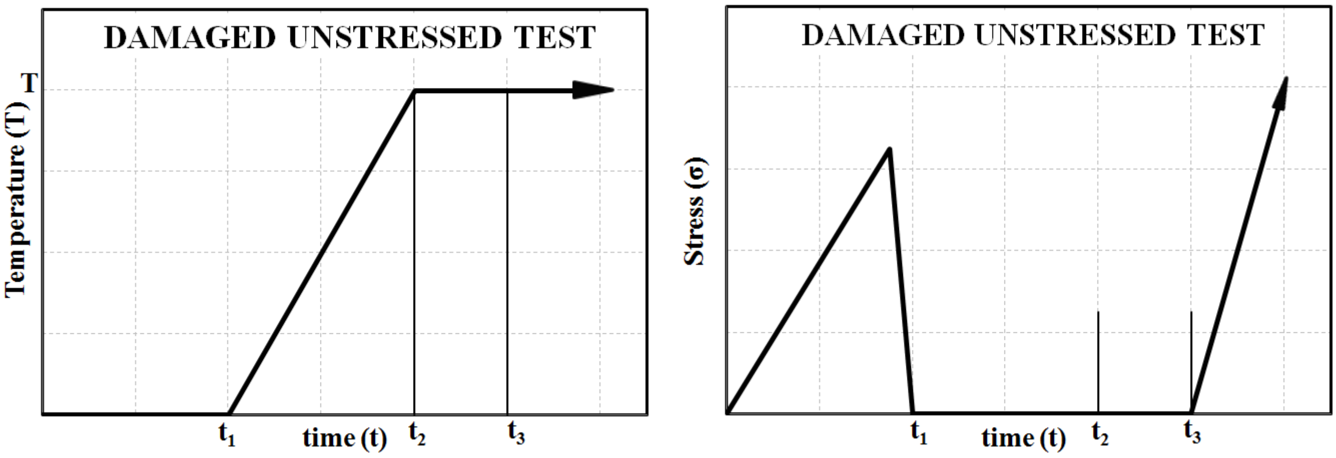

(a) (b)

Fig. 3.3: Schematics of damaged unstressed tests (a) Temperature-time (b) Stress-time

3.4 EXPERIMENTAL PROGRAMME

3.4.1 General

Testing of concrete at elevated temperatures are uncommon due to difficulties involved in the test-setup and instrumentation. In the present experimental investigation, confined concrete columns were tested at elevated temperatures. The specimens in damage category were initially preloaded to a certain level of pre-defined strain (0.0033, 0.0056 and 0.008), after which they were exposed to desired target temperature: Ambient, 250 °C, 500 °C and 750 °C in a split furnace coupled with a 500 ton compression testing machine. After achieving the desired steady state, the specimens were loaded to failure under uniaxial testing conditions.

3.4.2 Specimens

The specimens, both plain and confined concrete, considered for testing at elevated temperatures had a cylindrical cross-section of 150 *mm* diameter and a height of 600 *mm*. The dimensions of the concrete specimen were so chosen to accommodate a gauge length of 150 *mm* inside the furnace. A height of 450 *mm* of the specimen was encapsulated in the furnace and exposed to elevated temperature. About 75 *mm* height of the specimen protruded outside the furnace at the top and bottom. The specimen was made of normal strength concrete, which exhibited an average cube compressive strength 52.23 Mpa on the day of the test. An average moisture content as obtained from moisture meter was 44% on the day of the test. Locally available natural river sand and silicious coarse aggregates extracted from the river beds were used in the preparation of the concrete mix. A design mix of proportion 1 : 1.46 : 2.29 was adopted for casting of the concrete specimens. A water-cement ratio of 0.45 was used. No admixtures were used in casting. The concrete mix had a satisfactory workability and an average slump of 75 mm was obtained. The specimens were cured in water for 28 days before they were stacked up in the lab atmosphere for several days to ensure expulsion of moisture. It is very important that the moisture be expelled from the specimens before exposing them to elevated temperature to avoid the building up of pore water pressure, eventually resulting in spalling. The longitudinal reinforcement consisted of 6 number 8 $mm\ \phi$ TMT ribbed reinforcing bars. Circular hoop rings made out of 6 $mm\ \phi$ plain reinforcing bars were used for confining the longitudinal bars. Two different spacing of transverse reinforcement: 42 mm (Confinement C1) and 68 mm (Confinement C2), were considered for the investigation. Figure 3.4 (a) shows the 3D schematics of the reinforcement used in the confined concrete specimens. Two titanium grade 12 rods were embedded inside the concrete during casting. These rods marked the gauge length and facilitated the measurement of displacement with the help of displacement transducers. Split-type cast iron moulds were specially fabricated for casting of the confined concrete specimens. Openings were provided at the line of separation of the moulds, to accommodate the titanium rods and embedded sensors(Refer 3). Figure 3.4 (b) shows the 3D schematics of the split-type mould used to cast confined concrete specimens.

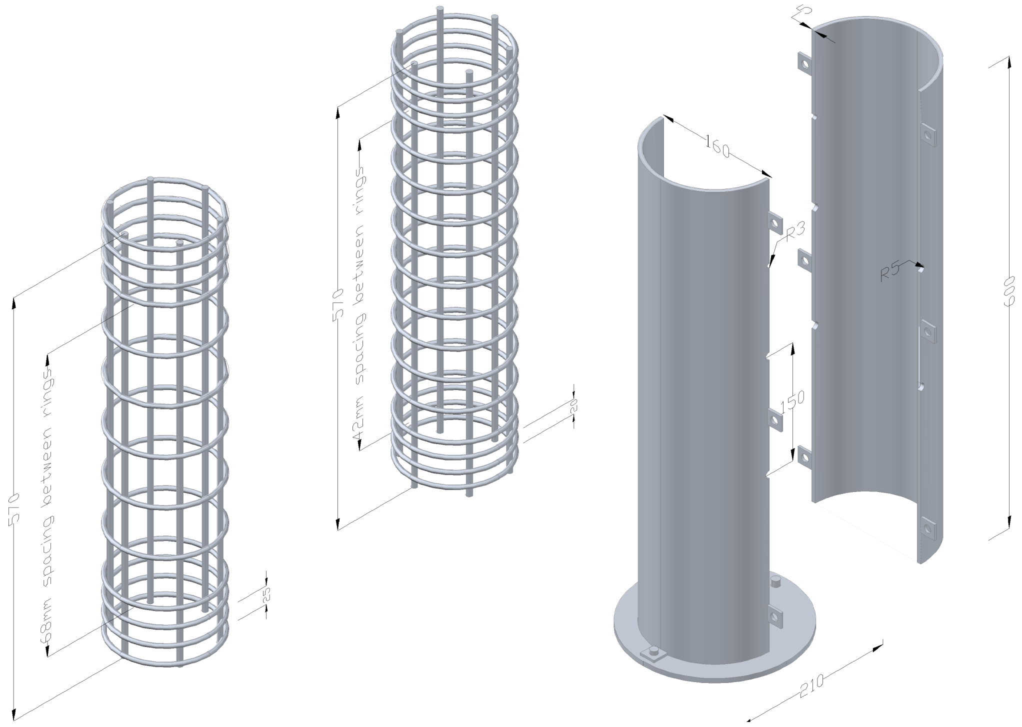

(a) (b)

Fig. 3.4: 3D schematics of: (a) Confined concrete reinforcement (b) Split-type mould

3.4.3 Instrumentation

Confined concrete specimens were well instrumented with embedded sensors to capture strains and temperature. Two K-type thermocouples one at the core and the other at the cover level at mid-height, were embedded inside the specimen during casting. Care was taken to maintain the position of the thermocouples intact during vibration. The split-vertical furnace was equipped with three thermocouples, one each at top, center and bottom, which helped in monitoring the furnace temperatures. The hydraulic unit of the compression testing machine was fitted with a pressure sensor, which was calibrated to record the load in kN. Displacements were measured using two Linear Variable Displacement Transformer (LVDT) transducers clamped on the titanium bars protruding outside the furnace. The LVDTs had a stroke length of 50 mm. However, the maximum displacements obtained in the test before failure were well within 25 mm. An attempt was made to record the strains in the confining steel during compression at elevated temperatures. Three type of strain gauges were used in specimens cast to test under Ambient, 250 °C, 500 °C and 750 °C. Weldable strain gauges (generically modified bondable strain gauges) were used for the specimens under the category of 500 °C. The strain gauges were either pasted / spot-welded to the confining ring at the mid-height of the specimen on the diametrically opposite sides. Special treatment against the temperature was given to the strain gauges in the specimens that were to be exposed to 250 °C and 750 °C. The gauges were pasted using a high temperature resistant adhesive (up to 350 °C). A coating of the same was applied on top of the pasted strain gauge, which formed a protective coating, thus preventing the gauges from direct exposure to heat. For specimens that fell under 250 °C category, the protected gauges were encapsulated in a flexible layer of waterproof gel whereas, for the specimens that fell under 750 °C category, the gauges were further protected by a layer of ceramic cement. This was to ensure the water-tightness and protection against very high temperatures. Figure 3.5 (a) shows the prepared surface on the confinement hoop ring for pasting of bondable strain gauges. An even surface was ensured for proper bonding of gauges using special use adhesives. Figure 3.5 (b) shows a bondable strain gauge mounted on the prepared surface. The gauges were further treated to resist high temperatures and water percolation . Figure 3.5 (c) shows the spot welding of weldable strain gauges in progress. Figure 3.5 (d) shows the spot-welded gauge ready for casting. These guages were further encapsulated in a layer of ceramic cement, capable of providing an heat insulation in temperatures as high as 1000 °C.

3.4.4 Test Setup

The cured specimens were heated to the target temperature in a specially fabricated split-type vertical furnace coupled with a $500kN$ existing compression testing machine without any structural / functional modifications of the machine. Figure 3.6 shows the 3D schematic of the electric furnace with the placement of the confined concrete specimen. The electric furnace was capable of attaining a maximum temperature of 1200 °C. The thermocouples in the furnace facilitated the measurement of temperature throughout the test. The furnace was attached to a control unit with programmable capabilities and a LCD display showing the real-time temperature at any instant. The heating

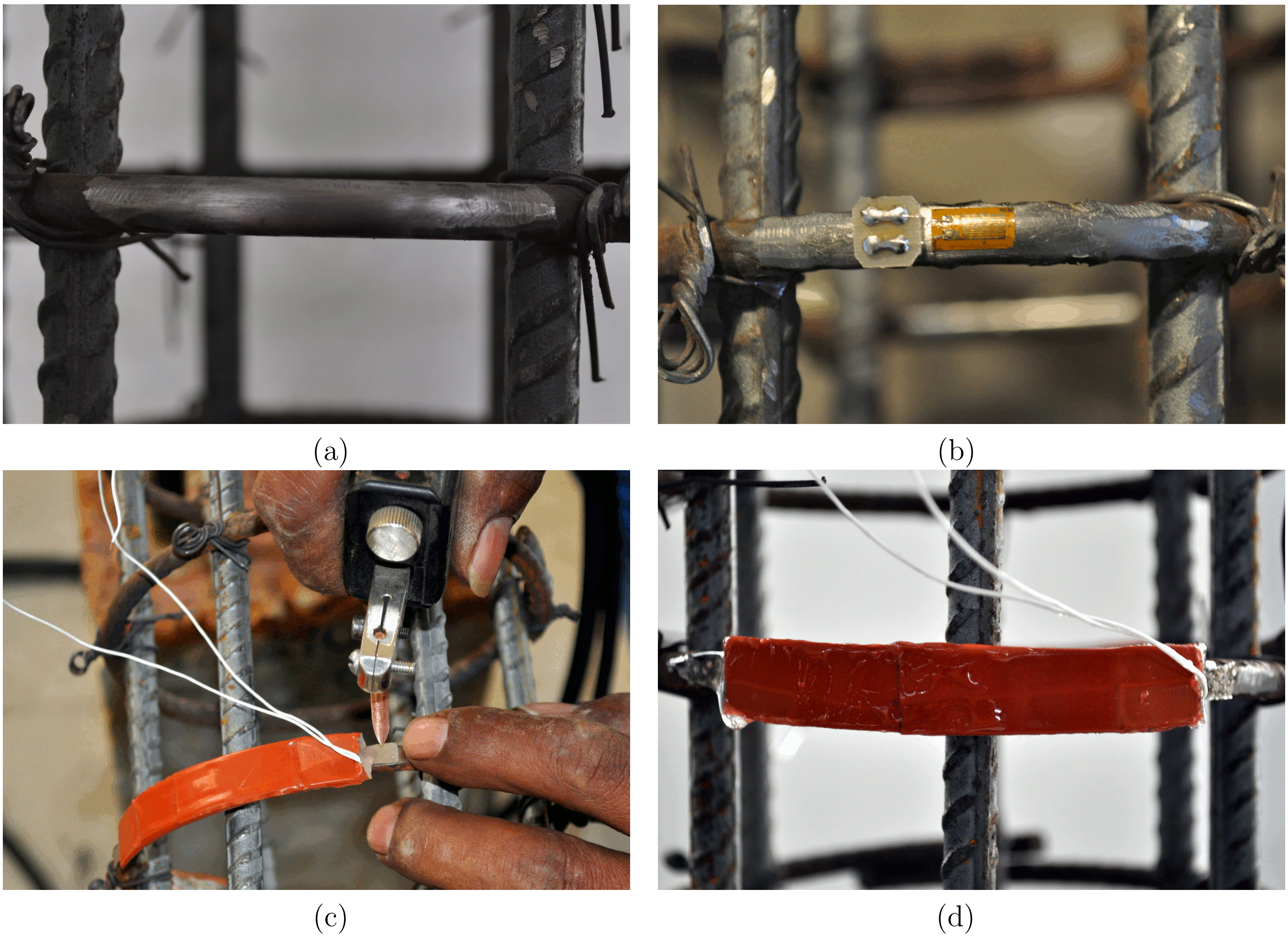
(a) (b) (c) (d)

Fig. 3.5: Strain gauges (a) Surface preparation (b) Bondable strain gauge (c) Spot welding (d) High-temperature resistant, weldable strain gauge

sequence was programmed for different temperatures and fed to the control unit. All the sensors (thermocouples, pressure sensor, displacement transducers and strain gauges) were connected to an automated data acquisition systems for efficient data logging at regular intervals. Figure 3.7 shows the schematic of the test setup.

3.4.5 Testing Methodology

A total of 108 specimens were cast which included plain concrete, confined concrete with 42 mm confinement spacing (Confinement - C1) and 68 mm confinement spacing (Confinement - C2). Atleast 3 specimens of each category were tested to ensure the consistency. The specimens in undamaged category were placed in the furnace and the furnace was sealed from top and bottom with layers of glass wool. The furnace is programmed to achieve the target temperature at the rate of 10 °C/min. and maintain it until the steady state is reached. The temperature is maintained for about an hour beyond reaching steady state and then being loaded to failure. In the process, once the target temperature is reached, the furnace latch is opened on both the sides to permit the free movement of titanium rods, to which the LVDTs are attached. The specimen is imparted a seating load of about 10% the ultimate capacity to ensure proper placement of the specimen and proper disposal of the load

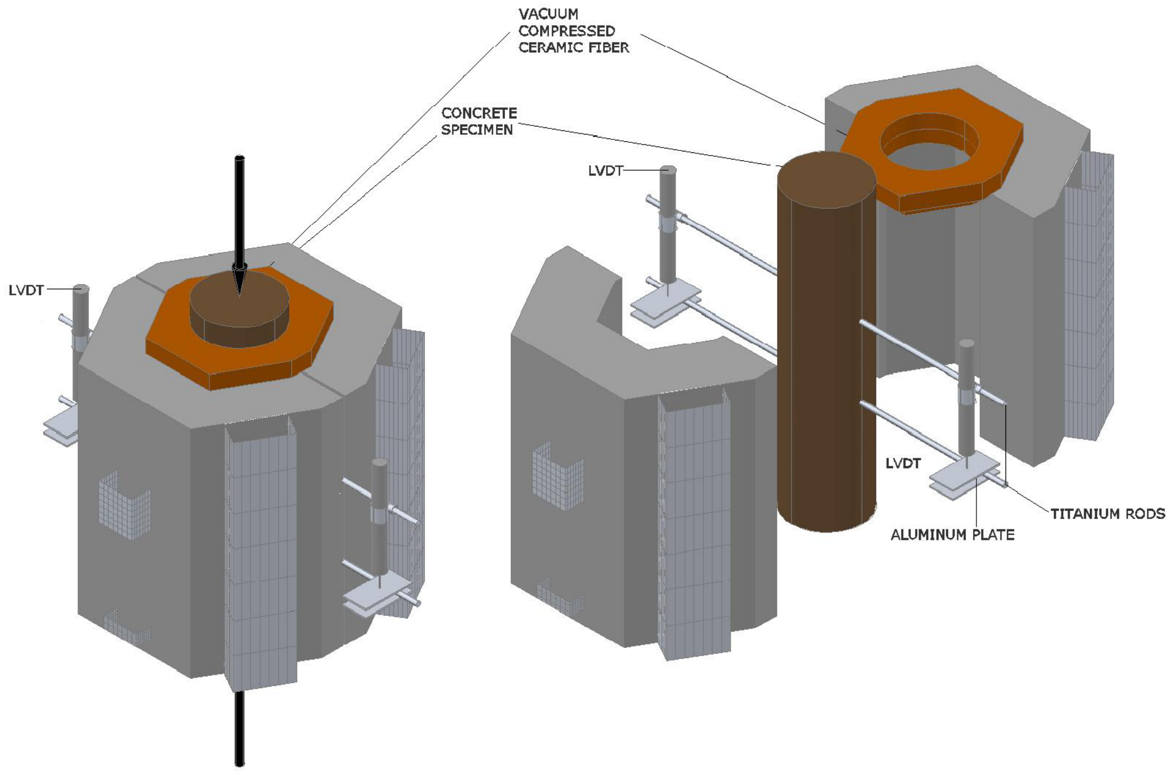

Fig. 3.6: 3D Schematic of the split-vertical furnace with the confined concrete specimen

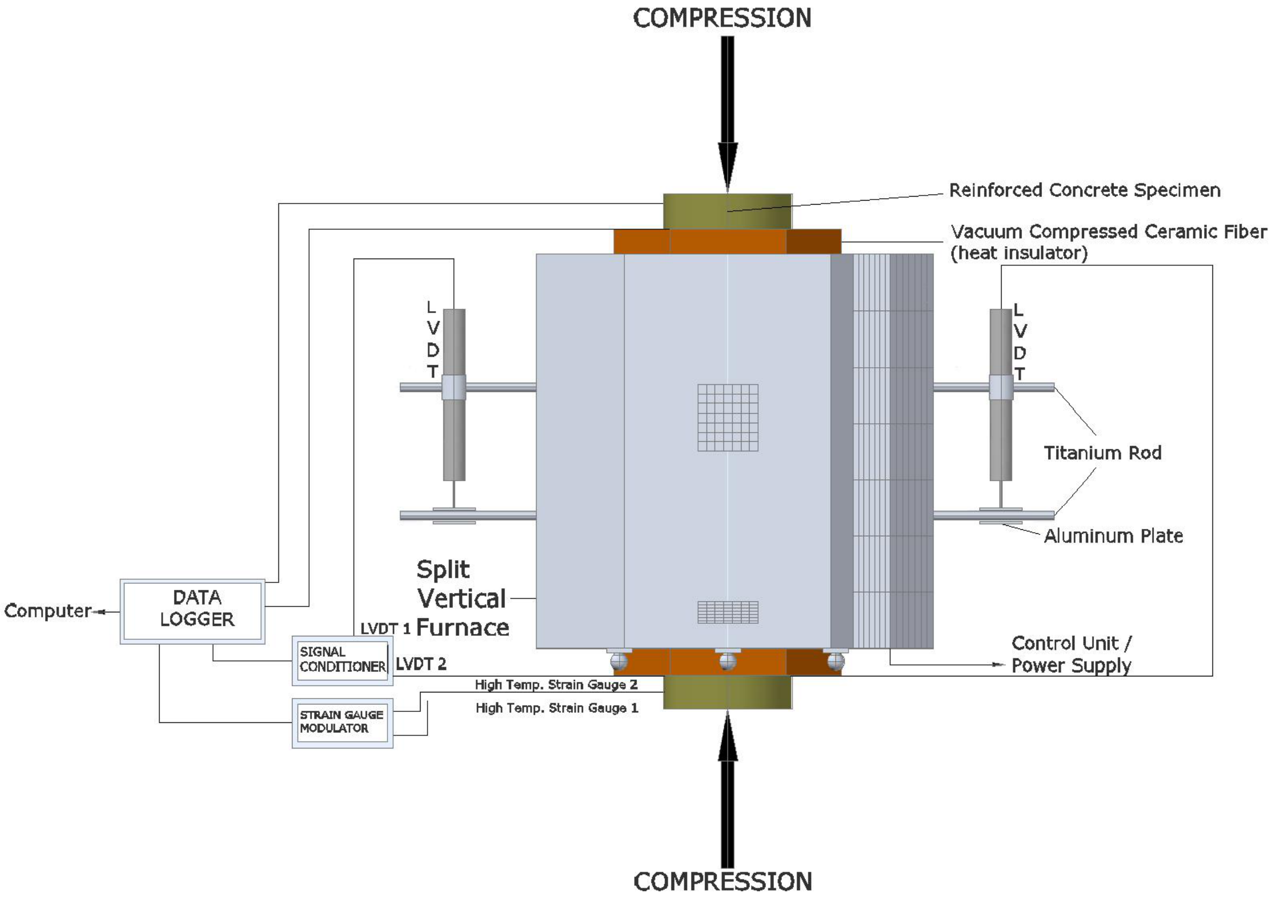

Fig. 3.7: 3D Schematic of the test setup

path through the specimen. This also removes the unwanted irregularities off the load-displacement plots. The loading is applied at a constant rate and the rate of loading is kept uniform throughout the test. The specimen is loaded to failure without interruptions. Load and displacement is monitored throughout the test.

The specimens in the 'damaged' category are imparted the displacements corresponding to the pre-defined displacement levels. Three damage levels: D1, D2 and D3 (as depicted in Table 3.1) corresponded to three different strain ordinates on the stress-strain curve obtained at ambient temperature for both C1 and C2 specimens.

Pre-loading of concrete specimens was achieved at a low and constant loading rate. Once the target displacement was observed, the load was released and the specimen was then exposed to the target elevated temperature. After achieving the target temperature, the specimen was loaded to failure under uniaxial loading similar to the specimens under the undamaged category. In both the categories, the temperature, load, displacement and strain were acquired automatically by the data acquisition system programmed at an interval of $2 seconds$. The loading was allowed to continue beyond cracking to capture the behaviour of the descending branch of the load-displacement plot. Figure 3.8 shows the damaged unstressed test at elevated temperature in progress.

Damage Level	**Strain Level**	**Displacement (mm)**	**Zone on the Stress-Strain Curve**
D0	-	-	Undamaged
D1	0.0033	0.50	Before Yield Point
D2	0.0056	0.85	At Yield Point
D3	0.0080	1.20	Post-Yield

Tab. 3.1: Damage levels

Fig. 3.8: Actual test setup with elevated temperature testing in progress

3.5 RESULTS AND DISCUSSION

3.5.1 Stress-Strain Curves

Literatures [90] [10] highlight the fact that the mechanical properties like concrete strength, concrete initial modulus of elasticity, concrete strain at maximum stress, thermal strain, transient creep strain, yield strength of reinforcing bars, and bond strength of reinforcing bars affect the stress-strain relationship of confined concrete at elevated temperature. In addition to this, present study introduces another variable, that is believed to affect the stress-strain relationship: an induced pre-damage imparted by pre-loading.

The experimental program carried out in the present investigation primarily consists of undamaged and damaged confined concrete members (four damage levels: D0, D1, D2, D3 and two confinement levels: C1 and C2) being tested in compression at ambient and elevated temperatures (three target temperatures: 250 °C, 500 °C and 750 °C), as illustrated in Figures 3.9 and 3.10. This section explains the behaviour of the confined concrete based on the set of data analysed by testing the specimens. Overall, a degradation in strength and stiffness was observed in terms of degradation in mechanical properties of confined concrete specimens at elevated temperatures. Different mechanical properties like modulus of elasticity, confined peak stress and strain at peak stress were worked out from the stress-strain relationships plotted using the experimental data both for damaged and undamaged specimens and are discussed in the following sections.

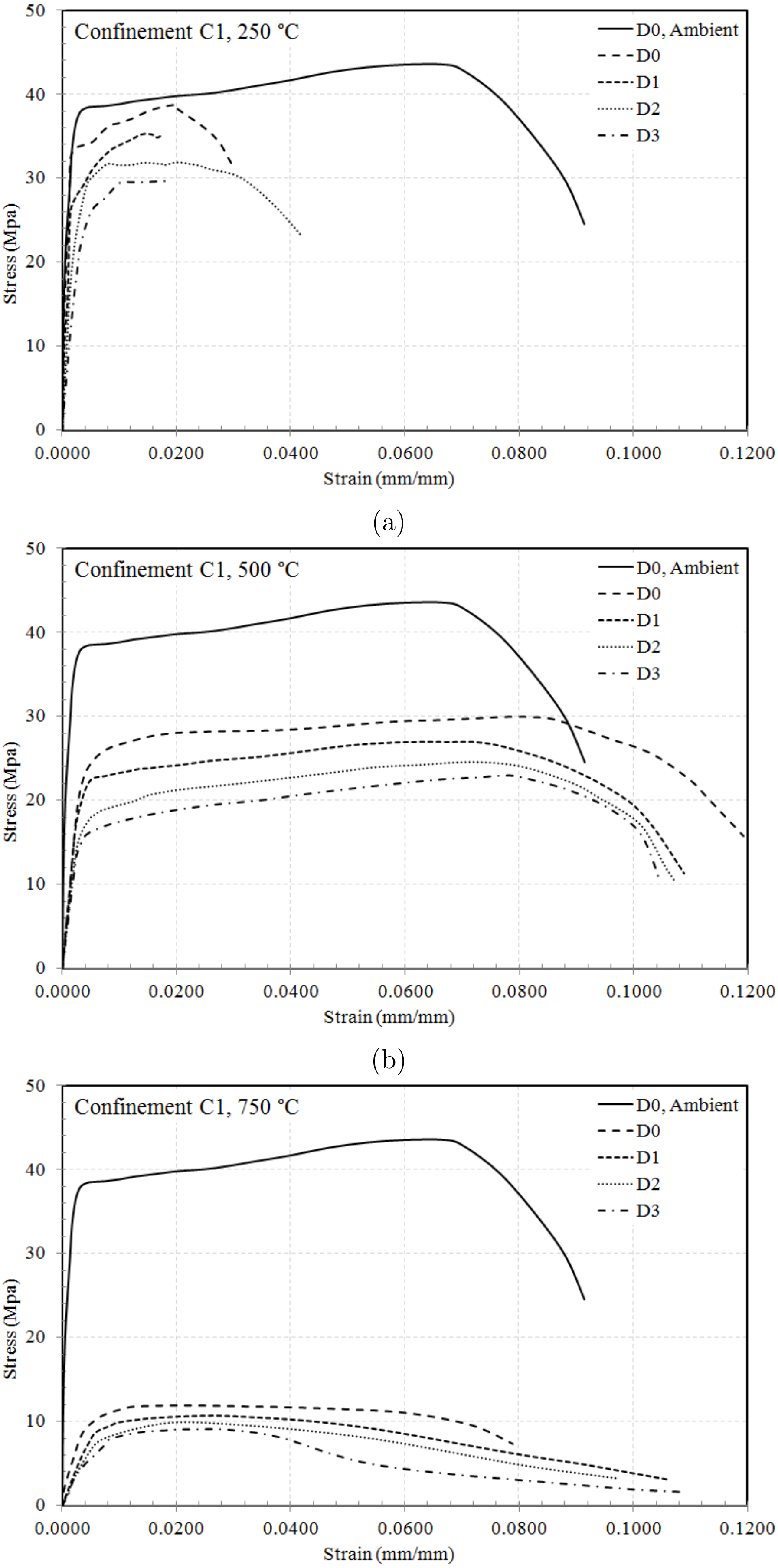

(a)

(b)

(c)

Fig. 3.9: Stress-strain plots for confinement C1 at elevated temperatures (a) 250 °C (b) 500 °C (c) 750 °C

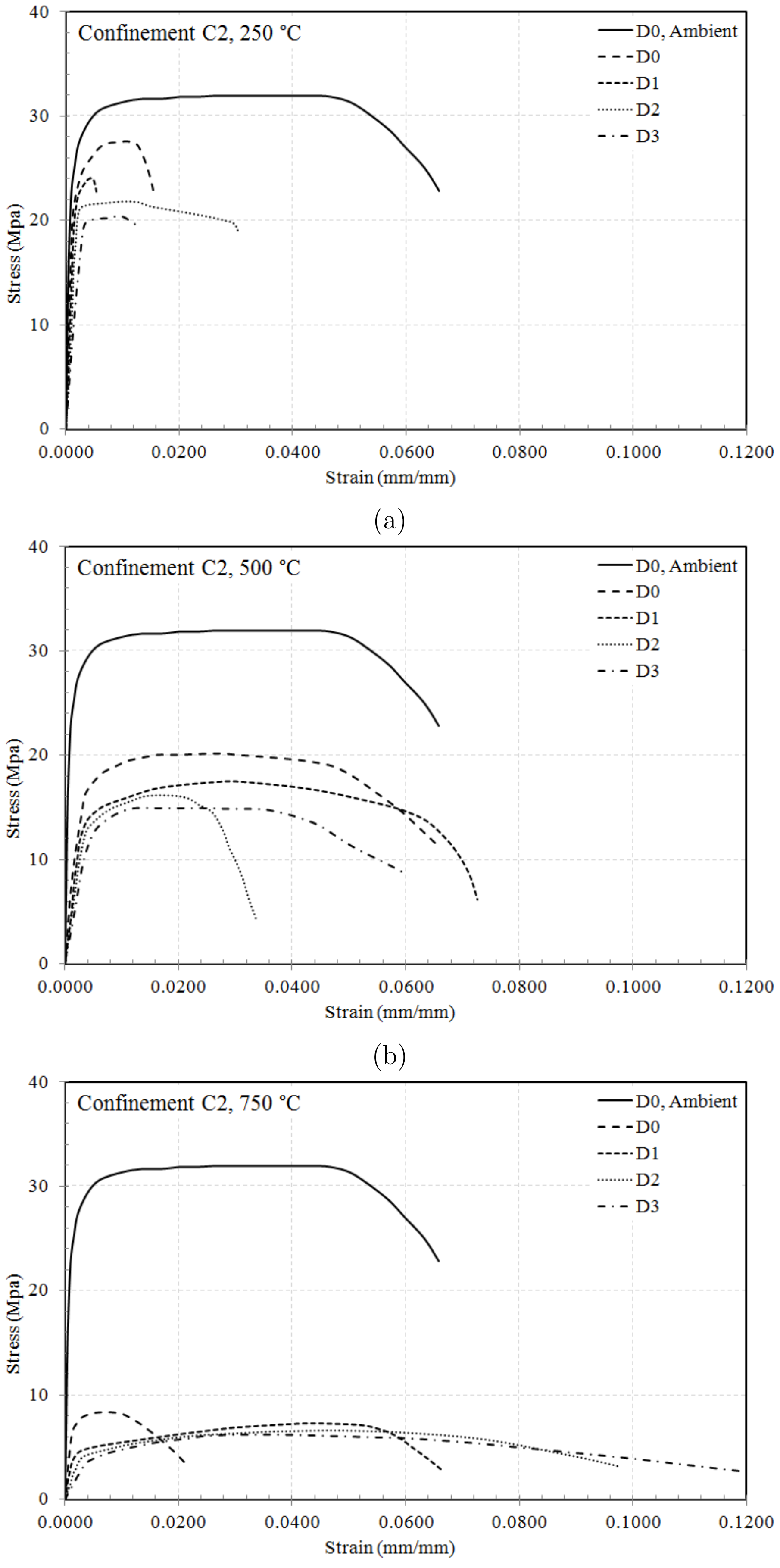

(c)

Fig. 3.10: Stress-strain plots for confinement C2 at elevated temperatures (a) 250 °C (b) 500 °C (c) 750 °C

	E_{cT}/E_{c0}			$\sigma'_{ccT}/\sigma'_{cc0}$		
	250 °C	500 °C	750 °C	250 °C	500 °C	750 °C
Ambient	1.00	1.00	1.00	1.00	1.00	1.00
D0	0.76	0.42	0.04	0.89	0.69	0.27
D1	0.50	0.21	0.03	0.81	0.62	0.25
D2	0.39	0.14	0.02	0.73	0.57	0.23
D3	0.27	0.09	0.02	0.68	0.53	0.21

Tab. 3.2: Mechanical properties for confined concrete at elevated temperatures: C1

	E_{cT}/E_{c0}			$\sigma'_{ccT}/\sigma'_{cc0}$		
	250 °C	500 °C	750 °C	250 °C	500 °C	750 °C
Ambient	1.00	1.00	1.00	1.00	1.00	1.00
D0	0.69	0.39	0.03	0.86	0.63	0.26
D1	0.44	0.19	0.02	0.75	0.55	0.23
D2	0.36	0.12	0.02	0.68	0.51	0.21
D3	0.24	0.07	0.02	0.64	0.47	0.19

Tab. 3.3: Mechanical properties for confined concrete at elevated temperature: C2

3.5.2 Modulus of Elasticity

An average value of 36000 Mpa of initial elastic modulus has been obtained under ambient conditions irrespective of degree of confinement. This confirms the fact that initial elastic modulus of concrete (unconfined / confined) for any grade at ambient temperatures is unaffected by the confinement [60, 65, 90]. Figures 3.11 and 3.12 depicts the ratio of initial elastic modulus of confined concrete at elevated temperatures, E_{cT}, with respect to ambient temperature, E_{c0}, for different damage levels and temperatures (refer Tables 3.2 and 3.3). Moreover,in contrast to the observation at ambient temperature, it may be noted that the confinement ratio does marginally effect the modulus of elasticity at elevated temperature. For confined specimens with no damage, a degradation of about 24%, 58% and 96% for C1 - confinement and 31%, 61% and 97% for C2 - confinement with respect to modulus of elasticity at ambient temperature has been recorded at temperatures 250, 500 and 750 °C respectively. It is also apparent from the figures that the degradation effect is more pronounced in the case of damaged confined specimens at temperatures 250 °C and 500 °C, though this trend was absent at 750 °C due to considerable loss of strength and stiffness.

Literature suggests various models where in an empirical function is described to calculate the initial modulus of elasticity for unconfined concrete at elevated temperature [4, 46, 74, 90],

Khennane and Baker

$$E_{cT} = (0.001282.T + 1.025641).E_{c0} \ ; \qquad 20 \leq T \leq 800\,^{\circ}\mathrm{C} \qquad (3.1)$$

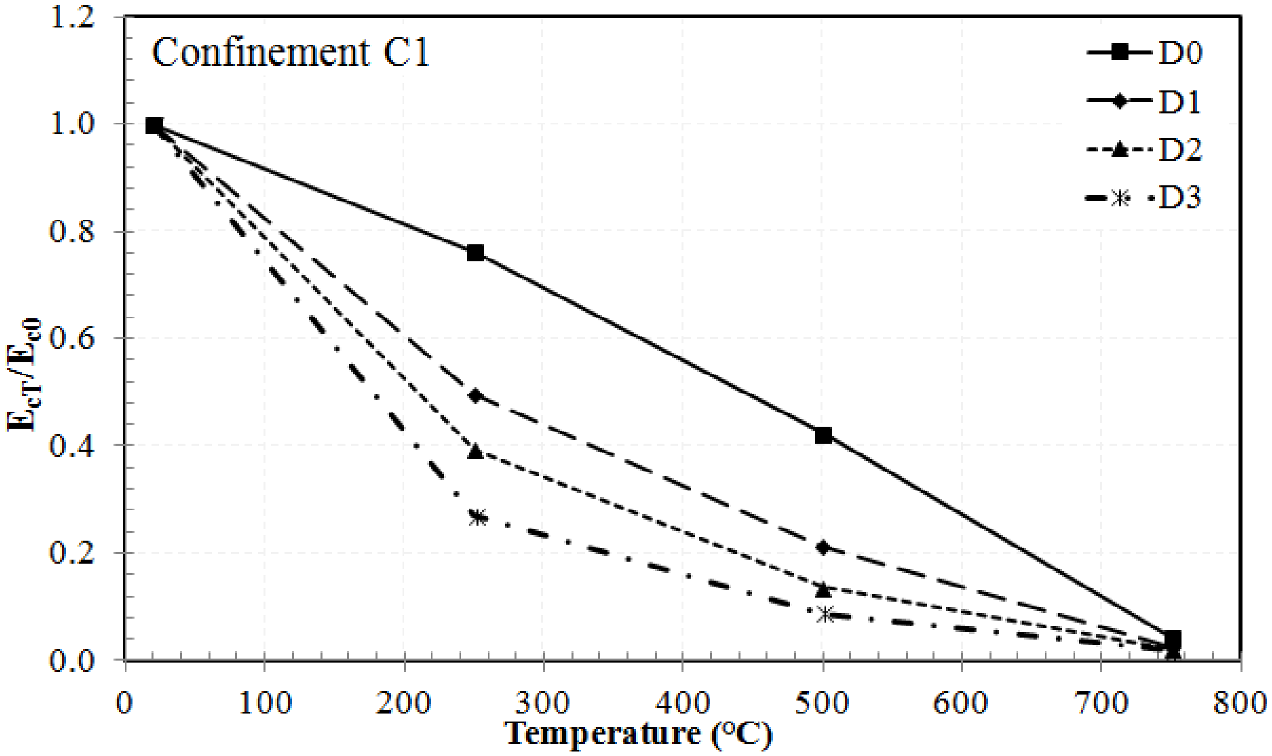

Fig. 3.11: Initial modulus of elasticity at elevated temperature for confined concrete with confinement C1

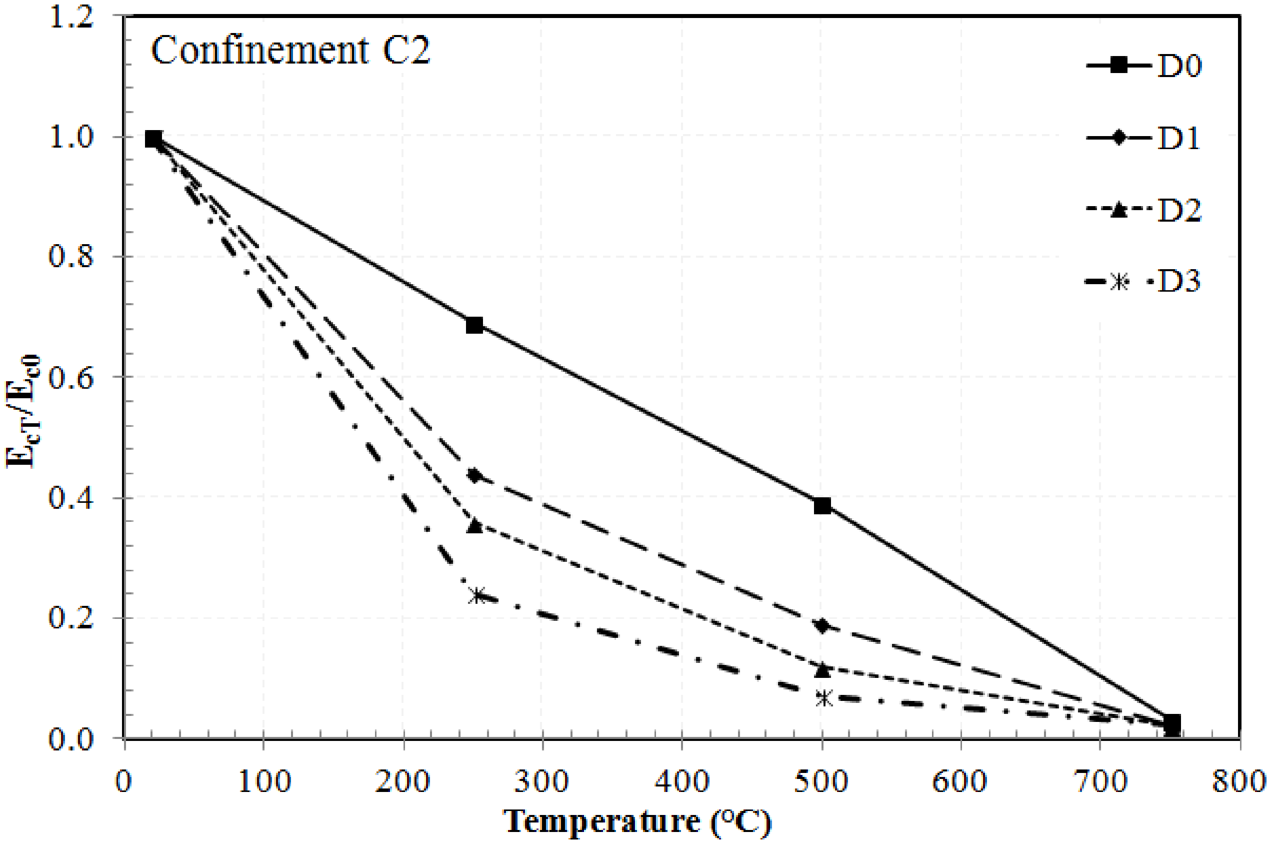

Fig. 3.12: Initial modulus of elasticity at elevated temperature for confined concrete with confinement C2

Anderberg and Thelanderson

$$E_{cT} = \frac{2 \cdot \sigma'_{cT}}{\epsilon'_{cT}} \tag{3.2}$$

Schneider

$$E_{cT} = (-0.001552.T + 1.03104) \cdot g \cdot E_{c0}; \qquad 20 \leq T \leq 600\,^{\circ}\mathrm{C} \qquad (a) \qquad (3.3)$$

$$E_{cT} = (-0.00025.T + 0.25) \cdot g \cdot E_{c0}; \qquad 600 \leq T \leq 1000\,^{\circ}\mathrm{C} \qquad (b)$$

However, the above models are silent about its applicability to confined concrete in an explicit manner. The author has computed the modulus of elasticity using these models and the comparative evaluation has been shown in Figure 3.13. It is evident from the figure that all the three models under reference seem to underpredict the degradation of initial modulus of elasticity. Following the outcome, an attempt has been made, to define the modulus of elasticity for confined concrete at elevated temperature taking into consideration the different damage levels also. To this end, various damage indices have been quantified as a ratio of Secant Modulus corresponding to the pre-specified strain level(s), E_{sec}, and the initial elastic modulus, E_{c0} under ambient temperature. Accordingly,

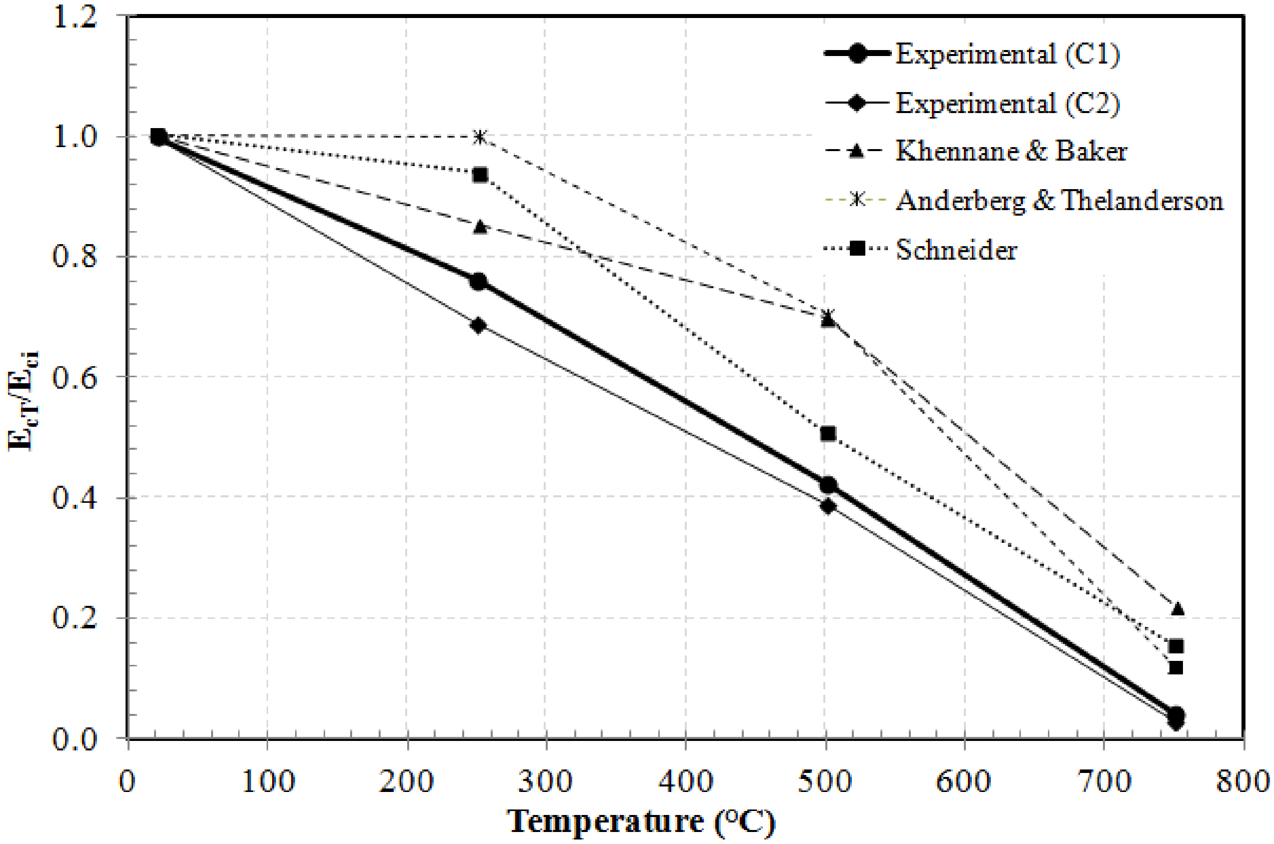

Fig. 3.13: Comparison of initial modulus of elasticity for confined concrete with existing models

based on regression analysis, the variable E_{cT}/E_{c0} has been expressed as a quadratic function of damage index. an equation (Equation 3.4 has been proposed as:

$$\left(\frac{E_{cT}}{E_{c0}}\right) = \chi_T \cdot \left(\frac{E_{sec}}{E_{c0}}\right)^2 + \upsilon_T \cdot \left(\frac{E_{sec}}{E_{c0}}\right) + \zeta_T \tag{3.4}$$

Where the coefficients χ_T, υ_T and ζ_T are being evaluated in terms of temperature and the confinement ratio and are given below,
For Confinement C1 ($20 \leq T \leq 750$),

$$\chi_T = 0.0019 \cdot T - 1.4341 \tag{3.5}$$

$$\upsilon_T = -0.0032 \cdot T + 2.3478 \tag{3.6}$$

$$\zeta_T = -0.0002 \cdot T + 0.1324 \tag{3.7}$$

For Confinement C2 ($20 \leq T \leq 750$),

$$\chi_T = 0.0023 \cdot T - 1.6879 \tag{3.8}$$

$$\upsilon_T = -0.0035 \cdot T + 2.6501 \tag{3.9}$$

$$\zeta_T = -0.0001 \cdot T + 0.095 \tag{3.10}$$

3.5.3 Peak Stress and Corresponding strain

Figures 3.9 and 3.10 suggest that the temperature, the confinement and the level of damage significantly influence the value of the confined peak stress and the corresponding strain value. It is apparent that the peak stress value reduces with an increase in the temperature and the effect becomes more pronounced in the case of pre-damaged specimens.
For C1 - confinement specimens, an average degradation of 22% in peak stress has been observed at a temperature of 250 °C, though for the undamaged specimens, degradation was limited to 11% in comparison to the peak stress at ambient temperature. The reduction in the peak stress was found to increase with an increase in the damage levels and was in the order of 19%, 27% and 32% of the peak stress. Specimens with damage registered a higher loss in peak stress in comparison with the specimens with no damage at 250 °C. Figure 3.9(b) suggests that at 500 °C, the degradation in peak stress almost got doubled indicating an average reduction of 40% in peak stress. Percentage reduction calculated in confined concrete specimens with no damage and the three damage levels were in the order of 31%, 38%, 43% and 47% respectively. At 750 °C, the confined concrete specimens experienced a rapid loss of strength and stiffness due to loss of confinement as shown in Figure 3.9(c). On an average, about 76% reduction of peak stress was registered and the effect of the imparted damage was negligible.
For C2 - Confinement specimens, as is evident from Figure 3.10(a), at 250 °C, an average degradation

of 27% in peak stress has been observed (D0: 14%, D1: 25%, D2: 32% and D3: 36%). Figure 3.10(b) gives the stress-strain relationship for confined concrete specimens with all damage levels exposed to a temperature of 500 °C. Congruent to the specimens with confinement C1, the degradation in peak stress doubled at 500 °C. An average degradation of 46% in peak stress was observed at this temperature. Percentage reduction observed for damage levels D0, D1, D2 and D3 were in the order of 37%, 45%, 47% and 53% respectively. At a target temperature of 750 °C, the confined concrete specimens experienced a greater loss of strength and stiffness due to loss of confinement. An average loss of 78% recorded for specimens with confinement C2, was although 2% less than that of the specimens with confinement C1, was merely signiificant. The stress-strain plots for all four damage levels at 750 °C is shown in Figure 3.10 (c). The effect of damage diminished to a greater extent at this temperature. About 74%, 77%, 79% and 81% reduction in peak stress was observed at the four damage levels respectively. Irrespective of the amount of confinement steel provided, at high temperatures, confinement effectiveness abates due to softening of steel reinforcement. The reinforcing bars become red-hot and soften . Any dilatation in the circumferential zone within the gauge length will not be restricted by the effect of confinement. The confining hoop reinforcement exhibits a very low or no-stress state. The hoop steel dilates along with the concrete thus leading to the failure of the specimen due to failure of concrete. Also, the difference in degradation of peak stress in damaged confined concrete is more pronounced at lower temperature levels and reduces with increase in temperature.

Figure 3.14 and Figure 3.15 depict the variation in normalized peak stress $\left(\frac{\sigma'_{ccT}}{\sigma'_{cc0}}\right)$ with temperature for concrete specimens with confinement C1 and C2. Tables 3.2 and 3.3 may also be referred for the purpose. Confined concrete compressive strength has shown considerable variations with temperature. Mander et al [60] has proposed a well-established, widely followed theoretical stress-strain relationship for confined concrete at ambient temperature. In this relationship, the confined concrete compressive strength, σ'_{cc0} is given considering the confined concrete core under tri-axial compression with equi-lateral confining stresses σ'_l from spiral to circular hoops. The confined concrete compressive strength is given as,

$$\sigma'_{cc0} = \sigma'_{c0} \cdot \left[-1.254 + 2.254 \cdot \sqrt{1 + \frac{7.94 \cdot \sigma'_l}{\sigma'_{c0}}} - \frac{2 \cdot \sigma'_l}{\sigma'_{c0}} \right] \quad ; \quad \sigma'_l = K_e \cdot \frac{2 \cdot \sigma_y \cdot A_s}{d_s \cdot S_h} \tag{3.11}$$

Where,

$\sigma'_{c0} \longrightarrow$ Unconfined concrete compressive strength at ambient temperature

$\sigma_y \longrightarrow$ Yield strength of reinforcing bar at ambient temperature

$d_s \longrightarrow$ Diameter of transverse rebars

$A_s \longrightarrow$ Cross-sectional area of transverse reinforcement

$S_h \longrightarrow$ Spacing between transverse hoop rebars, and

K_e is the confinement effectiveness coefficient , which is the ratio between the area of effectively confined concrete core and the area of concrete within the centreline of the transverse reinforcement. To the best of author's knowledge, there exists only one model, proposed by Youssef and Moftah [90]

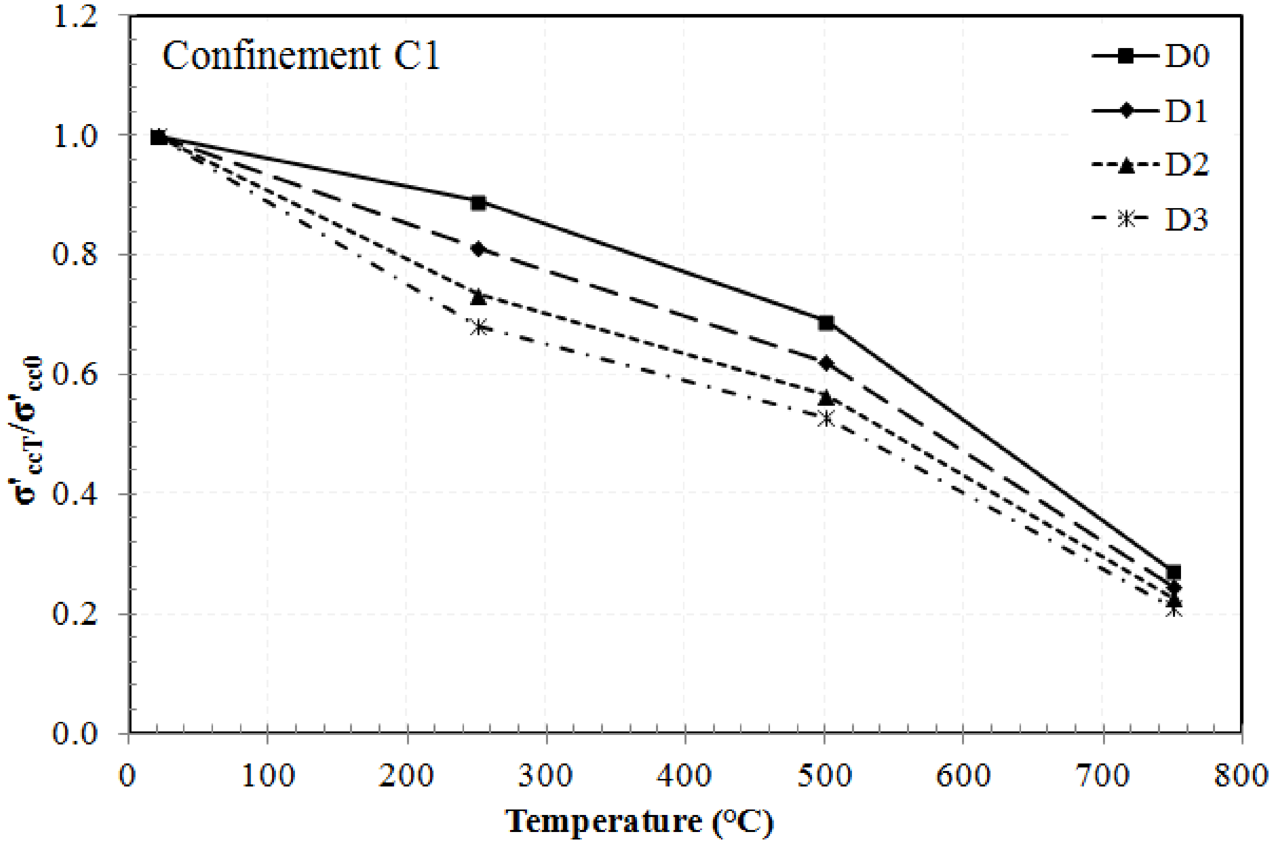

Fig. 3.14: Peak stress at elevated temperature for confined concrete with confinement C1

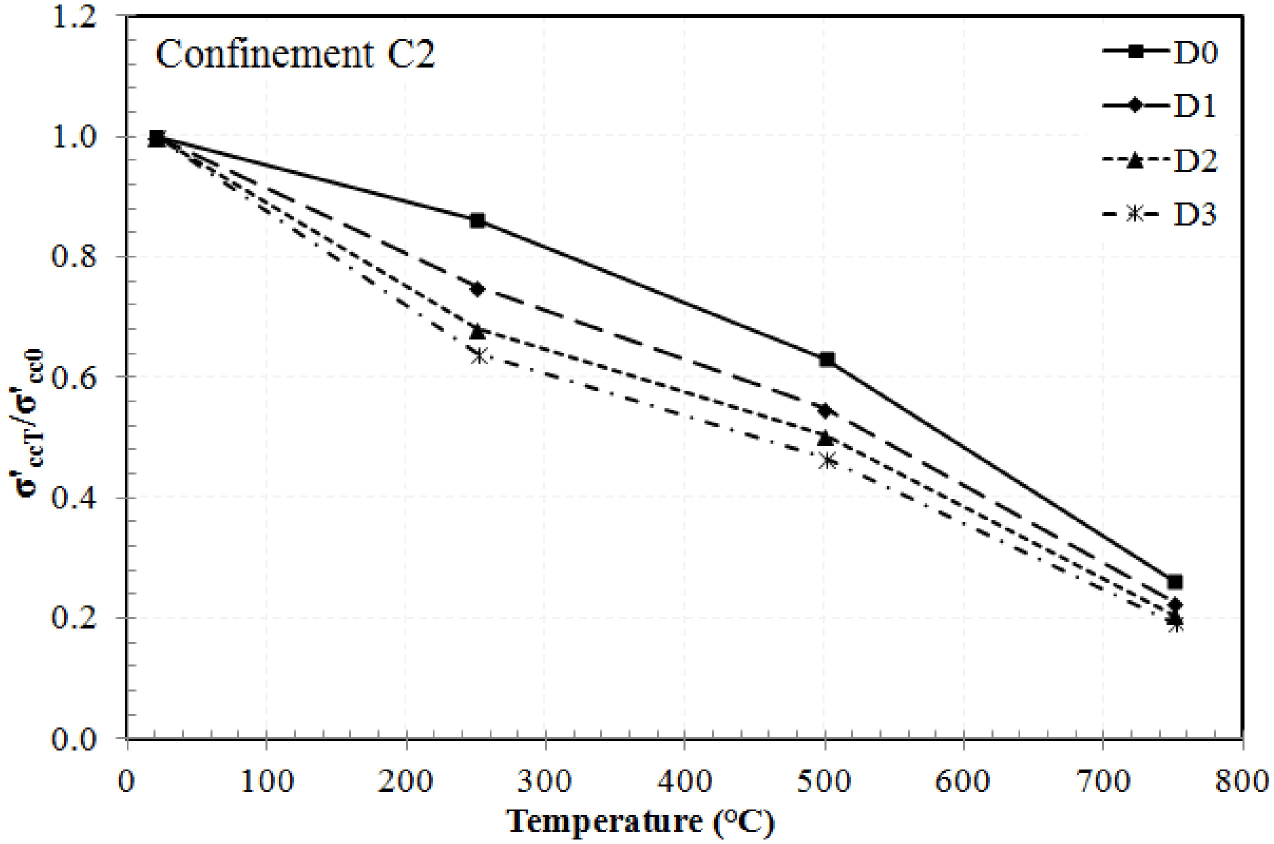

Fig. 3.15: Peak stress at elevated temperature for confined concrete with confinement C2

that predicts the stress-strain relationship of confined concrete at elevated temperatures via Equations 3.12 and 3.13. Youssef and Moftah [90] modified Mander's model by merely replacing the ambient mechanical properties by temperature dependent properties, though there is no evidence of the model being validated with experimental results. Accordingly, temperature dependent confined concrete compressive stress, σ'_{ccT} is,

$$\sigma'_{ccT} = \sigma'_{cT} \cdot \left[-1.254 + 2.254 \cdot \sqrt{1 + \frac{7.94 \cdot \sigma'_{lT}}{\sigma'_{cT}}} - \frac{2 \cdot \sigma'_{lT}}{\sigma'_{cT}} \right] \quad ; \quad \sigma'_{l} = K_e \cdot \frac{2 \cdot \sigma_{yT} \cdot A_s}{d_s \cdot S_h} \tag{3.12}$$

Where,

$\sigma_{yT} \longrightarrow$ Yield strength of the reinforcing bar at elevated temperature.

And, the stress-strain model is predicted by the equations given as:

$$\sigma_{cT} = \frac{2 \cdot \sigma'_{ccT} \cdot \epsilon_{cT}}{(\epsilon'_{ccT} + \epsilon_{tr}) \cdot \left[1 + \left(\frac{\epsilon_{cT}}{\epsilon'_{ccT} + \epsilon_{tr}} \right)^2 \right]} \quad ; \quad \epsilon'_{ccT} = \epsilon'_{cT} \cdot \left[1 + 5 \left(\frac{\sigma'_{ccT}}{\sigma'_{cT}} - 1 \right) \right] \tag{3.13}$$

The performance of the above expression has been examined in the context of the test results observed in the present study for the undamaged confined concrete. The temperature dependent mechanical properties such as unconfined concrete compressive strength (σ'_{cT}), corresponding strain (ϵ'_{cT}) and the lateral confining stress (σ'_{lT}) were calculated using Eurocode 2 [34] recommendations. It is evident from Table 3.4, 3.5 and 3.6 that predicted confined strength at elevated temperatures match well to the observed values; however the same is not true with respect to the strain corresponding to peak stress and the strain ordinates. Literature also highlights a big variability in respect to the strain components at elevated temperature obtained using various existing models. It may also be emphasized that the above equations are applicable to undamaged confined concrete specimens.

	Damage D0 / Confinement C1				Damage D0 / Confinement C2			
Temperature (C)	σ'_{cT} (Mpa)	σ'_{lT} (Mpa)	σ'_{ccT} [90] (Calculated) (Mpa)	σ'_{ccT} (Experimental) (Mpa)	σ'_{cT} (Mpa)	σ'_{lT} (Mpa)	σ'_{ccT} [90] (Calculated) (Mpa)	σ'_{ccT} (Experimental) (Mpa)
Ambient	24.00	4.06	44.59	43.48	24.00	1.93	35.29	31.95
250	21.59	4.06	41.64	38.69	21.59	1.93	32.70	27.54
500	20.78	3.17	29.55	29.99	20.78	1.51	22.97	20.19
750	19.98	0.69	8.08	11.84	19.98	0.33	6.45	8.34

Tab. 3.4: Confined peak stress: Experimental vs. Predicted

Once again, an attempt has been made to obtain an expression for predicting the confined peak stress at elevated temperature as a function of the confinement ratio and the level of damage. To this end, confined peak stress at elevated temperature has been evaluated in terms of damage index defined as the ratio E_{sec}/E_{c0} at ambient temperature and given as,

$$\left(\frac{\sigma'_{ccT}}{\sigma'_{cc0}} \right) = \alpha_T \cdot \left(\frac{E_{sec}}{E_{c0}} \right)^2 + \beta_T \cdot \left(\frac{E_{sec}}{E_{c0}} \right) + \gamma_T \tag{3.14}$$

	ϵ'_{cT} **Youssef et. al. [90]**				ϵ'_{ccT} **Youssef et. al. [90]**				
Temp.	**ASCE**	**Khennane and Baker**	**Kodur et. al.**	**Li and Purkiss**	**ASCE**	**Khennane and Baker**	**Kodur et. al.**	**Li and Purkiss**	**Experimental**
250	0.0065	0.0030	0.0057	0.0063	0.0367	0.0169	0.0322	0.0356	0.0199
500	0.0155	0.0065	0.0128	0.0100	0.0957	0.0399	0.0793	0.0615	0.0695
750	0.0295	0.0082	0.0237	0.0125	0.1469	0.0408	0.1181	0.0622	0.0287

Tab. 3.5: Strain at confined peak stress: Experimental vs. Predicted (Damage D0 / Confinement C1)

	ϵ'_{cT} **Youssef et. al. [90]**				ϵ'_{ccT} **Youssef et. al. [90]**				
Temp.	**ASCE**	**Khennane and Baker**	**Kodur et. al.**	**Li and Purkiss**	**ASCE**	**Khennane and Baker**	**Kodur et. al.**	**Li and Purkiss**	**Experimental**
250	0.0065	0.0030	0.0057	0.0063	0.0232	0.0107	0.0204	0.0226	0.0112
500	0.0155	0.0065	0.0128	0.0100	0.0606	0.0253	0.0502	0.0390	0.0271
750	0.0295	0.0082	0.0237	0.0125	0.0933	0.0259	0.0750	0.0395	0.0091

Tab. 3.6: Strain at confined peak stress: Experimental vs. Predicted (Damage D0 / Confinement C2)

Where the temperature dependent coefficients α_T, β_T and γ_T may be calculated from the equations given below.
For Confinement C1 ($20 \leq T \leq 750$),

$$\alpha_T = 0.001 \cdot T - 0.9723 \tag{3.15}$$

$$\beta_T = -0.0015 \cdot T + 1.298 \tag{3.16}$$

$$\gamma_T = -0.0008 \cdot T + 0.7812 \tag{3.17}$$

For Confinement C2 ($20 \leq T \leq 750$),

$$\alpha_T = 0.0009 \cdot t - 0.9282 \tag{3.18}$$

$$\beta_T = -0.0014 \cdot T + 1.2829 \tag{3.19}$$

$$\gamma_T = -0.0007 \cdot T + 0.7317 \tag{3.20}$$

The proposed equations , both for Modulus of Elasticity and the peak stress, perform well for the temperature range as specified in the present study. For a confinement different than C1 and C2 the coefficients may be calculated on the basis of linear interpolation. However, author is of the opinion that more elaborate experimental study needs to undertaken before the model may be acceptable in a wider perspective.

3.5.4 Damage Induced in Confined Concrete Specimens

The damage was induced in confined concrete specimens by means of pre-loading it prior to exposing it to the elevated temperature. At damage level D1, a load corresponding to the displacement 0.5 mm was imparted. The specimen experienced an internal damage of very low order. Lightly visible cracks were formed on the surface of the specimen at this damage level. However, a few micro-cracks are anticipated to occur in the specimen that hardly affects the integrity of the specimen. Occasional cracks were observed at the contact surfaces near the loading platens which were due to surface irregularities in the specimen. Significant cracking occurred at damage level D2 when the strains reached the yield. Cracking of concrete initiated at this stage. Several micro-cracks appeared at the surface of the specimen. However the location of cracks varied from specimen to specimen depending on the formation of first crack. Generally the cracks were much pronounced in and around the gauge length at the mid-height. Confinement effect is anticipated to play a major role at this damage level. At damage level D3, a great deal of cracking was visualized in the specimen. Since the stresses reached beyond the yield stress, the cracks started growing with the increasing load. Wide longitudinal cracks were observed all over the specimen. Figure 3.16 shows the cracks formed in the specimens during the damage cycle. The increasing stresses were well-handled by the confinement in the specimen. Occasional spalling of cover concrete was observed due to excessive cracking in some specimens.

Fig. 3.16: Cracks induced in damage cycle

3.5.5 Specimen Behaviour at Elevated Temperatures

A thermal gradient was attained in the overall length of the specimen due to different exposure conditions. However, the gauge length of the specimen, marked by the two titanium rods was exposed to a uniform temperature inside the furnace. This behaviour is evident from the picture shown in Figure 3.17, exposed to a temperature of 750 °C and tested to failure in compression. The exposed face turned white, since the concrete ingredients underwent phase transformations, the intermediate zone is marked by a smoky colour and the unexposed face remained in the original grey colour after the test. Strain gauges mounted on the confinement to measure the confinement strains either de-bonded or burnt out at temperatures beyond $300-400\,^{\circ}$C, thus making the exercise unsuccessful. In bondable strain gauges, the prime reason for the failure of strain gauges was de-bonding of the adhesive and burning the strain gauge's backing material (bakelite). Despite providing a fairly good insulation on the surface, the temperature propagated through the base material, steel, due to its high rate of conduction, thus de-activating the bond between the gauge and the surface. The main reason in case of weldable strain gauges more or less remained the same. However the gauge was not in direct contact with the rebar and the failure occurred through the loss of spot welding at elevated temperatures. It was observed under very rare circumstances, the strain gauges stopped functioning due to loss of solder of the Teflon cables. Figure 3.18 shows the failure of bondable and weldable strain gauges mounted on the confinement at elevated temperatures. The strain gauges in specimens in the damaged category, the temperature at which the gauges sustained dropped down to $200-300\,^{\circ}$C. The behaviour may be attributed to the fact that the damaged specimens contained several micro-cracks, which helped the temperature penetrate at a much higher rate than in the specimens in the undamaged category.

3.5.6 Failure Modes

The confined concrete specimens failed in compression generally in the middle third of the specimen under uniform temperature exposure and high confinement pressure. An estimate of the confinement pressure was unable to be established due to failure of strain gauges at elevated temperatures. Failure widely occurred due to buckling of longitudinal reinforcement under direct compression and opening of lateral ties (hoop rings)as shown in Figure 3.19 (a) and (b) respectively. At elevated temperatures, it was also observed that the bond between aggregate surface and cement paste separated, which resulted in the loss of integrity in the aggregate-cement paste matrix, which is evident from Figure 3.20. The coefficients of thermal expansion of steel and concrete being different, exposure of the specimens to elevated temperature introduces a differential thermal gradient. This results in separation of cover concrete from core concrete due to loss of bond between them. Figure 3.21 shows the failure of specimens where loss of cover is observed.

In specimens with confinement C1, one of the longitudinal bars was seen buckling under compression. This behaviour shows that a well-distributed confinement action was achieved. Whereas, in specimens with confinement C2, 2-3 or in some cases, all the longitudinal bars buckled before failing in compression. Failure due to buckling of longitudinal bars governed over failure due to opening of lateral ties. Figure 3.22 to Figure 3.27 shows the failure of specimens at different damage levels and elevated temperatures. Figure 3.22, 3.23 and 3.24 shows the failure of specimens with confinement C1 under damage categories

Fig. 3.17: Thermal Gradient evident from color change

Fig. 3.18: Failure of Strain Gauges

D1, D2 and D3 at ambient temperature, 250 °C, 500 °C and 750 °C. Figure 3.25, 3.26 and 3.27 shows the failure of specimens with confinement C2 under damage categories D1, D2 and D3 at ambient temperature, 250 °C, 500 °C and 750 °C.

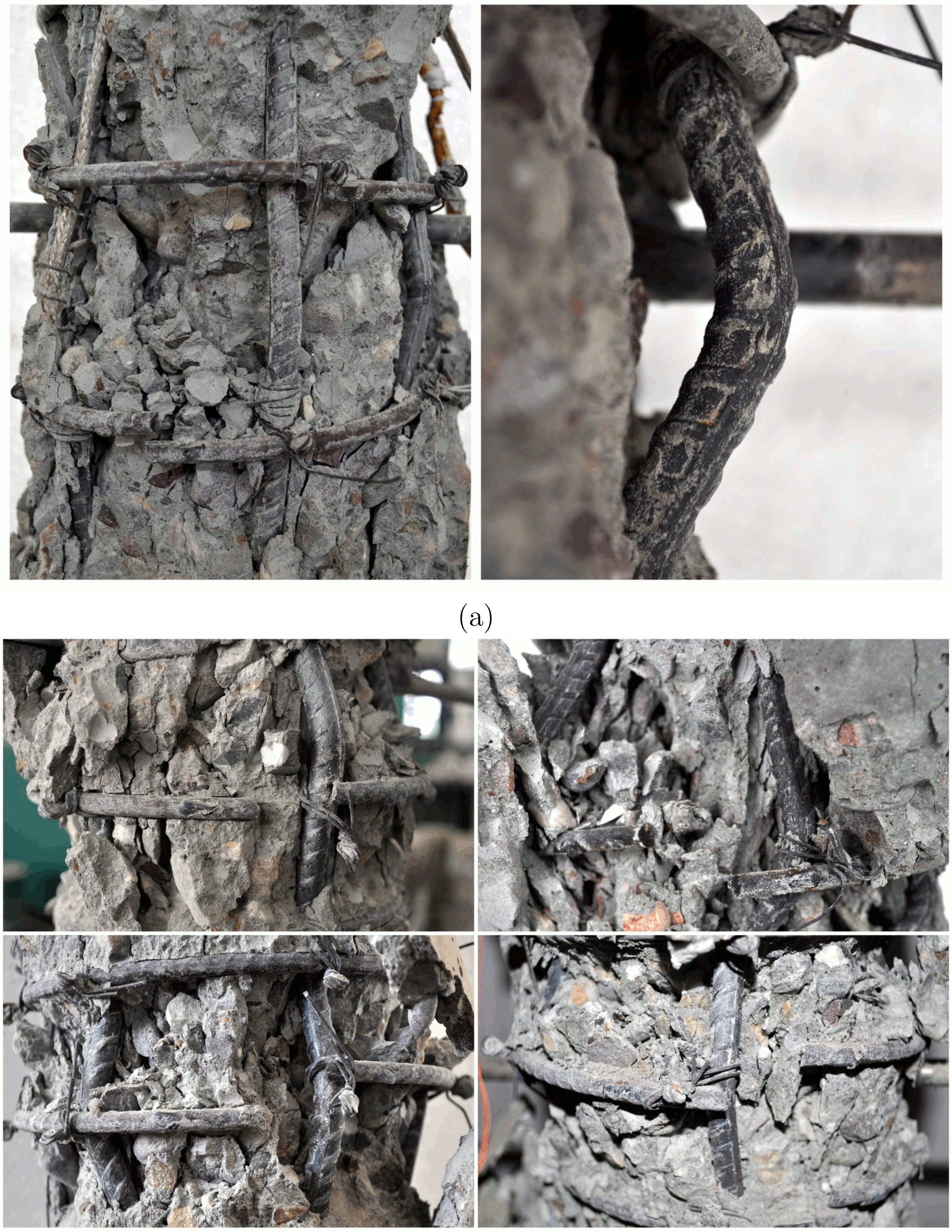

(a)

(b)

Fig. 3.19: Failure of confined concrete specimens by: (a) Buckling of longitudinal reinforcement (b) Opening of lateral ties

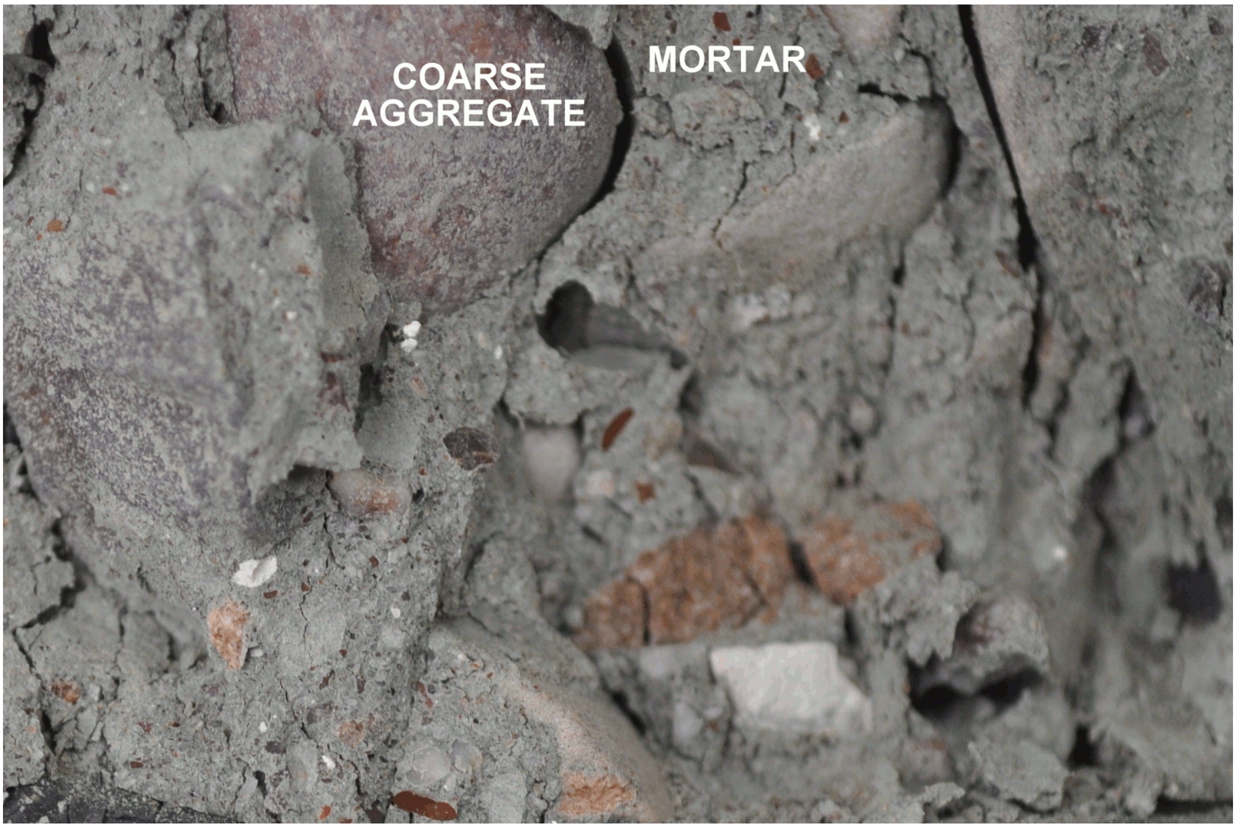

Fig. 3.20: Aggregate-mortar separation

Fig. 3.21: Loss of cover concrete

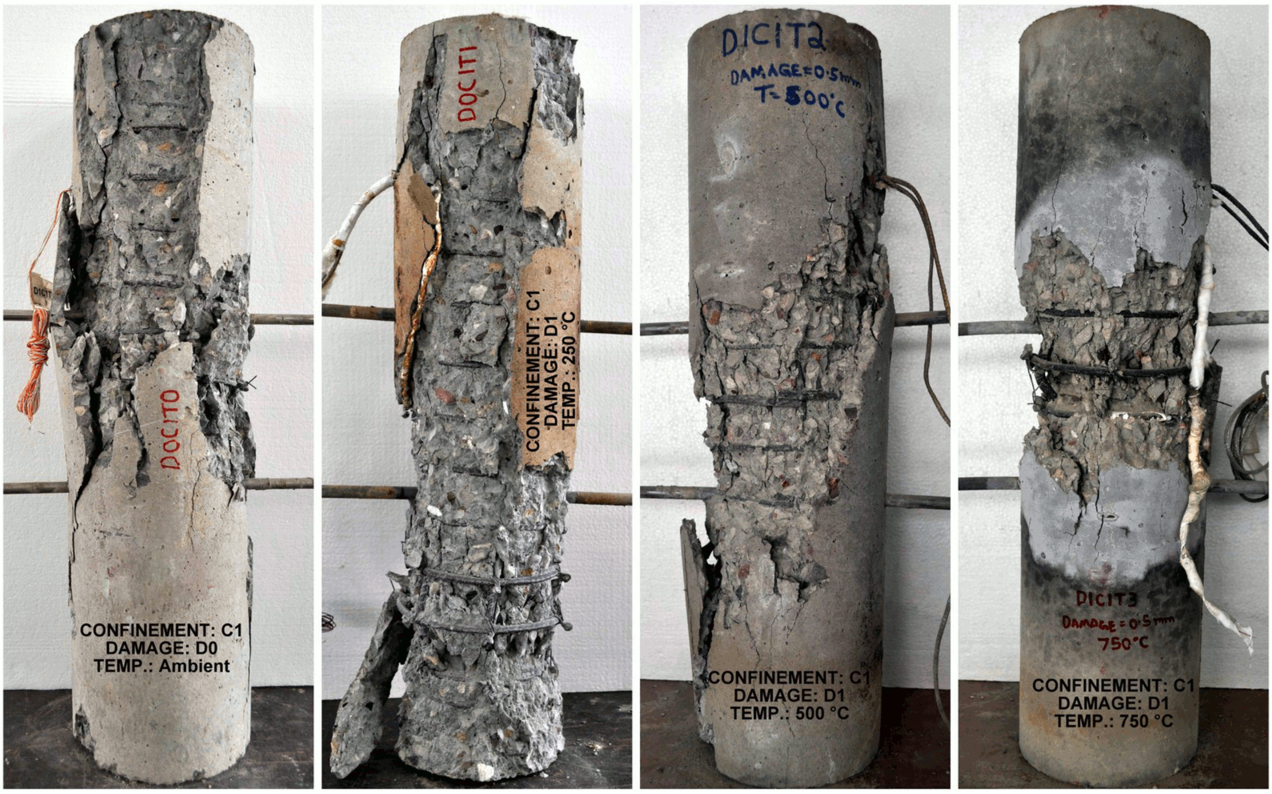

Fig. 3.22: Failure of specimens with confinement C1 under damage category D1

Fig. 3.23: Failure of specimens with confinement C1 under damage category D2

Fig. 3.24: Failure of specimens with confinement C1 under damage category D3

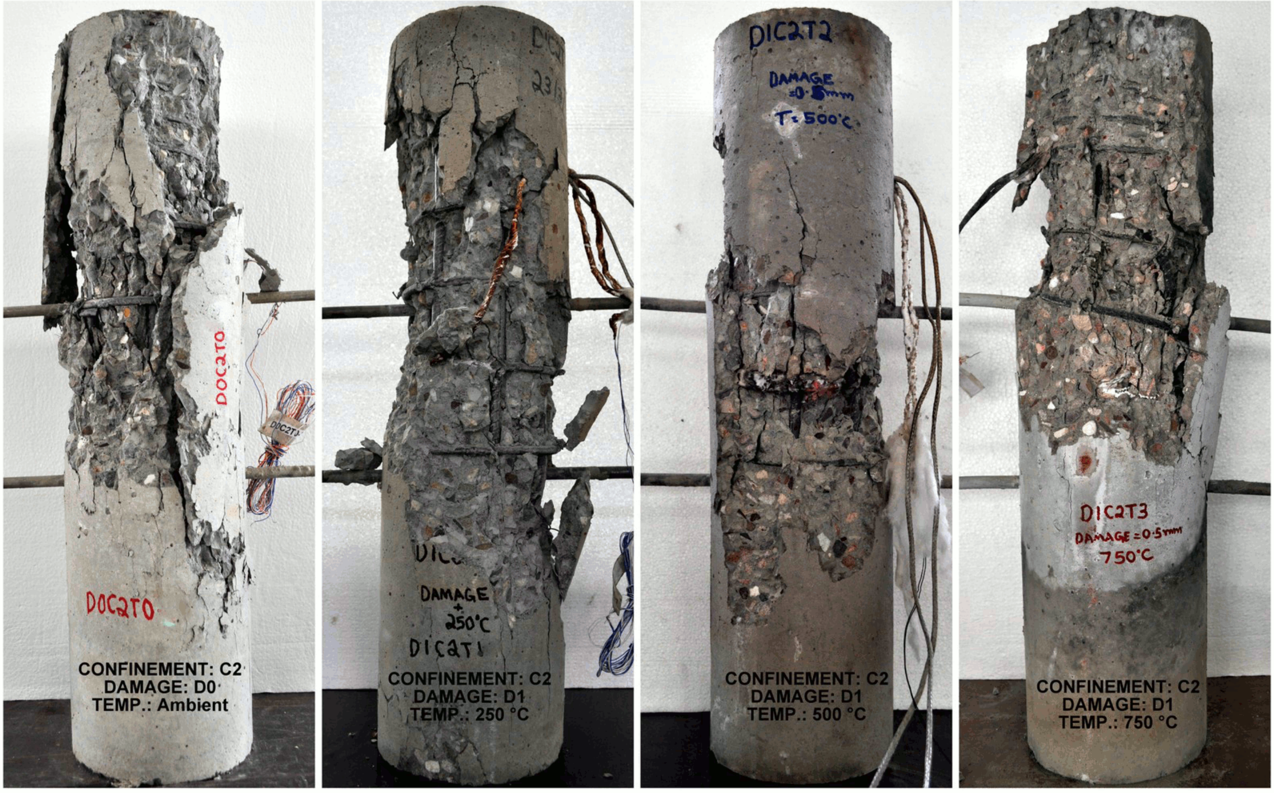

Fig. 3.25: Failure of specimens with confinement C2 under damage category D1

Fig. 3.26: Failure of specimens with confinement C2 under damage category D2

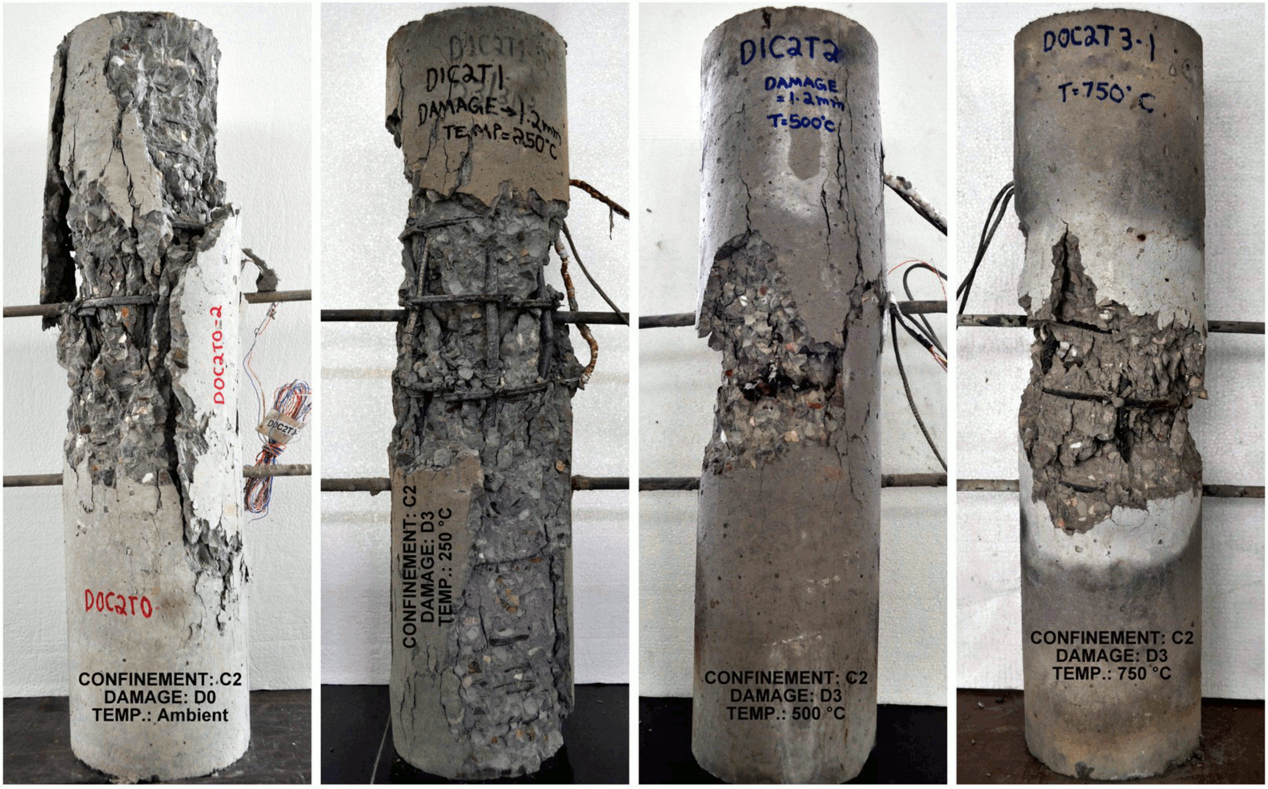

Fig. 3.27: Failure of specimens with confinement C2 under damage category D3

It is evident from the pictures that the failure generally occurred in the middle-third of the specimens. It is also observed that the thermal gradients were pronounced more severe at very high temperatures (750 °C). Explosive failure of concrete under high temperatures (500 °C and 750 °C) was observed. When a temperature of 750 °C was maintained inside the furnace for a long duration in order to achieve the steady state, the steel reinforcement, being a very good conductor of heat, reaches its austenitizing temperature which is beyond 900 °C resulting in excessive softening. When tested at 750 °C, confined concrete specimen completely loses its confinement action. When compression force if applied on the specimen, the reinforcement expands along with the concrete till it fails. Surface cracks start appearing on steel at a temperature of 500 °C. Figure 3.28 shows the expanded transverse reinforcement and surface cracks generated after exposure to 750 °C. Opening of ties was not observed in the specimens exposed to 750 °C.

Fig. 3.28: Confinement failure at 750 °C

3.6 CONCLUDING REMARKS

This chapter summarizes the testing methods and results of undamaged and damaged confined concrete specimens subjected to elevated temperatures. In the present study, two different levels of confinement were considered. Three pre-defined levels of damage were induced to the specimens in the 'damaged' category before exposing them to target temperatures. The study was primarily focussed on reckoning the effect of damage on confined concrete specimens exposed to three different levels of target temperatures. The fundamental mechanical properties such as peak stress, modulus of elasticity, strain at peak stress and ultimate strain were considered as the attributes of interest. Effect of damage and the effect of confinement on damaged concrete were considered as the significant findings of the study. The specimen behaviour and failure modes observed were explicitly discussed in this chapter. It was observed that the mechanical properties such as peak stress and modulus of elasticity showed a degradation with an increase in temperature in the specimens under undamaged category. Damage induced prior to heating causes further degradation of these properties. From the current study it may be inferred that damaged concrete is more vulnerable in case of fire accidents in reinforced concrete structures. From the tests, it was also evident that the effect of confinement is greatly reduced at a temperature of 750 °C. The results of current experimental research have been compared with some of the works of previous researchers found in the literature. Also, the numerical constitutive stress-strain relationship of undamaged confined concrete, proposed in the past has been compared with the present experimental results.

Structural Response of RC Frame Under Fire Following Earthquake

4

4.1 INTRODUCTION

Even though fires in structures due to an earthquake have a low probability of occurrence, they have induced some large conflagrations in the history, where fire was found to be predominant over earthquake. Earthquake triggered fires appear to be rather a scarce phenomenon that structures experience in their lifetime. But literature [27] [44] suggests that many of the earthquakes often leave behind a great deal of after effects such as fault rupture, shaking, liquefaction, landslides, fires, release of hazardous materials, tsunami, etc [27]. Fire is one such phenomenon which ignites and propagates at a rapid rate yielding to post-earthquake conflagrations. The main reason for the ignition is attributed to rupture of underground gas lines and fuel lines, electric short-circuiting and improper storage and disposal of hazardous materials. Occasionally, building characteristics and meteorological conditions combine to create a situation in which fire following earthquake is the predominant agent of damage. Large fires, despite their low probability of occurrence after an earthquake, have been very severe. History has produced two largest urban fires following earthquake, which have caused tremendous devastation of life and property - San Francisco 1906 and Tokyo 1923. More than 600 km region was incinerated in San Francisco and Kanto earthquake in Tokyo claimed more than 140000 lives. Apart from these major events, various incidents of fire were reported in 1989 Loma Prieta earthquake in California, 1994 Northridge, earthquake in California, 1995 Hanshin (Kobe) earthquake in Japan, 1999 Marmara earthquake in Turkey. The duration of fire in these earthquakes varied from few hours to three days [27]. An occurrence of earthquake and tsunami in Fukushima, Japan, 2011 also reported fire in a nuclear reactor turbine building. Engineering professionals now believe that earthquake triggered fires pose a very substantial threat in urban areas located all around the major fault lines across the globe. Structural engineers, practising professionals and seismologists are often uninformed about the effects on structures caused by a fire after an earthquake and fire protection engineers cater only to mitigate the fire loss by code implementation and other techniques. The role of earthquake triggered fires is apparently neglected and common practice addresses the two risks separately. However, the sequential effects govern during large conflagrations and the structures designed considering the effects separately may not withstand the after effects. A rigorous understanding of earthquake triggered fire scenario is required to account for their sequential effects. Existing literature [19, 28, 71, 85] discuss new research efforts required to meet the challenges of earthquake triggered fire. Past work from the authors [75] describes a series of full-scale tests planned on reinforced concrete frame subjected to simulated earthquake effects. Three full-scale tests were planned to experimentally investigate earthquake triggered fire effects on structures. Preliminary results of the first tests have been analysed and reported [75, 76]. Current chapter describes the second test in the series.

4.2 CONSTRUCTION OF REINFORCED CONCRETE TEST FRAME

A series of three tests were planned on a reinforced concrete frame sub-assemblage to study their behaviour in earthquake triggered fire events. A four storey framed structure with 4 bays in west-east and 3 bays in north-south direction was proposed as the structure under consideration. However, due to feasibility issues, the structure to be constructed and tested was limited to a symmetric frame sub-assemblage in the building structure. Figures 4.1 (a) and (b) show the plan and elevation of the proposed four storey framed structure. The hatched area in the figure designates the portion of frame finalized for construction. A reinforced concrete frame sub-assemblage was constructed monolithically on a raft in the existing outdoor testing facility. The sub-assemblage, which is basically a part of four storey building, consisted of 4 floor beams, 4 columns and a slab resting on 4 roof beams.

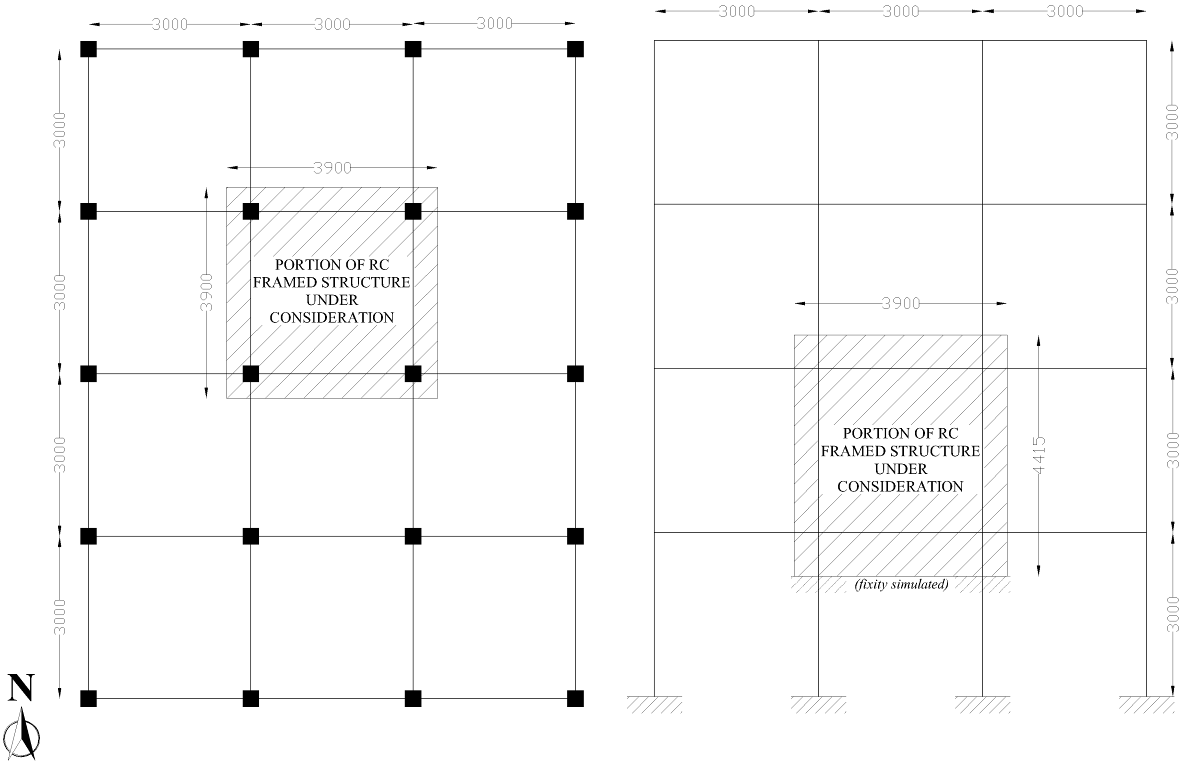

(a) (b)

Fig. 4.1: RC structure layout (a) In plan (b) In elevation

The test program was sub-divided into three stages; simulated earthquake load test, fire test and residual capacity test. In the first stage, the frame was initially subjected to simulated gravity load by mechanical means, unlike the first frame test, where slab loading was achieved using precast concrete slabs and sand bags [75]. A quasi-static lateral loading on the frame was achieved against a reaction wall using two double-acting hydraulic jacks capable of producing 300 *mm* lateral displacement in either direction. In the second stage, damaged frame was enclosed in a fire compartment and exposed to a one-hour pool fire capable of attaining temperatures beyond 1300 °C. The frame was then allowed to cool and taken to the third and last stage of testing where it was pushed to the full-capacity of hydraulic jacks (300 *mm*) to work out its residual capacity. Figure 4.2 shows the frame test strategy.

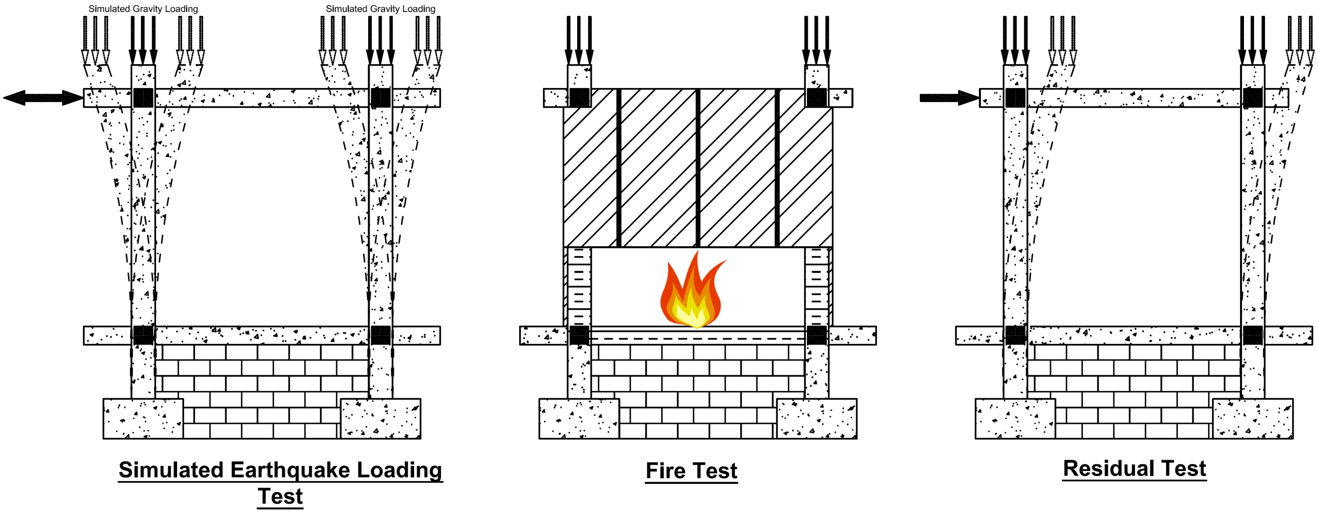

Fig. 4.2: Frame test strategy

The reinforced concrete frame was designed based on Indian standard code of practice, IS 456:2000 [15]. Ductile detailing of reinforced concrete was followed complying with the seismic code of practice, IS:13920-1993 [14]. Columns were 300 *mm* × 300 *mm* in cross-section whereas the beams were 230 *mm* × 230 *mm* in cross-section satisfying the "strong columns weak beams" system of seismic design of structures. Slab thickness was chosen to be 120 *mm*. A concrete mix of M30 (characteristic strength = 30 MPa) was used in combination with thermo-mechanically treated earthquake resistant steel reinforcing bars of grade Fe500 (yield stress = 500 MPa). Figure 4.3 (a) and (b) represent the schematic of the test setup in plan and elevation respectively. The frame was built on a 1.2 *m* thick raft constructed monolithically with a 5 *m* tall, 0.9 *m* thick reaction wall. Gravity loading was facilitated using a self-equilibrating loading arrangement as shown in 4.3 (b). Vertical loading was applied using 4 hydraulic jacks positioned over each column. Two steel girders were placed on four hydraulic jacks, which were positioned on the columns opposite to each other and parallel to the reaction wall. Bottom flanges of these girders rested on the hydraulic jacks with a base plate. These girders were connected to each other by means of cross-girders. This arrangement ensured a rigid diaphragm effect during lateral loading and was helpful in preventing the overturning of jacks. Two tie rods were connected with two MS plates at the ends, seated on neoprene padding (to ensure flexibility during lateral movement). This arrangement was positioned between the protruded part of the girder at the top and protruding floor beams at the bottom and tightened. The protruding portions of floor beams were checked for adverse effects caused by end moment caused due to lateral loading. Superimposed gravity loads corresponding to gravity loads of floors above were applied by the hydraulic Jacks and were maintained constant throughout the test.

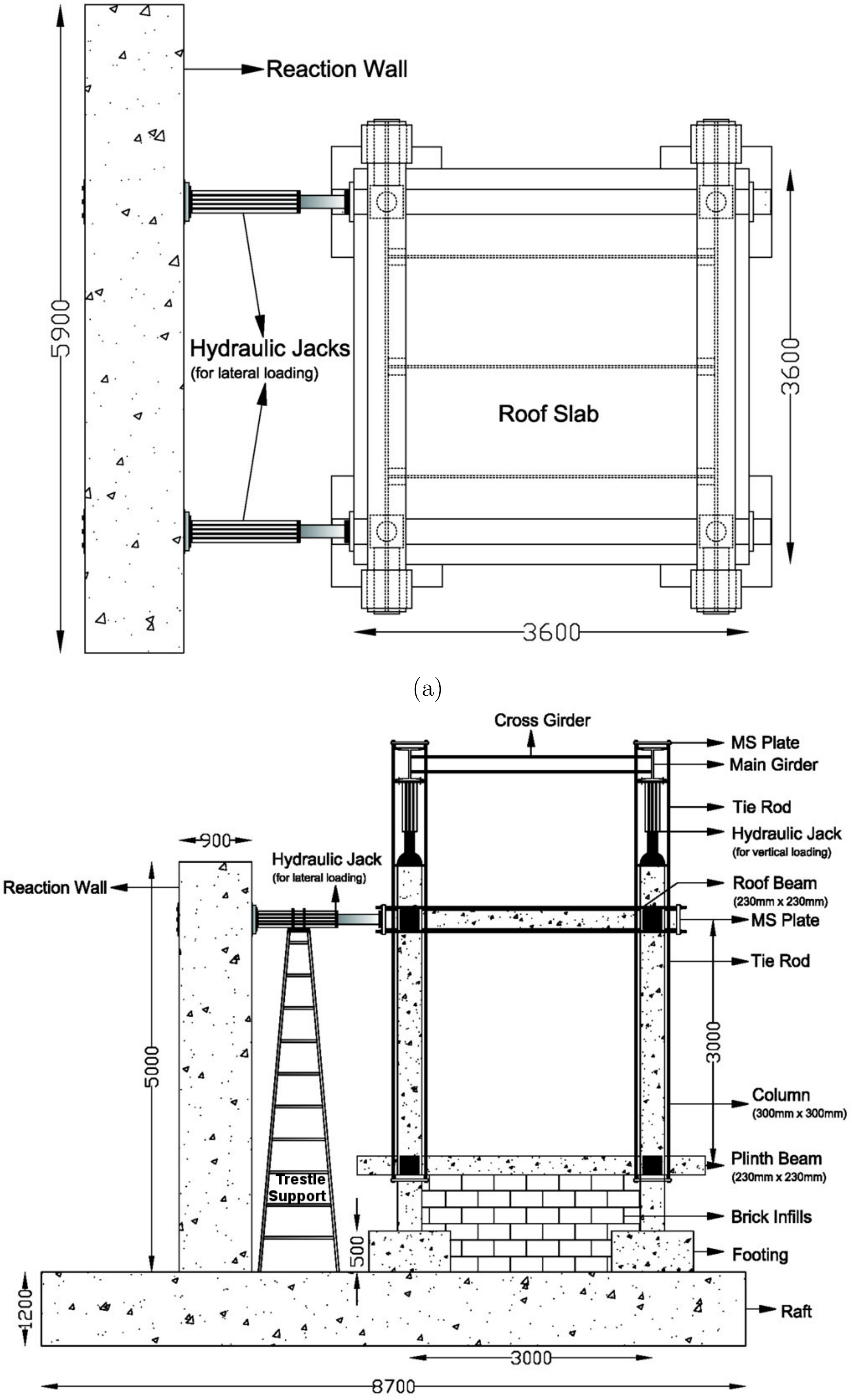

(a)

(b)

Fig. 4.3: Schematic diagram of the test setup (a)Plan (b)Elevation

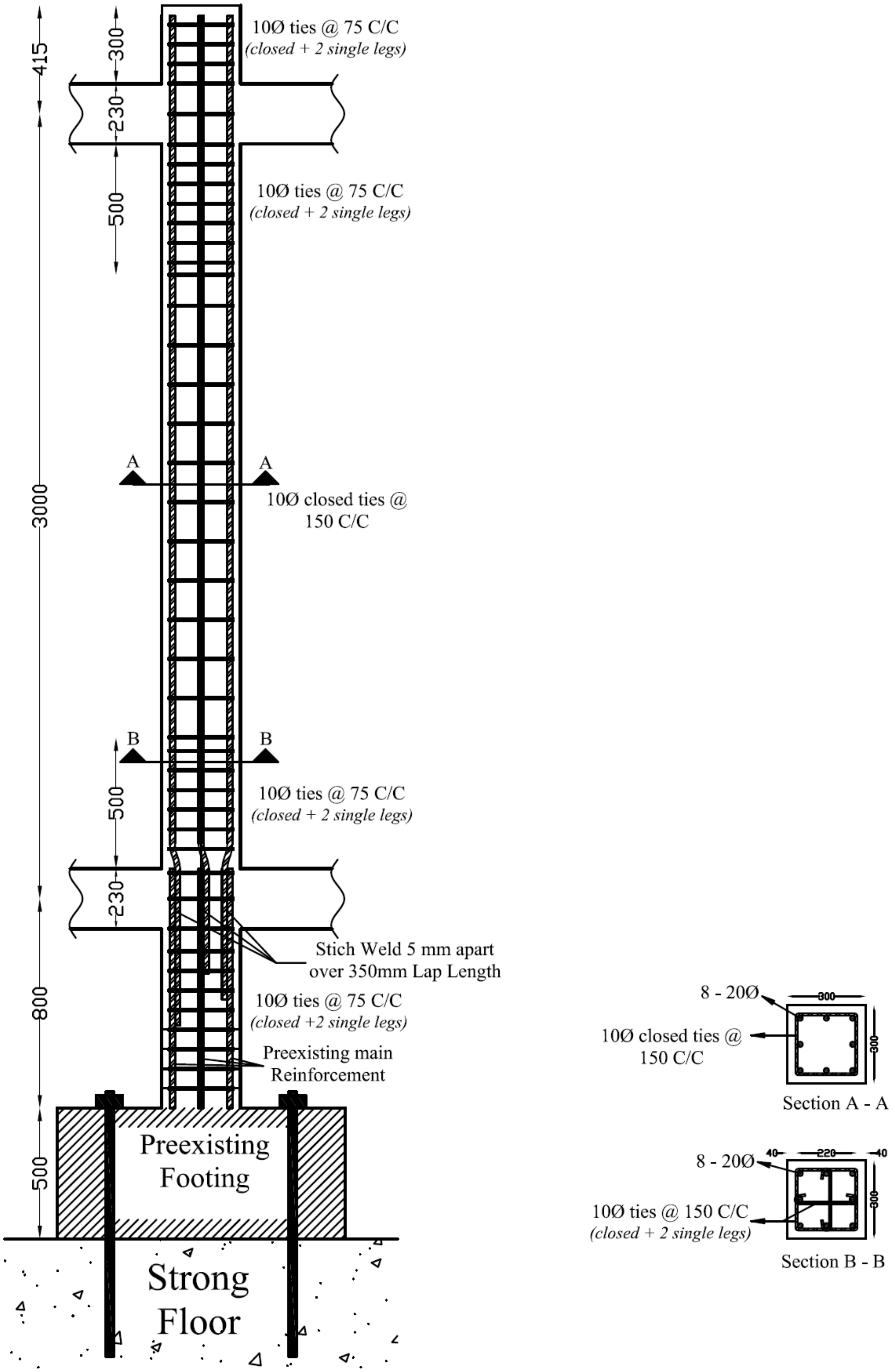

Fig. 4.4: Detailing of a column reinforcement

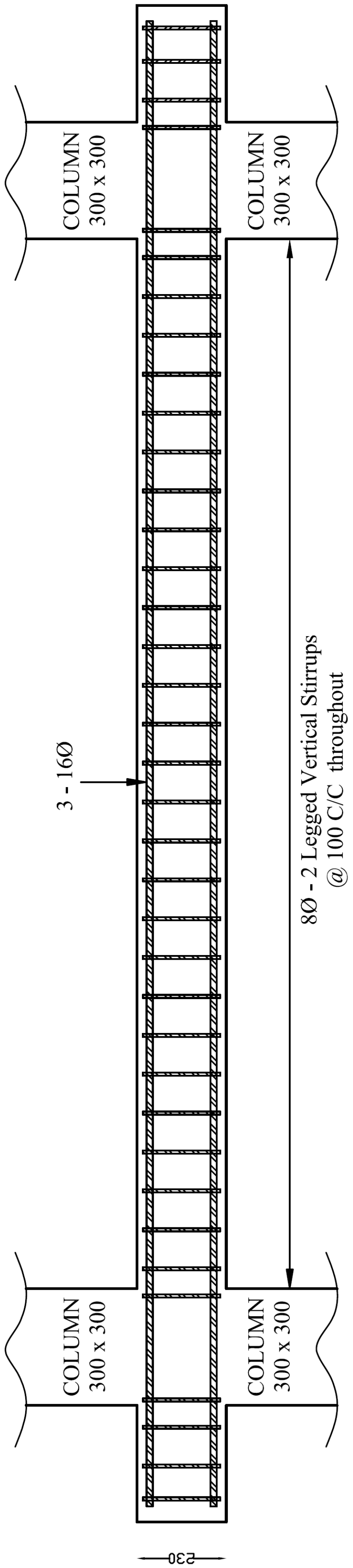

Fig. 4.5: Detailing of beam reinforcement

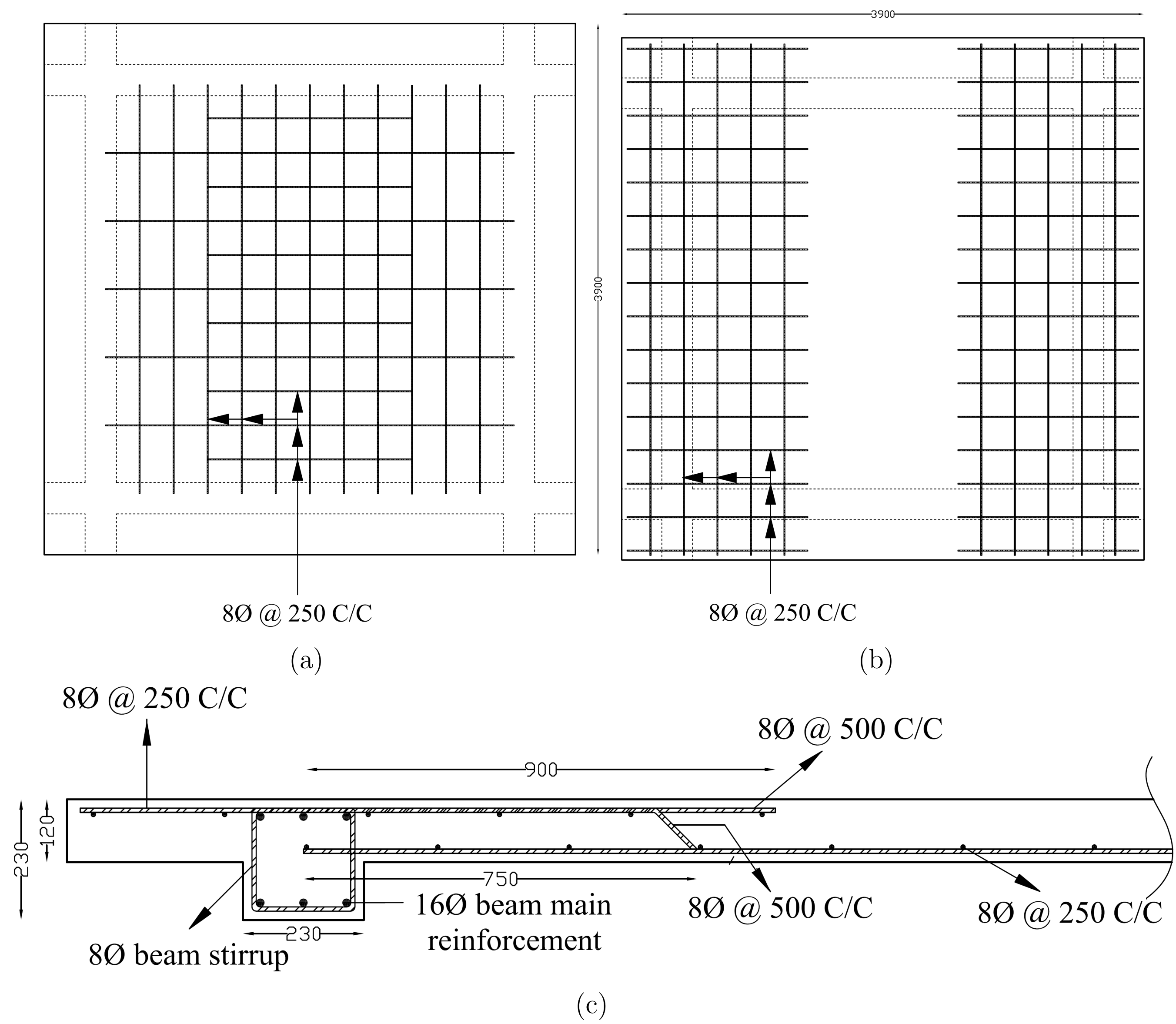

Fig. 4.6: Detailing of slab (a) Plan showing bottom reinforcement (b) Plan showing top reinforcement (c) Section though the slab

4.3 INSTRUMENTATION

The truncated frame was instrumented extensively with strain gauges, thermocouples, and LVDTs. Figure 4.7 shows the nomenclature of members and location of strain gauges embedded in the concrete. Three types of strain gauges of thermal sensitivity were used: ambient temperature, mid-range temperature resistant and high temperature resistant. Strain gauges were mounted on steel rebars at six different locations in each structural member and treated with temperature resistant and water proof coatings. Care was taken to ensure no vibration of concrete near the instrumented sections ensuring protection against debonding.

Figure 4.8 (a), (b) and (c) show the typical locations of thermocouples in floor beam, roof beam

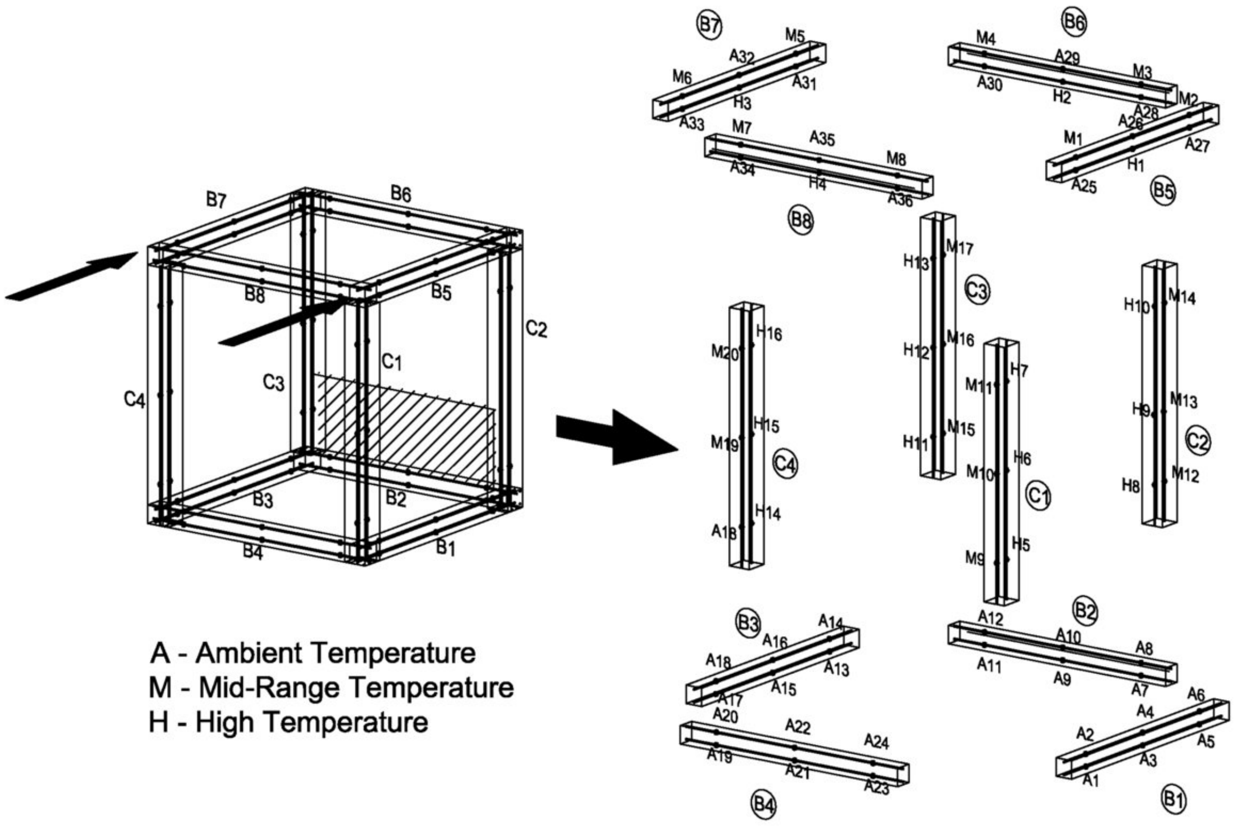

Fig. 4.7: Member nomenclature and location of strain gauges in the frame sub-assemblage

and columns respectively. Three sections, two near the joints and one at the center were chosen to be instrumented in each member. Figure 4.8 (d) shows the location of thermocouples along the depth of the slab. Five locations in plan were identified on the slab to record the temperature distribution. Figure 4.8 (e) shows the distribution of thermocouples inside the fire compartment. Three thermocouple trees were positioned inside the compartment. Each tree consisted of five thermocouples positioned at different heights to obtain the thermal profiles throughout the compartment. The lateral displacements throughout the test were recorded using long stroke length linear variable displacement transducers (LVDTs) placed on the section of the slab, on two extreme opposite ends. Vertical displacements during fire were captured using five LVDTs positioned vertically on top of the roof slab. All the LVDTs were mounted on an externally erected secondary frame independent of the test frame. All the cables were well insulated in fire proof encapsulation to avoid damage due to high temperature during the fire test. Lateral loads were monitored at constant intervals throughout the first and last test stages using pressure sensors connected to the hydraulic jacks. All the sensors were connected to a series of data logger units stationed at an onsite control center. A data logging frequency of 20 seconds was maintained throughout the tests. During the fire test, a 48 hour history was logged to capture the temperature in pre-flashover, flashover, post-flashover and cooling regimes.

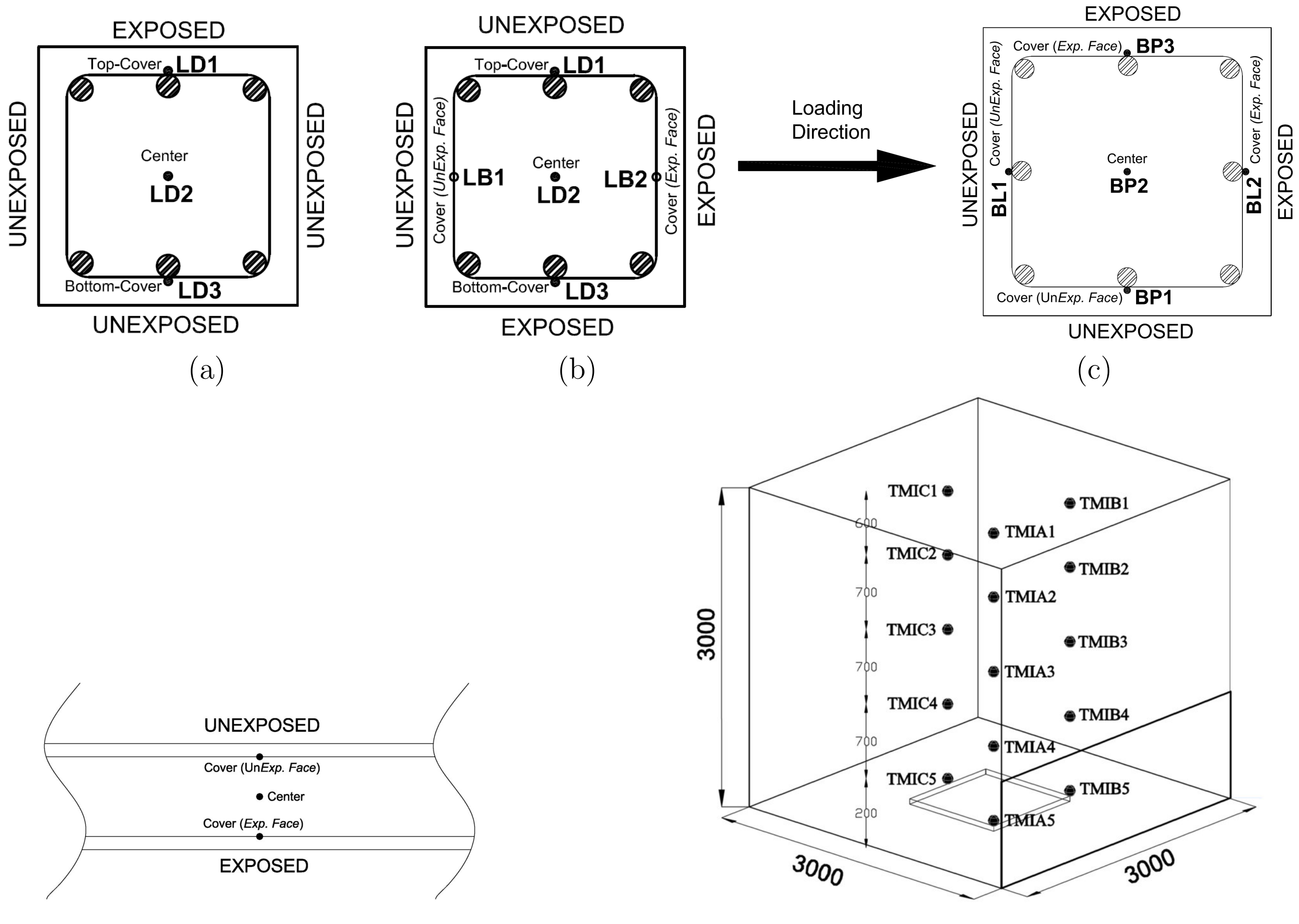

(a) (b) (c)

(d) (e)

Fig. 4.8: Location of thermocouples (a) Floor beam (b) Roof beam (c) Column (d) Slab (e) Compartment

4.4 FRAME TEST STAGE I: SIMULATED EARTHQUAKE LOAD TEST

4.4.1 Gravity and Seismic Loads

4.4.1.1 Gravity Load

Prior to the application of simulated earthquake loading, the frame was imparted dead load and live load according to Indian Standards for general loading, IS:875 (Part 1 and 2) : 1987 [12, 13] and earthquake resistant design of structures, IS 1893 (Part 1) : 2002 [16]. Gravity load and imposed loads applied were 1 kN/m^2 and 2 kN/m^2 respectively. However, a design imposed load of 25% of 2 kN/m^2, i.e., 0.5 kN/m^2 was imparted based on IS 1893 (Part 1) : 2002 recommendation.

4.4.1.2 Seismic Loading Calculation

Seismic loading to be imposed on the RC frame was computed based on Indian Standard, IS 1893 (Part 1) : 2002, as mentioned above. Roorkee, located in the state of Uttarakhand, India lies in the seismic zone IV according to Figure 1., pp.5 of the standard [16]. Zone IV is regarded as a zone with severe seismic intensity having a zone factor (Z) 0.24 (Table 2, pp.16.). The building is considered as a non-service building with an importance factor (I) of 1 (Table 6, pp.18). Since the RC frame is a special moment-resisting frame, a response reduction factor (R) of 5.0 is implied (Table 7, pp.23). For a soil type 'medium', a spectral acceleration coefficient considered from the response spectra (Figure 2, pp.16) is shown in Equation 4.1.

$$\frac{S_a}{g} = \begin{cases} 1 + 15T; & 0.00 \leq T \leq 0.10. \\ 2.50 & 0.10 \leq T \leq 0.55. \\ \dfrac{1.36}{T} & 0.55 \leq T \leq 4.00. \end{cases} \tag{4.1}$$

Also, a damping of 5% is considered. The fundamental natural time period is calculated from Equation 4.2.

$$T_s = \frac{0.09}{\sqrt{d}} h \tag{4.2}$$

Where,
$d \longrightarrow$ Base dimension in the considered direction
$h \longrightarrow$ Height of the Building

4.4.1.3 Load Combinations

Considering the limit state design of reinforced concrete structures, the following load combinations *(with partial factors of safety)* were accounted for the initial design of the frame.

1) $1.5\,(DL + IL)$

2) $1.2\,(DL + IL \pm EL)$

3) $1.5\,(DL \pm EL)$

4) $0.9DL \pm 1.5EL$

4.4.2 Simulated Earthquake Load

Simulated earthquake loading was induced in the frame in terms of lateral drift experienced by a typical concrete building frame for a particular structural performance level per FEMA 356:2000 [36]. Structural performance of a building is generally associated with four discrete levels of structural performance, which correlates with specified structural performance requirements: "Immediate occupancy", "life safety", "collapse prevention" and "not considered *(collapse)*". In the current evaluation, collapse prevention level of structural performance was considered. At this level, structural components, despite experiencing damage, continues to support gravity loads but retains no margin against collapse in compliance with the acceptance criteria specified. The code specifies a substantial damage to the structure, potentially including significant degradation of strength and stiffness of the lateral force resisting system, large permanent and lateral deformation of the structure and degradation of vertical-load-carrying capacity (less likely) in collapse prevention level of seismic performance. As per the code [36], a 4% lateral drift, yielding a displacement of 152 *mm* was imparted to the frame. The displacements were incrementally imparted in push and pull cycles of 10 *mm* each.

Figures 4.9 (a) and (b) show the cycles of displacements imparted and the load recorded from the simulated earthquake loading respectively. After achieving the desired displacement in each cycle, the recorded lateral load was maintained in order to map the cracks and study their growth pattern. Numerous cracks developed near beam-column intersection, both at floor as well as roof level during push and pull cycles. Cracks on columns were initiated during 20 *mm* push cycle whereas those on beams were initiated during 30 *mm* push cycle. Cracks were initiated on the plane perpendicular to the loading direction and these cracks further propagated in the subsequent cycles. The crack widths in different members were measured using a crack micro-scope and they varied from 0.1 *mm* to 2.4 *mm*. Most severe cracks were developed at the beam-column junctions at 130 *mm* and 140 *mm* displacement cycles. The average growth rate of crack width was found to be 0.1 *mm* per 20 *mm* cyclic displacement.

Figures 4.10 (a), (b), (c) and (d) show the cracks developed at floor beam column junctions. A crack of width 2.4 *mm* formed at the intersection of beam B1 with columns C1 and C2, which is shown in Figures 2.8 (a) and 2.8 (b). Loss of concrete cover could be marked from Figure 2.8 (d), which occurred during greater displacement cycles. Figures 4.11 (a), (b), (c) and (d) depict the cracks formed at roof beam-column intersection. Loss of concrete cover was observed at the intersection of roof beam B5 and columns C1 and C2 as shown in Figures 4.11 (a) and (b). Cracks of widths 2.4 *mm* and 0.4 *mm* appeared at B5 C1 intersection. Load-displacement history as obtained from the loading cycles is shown in Figure 4.12. Target displacement of 150 *mm* was achieved in 11 displacement cycles. Each cycle had a push and a pull event. A displacement interval of 10 *mm* was considered upto a displacement of 50 mm, after which it was increased to 20 mm upto 130 mm displacement cycle. In the last displacement cycle, the frame was pushed forward by 150mm and unloaded. The maximum recorded load was 401 kN at a lateral displacement of 150 mm. A plastic residual displacement of 19 mm was registered upon unloading.

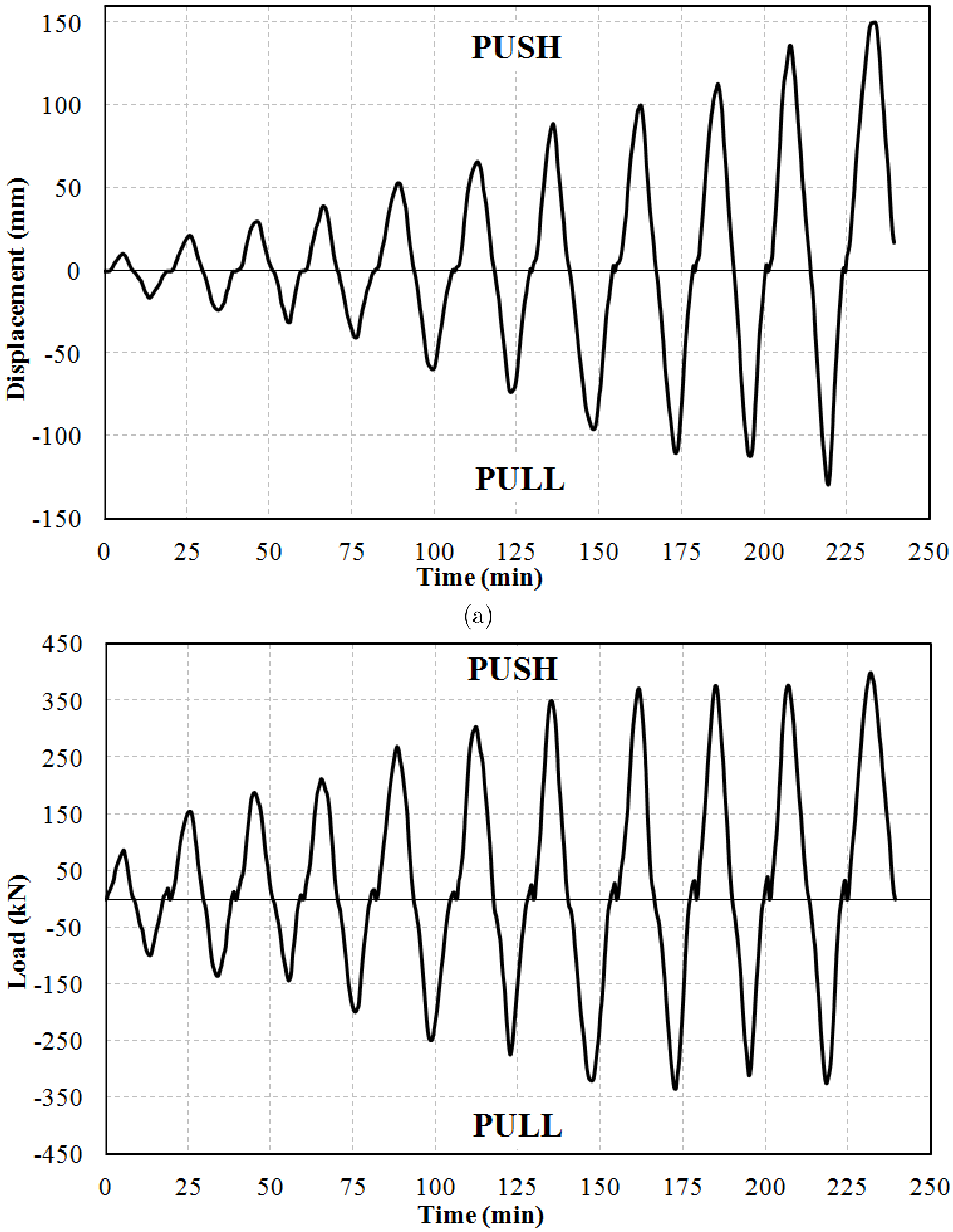

(a)

(b)

Fig. 4.9: Simulated earthquake cycles (a) Displacement (b) Load

(a) (b)

(c) (d)

Fig. 4.10: Damage induced at floor beam column joints

(a) (b)

(c) (d)

Fig. 4.11: Damage induced at roof beam column joints

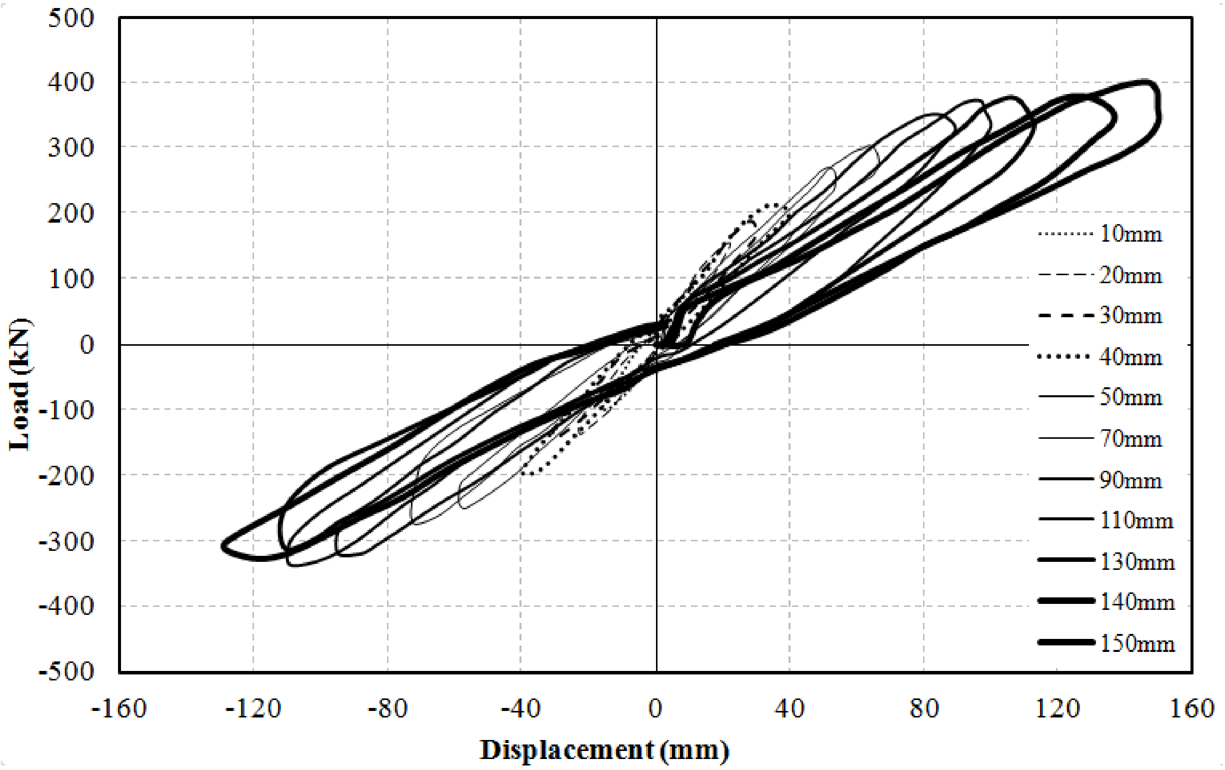

Fig. 4.12: Load-Displacement hysteresis for simulated earthquake loading

4.4.3 Strain Data

Figures 4.13 to 4.24 represent the strains registered on the rebars of the frame sub-assemblage at various locations during the simulated earthquake loading. Strains were recorded during all push and pull cycles of loading. Most of the strain gauges performed fairly well in recording the microstrain. However, some of the strain gauges malfunctioned due to the damage experienced during mounting, placing of rebars, casting of concrete and removal of formwork. Maximum strains were logged in the members that were parallel to the loading direction i.e., beams B1, B3, B5 and B7. Figure 4.13 (a) to (d) shows the strains obtained in Beam B1 during different cycles. A maximum strain of 3565×10^{-6} and 3499×10^{-6} was recorded during push cycle and 408×10^{-6} and 1596×10^{-6} during pull cycle at left section of the top rebar and right section of the bottom rebar respectively.

Figures 4.14 (a) to (d) show the strains obtained in Beam B2 during different cycles of simulated earthquake loading. Negative strains of low values were observed, which suggest that the strains were recorded only during the pull cycle. This was mainly due to the non-uniform loading on the structure using two different hydraulic jacks. The strains were in the order of 150 to 900.

Beam B3 (Figures 4.15 (a-d)), exhibited a similar trend alike Beam B1. Microstrains of order 3272 and 618 were noticed in the push cycle at the bottom rebar of left section and top rebar at right section respectively. During the pull cycle, a microstrain of order 775 and 1019 were recorded at the same locations. Similar strain behaviour was observed in top rebars on both right and left sections as shown in Figures 4.15 (b) and (d). It is observed from Figure 4.15 (a) that the strains increase with time which is attributed to higher levels of load experienced by the structure subject to greater displacements.

Beam B4, located in the direction perpendicular to the direction of loading registered the strain values similar to that of Beam B2. As observed in Figure 4.16 (a), (c) and (d), the strains were mostly registered in the pull cycle. However, a low microstrain value of 436 was recorded on top rebar of the left section [Figure 4.16 (b)].

Roof beams B5, B6, B7 and B8 exhibited a higher strain in the push cycle and lower strains in the pull cycle. Figures 4.17 (a-d) show the strain variations in beam B5. Similar trends of strains were observed in bottom rebar of the left sections and top rebar of the right section during the alternate push and pull cycles. The mid-span section registered lower value of strains (440) as shown in Figure 4.17 (b). This is due to the fact that prominent bending is always seen at the member ends.

Beam B6 located in the direction perpendicular to the loading direction produced microstrains under 1000 in both push and pull cycles of loading. The rebars located at the bottom on the left and right sections exhibited a similar trend whereas, the rebars located on the top of left and right section recorded similar strains.

Figures 4.19 (a-d) represent the strain patterns obtained in the roof beam B7. The bottom rebars of the member at left and right sections show an increment in strains with an increasing loading following the displacement. A lower value of microstrain is observed in the mid-span section. The strain gauges on Beam B8 recorded higher value of microstrains (> 2000) at the top rebar of the left section. as shown in Figure 4.20 (b).

Figures 4.21 to Figure4.24 show the strain variations obtained in columns during simulated earthquake loading. [1] From Figure 4.21 (a-d), it is observed that the microstrain values were higher at the top and bottom joints than at the mid-section as expected. A maximum microstrain value of 2592 during push and 2594 during pull cycle were registered in column C1 at the rebar located at the unexposed face of the bottom section [Figure 4.21 (b)].

In column C2, highest microstrain of 2790 was recorded on the bottom rebar located on the unexposed face as shown in Figure 4.22 (b). Similar trends were observed at the bottom and mid-height section of column C2 on the exposed face. The value of microstrains increased from bottom section to the top section of the columns.

Figure 4.23 (a-c) shows the microstrains registered by strain gauges mounted on the rebars of column C3 along exposed and unexposed faces. It was observed that the values of microstrains and the trend was fairly similar on both exposed and unexposed faces in a section.

Strains obtained by the strain gauges mounted on exposed and unexposed faces of column C4 are as shown in Figure 4.24 (a-d). High value of microstrains were observed in column C4 at the mid-height section of exposed face.

---

[1] Refer Figure 4.8 (c) for fire exposure conditions in the column

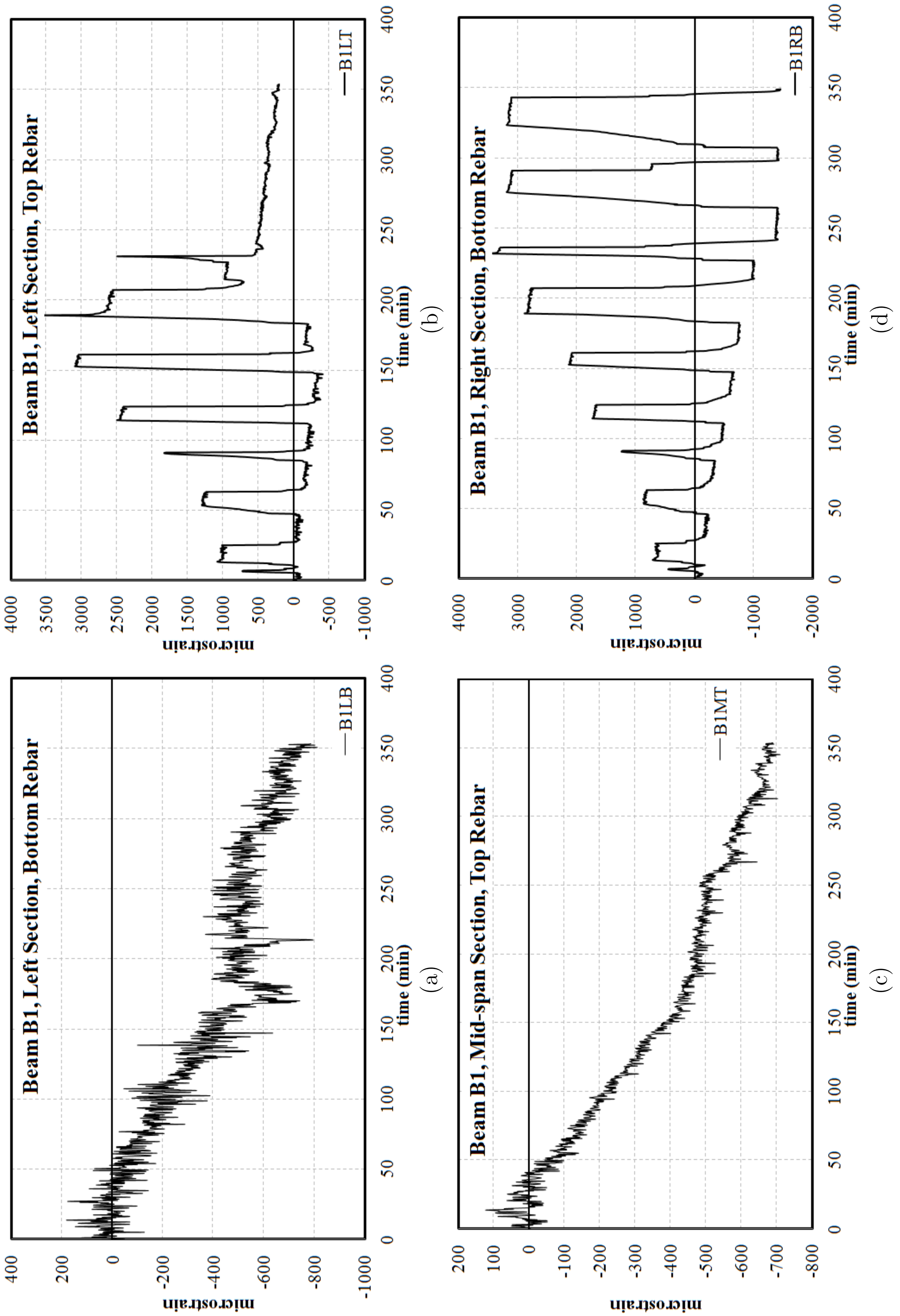

Fig. 4.13: Strain profile in beam B1 (a) Left section, bottom rebar (b) Left section, top rebar (c) Mid-span section, top rebar (d) Right section, bottom rebar

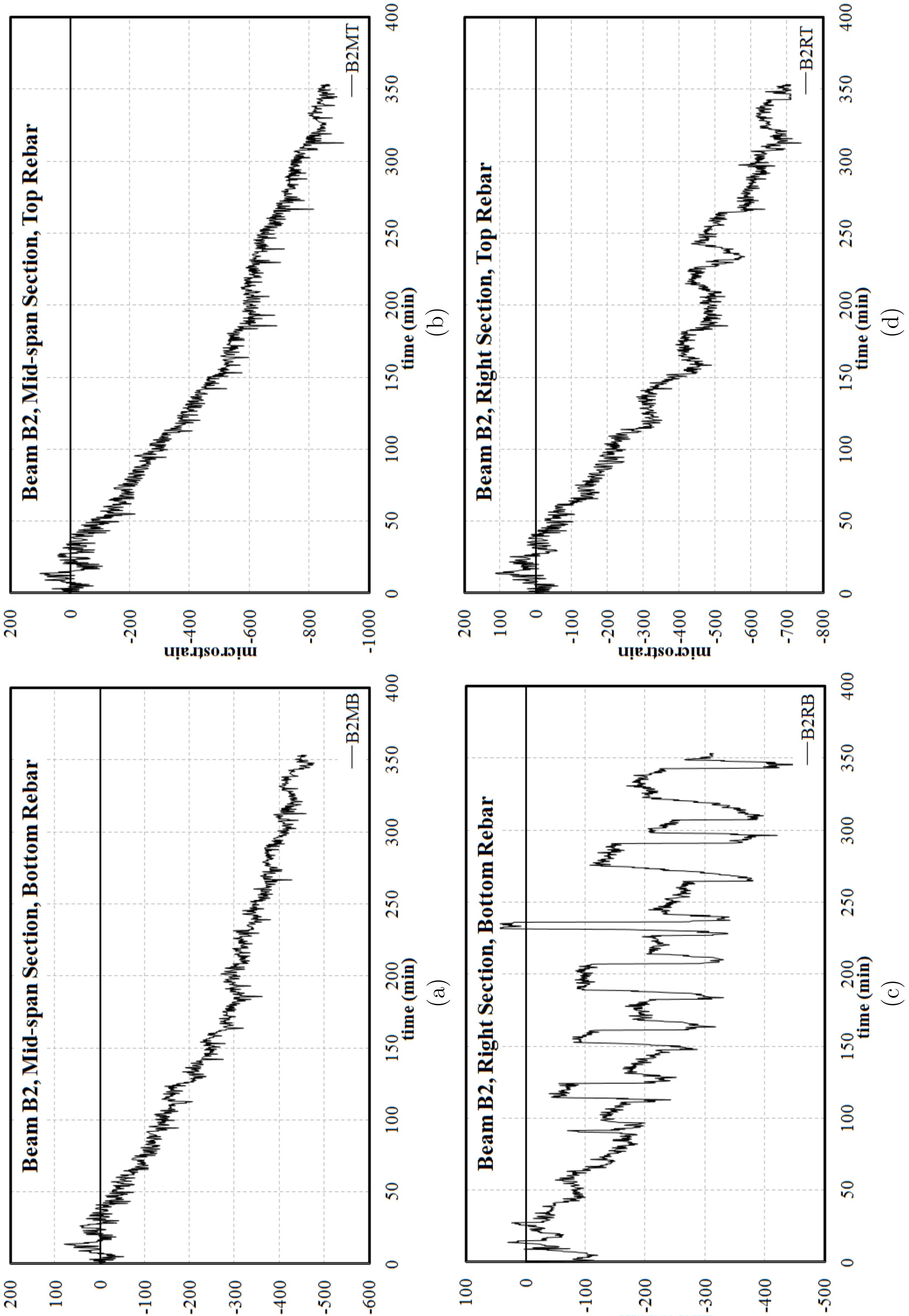

Fig. 4.14: Strain profile in beam B2 (a) Mid-span section, bottom rebar (b) Mid-span section, top rebar (c) Right section, bottom rebar (d) Right section, top rebar

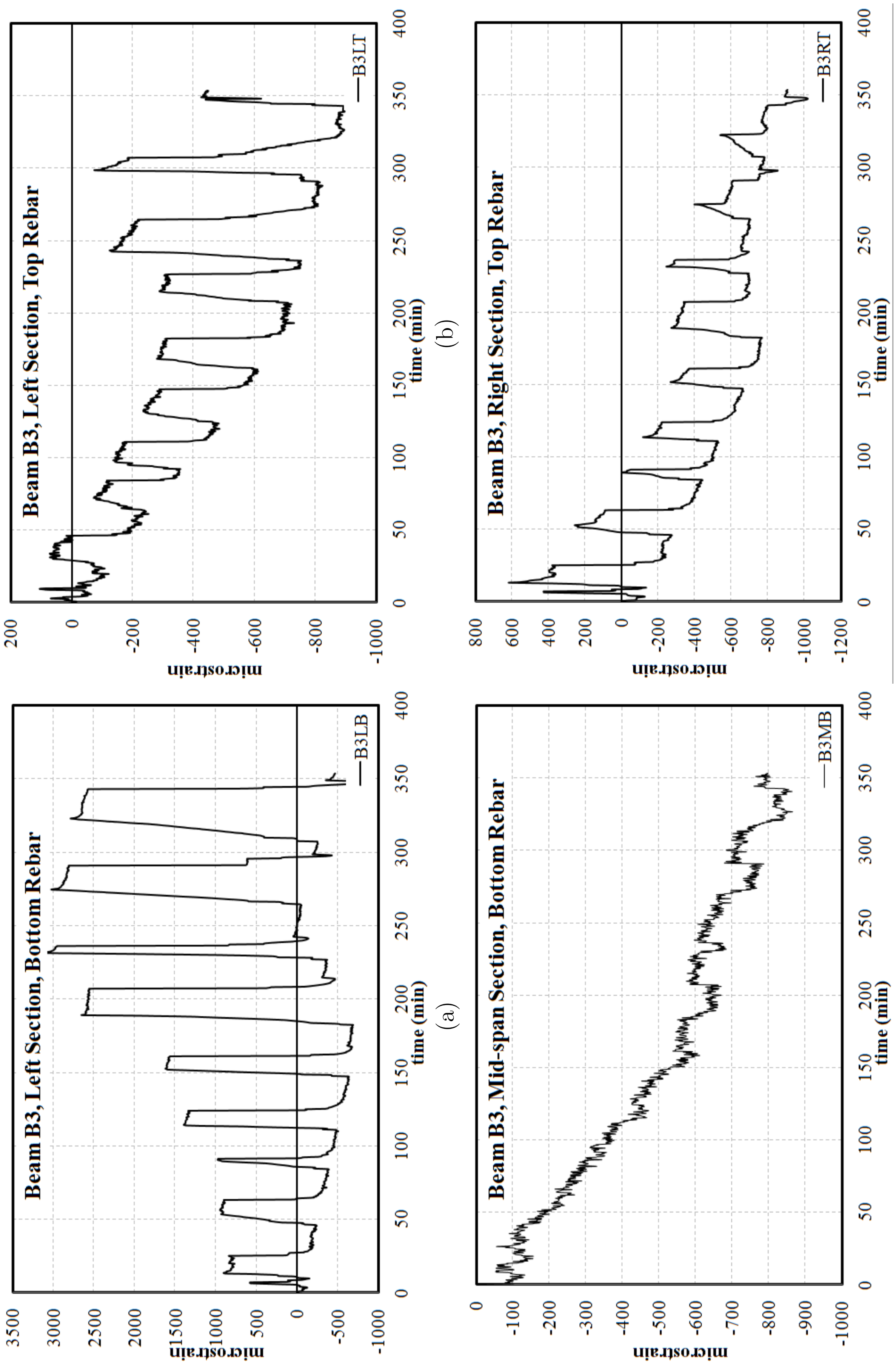

Fig. 4.15: Strain profile in beam B3 (a) Left section, bottom rebar (b) Left section, top rebar (c) Mid-span section, bottom rebar (d) Right section, top rebar

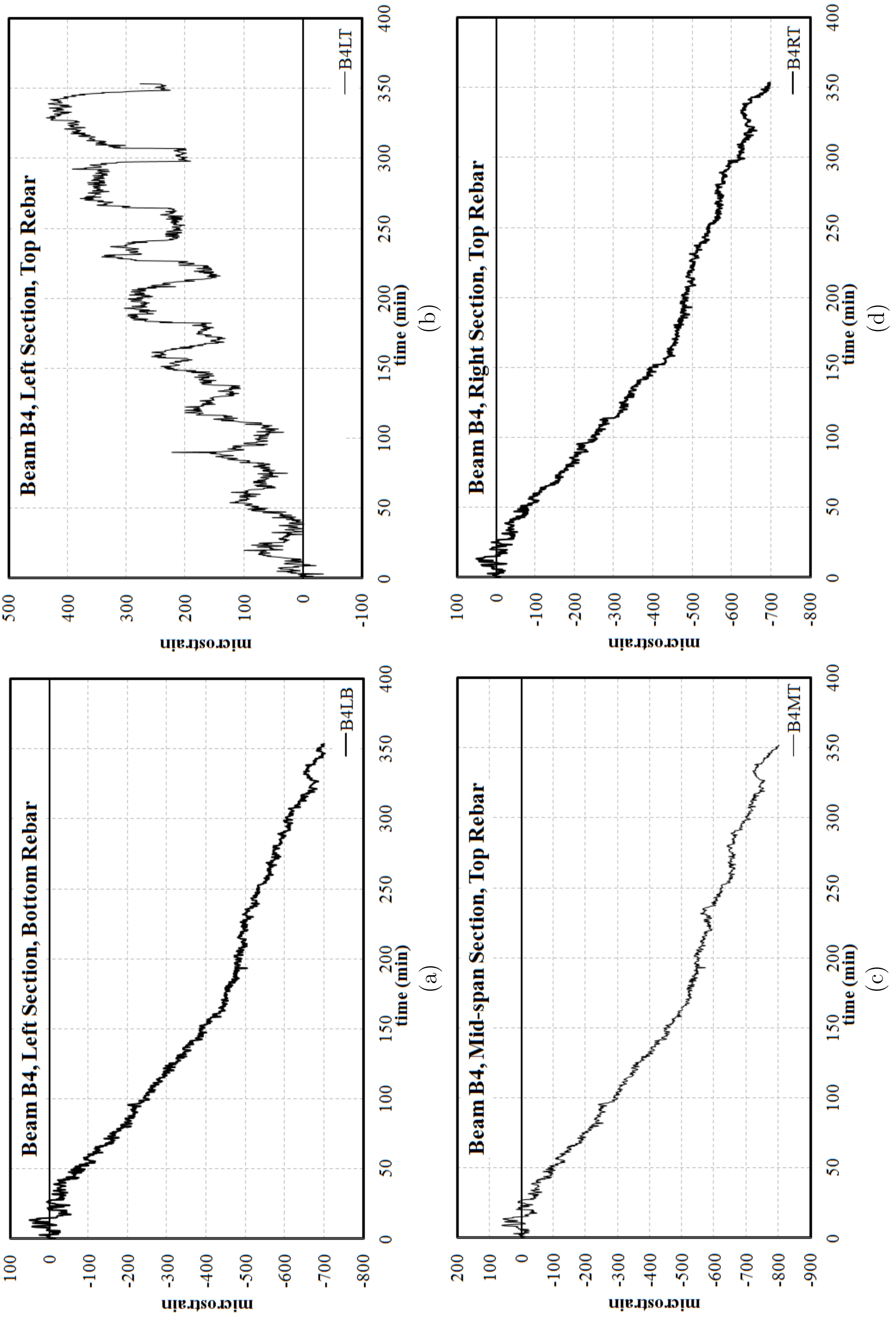

Fig. 4.16: Strain profile in beam B4 (a) Left section, bottom rebar (b) Left section, top rebar (c) Mid-span section, top rebar (d) Right section, top rebar

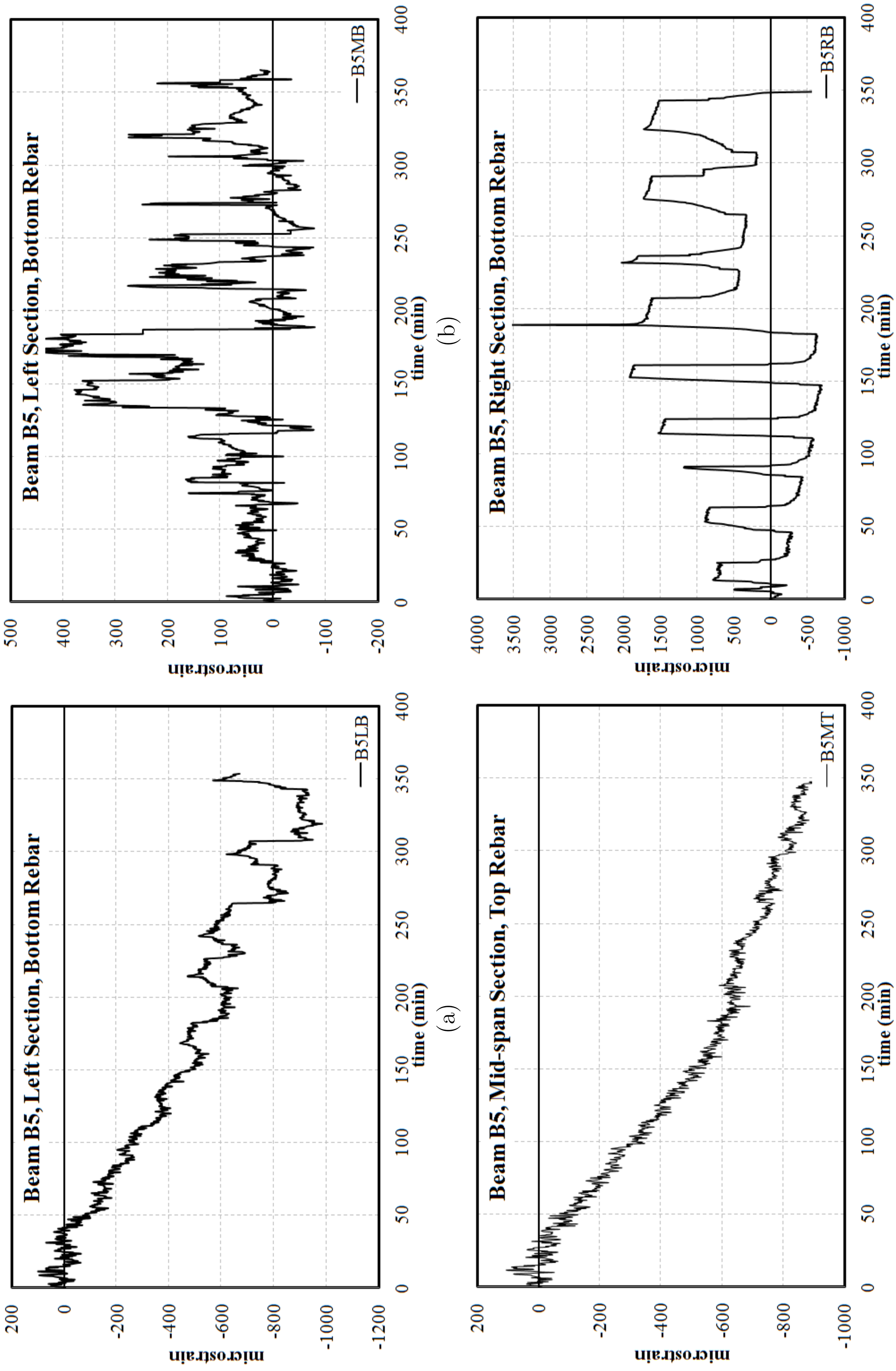

Fig. 4.17: Strain profile in beam B5 (a) Left section, bottom rebar (b) Mid-span section, bottom rebar (c) Mid-span section, top rebar (d) Right section, bottom rebar

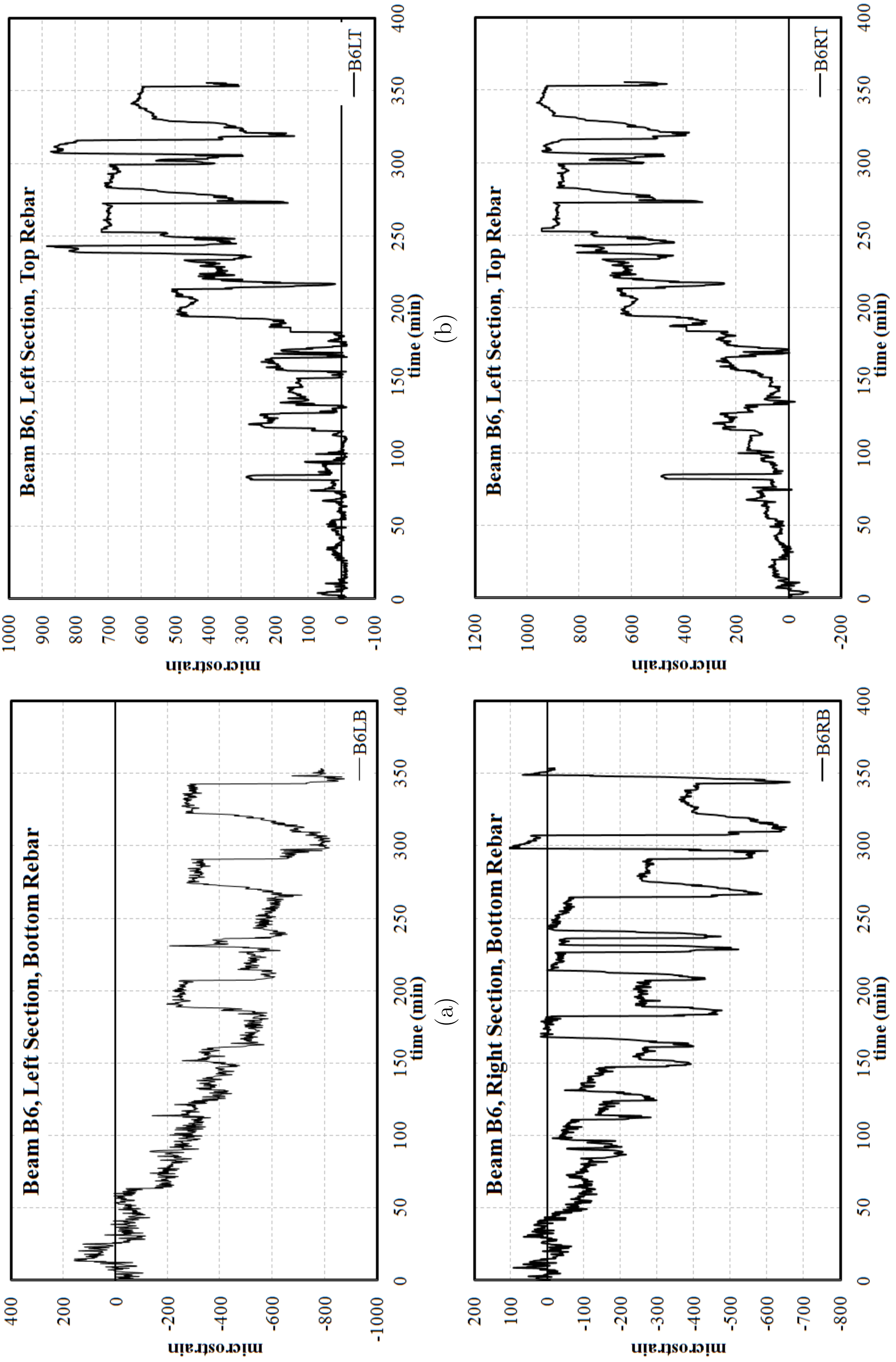

(a)

(b)

(c)

(d)

Fig. 4.18: Strain profile in beam B6 (a) Left section, bottom rebar (b) Left section, top rebar (c) Right section, bottom rebar (d) Right section, top rebar

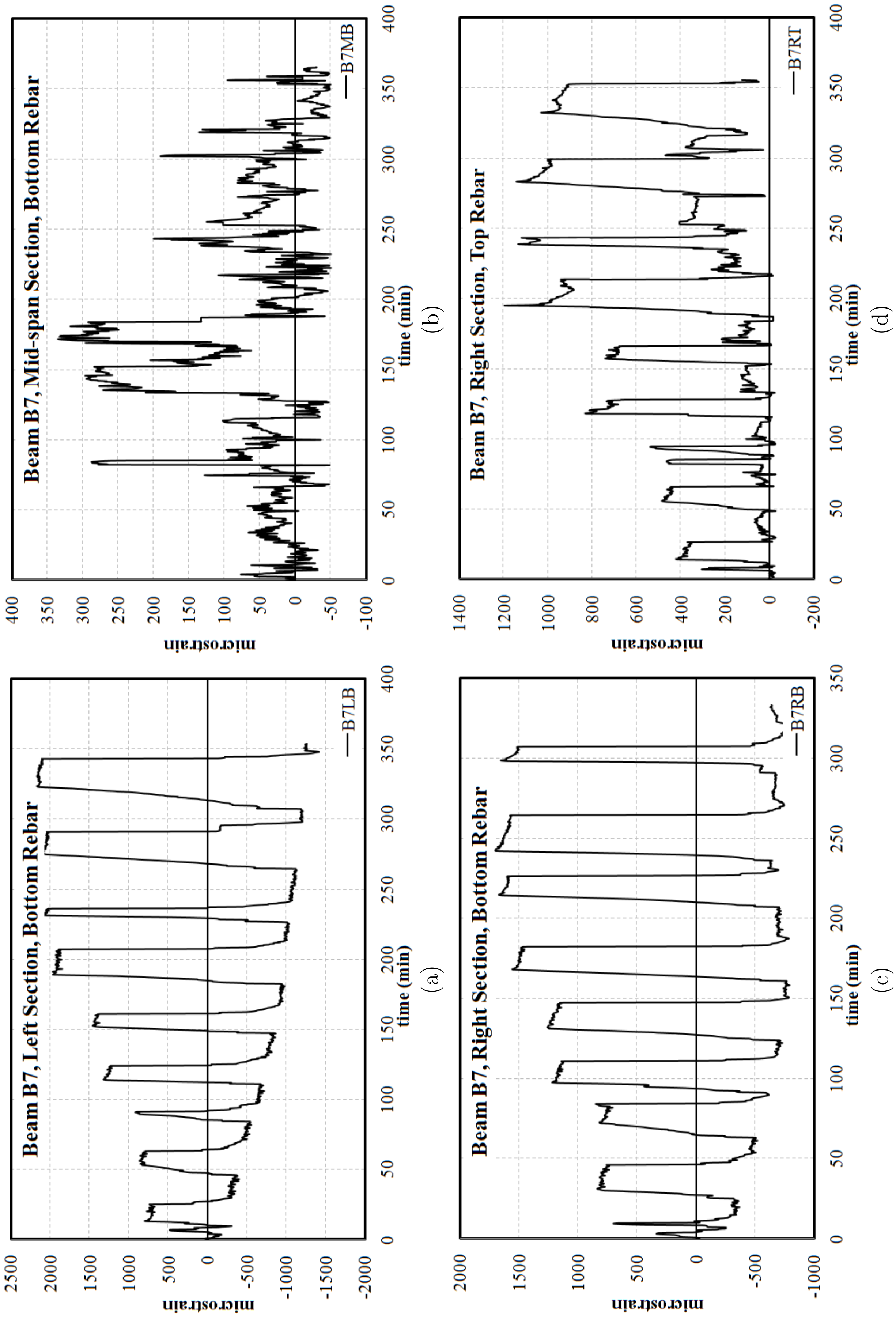

Fig. 4.19: Strain profile in beam B7 (a) Left section, bottom rebar (b) Mid-span section, bottom rebar (c) Right section, bottom rebar (d) Right section, top rebar

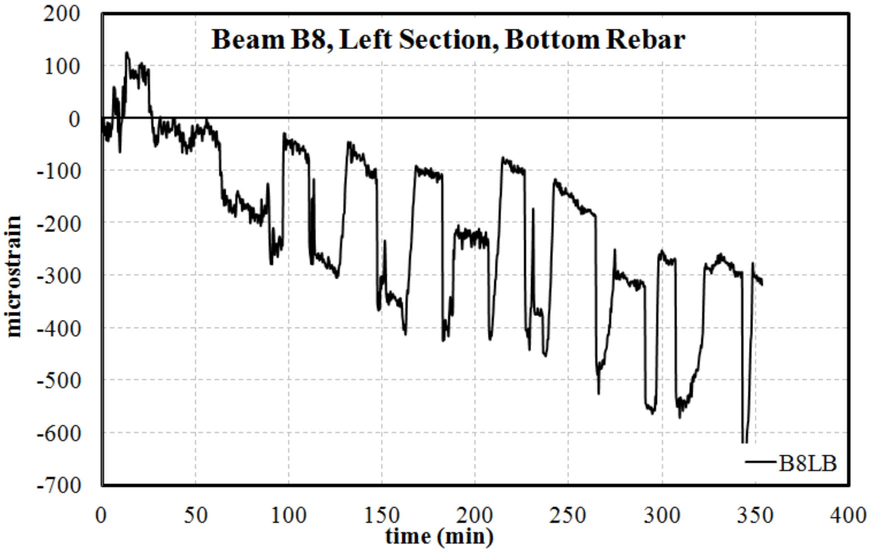

(a)

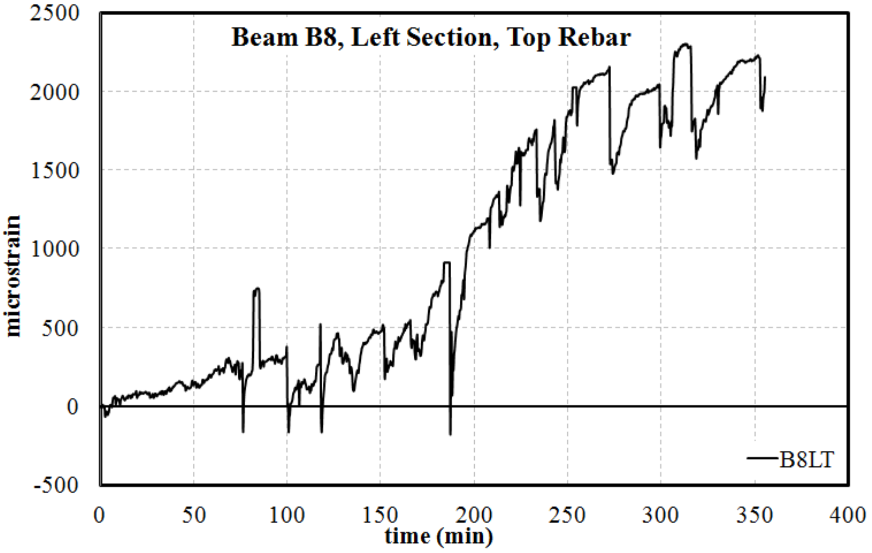

(b)

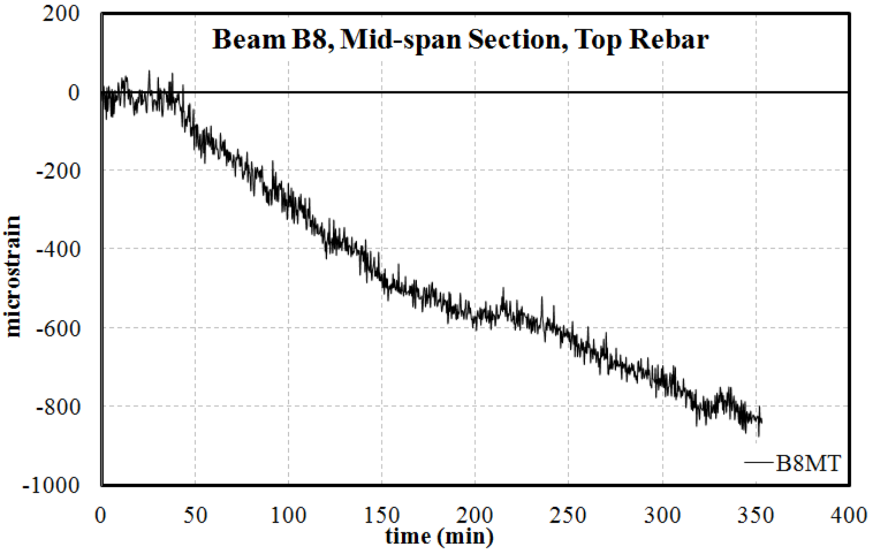

(c)

Fig. 4.20: Strain profile in beam B8 (a) Left section, bottom rebar (b) Left section, top rebar (c) Mid-span section, top rebar

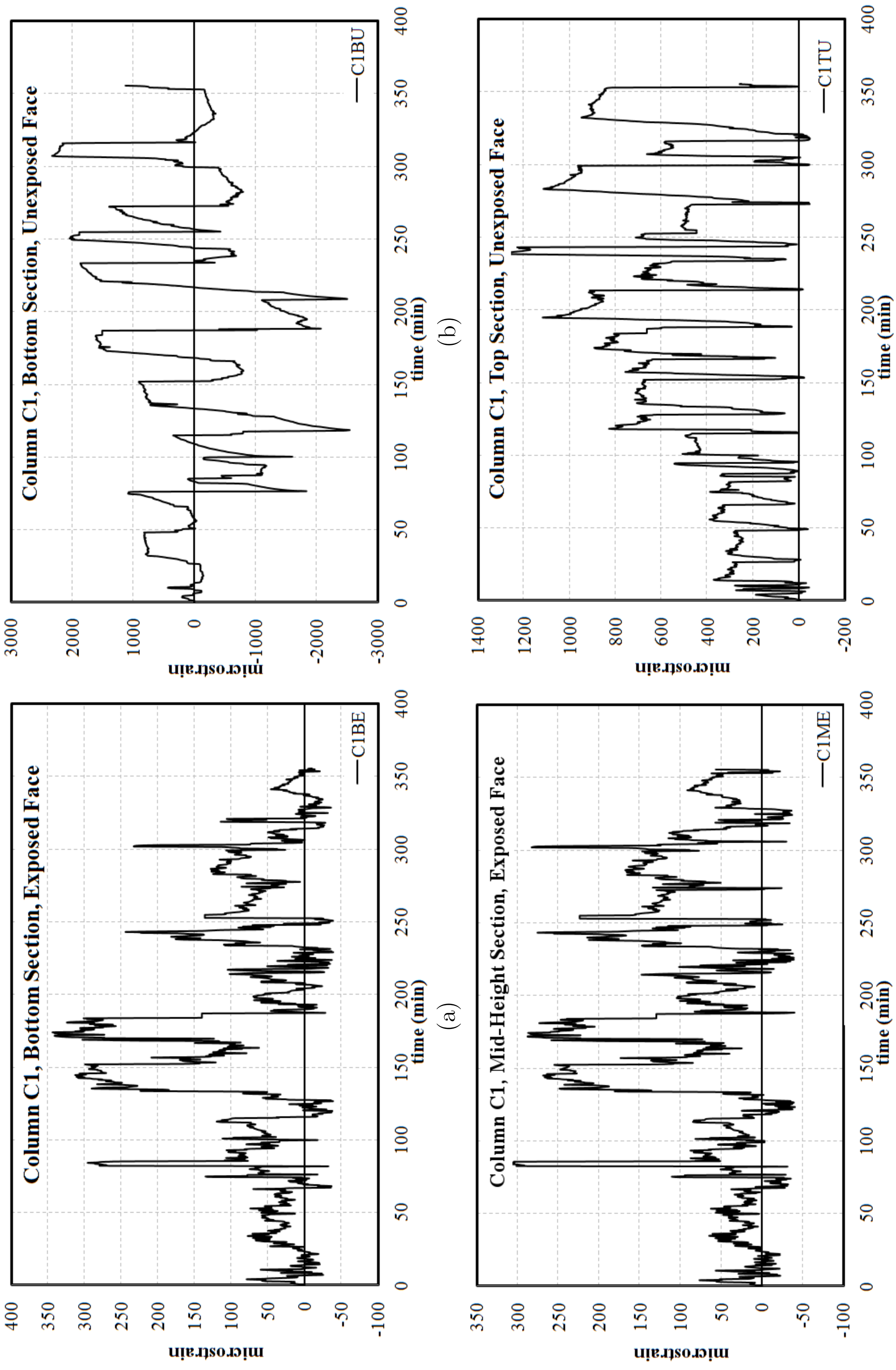

(a) (b) (c) (d)

Fig. 4.21: Strain profile in column C1 (a) Bottom section, exposed face (b) Bottom section, unexposed face (c) Mid-Height section, exposed face (d) Top section, unexposed face

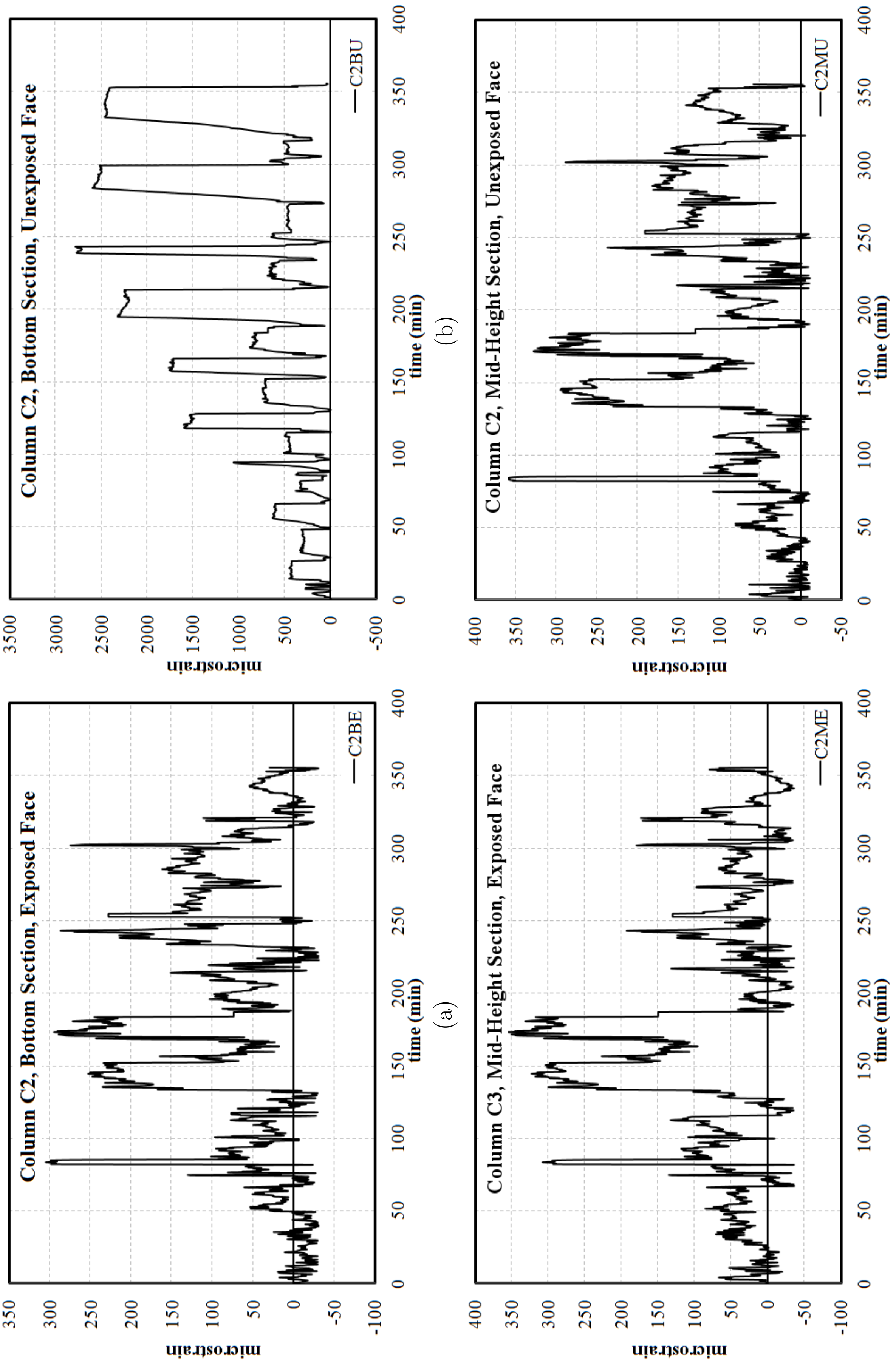

Fig. 4.22: Strain profile in Column C2 (a) Bottom section, exposed face (b) Bottom section, unexposed face (c) Mid-Height section, exposed face (d) Mid-Height section, unexposed face

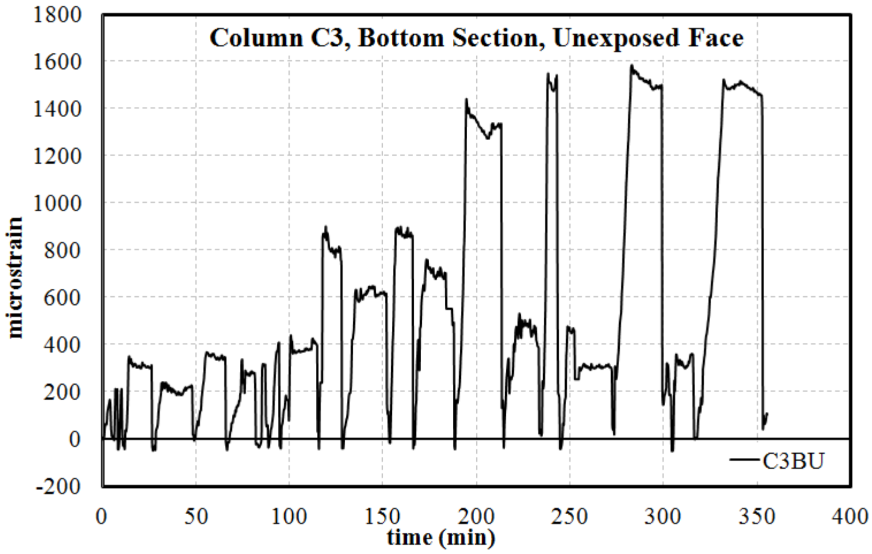

(a)

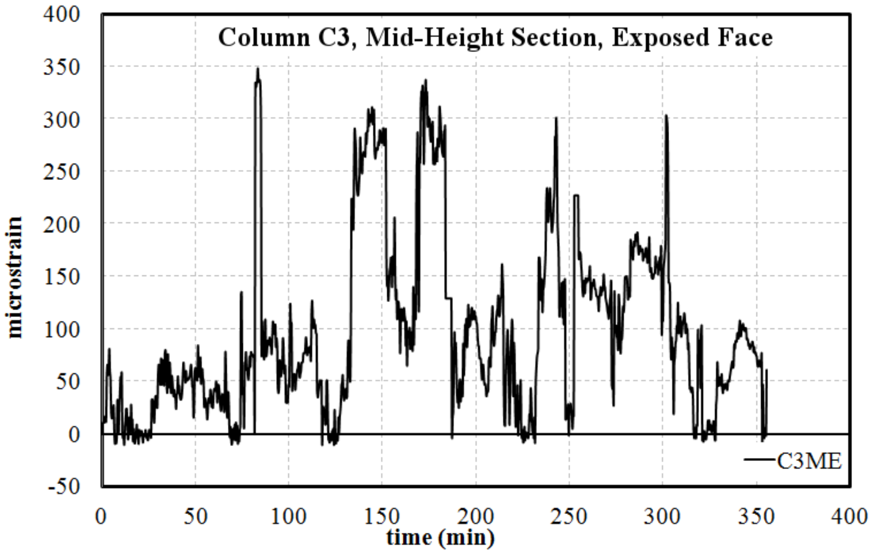

(b)

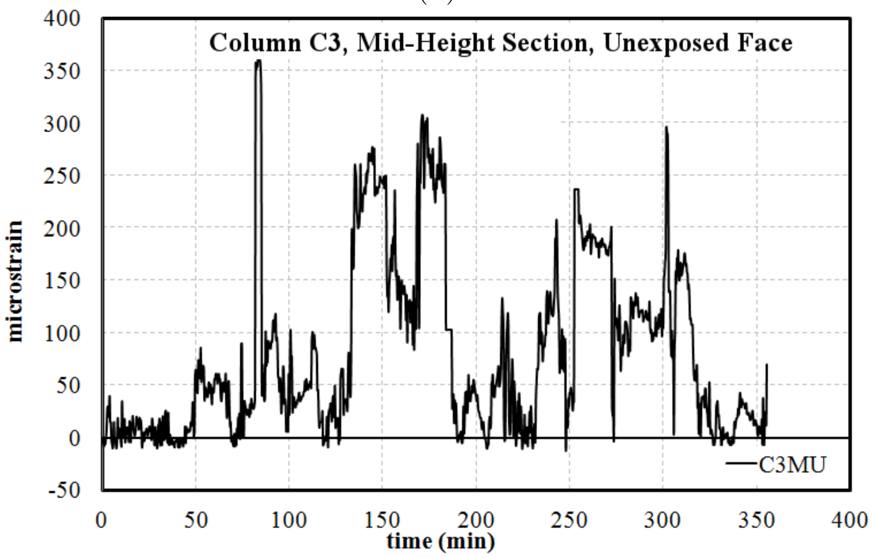

(c)

Fig. 4.23: Strain profile in Column C3 (a) Bottom section, unexposed face (b) Mid-Height section, exposed face (c) Mid-Height section, unexposed face

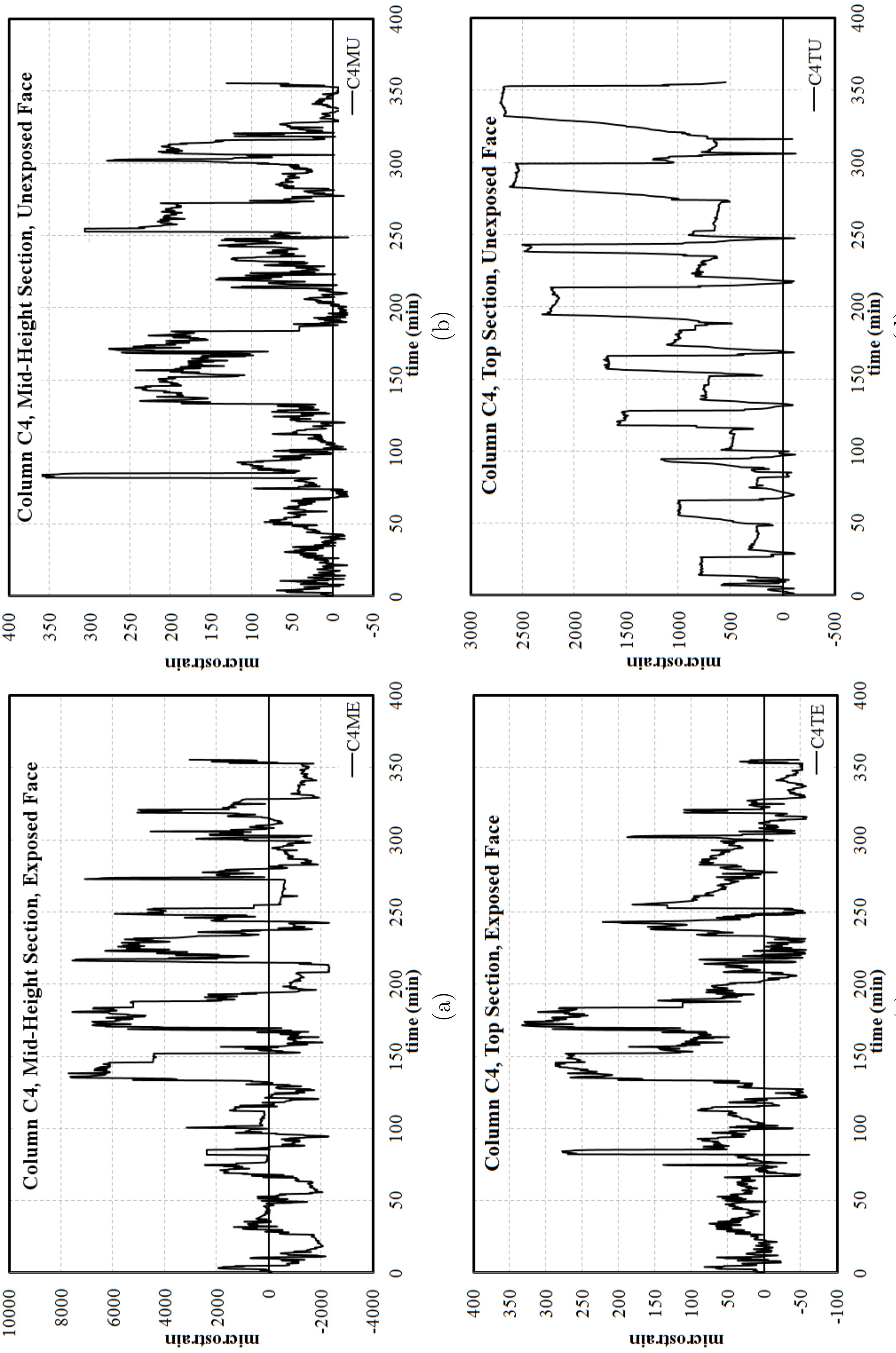

Fig. 4.24: Strain profile in Column C4 (a) Mid-Height section, exposed face (b) Mid-Height section, unexposed face (c) Top section, exposed face (d) Top section, unexposed face

4.5 FRAME TEST STAGE II: FIRE TEST

The earthquake damaged frame was enclosed in a 3 m × 3 m × 3 m compartment and exposed to a compartment fire of one hour duration.

4.5.1 Compartment Fire

Normally, design fire scenarios are reckoned in one of the following modes:

1. **Hand calculations:**
   This mode is simple, yet accurate for general fire design. In case of a simple design, the temperatures are assumed to be constant throughout the burning period. The maximum temperature and duration in this method is either assumed or calculated from the equation proposed by Kawagoe [45].

2. **Parametric / temperature-time curves specified in standards:**
   Parametric / temperature-time curves are the most common types of curves used by researchers across the world to evaluate the performance of building materials such as steel and concrete and assess their fire rating. The fire designed using these curves is termed as "parametric fire" or "standard fire". Some of the commonly used parametric curves are: British Standard BS 476 Part 20-23 [20–23], Eurocode 1 [33], Australian Standard AS 1530, Part 4 [73], American Standard ASTM E119 [9] and ISO 834 [41]. Frequently used codes/standards in fire testing are ASTM E119 and ISO 834. A comparison of these curves, along with the Eurocode 1 curve is shown in Figure 4.25. To begin with, the ISO 834 and ASTM E119 curves appear similar. However after 30 *minutes*, ISO 834 curve supersedes the ASTM E119 curve. At the end of 180 *minutes*, a temperature difference of 60 °C is noted between them. ASTM E119 presents several equations to define the temperature. Equation 4.3 shows a simple approach derived by Lie [55].

$$T = 750\left[1 - e^{-3.79553\sqrt{t_h}}\right] + 170.41\sqrt{t_h} + T_0 \tag{4.3}$$

   Where,
   $t_h \longrightarrow$ Time (hours)
   $T_0 \longrightarrow$ Ambient temperature °C
   The curve given in ISO 834 is derived using Equation 4.4.

$$T = 345log_{10}\left(8t + 1\right) + T_0 \tag{4.4}$$

   Where,
   $t \longrightarrow$ Time in minutes
   Eurocode gives an equation for hydrocarbon fires, which is designed to attain a very high temperature rapidly *(10 mins)*. In a hydrocarbon fire, temperature is calculated using Equation 4.5. Eurocode proposes this curve in view of an increased usage of constituents of petrochemical

origin. This fire is nevertheless considered too severe for load carrying members in a facade adjoining the load bearing structure. Hence, another equation (Equation 4.6) is proposed for external fire by Eurocode.

$$T = T_0 + 1100 \left[1 - 0.325e^{-0.1667t} - 0.204e^{-1.417t} - 0.471e^{-15.833t}\right] \tag{4.5}$$

$$T = T_0 + 660 \left(1 - 0.687e^{-0.32t} - 0.313e^{-3.8t}\right) \tag{4.6}$$

3. **Real fire data recorded by conducting mock fire tests:**
   The most accurate way of considering the real life fire scenario is by obtaining the temperature-time data from real fires. The data from real fire varies with three parameters: size of ventilation, fuel load and surface lining characteristics of the compartment material. Magnusson and Thelandersson [57] derived the curves from a heat balance calculation using Kawagoe's equation to estimate the burning rate of ventilation controlled fires. The curves are plotted for different ventilation factor with an increasing fuel load as shown in Figure 4.26. The hand calculated design fire exhibits a constant temperature throughout the burning period, whereas, the real fires exhibit a descending branch post flashover.

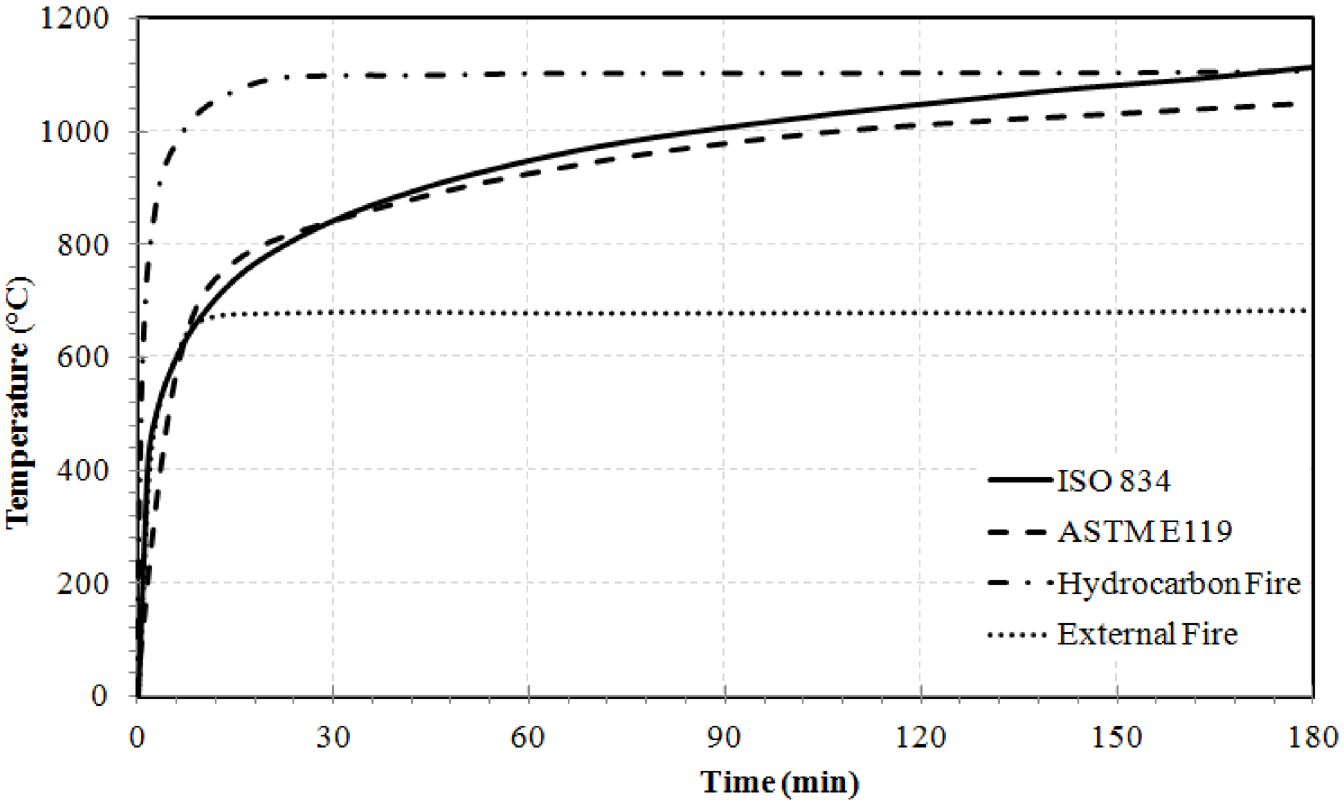

Fig. 4.25: Comparison of different parametric fire curves

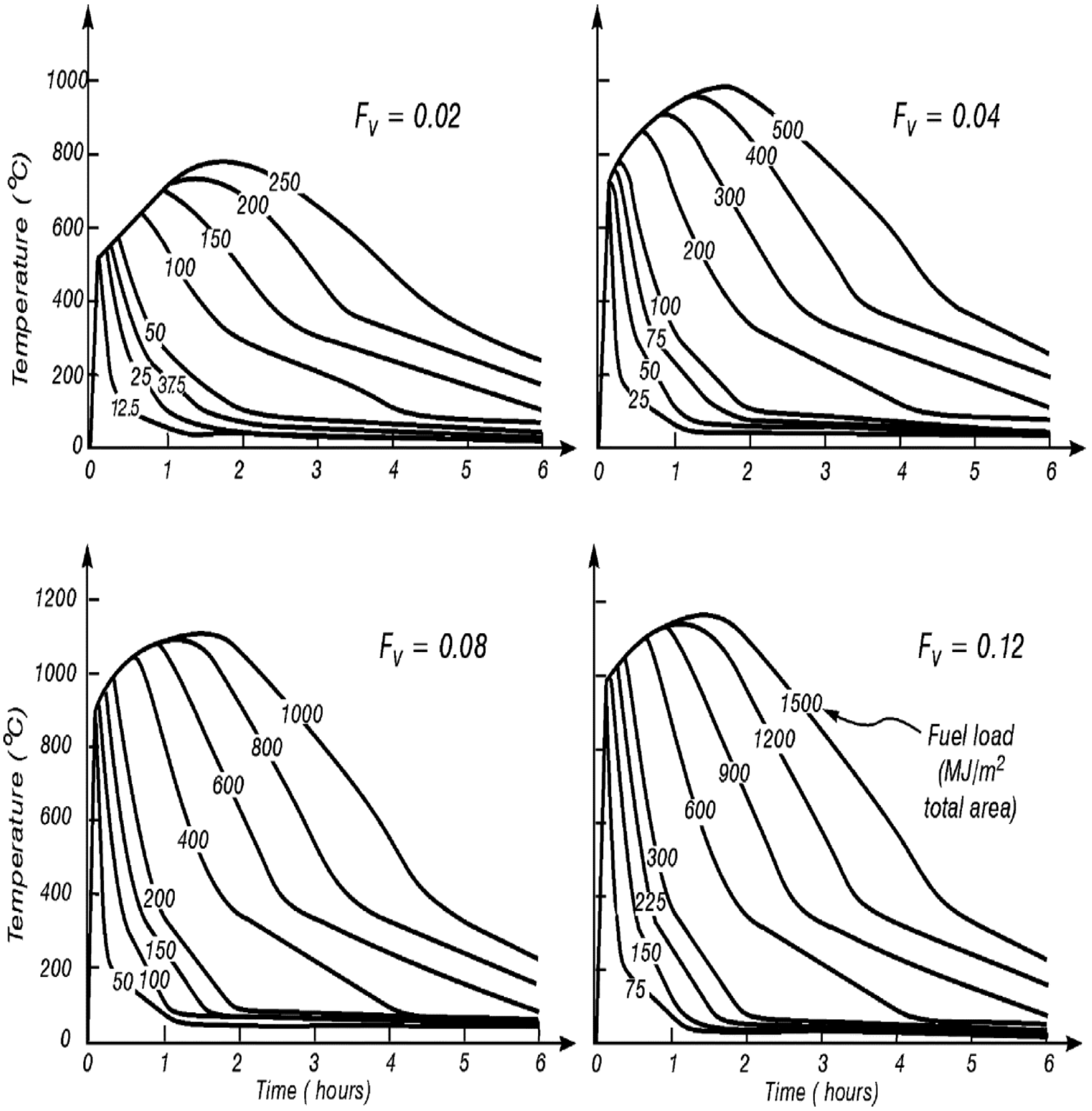

Fig. 4.26: Generic temperature-time *(Swedish Fire)* curves for different ventilation factors and fuel loads (from Table 10.2, Drysdale [29])

4.5.2 Fire Design

The objective was to maintain temperatures within the compartment at an average of 900 °C < T_c < 1000 °C for a period of one hour and to attain a steady state as fast as possible. Kerosene pool fire was adopted with the above mentioned pool size, which estimates the flashover to take place in less than 5 minutes. The desired temperature-time curve is given in Figure 4.27.

In order to achieve the desired temperatures, the ventilation requires to be altered according to Thomas and Heselden [82]. From Figure 4.28, it is inferred that the condition to maintain a required temperature is given by Equation 4.7.

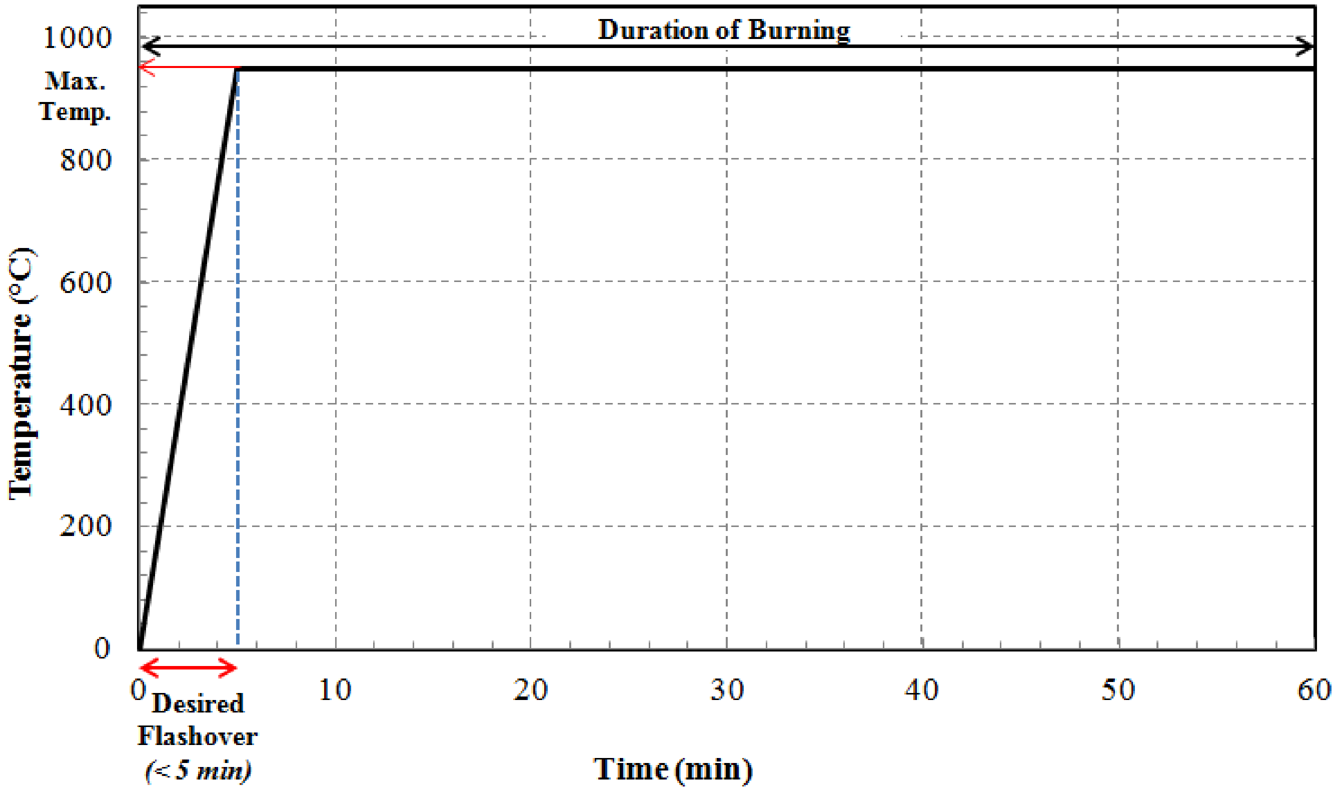

Fig. 4.27: Desired constant temperature fire curve

$$10 < \frac{A}{A_0 H_0^{\frac{1}{2}}} < 15 \tag{4.7}$$

Where,

$A \longrightarrow$ Total Internal Area of the Compartment

$A_0 \longrightarrow$ Area of the Opening

$H_0 \longrightarrow$ Height of the Opening

To enhance the flashover, it is imperative to allow rapid accumulation of smoke. It is therefore considered to make the opening as low as possible. This arrangement facilitates the accumulation of smoke heating up the structure and eventually leading to a rapid flashover. Hence the shape of the compartment was chosen as shown in Figure 4.29.

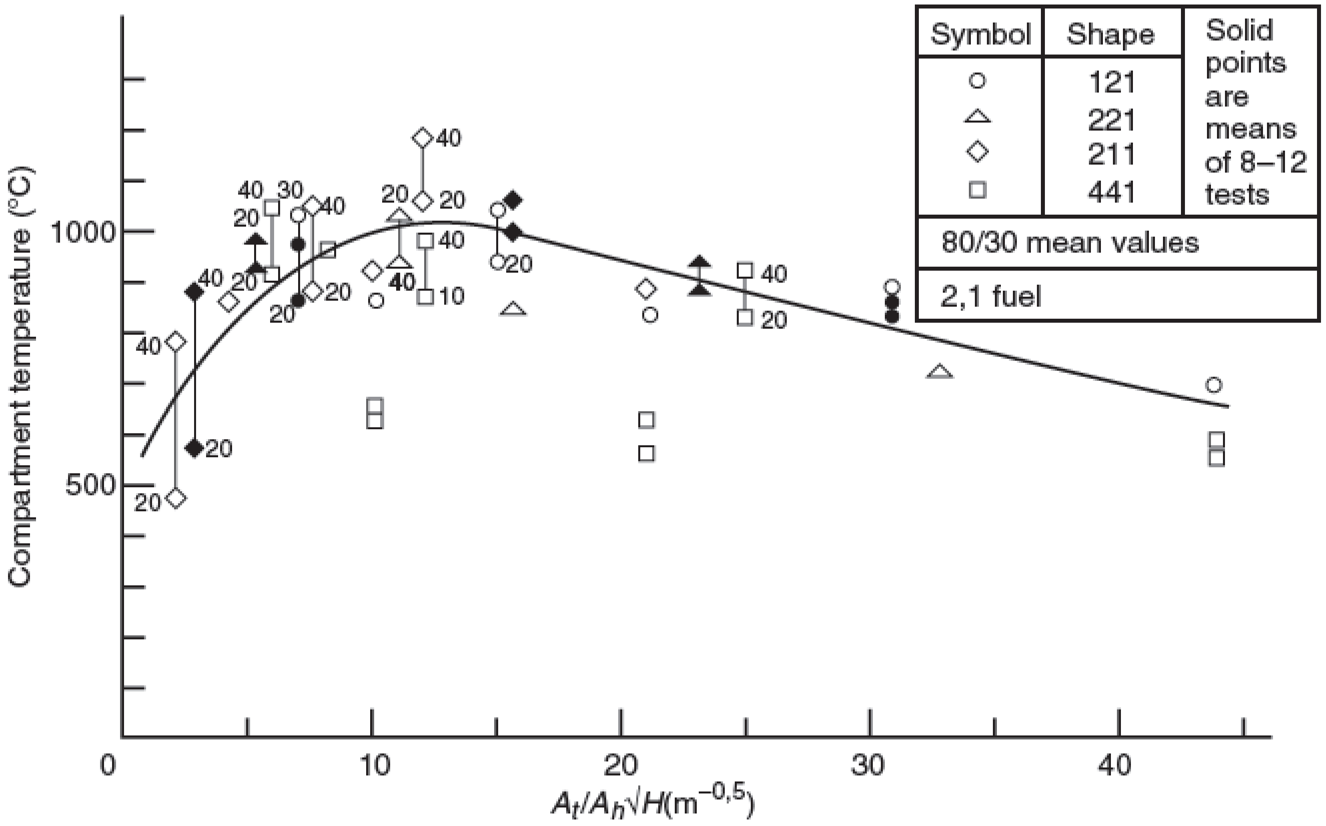

Fig. 4.28: Compartment temperature - compartment shape relationships (from Purkiss [69], pp. 59)

This leads to the height of the opening,
$0.96\ m < H_0 < 1.27\ m$.
Therefore, an adequate choice of opening chosen was $H_0 = 1\ m$.
The rate of burning of kerosene for pre-flashover is: $\dot{m}_f^{"} = 0.039\ kg/m^2s$
From Figure 4.30, at peak temperatures of $100\tilde{0}$ °C, the ratio of pre-flashover and post-flashover burning rates is $\tilde{3}$. Therefore, a post-flashover burning rate is chosen to be:
$\dot{m}_f^{"} = 0.117\ kg/m^2s$

4.5.3 *Mock Fire Tests*

Prior to the fire test on the RC frame, the fire designed in the previous section was verified by conducting several mock fire tests. The size of the compartment proposed in the Figure 4.29 was constructed using brick masonry. Figure 4.31 (a) shows the brick masonry frame constructed for performing mock fire tests. The compartment had a clear inner dimensions of $3\ m \times 3\ m \times 3\ m\ \times$ with a $1\ m \times 3\ m$ opening. A mild steel sheet tray burner of size $1\ m \times 1 \times 0.05\ m$, which formed the pool for kerosene, was positioned at the centre of the floor area. Kerosene oil was supplied to the pool via conduits running from a tank maintained with a fixed head. The brick masonry walls remained unplastered. Three trees of mineral insulated thermocouples were installed inside the compartment at five different heights. The temperature was monitored with a triggering rate of 1 minute. During the

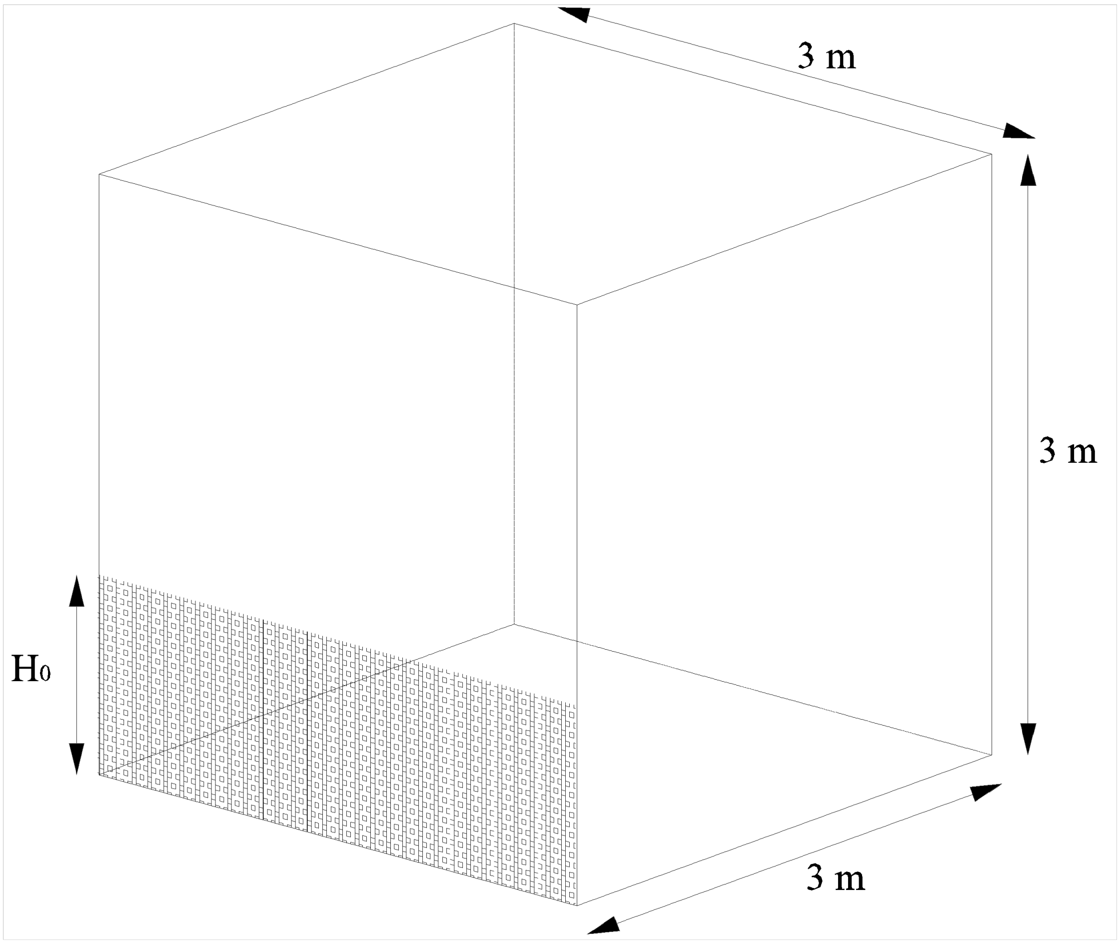

Fig. 4.29: Proposed shape of the compartment

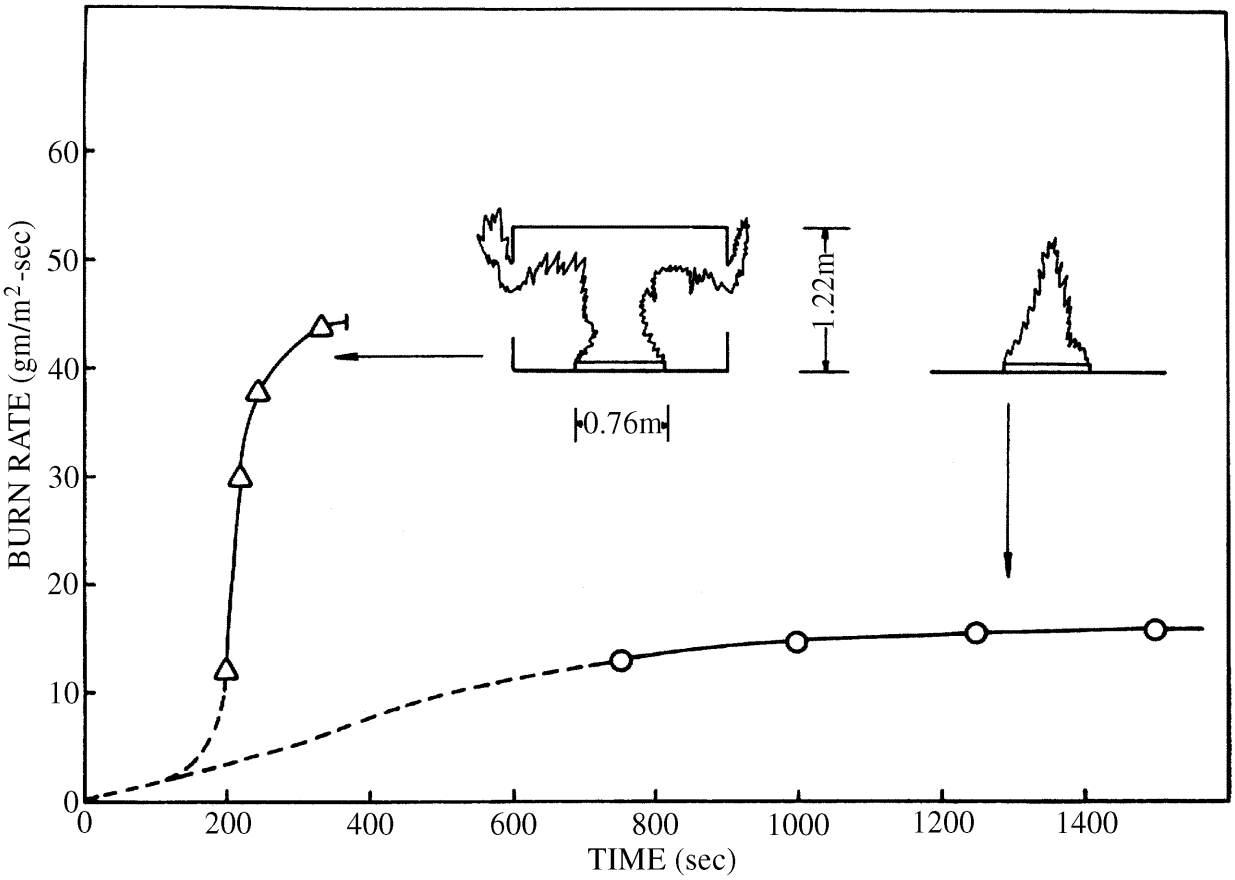

Fig. 4.30: Rate of burning vs. time from laboratory scale experiment by Friedman 1975(from Figure 9.2, Drysdale [29], pp 353)

first mock fire test, a conduit diameter of 1.27 cm was used for supplying fuel to the burner. However, the target temperature of 1000 °C was not achieved in less than 5 minutes as expected. This can be attributed to the dampness of brick walls following an overnight precipitation. The damp walls were suspected of absorbing the radiant heat from the fire. In the second mock fire test, the size of the conduit supplying the fuel was increased to 2.54 cm and the brick masonry walls were plastered with a cement mortar having a cement-sand ratio of 1 : 3. A peak burning rate of $0.117kg/m^2s$ and a peak fuel flow rate of $1.43 \times 10^{-4}m/s$ was maintained. The target temperature of 1000 °C was achieved within 5 minutes as indicated from temperature-time curve for the compartment shown in Figure 4.31 (b).

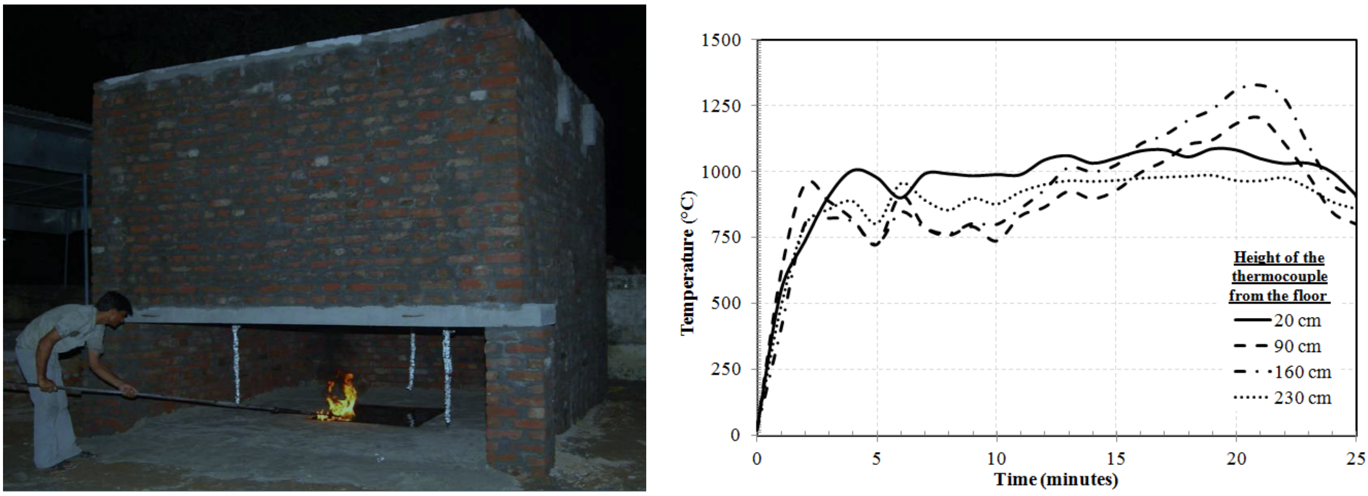

(a) (b)

Fig. 4.31: Mock fire test (a) Brick masonry compartment (b) Temperature-time curve for the compartment

4.5.4 Compartment Fire for the RC Frame

After inducing the desired pre-damage corresponding to 4% drift, the test frame was exposed to a one-hour fire test. Reinforced concrete frame was enclosed in a fire compartment fabricated on site. The compartment was fabricated using four detachable mild steel fire-proof panels. These panels were provided with a lining of fire-proof glass wool followed by 0.45m thick layer of glass wool brick modules. The compartment was provided with a 1m wide opening at bottom on one of the faces to simulate the ventilation. A pool of size $1\ m \times 1\ m \times 0.05\ m$ was fabricated using special alloy of stainless steel (SS 304) to withstand high temperatures unlike the normal grade stainless steel to ensure reusability. The fire scenario remained as that of second mock fire test and first RC frame test, where the desired flashover was achieved. However, in the actual test, The flashover was achieved in 8-10 minutes after fire ignition, as seen in Figure 4.32. A maximum temperature of 1370 °C was recorded inside the compartment at a height of 0.9m from the floor of the compartment. Figures 4.33 (a), (b) and (c) depict the time-temperature plot for thermocouple trees positioned at locations A, B and C inside the compartment. [See Figure 4.8 (e)]. The temperature history shows a 16 hour log with a complete heating and cooling cycle. Three locations in plan and five locations along the height of the compartment captured the detailed temperature variations throughout the compartment. Care was taken to seal the compartment thoroughly to prevent any escape of fire / heat from the compartment. Figure 4.34 show a 90 minute record of time-temperature for the same location, showing the variation of temperature during one-hour fire. Figure 4.35 and Figure 4.36 show the vertical and lateral displacements measured on the slab during and after the compartment fire respectively. From the displacement history, it can be distinctly noted that the frame retrieved its straightness during the fire. It is also evident that there was skewness in the slab laterally and vertically. This phenomenon is attributed to the fact that the columns on which the slab was supported suffered a differential damage due to spalling. Registered displacements during and after one hour fire have been pictorially represented in Figures 4.37 (a) and (b) respectively. After one hour fire, a maximum vertical displacement of 19 *mm* was recorded on the edge of the slab, mid-way between column 1 and column 2. A lateral drift of 7 *mm* was recorded away from the reaction wall at the slab location near beam B7, whereas, the drift remained 1 *mm* towards the wall near beam B5, clearly indicating a skewness in the slab. After the fuel supply was cut off, the temperatures continued building up inside the structural members and the displacements continued to vary. Maximum lateral drifts of 14 *mm* away from the reaction wall and 7 *mm* towards the reaction wall were recorded at the tip of the slab near beams B7 and B5 respectively.

Fig. 4.32: Flashover

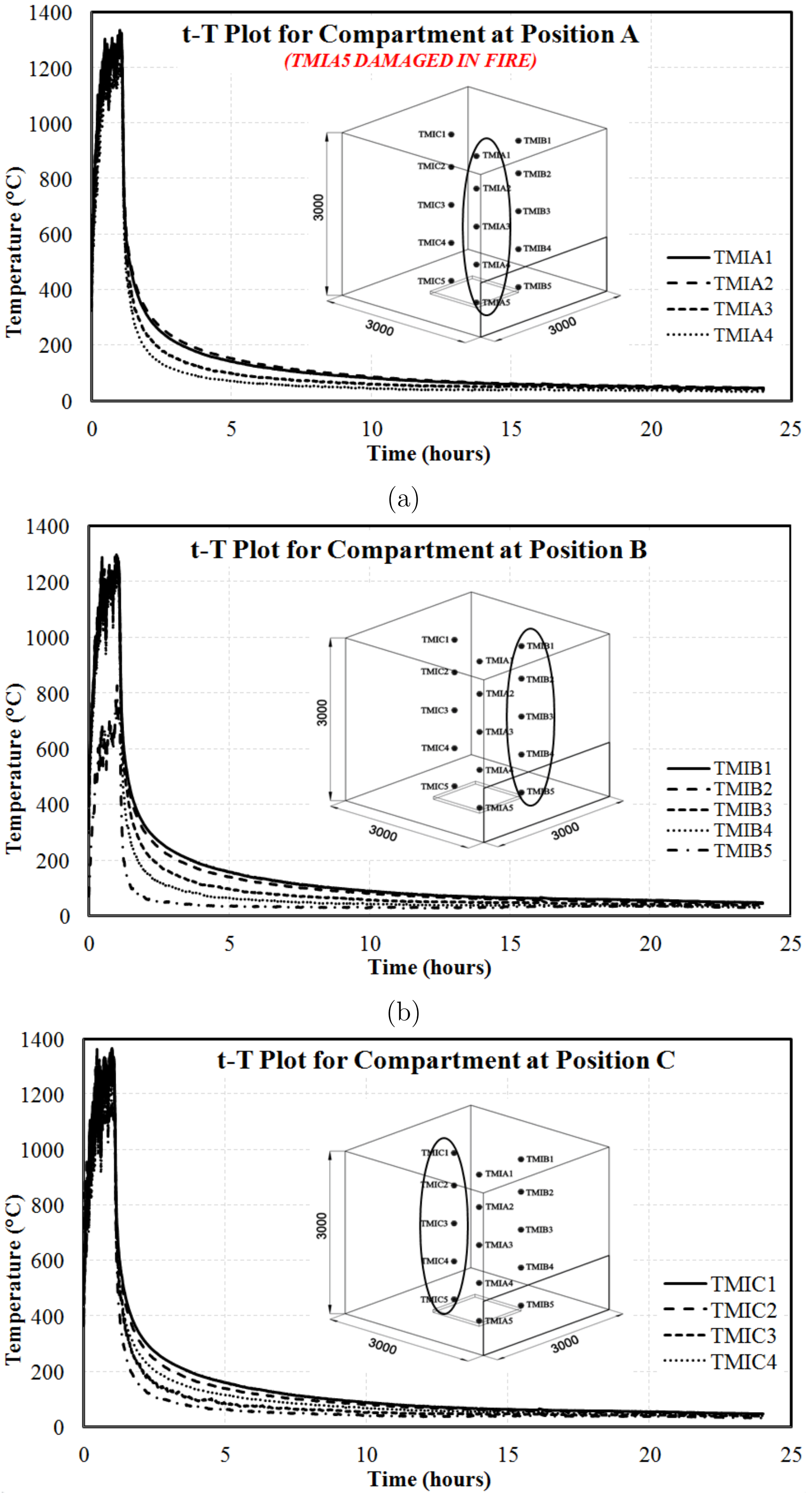

(a)

(b)

(c)

Fig. 4.33: Compartment temperature-time history at (a)Location A (b)Location B (c)Location C *(ref. Fig. 8(e))*

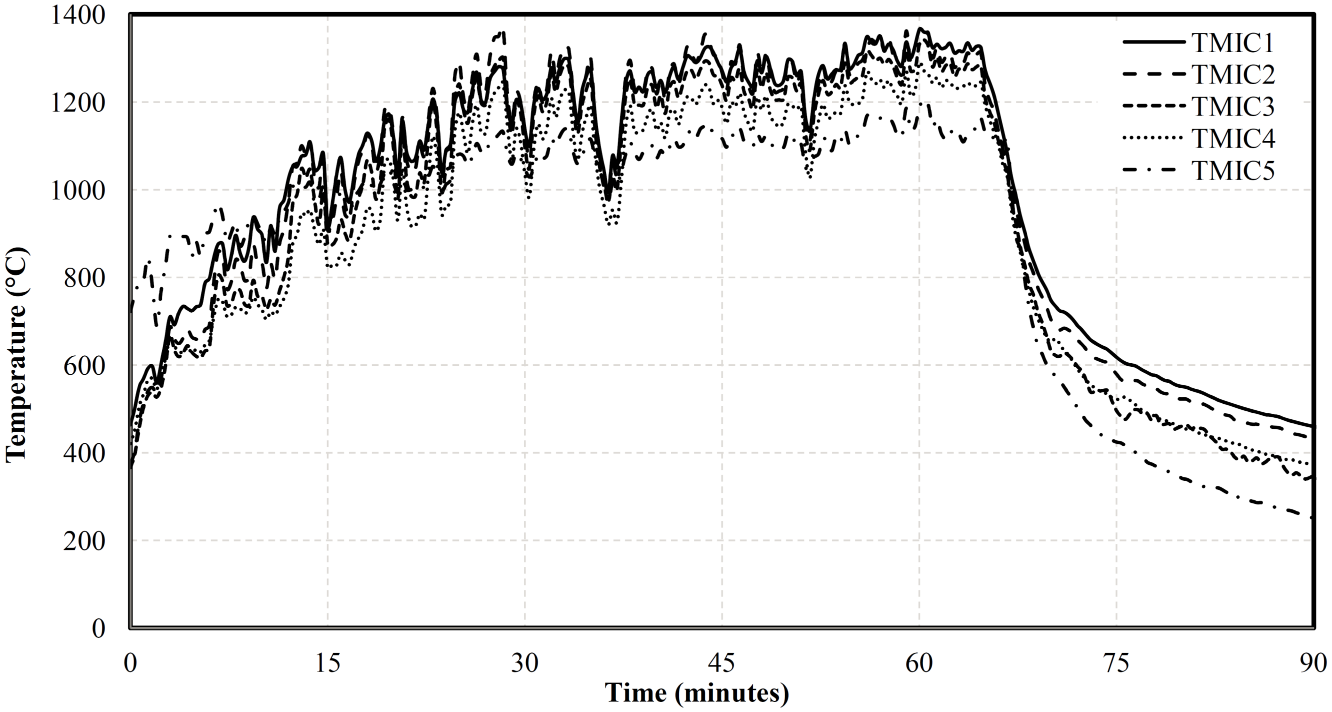

Fig. 4.34: Compartment temperature history for 90 minutes at location C

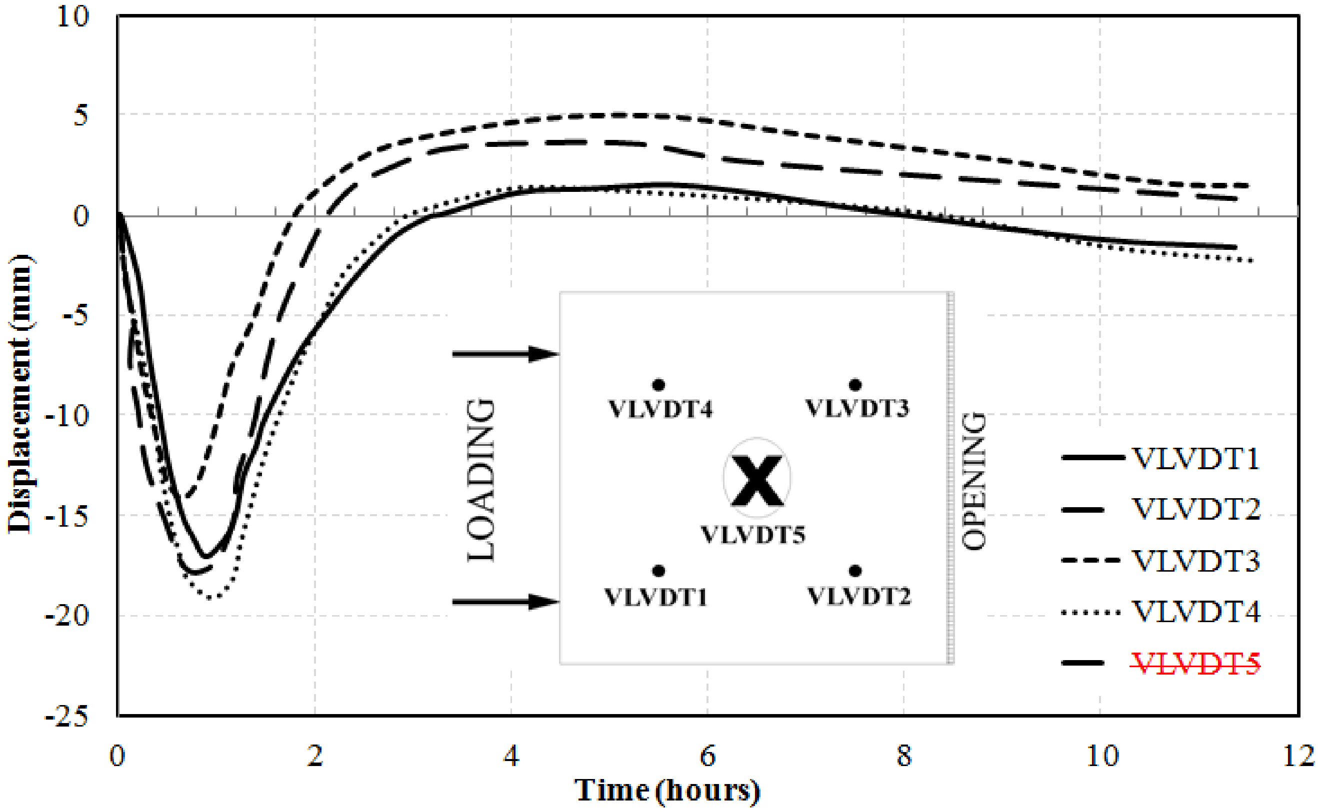

Fig. 4.35: Slab vertical deflections during and after the fire

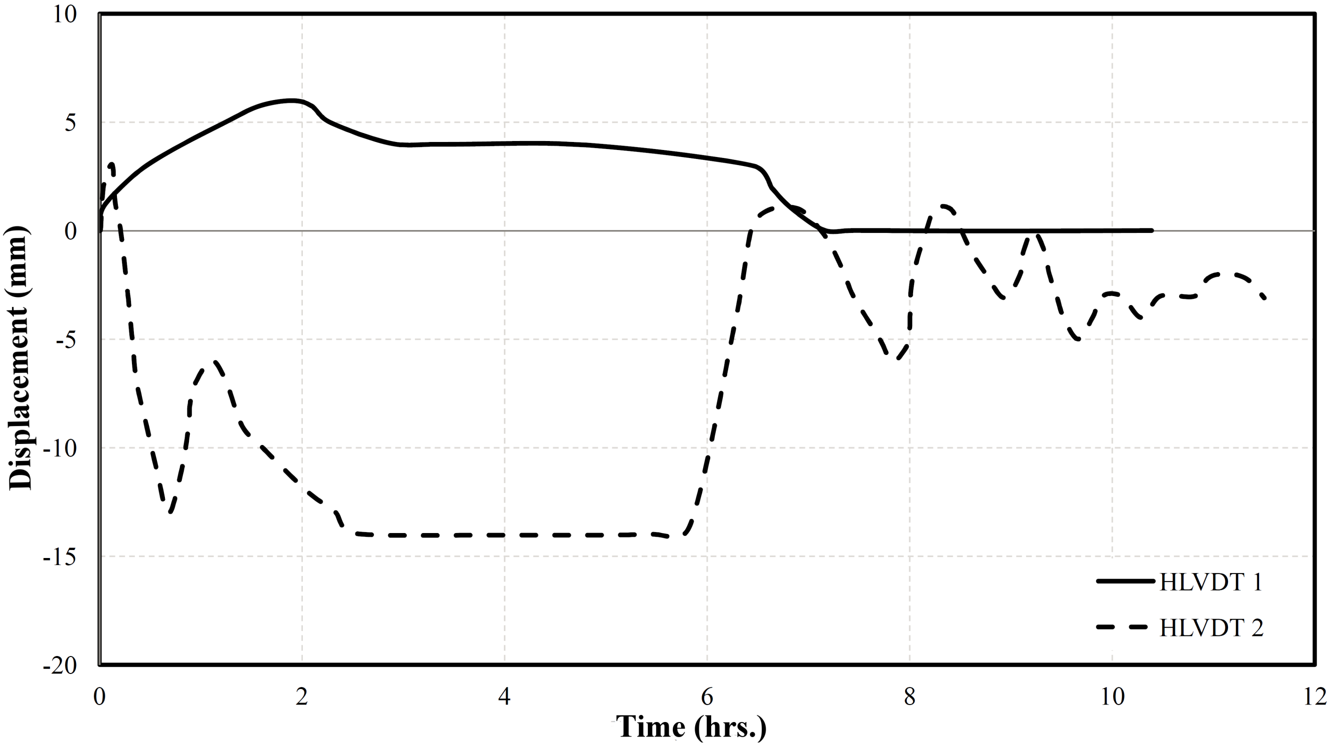

Fig. 4.36: Lateral deflections at roof level during and after the fire

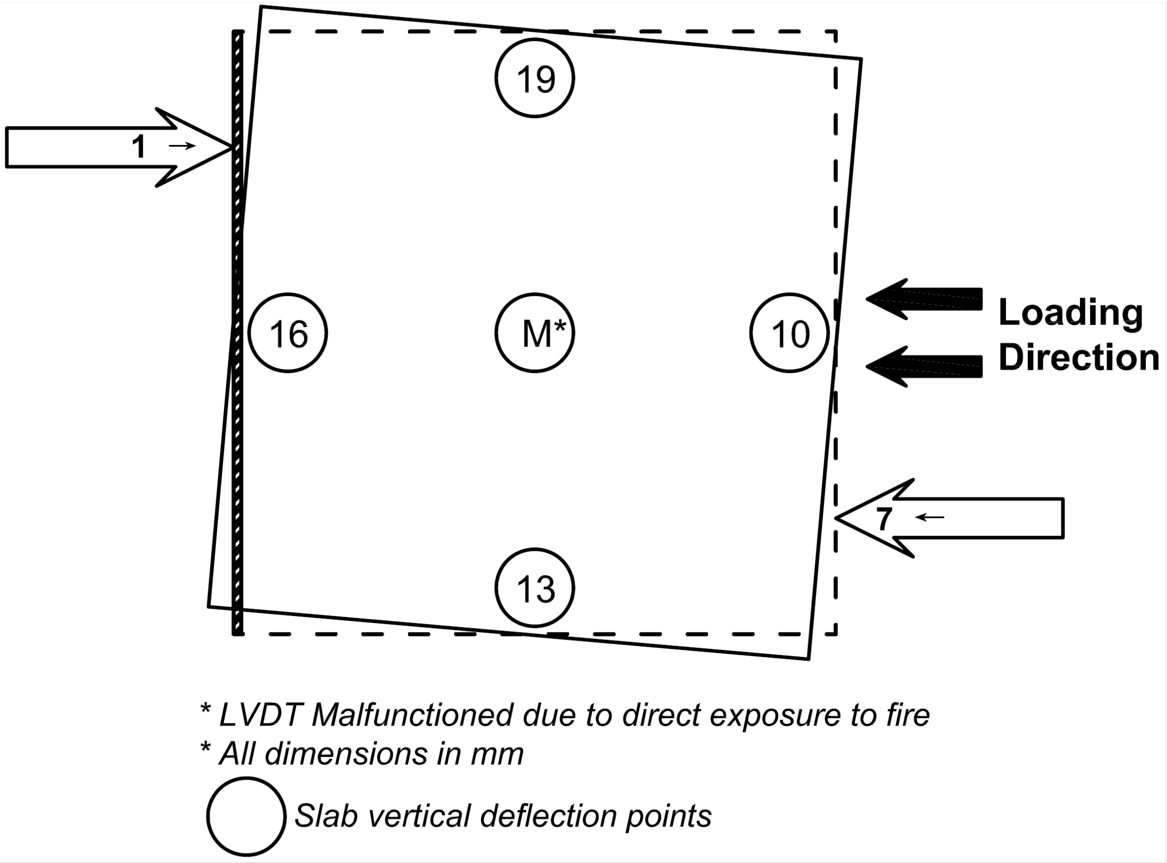

(a)

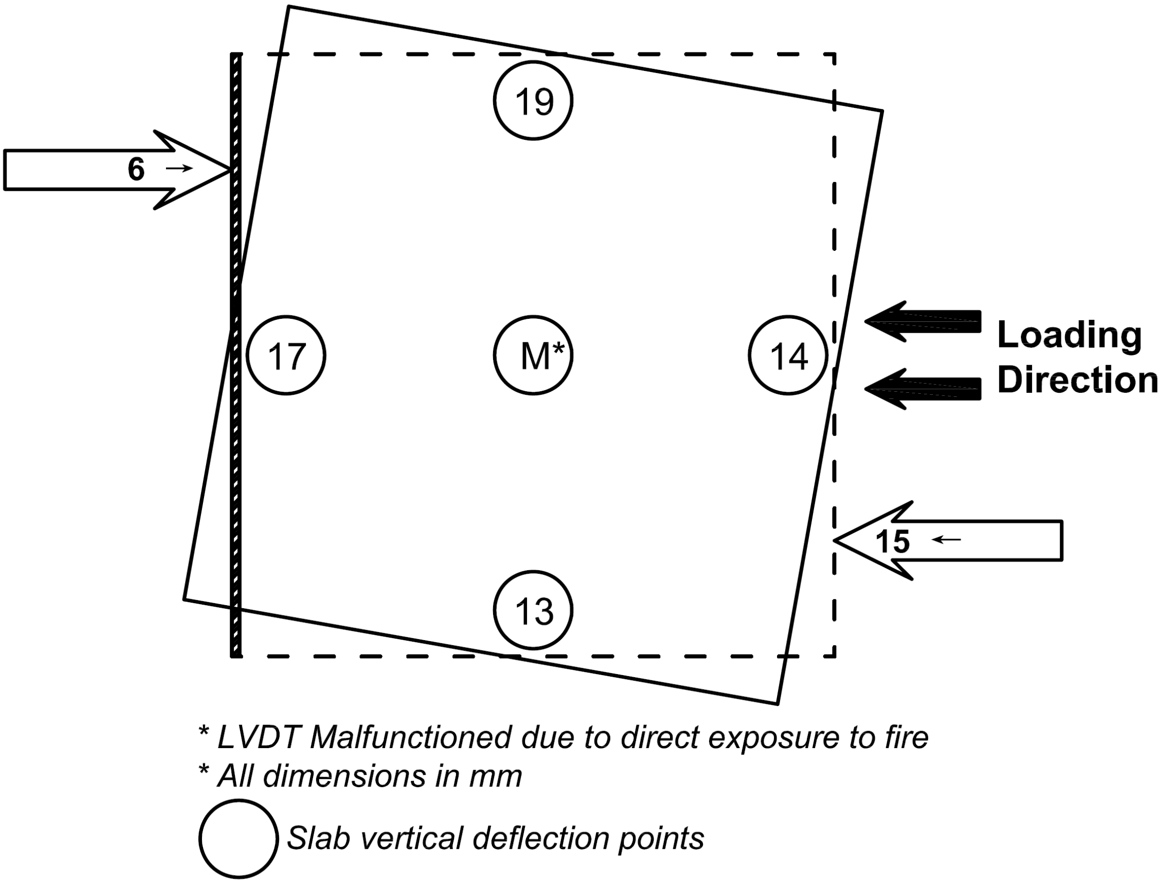

(b)

Fig. 4.37: Slab vertical and lateral deflections (a) After 1 hour fire (b) Max. Obtained

Figures 4.38 (a-d), 4.39 (a-c) and Figure 4.40 (a-c) show the 12 hour temperature-time histories of different members of the frame sub-assemblage. Figure 4.38 (a-d) depicts the time-temperature plots for the floor beams B1, B2, B3 and B4 respectively. All floor beams had top surface exposed to fire and other faces were well insulated. A maximum temperature of 307 °C was registered in floor beams at 73 minutes after fire ignition. The maximum temperatures of 614 °C and 553 °C were recorded at 70 minutes and 69 minutes at 25 *mm* width from exposed concrete surface and 25 *mm* depth from exposed concrete face respectively [Figure 4.8 (b)].

Figure 4.49 shows the variation of temperature along the width of the column C1 near the roof beamcolumn joint. A linear temperature variation was observed at 10 minutes after fire ignition, which gradually changed to exponential variation in the subsequent cycles. The fuel supply was cut off after 60 minutes; thereafter the temperature at surface receded and started building inside the member establishing a reverse trend.

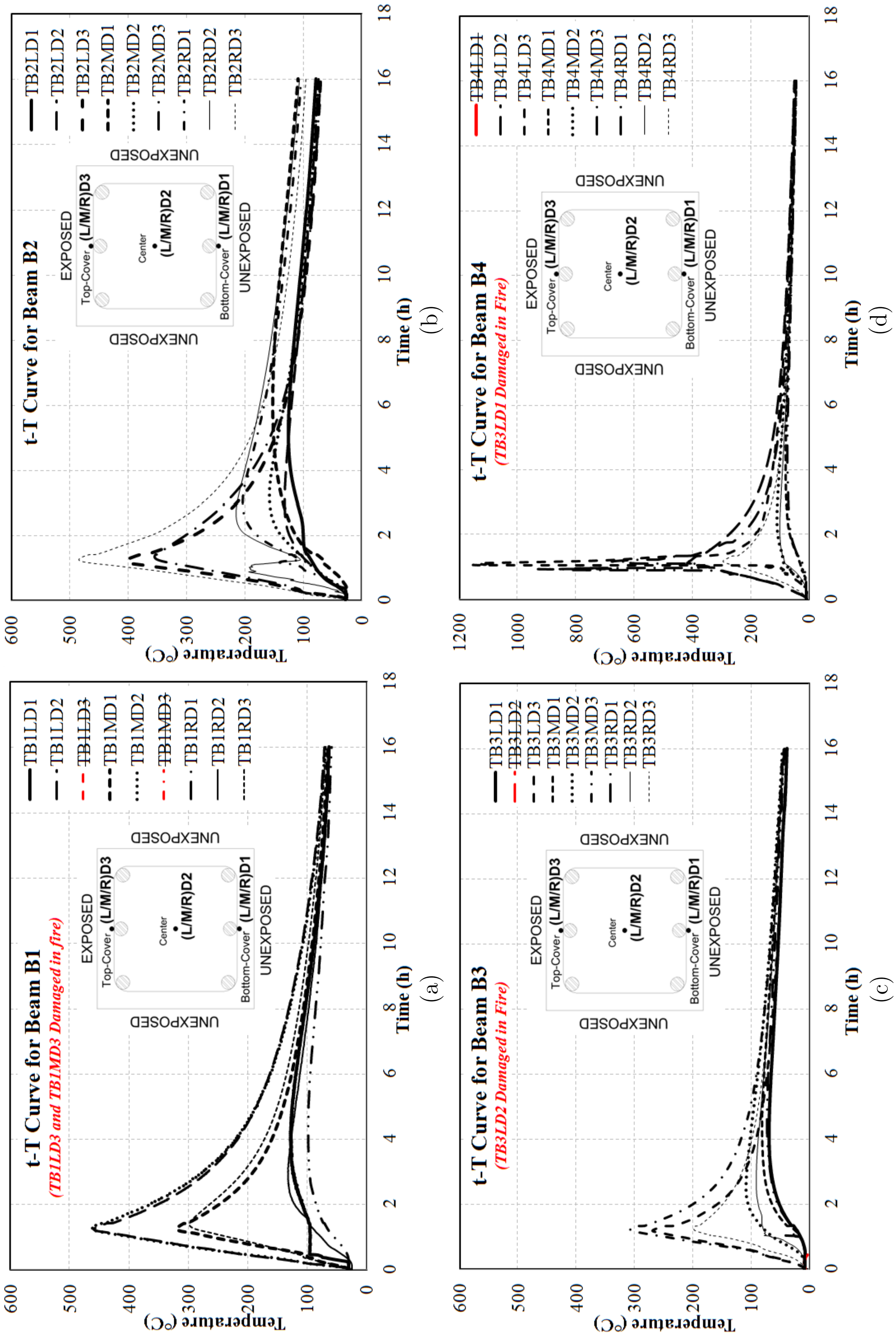

Fig. 4.38: Temperature profile for floor beams (a) Beam B1 (b) Beam B2 (c) Beam B3 (d) Beam B4

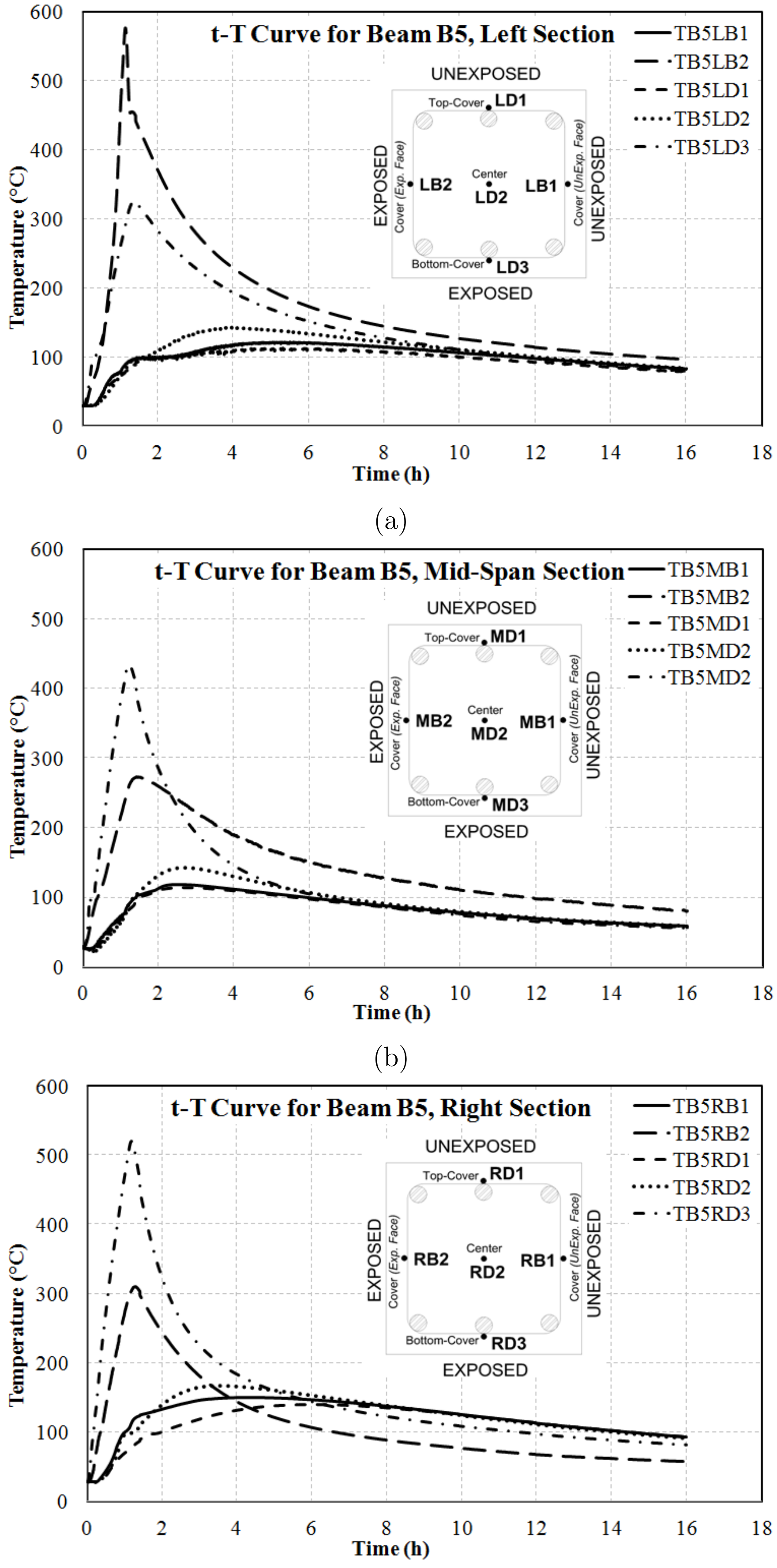

Fig. 4.39: Temperature profile for roof beam B5 at (a) Left section (b) Mid-span section (c) Right section

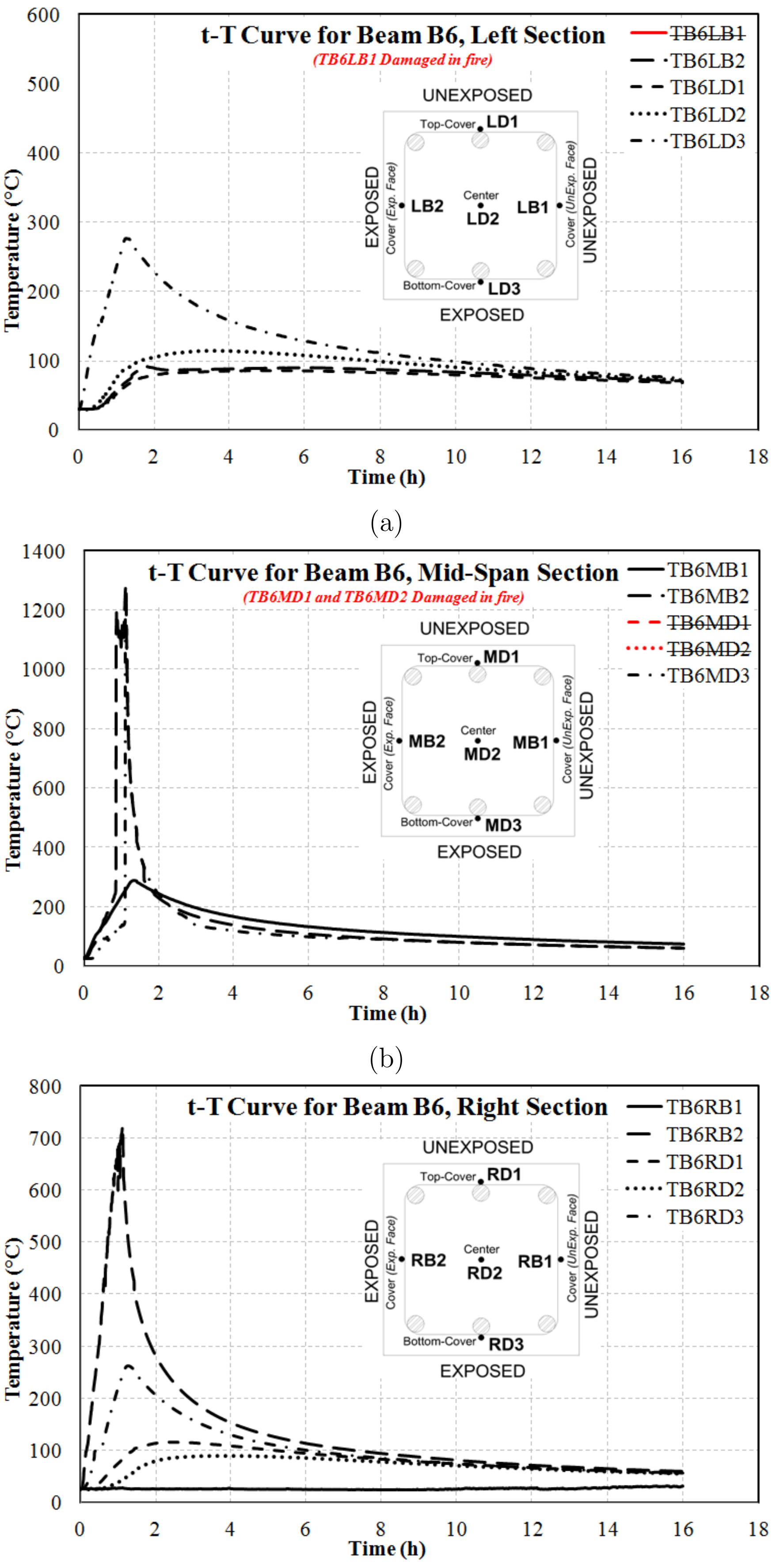

(a)

(b)

(c)

Fig. 4.40: Temperature profile for roof beam B6 at (a) Left section (b) Mid-span section (c) Right section

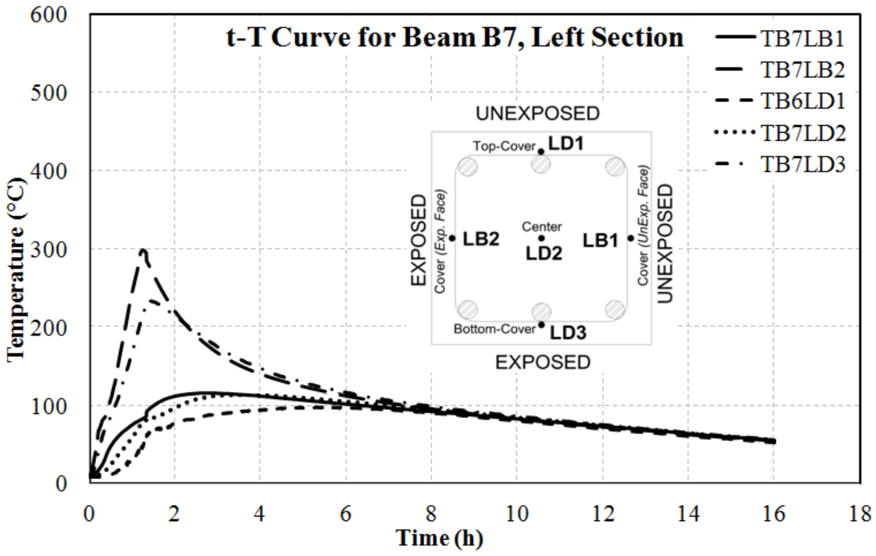

(a)

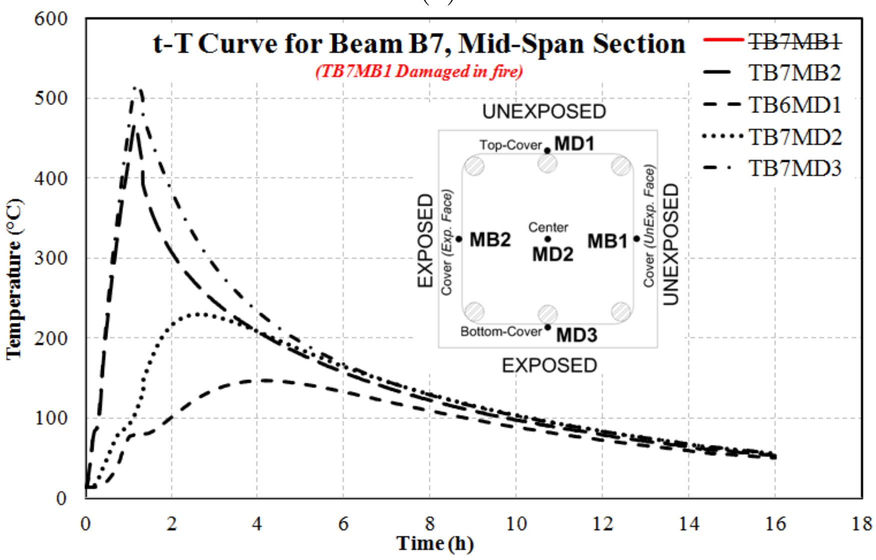

(b)

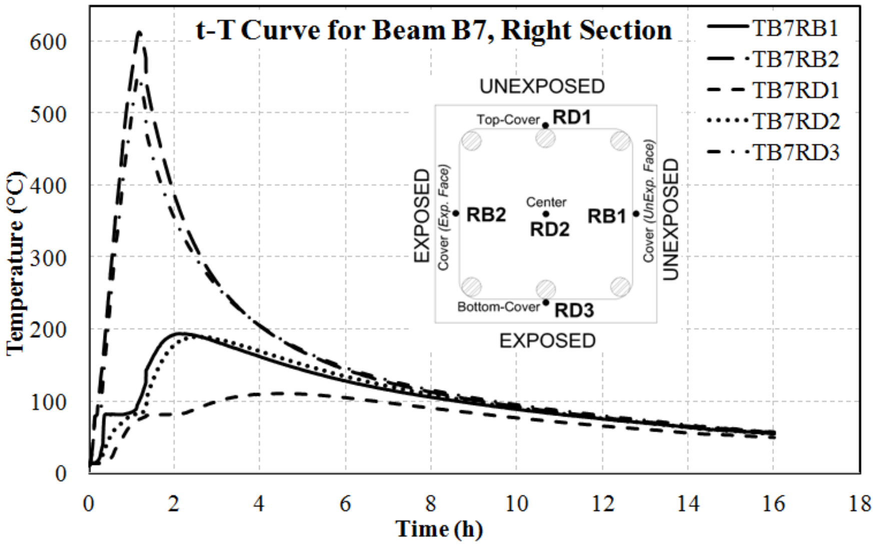

(c)

Fig. 4.41: Temperature profile for roof beam B7 at (a) Left section (b) Mid-span section (c) Right section

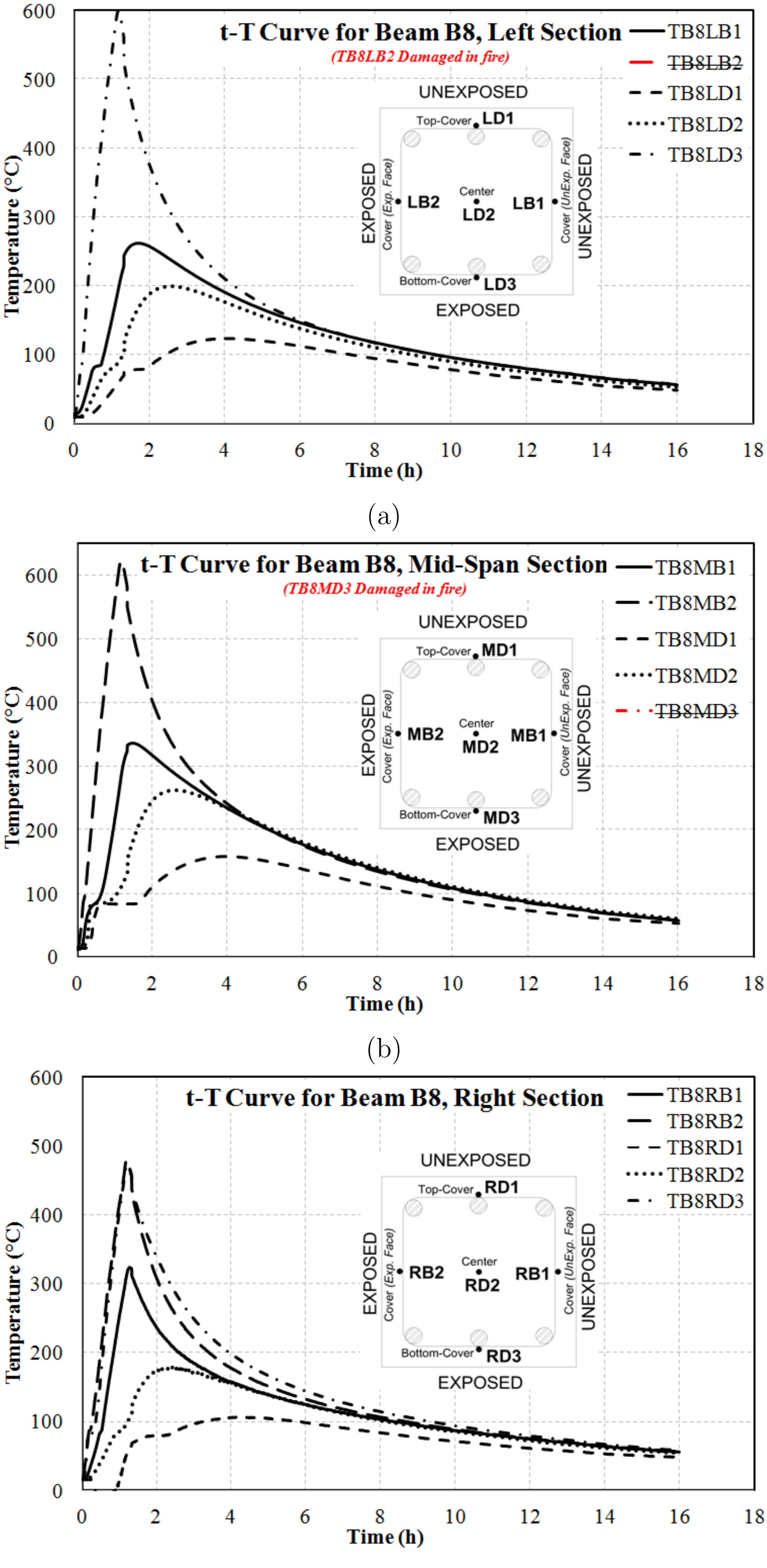

(a)

(b)

(c)

Fig. 4.42: Temperature profile for roof beam B8 at (a) Left section (b) Mid-span section (c) Right section

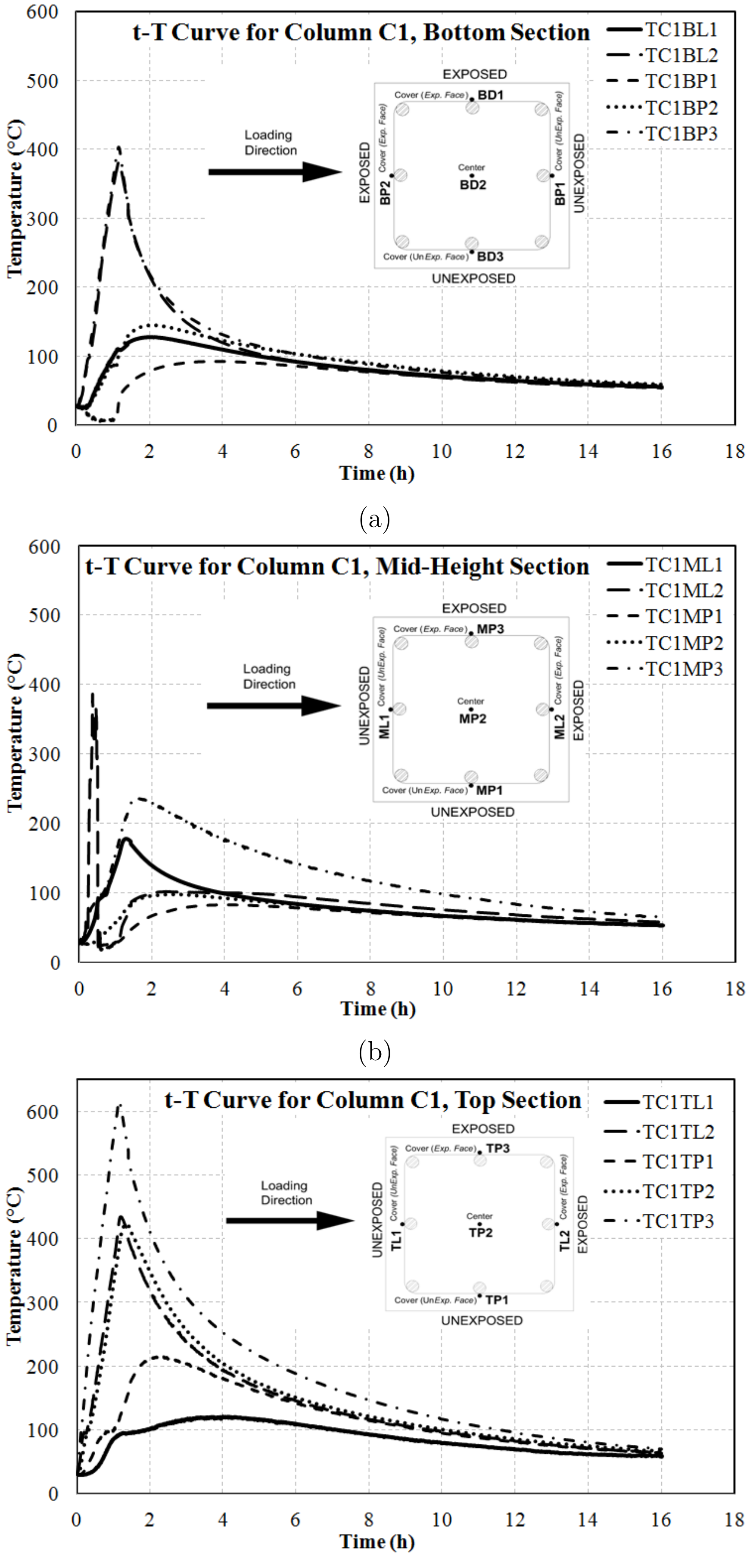

(a)

(b)

(c)

Fig. 4.43: Temperature profile for column C1 at (a) Bottom section (b) Mid-height section (c) Top section

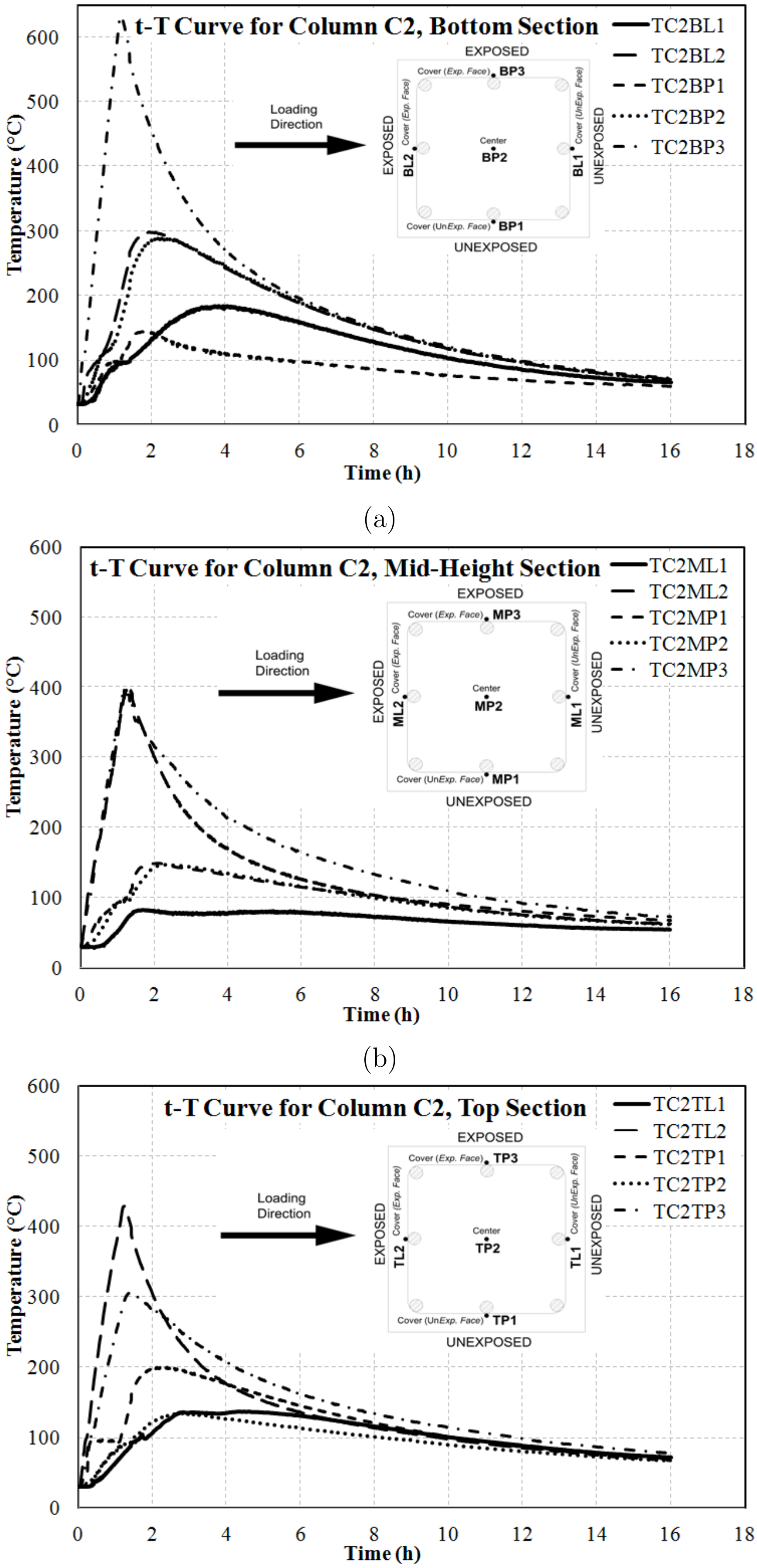

(a)

(b)

(c)

Fig. 4.44: Temperature profile for column C2 at (a) Bottom section (b) Mid-height section (c) Top section

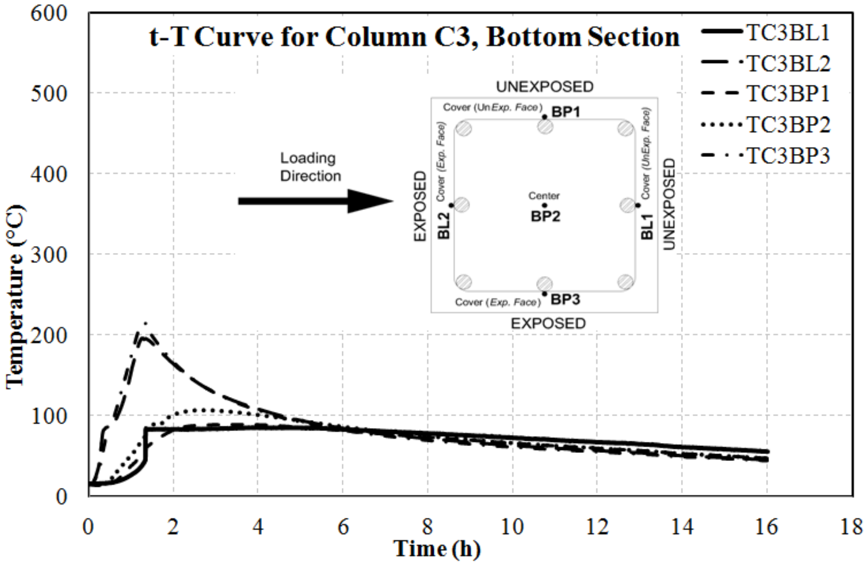

(a)

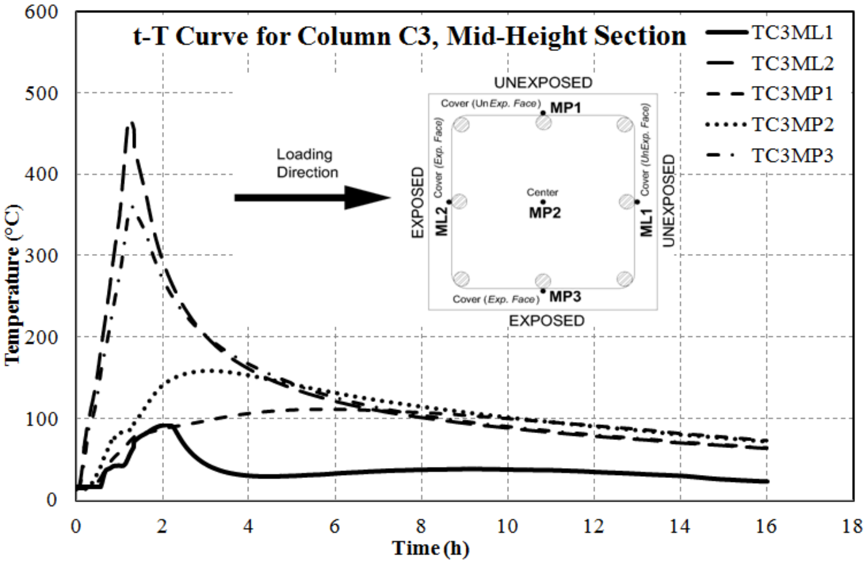

(b)

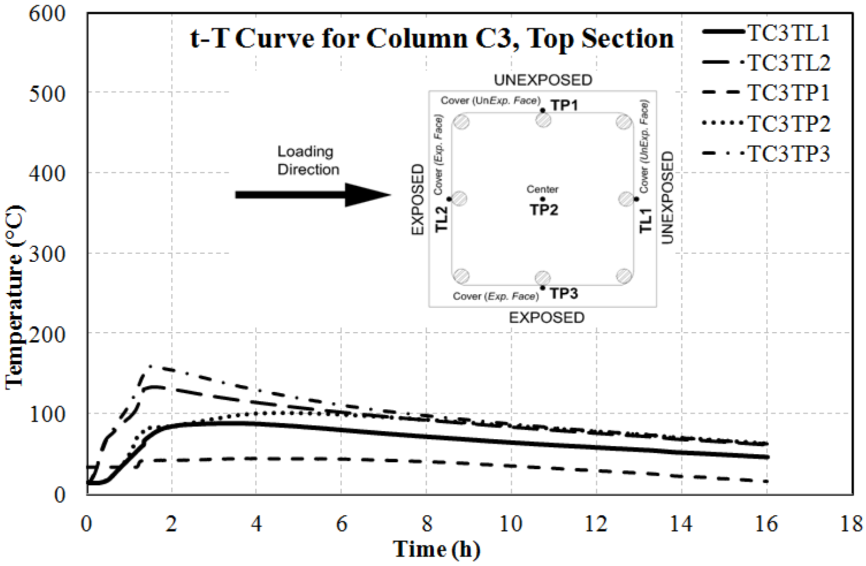

(c)

Fig. 4.45: Temperature profile for column C3 at (a) Bottom section (b) Mid-height section (c) Top section

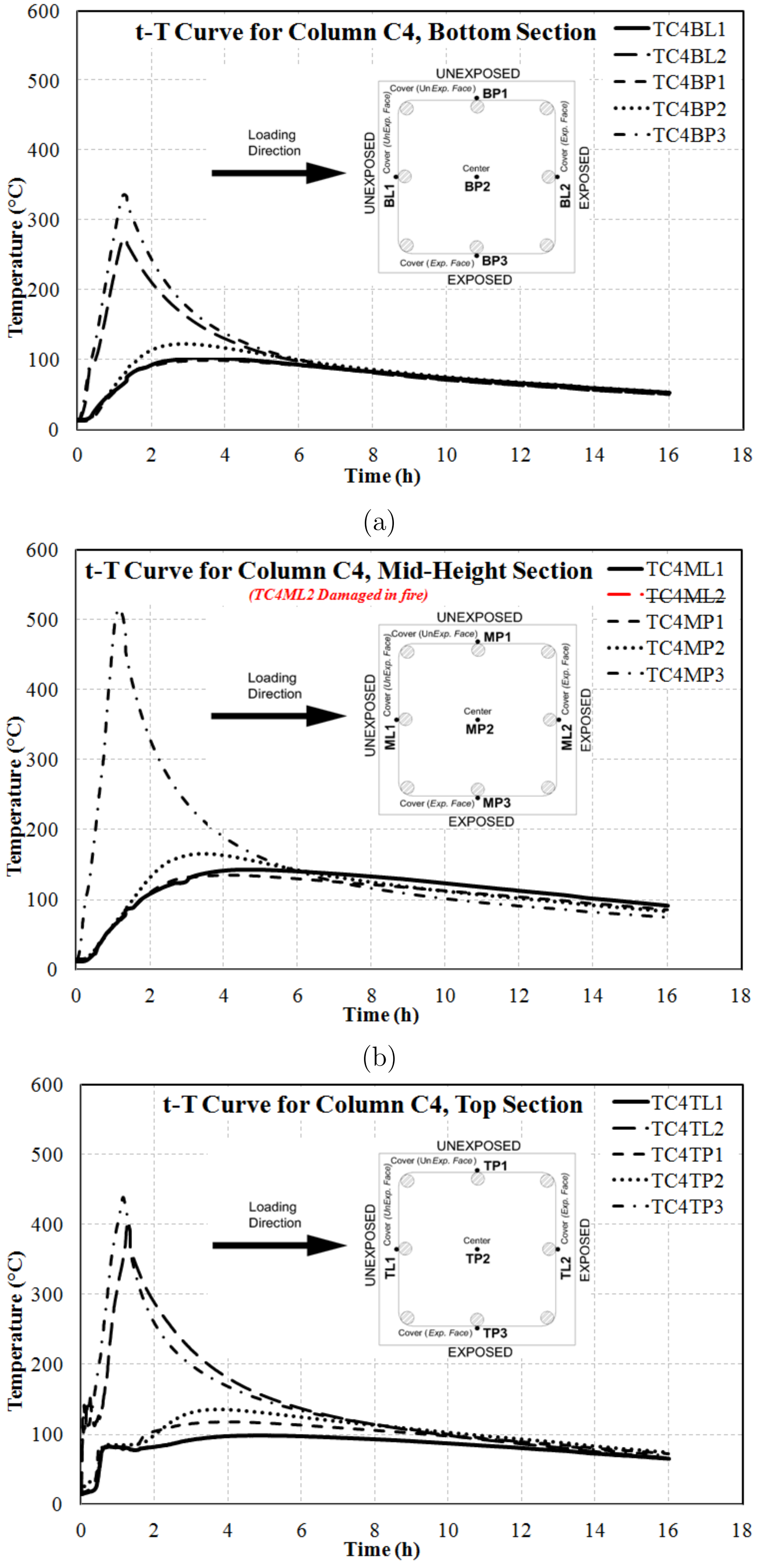

(a)

(b)

(c)

Fig. 4.46: Temperature profile for column C4 at (a) Bottom section (b) Mid-height section (c) Top section

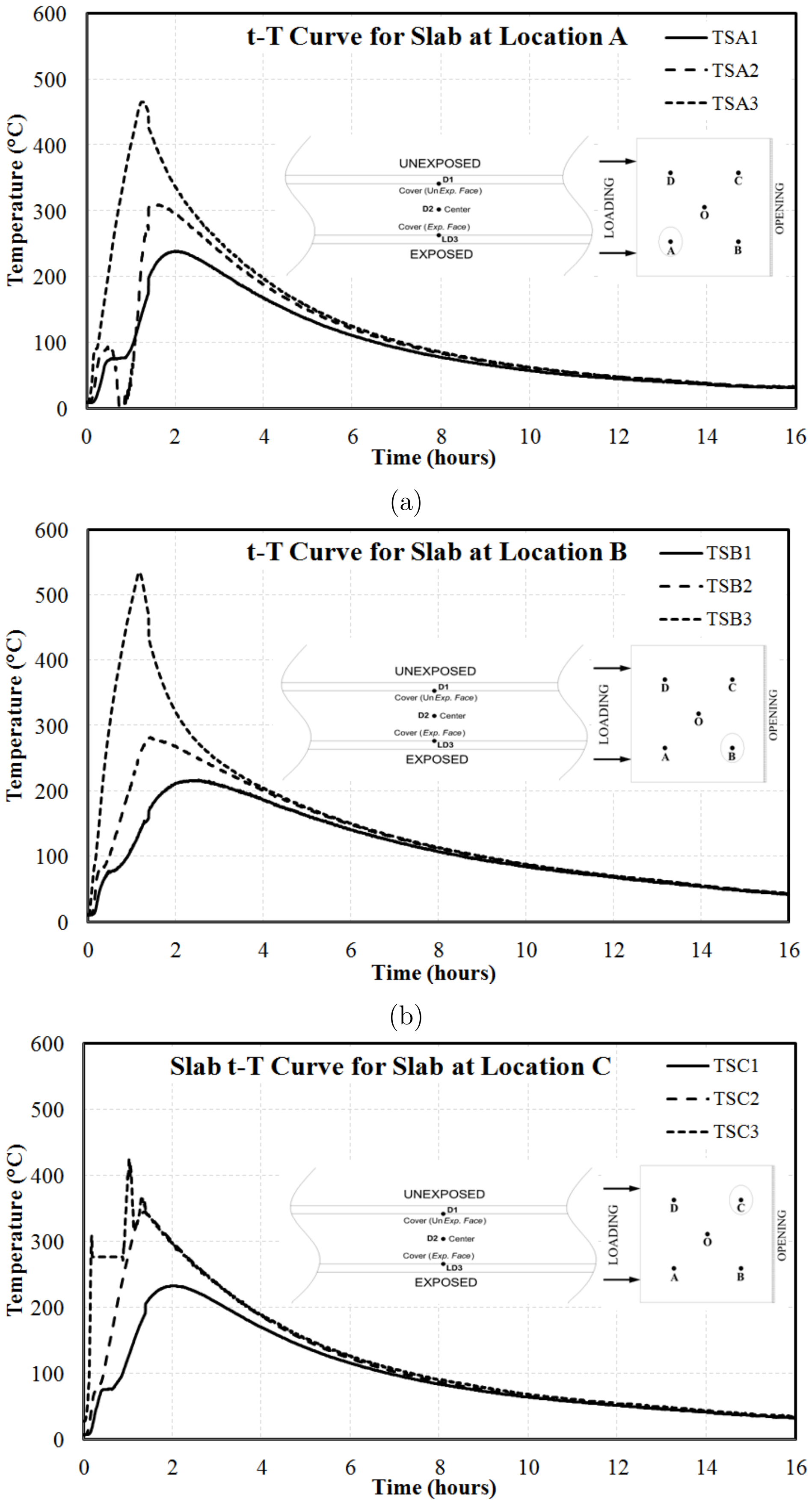

(a)

(b)

(c)

Fig. 4.47: Temperature profile for slab (a) Location A (b) Location B (c) Location C

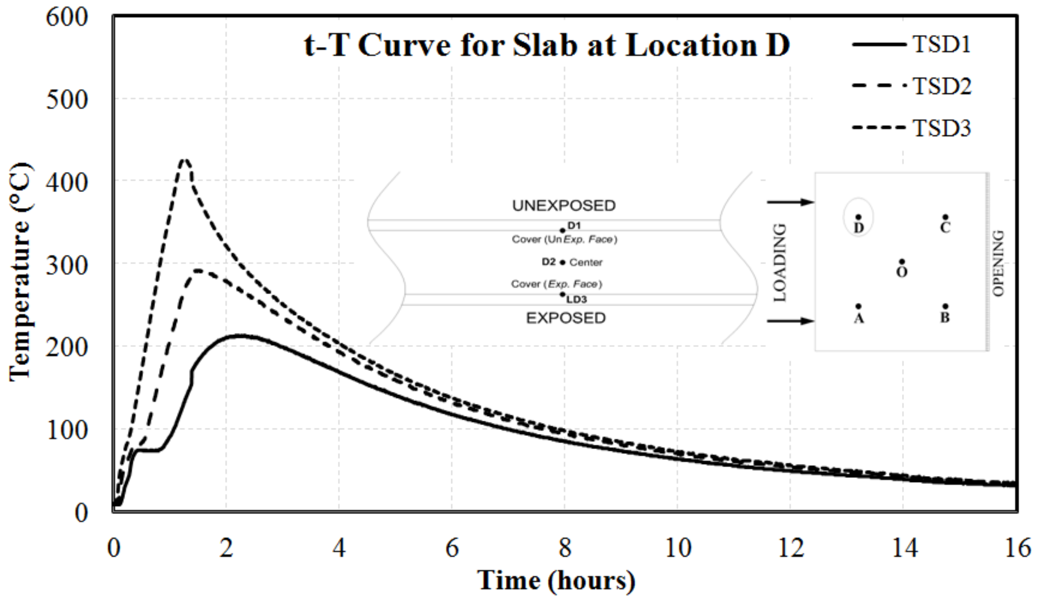

(d)

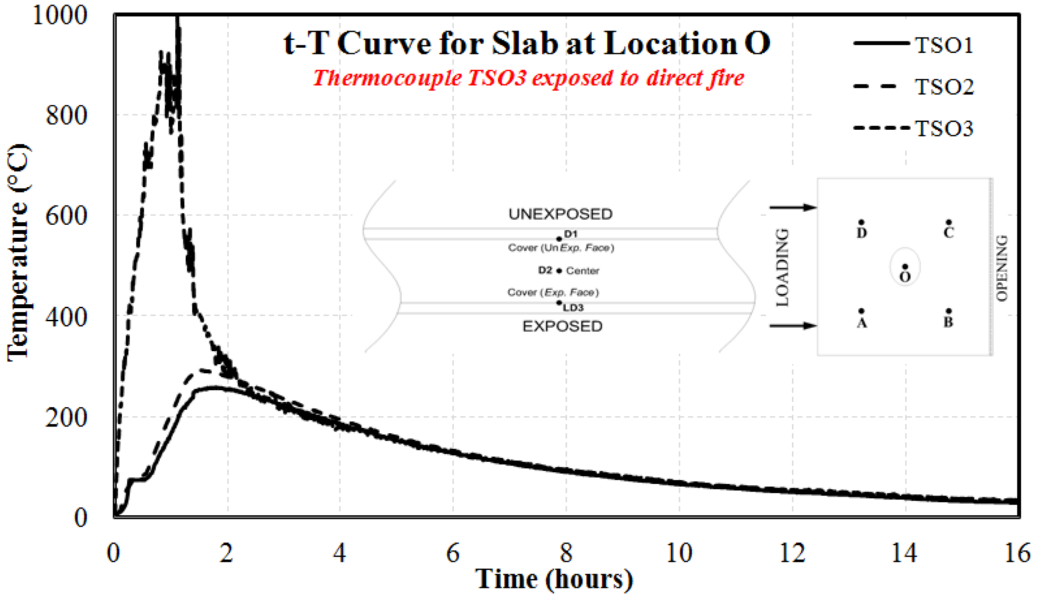

(e)

Fig. 4.48: Temperature profile for slab (d) Location D (e) Location O

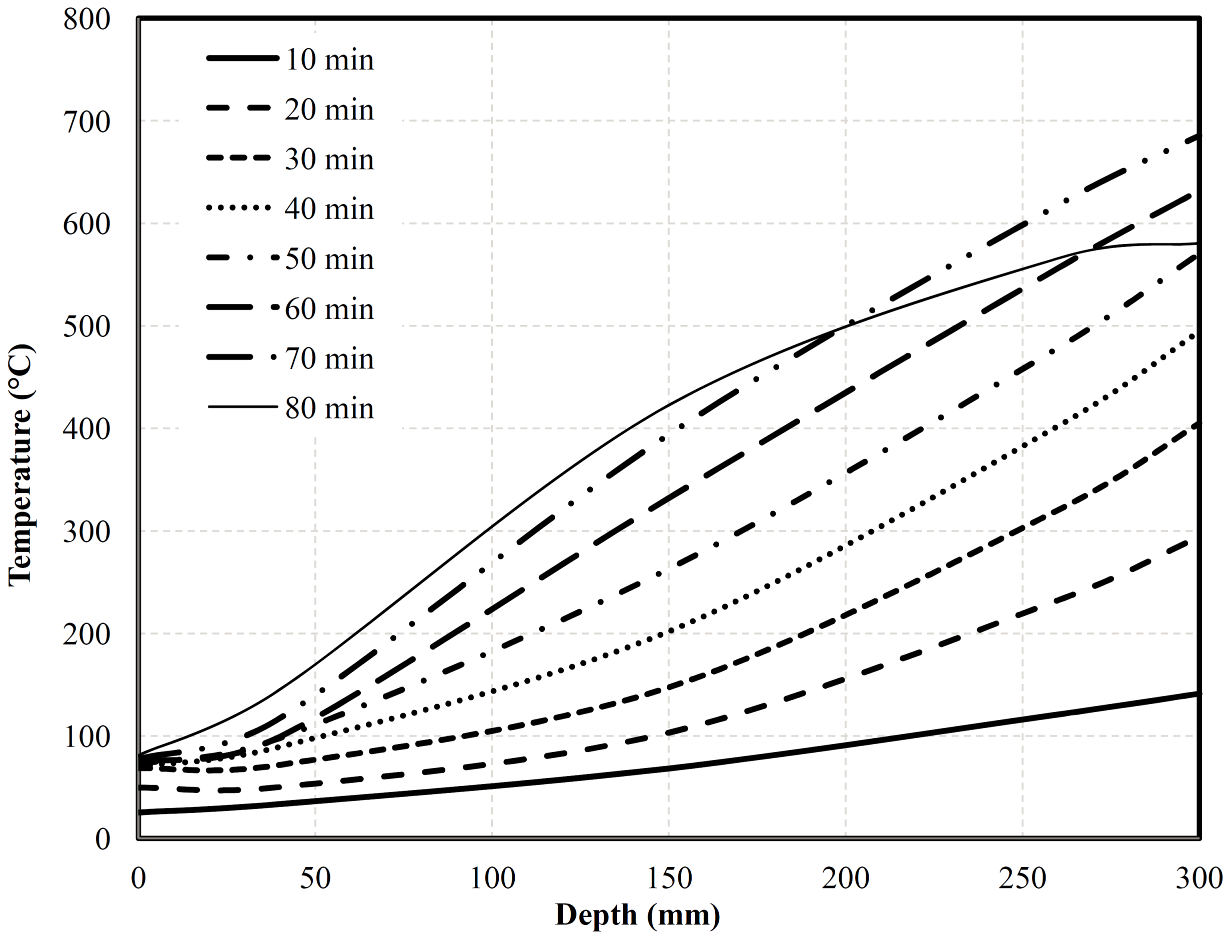

Fig. 4.49: Temperature gradient column (C1, top)

4.5.4.1 Extent of Damage

Figures 4.50 (a), (b), (c) and (d) illustrate the extent of damage in the frame after fire test. Figure 4.50 (a) shows a typical spalling of corner concrete 40 minutes after the fire ignition. Cracks started developing on the exposed face, which propagated along the sharp corners and eventually led to spalling. Similar trends were observed in all the four columns. Figure 4.50 (b) shows the micro-cracks developed on the column surface due to an accelerated cooling of cover concrete. Figure 4.50 (c) shows one of the corners that experienced wide cracks as a result of spalling during the cooling stage. All four columns experienced a loss of corner cover exposing the main reinforcement. From Figure 4.50 (d), a loss of bond between the rebar surface and concrete can be distinctly observed. Beams B7, B8 and B9 showed a significant spalling on the exposed edge making visible the reinforcing bars. The slab remained intact with very less or negligible spalling. Figure 4.51 (a) and Figure 4.51 (b) show the fire damaged beam-column intersection and column C2 respectively. Cracking / spalling of cover concrete was more pronounced in region where cracking due to simulated earthquake loading was significant.

(a)

(b)

(c)

(d)

Fig. 4.50: Structural damage in Fire (a) Spalling during fire (b) Surface microcracks (c) Spalling of cover concrete in cooling regime (d) Debonding of reinforcement

(a)

(b)

Fig. 4.51: Concrete spalling (a) Beam-column joints (b) Corners of the column

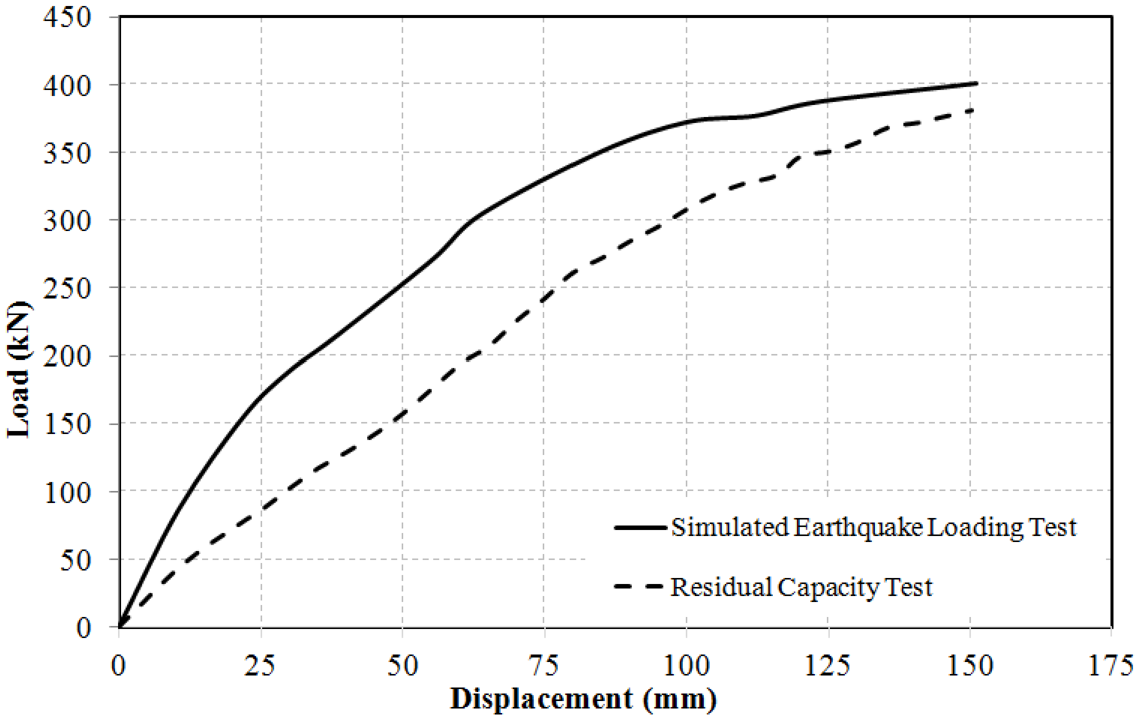

Fig. 4.52: Load-Displacement plot from residual capacity test

4.6 FRAME TEST STAGE III: RESIDUAL CAPACITY TEST

The reinforced concrete frame damaged by simulated earthquake and subsequent fire was thereafter tested for stability and residual capacity in the last stage of the test. The frame was given uni-directional lateral displacements to the full capacity of hydraulic jacks, i.e., 300 mm. However, the displacement and load history could be recorded up to 200 mm. A comparison of load-displacement behavior during simulated earthquake loading test and residual capacity test is presented in Figure 4.52. It is observed that the load carrying capacity of the reinforced concrete frame is only marginally affected by both earthquake loading and subsequent fire. During initial displacements, a higher reduction in load carrying capacity was observed. But as the loading continued, the reduction in load carrying capacity decreased. At 10 mm displacement, the frame showed a loss of 51% reduction in load carrying capacity. An average reduction in the load carrying capacity of 45% was observed up to 50 mm displacement. Thereafter, the reduction in load carrying capacity gradually scaled down to only 5% at the displacement of 150 mm. It is believed that the tensile forces developed in the tie rods, used to facilitate vertical loading, added to increase the lateral load carrying capacity at displacements greater than 70 mm. Spalling of weaker cover concrete was predominantly observed during the loading and upon release. Degradation of strength and stiffness in the reinforced concrete frame sub-assemblage caused a free lateral displacement in the frame. After achieving 300 mm lateral displacement, the load was gradually released. The reinforced concrete frame sub-assemblage remained intact without collapse.

4.7 CONCLUDING REMARKS

Current chapter describes the behaviour of a reinforced concrete frame subjected to fire following earthquake scenario. The main aim of this chapter is to elucidate the experimental technique involved in the full-scale testing of RC frame under simulated fire following earthquake and discuss the results and observations. A detailed analysis was carried out on the results obtained. Displacement and temperature histories for different structural elements: floor beams, columns, roof beams and slabs with different condition of exposure have been plotted and discussed. The frame was initially subjected to a lateral displacement of 150 mm using hydraulic jacks, which yielded an in-elastic lateral deformation of 19 mm. A maximum lateral load of 400.87 kN was applied to achieve the target displacement. Visible cracks and minor concrete cover spalling was observed in simulated earthquake loading. The damaged structure was exposed to compartment fire for one hour, after which the fuel supply was cut-off. Maximum temperature recorded in the compartment was 1370 °C. Temperature-time plots for all the members have been furnished in this chapter, of which, some of the plots of typical members have been discussed. Maximum temperature in the members were recorded within 10 to 15 minutes after one hour. As a result of fire following a simulated earthquake loading, a variety of distresses were recorded in the structural members. The damage caused in the fire was primarily governed by the propagation of hot air currents generated post flashover. Spalling during and after the fire, thermal micro-cracking, deterioration of concrete and loss of bond between rebar and concrete was predominantly observed in columns and beams. The RC frame remained visibly intact without collapse during the residual test. However, the frame experienced a great loss of strength and stiffness. Further validation of experimental results is proposed using commercial finite element simulation packages, ABAQUS version 6.9 in Chapter 5.

Numerical Analysis of RC Frame Under Fire Following Earthquake

5

5.1 INTRODUCTION

It is imperative to reckon the response of reinforced concrete (RC) frame under fire following earthquake with the help of numerical models. Finite element modelling and analysis is considered as one of the robust numerical techniques for solving civil engineering problems. As a validation exercise, an attempt was made to simulate the behaviour of the three - phase test on reinforced concrete frame subject to fire following earthquake, presented in Chapter 4. This chapter includes the finite element modelling and analysis of the RC frame subject to the following sequence using ABAQUS (version 6.8), a commercial software suite for FEM and computer aided engineering (CAE).

1. Static pushover analysis representing the simulated earthquake loading
2. Heat transfer analysis followed by thermal stress analysis representing the fire loading
3. Monotonic push loading representing the residual capacity test

The sequence of analyses is as shown in Figure 5.1. Pushover analysis is carried out to induce the damage in the constituent materials followed by a heat transfer analysis. The final state of stress obtained in the last step of pushover analysis and the temperature profiles obtained from heat transfer analysis are input to the frame that constitutes the thermal stress analysis. The final state of frame in thermal stress analysis is imparted a monotonic push loading to perform an analysis for the assessment of the residual capacity of the reinforced concrete frame subject to earthquake and fire loads.

5.2 MODELLING OF REINFORCED CONCRETE FRAME

Modelling of the reinforced concrete frame was carried out in the FEM/CAE package ABAQUS. This section of 5 deals with different stages of modelling considered to generate the RC frame for analysis: building the model geometry, assigning materials and meshing the model.

5.2.1 Geometric Modelling of RC Frame on ABAQUS

A 3D modelling of reinforced concrete frame was accomplished using Abaqus CAE Version 6.8. The dimensions of the frame model were the same as that of the full-scale reinforced concrete frame

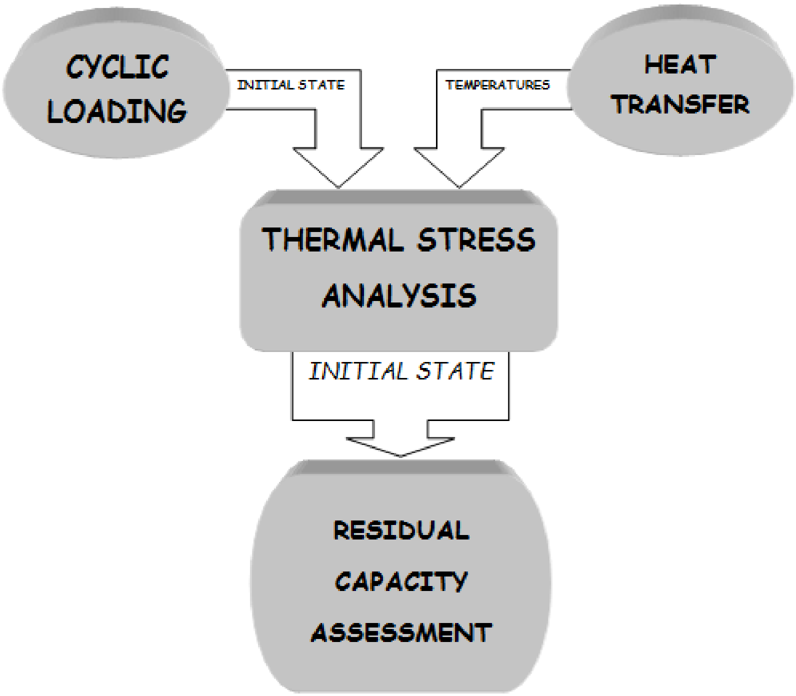

Fig. 5.1: Sequence of analysis

constructed and tested for simulated fire following earthquake, described in Chapter 4. The reinforced concrete frame sub-assemblage under consideration consists of four floor beams, four columns, four roof beams and a slab. Section 4 of Chapter 4 gives the details on the frame construction geometry. Footing was excluded from the modelling. However, the base of the columns were constrained to simulate the fixed boundary condition. The clear-height between the beams and the columns was 3000 mm. Columns had a square cross-section of 300 mm × 300 mm whereas the floor beams and roof beams had a square cross-section of 230 mm × 230 mm. A slab of 120 mm thickness was modelled monolithically with the roof beams. Figure 5.2 shows the geometric model of RC frame generated in ABAQUS.

5.2.2 *Material Modelling: CDP Model for Tension and Compression*

Concrete material modelling was achieved using linear elasticity and concrete damaged plasticity models to simulate the elastic and plastic behaviour of concrete.

5.2.2.1 *Linear Elasticity*

Linear elasticity was defined for the concrete material using the linear elastic material model available in the material library of ABAQUS. Young's modulus of elasticity (E) and Poisson's ratio (ν) were specified as input parameters. In this model, the total stress is defined from the total strain using the relationship given in Equation 5.1.

$$\sigma = D^{el}\epsilon^{el}, \tag{5.1}$$

Where,

$\sigma \longrightarrow$ Total stress: True or Cauchy stress in finite-strain problems.

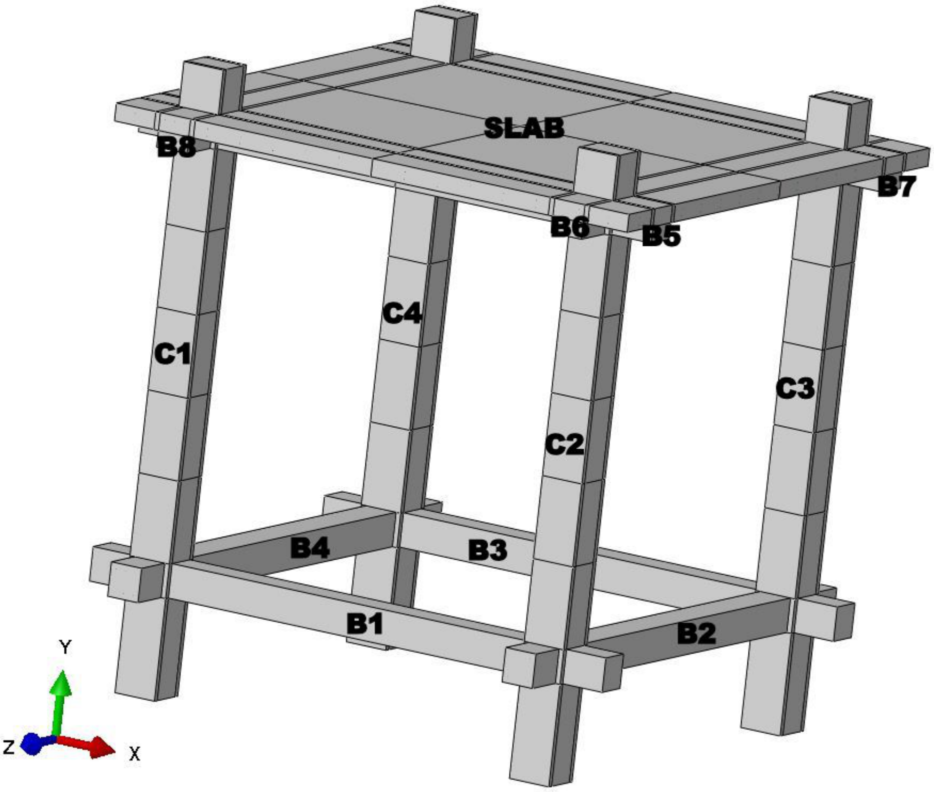

Fig. 5.2: Geometric model of Reinforced Concrete frame generated in ABAQUS

D^{el} ⟶ Fourth order elasticity tensor.
ϵ^{el} ⟶ Total elastic strain or log strain in finite strain problems.

5.2.2.2 *Inelastic Behaviour of Concrete*

The inelastic behaviour of concrete was represented by using the Concrete Damaged Plasticity (CDP) Model from the ABAQUS material library. The concrete damaged plasticity model is built to provide a general capability for analysing reinforced concrete models under cyclic / dynamic loading. Normally, concrete under low confining pressures behaves as a brittle material with prime failure mechanisms: cracking in tension and crushing in compression. The analysis of reinforced concrete structural members demand the behaviour of concrete as a non-brittle material due to a high confining pressure provided by confining reinforcement. Crack propagation is prevented in the confined concrete members by virtue of secondary reinforcement or confinements. The failure is thus governed by the collapse of concrete micro-porous structure leading to a macroscopic response likewise the behaviour of a ductile material with work hardening. An additive strain rate decomposition is considered in this model, where the total strain is calculated as the sum of elastic strain and plastic strain.
The stress-strain relations are governed by scalar damaged elasticity expressed as Equation 5.2.

$$\sigma = (1-d)D_0^{el} : (\epsilon - \epsilon^{pl}) = D^{el} : (\epsilon - \epsilon^{pl}) \tag{5.2}$$

Where,
$D_0^{el} \longrightarrow$ Initial / undamaged elastic stiffness of the material
$D^{el} \longrightarrow$ Degraded elastic stiffness
$d \longrightarrow$ Scalar stiffness degradation variable
The scalar stiffness degradation variable d takes values in the range from 0(undamaged material) to 1(completely damaged material). Cracking and crushing damage associated with the failure mechanisms of the concrete hence causes a reduction in elastic stiffness. Two hardening variables, $\tilde{\epsilon}_t^{pl}$ and $\tilde{\epsilon}_c^{pl}$. Figure 5.3 (a) and Figure 5.3 (b)shows the behaviour of reinforced concrete assumed in tension and compression respectively. It is observed that the unloading response weakens upon unloading from any point on the strain softening branch of the stress-strain curves. This suggests a degradation in the elastic stiffness of the material, which is significantly different under tension and compression loading. However, in both behaviours, the effect significantly increases with an increase in plastic strain. The damage in concrete is identified by introducing two independent uniaxial damage variables, d_t and d_c, which are dependent on plastic strains, temperature and field variables. These damage variables are incremental functions of equivalent plastic strains. The stress-strain relationships under uniaxial tension and compression are as shown in Equation 5.3.

$$\begin{aligned} \sigma_t &= (1-d_t)E_0(\epsilon_t - \tilde{\epsilon}_t^{pl}) \quad ; \quad d_t = d_t\left(\tilde{\epsilon}_t^{pl}, \theta, f_i\right), (0 \leq d_t \leq 1) \\ \sigma_c &= (1-d_c)E_0(\epsilon_c - \tilde{\epsilon}_c^{pl}) \quad ; \quad d_t = d_c\left(\tilde{\epsilon}_c^{pl}, \theta, f_i\right), (0 \leq d_c \leq 1) \end{aligned} \tag{5.3}$$

Where,
$E_0 \longrightarrow$ Initial / Undamaged elastic stiffness of the material
Cracks propagate in a direction transverse to the stress direction in case of a uniaxial loading. The formation of cracks and their propagation leads to a reduction in the load carrying area causing an increase in the effective stress. This effect is very small in case of compressive loading since the cracks propagate parallel to the loading direction. Nevertheless, after a certain level of crushing, the effective load-carrying area reduces significantly. The effective uniaxial cohesion stress in tension ($\bar{\sigma}_t$) and compression ($\bar{\sigma}_c$) used in determining the size of yield surface, are as given in Equation 5.4.

$$\begin{aligned} \bar{\sigma}_t &= \frac{\sigma_t}{(1-d_t)} = E_0(\epsilon_t - \tilde{\epsilon}_t^{pl}) \\ \bar{\sigma}_c &= \frac{\sigma_c}{(1-d_t)} = E_0(\epsilon_c - \tilde{\epsilon}_c^{pl}) \end{aligned} \tag{5.4}$$

$$\sigma = (1-d)D_0^{el} : (\epsilon - \epsilon^{pl}), \tag{5.5}$$

Where,
$D_0^{el} \longrightarrow$ Initial / undamaged elasticity matrix
A non-associated potential flow is used in the plastic damage model as shown in Equation 5.6.

$$\dot{\epsilon}^{pl} = \dot{\lambda}\frac{\partial G(\bar{\sigma})}{\partial \bar{\sigma}} \tag{5.6}$$

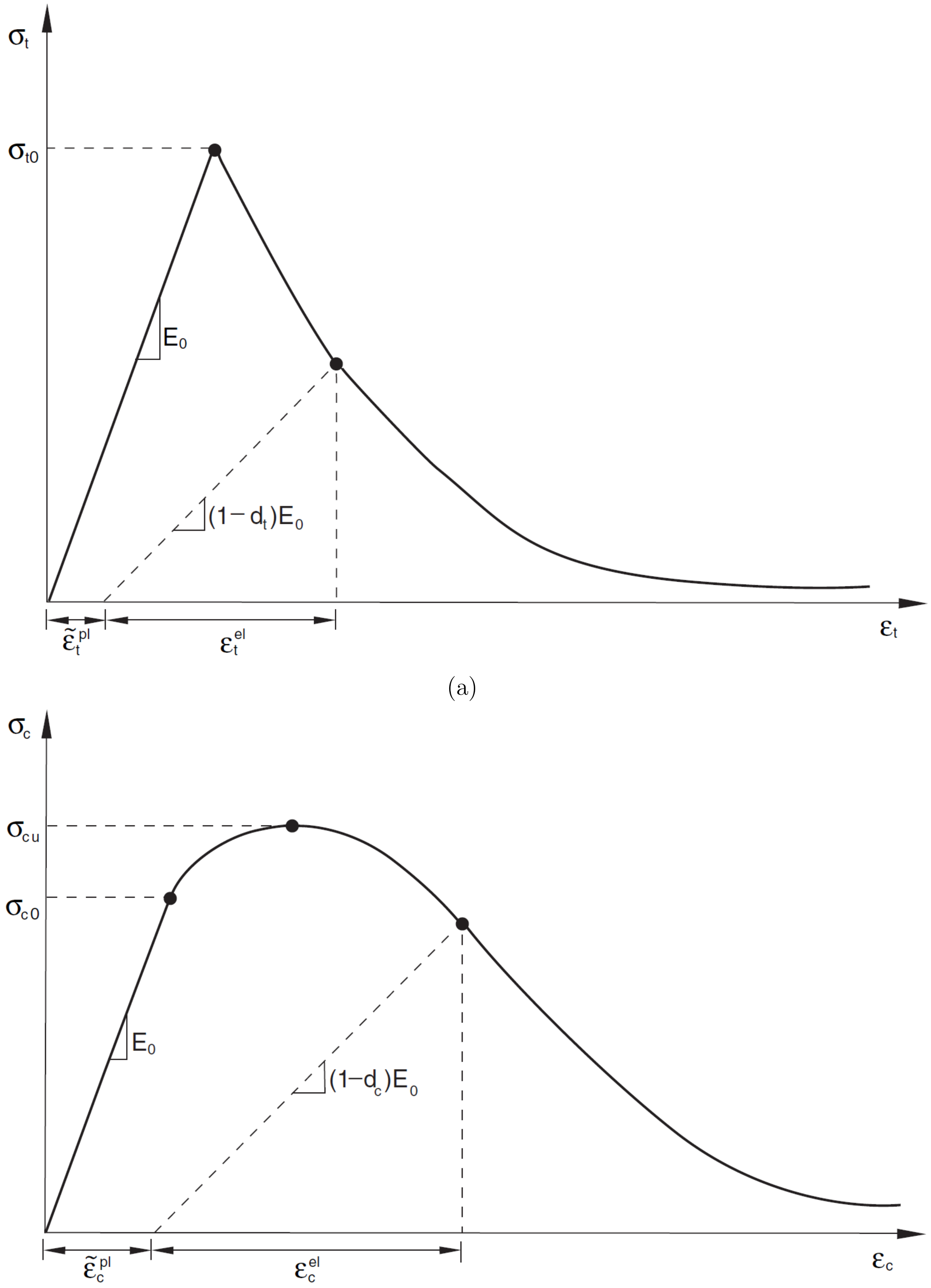

(a)

(b)

Fig. 5.3: Behaviour of Concrete in (a) Uniaxial Tension (b) Uniaxial Compression

The Drucker-Prager hyperbolic function is used as the non-associated flow potential G as shown in Equation 5.7.

$$G = \sqrt{(\epsilon \sigma_{t0} tan\psi)^2 + \bar{q}^2} - \bar{p} tan\psi \tag{5.7}$$

Where, $\psi(\theta, f_i) \longrightarrow$ Dilation angle measured in the p-q plane at high confining pressure
$\sigma_{t0}(\theta, f_i) \longrightarrow$ Uniaxial tensile stress at failure, taken from the user-specified tension stiffening
Yield condition in the CDPM is represented by the yield function proposed by Lubliner et. al. [56] and follows the modifications for evolution of strength under tension and compression, proposed by Lee and Fenves [54]. Yield function is expressed in terms of effective stress as shown in Equation 5.8.

$$F(\bar{\sigma}, \tilde{\epsilon}^{pl}) = \frac{1}{1-\alpha}(\bar{q} - 3\alpha\bar{p} + \beta(\tilde{\epsilon}^{pl})\langle\bar{\sigma}_{max}\rangle - \gamma\langle-\hat{\bar{\sigma}}_{max}\rangle) - \bar{\sigma}_c(\tilde{\epsilon}_c^{pl}) = 0 \tag{5.8}$$

Where,
The dimensionless constants, α and γ are as given in Equation 5.9 and Equation 5.11 respectively.

$$\alpha = \frac{(\sigma_{b0}/\sigma_{c0}) - 1}{2(\sigma_{b0}/\sigma_{c0}) - 1}; \qquad 0 \leq \alpha \leq 0.5 \tag{5.9}$$

The function $\beta\,(\tilde{\epsilon_{pl}})$ is shown in Equation 5.10.

$$\beta\,(\tilde{\epsilon_{pl}}) = \frac{\bar{\sigma}_c(\tilde{\epsilon}_c^{pl})}{\bar{\sigma}_t(\tilde{\epsilon}_t^{pl})}(1-\alpha) - (1+\alpha) \tag{5.10}$$

Where,
$\bar{\sigma}_t \longrightarrow$ Effective tensile cohesion stress
$\bar{\sigma}_c \longrightarrow$ Effective compressive cohesion stress

$$\gamma = \frac{3(1-K_c)}{2K_c - 1} \tag{5.11}$$

Where,
$\hat{\bar{\sigma}}_{max} \longrightarrow$ The maximum principal effective stress
$(\sigma_{b0}/\sigma_{c0}) \longrightarrow$ The ratio of equi-biaxial compressive yield stress to initial uniaxial compressive yield stress (Default Value = 1.6)

5.2.3 Meshing the Model

The model created in ABAQUS was assigned a suitable element type in order to generate finite element mesh in them for analysis.

5.2.3.1 *Assigning ABAQUS Element Type*

Beams and columns were assigned 3D continuum element, C3D8. The element C3D8 is a general purpose linear brick element and uses $2 \times 2 \times 2$ or full integration. linear interpolation in between the nodes. The steel reinforcing bars are modelled using two-noded truss elements in three dimensions, T3D2. Truss elements carry tensile and compressive loads and are ideal for reinforcing bars. In addition, an embedded constraint is imposed by considering the concrete region as master surface and the re-bar cage as the slave surface.

5.2.3.2 *Meshing of the Frame Geometry*

Before meshing the model geometry, the part is seeded at desired locations. Further, the seeds were selected based on the desired element size and ABAQUS generated the nodes in the mesh wherever possible. The approximate mesh size used for concrete elements is 50 *mm* and that of rebar elements is 28 *mm*. Total number of elements in the model are as given in Table 5.1.

Total number of elements generated in the model were 66868, out of which 38112 were $C3D8$ and 28756 were $T3D2$. Meshing was achieved through structured mesh generation technique, where a preestablished octahedral mesh pattern was applied to the model topology. Figure 5.4 shows the meshed model ready for analysis.

Element Type	**Number**
Continuum elements (C3D8)	38112
Truss elements (T3D2)	28756

Tab. 5.1: Mesh details

5.3 *SIMULATED EARTHQUAKE LOADING IN ABAQUS*

A pushover loading was imparted to the reinforced concrete frame model generated in ABAQUS. Each cycle of displacement was defined as a separate loading step. Displacements were applied to the frame in eleven cycles analogous to the experimental study. The displacement cycles given as input are as shown in Table 5.2. After a push cycle of 150 *mm*, the lateral load applied was removed by releasing the oil pressure in the hydraulic jacks. The frame retracts yielding a plastic displacement of 19 *mm*. This event was simulated in ABAQUS by defining the last step of loading cycle, where, a pull-cycle in terms of 131 *mm* displacement was imparted. This completed the analysis by introducing the plastic displacement of 19 *mm*. Analysis was directed by the displacement cycle given as input. Upon completion of analysis, results were obtained in terms of loads, displacements and strains.

5.3.1 *Comparison of Simulated Earthquake Loading Test Results*

The results obtained by ABAQUS in simulation of RC frame model were compared with the results obtained in the simulated loading phase of experimental evaluation.

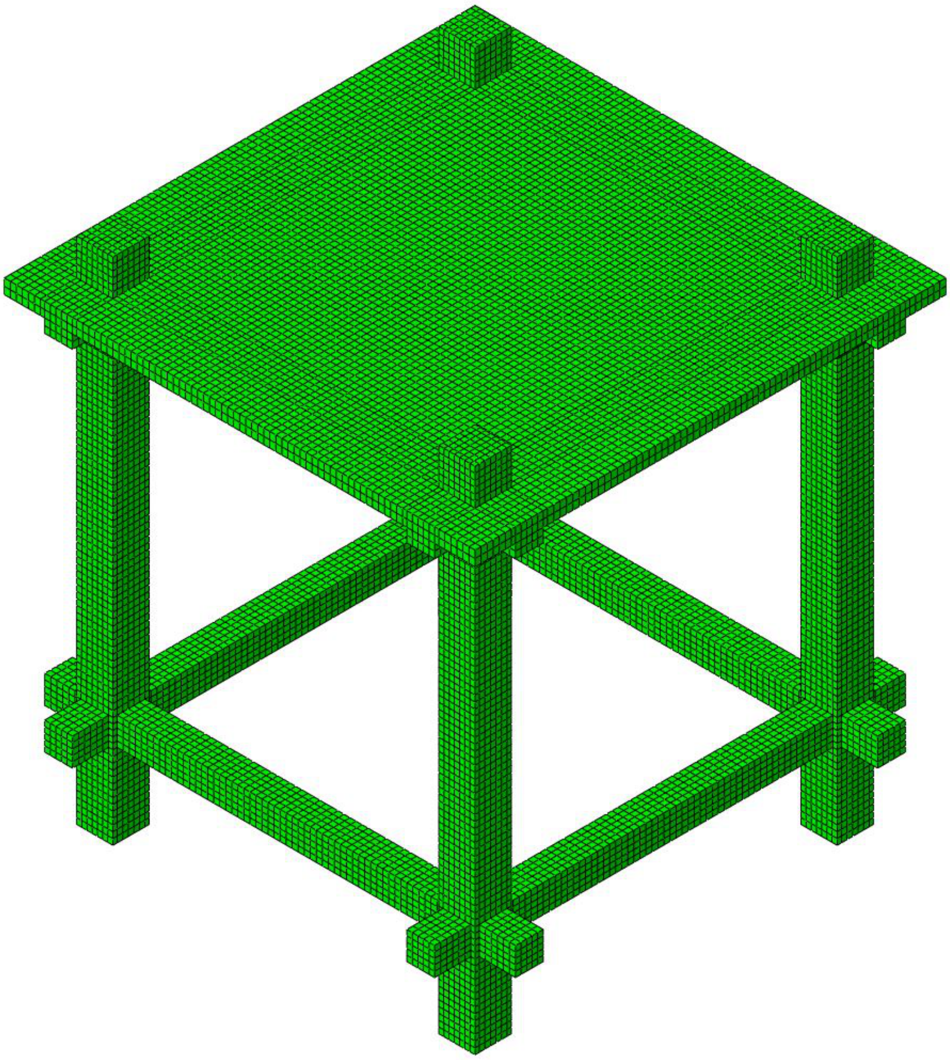

Fig. 5.4: Meshing of the model

Step	Displacement PUSH (mm)	Step	Displacement PULL (mm)
1	Gravity Loading / Superimposed Load 10 Ton on C1, C2, C3 and C4		
2	11	3	16
4	22	5	23
6	30	7	31
8	39	9	40
10	54	11	59
12	66	13	73
14	89	15	96
16	100	17	110
18	113	19	112
20	136	21	129
22	150	23*	134

** Step for simulating the plastic displacement of 19mm*

Tab. 5.2: Input displacements for earthquake loading simulation

5.3.1.1 Load-Displacement Hysteresis

Figure 5.5 shows the cyclic response of the RC frame in terms of load-displacement hysteresis. Although a strength degradation is notable from the hysteretic loop, no effect of pinching was observed. Pinching usually occurs due to rebar bond slip and shear cracking in the concrete. This behaviour can be attributed to the default damage parameters in the concrete damage plasticity model, which is not a good representation of strength and stiffness degradation. Another attribute is the inadequacy of functions in the element modelling. It is necessary that the concrete constitutive model requires a right set of damage parameters to account for cracking and softening. Due to the lack of robustness in acquiring displacements and since the cycles were load controlled, accurate damage parameters could not be worked out experimentally. Hence the load-displacement hysteresis obtained in ABAQUS does not include the pinching effect.

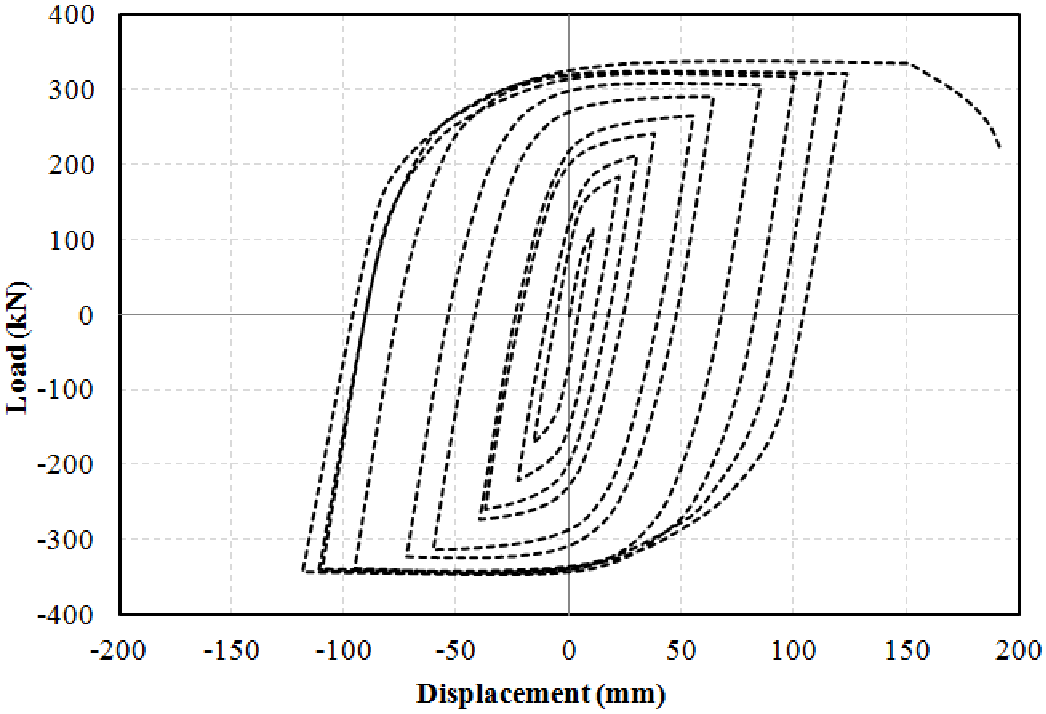

Fig. 5.5: Load-Displacement hysteresis under pushover loading for RC frame model generated in ABAQUS

5.3.1.2 Output Load History

The load history obtained in the analysis was plotted and compared against the experimentally obtained results as shown in Figure 5.6. Overall, ABAQUS overestimated the load carrying capacity of the frame. However, in the last six displacement cycles, a disparity in the results of push cycles was observed from that of pull cycles. In 70 mm, 90 mm, 110 mm, 130 mm , 140 mm and 150 mm displacement cycles, an average overestimation of 15% in push cycles and an average underestimation of 8% in the pull cycles was calculated. A least match of 55% was registered in 30 mm pull cycle, where the ABAQUS predicted value of load was 258 kN against an experimental value of 141 kN. Maximum predicted value of load in push cycle was 339 kN against an experimentally obtained value of 397 kN at a displacement of 150 mm. Whereas, the maximum predicted value of load in pull cycle was slightly higher (345 kN) as compared to the push cycle, obtained against an experimental value of 333 kN at a displacement of 110 mm. Table 5.3 shows the comparison of predicted load and their respective experimental values. Also, the results indicate a degradation in load carrying capacity beyond 130 mm displacement cycle. No increase or slight reduction in the load carrying capacity was reported beyond that. This phenomenon is attributed to the reduction in strength and stiffness of the frame. Figure ??(a) and (b) shows the comparison of numerically obtained loading envelope against the experimental values in push and pull cycles respectively.

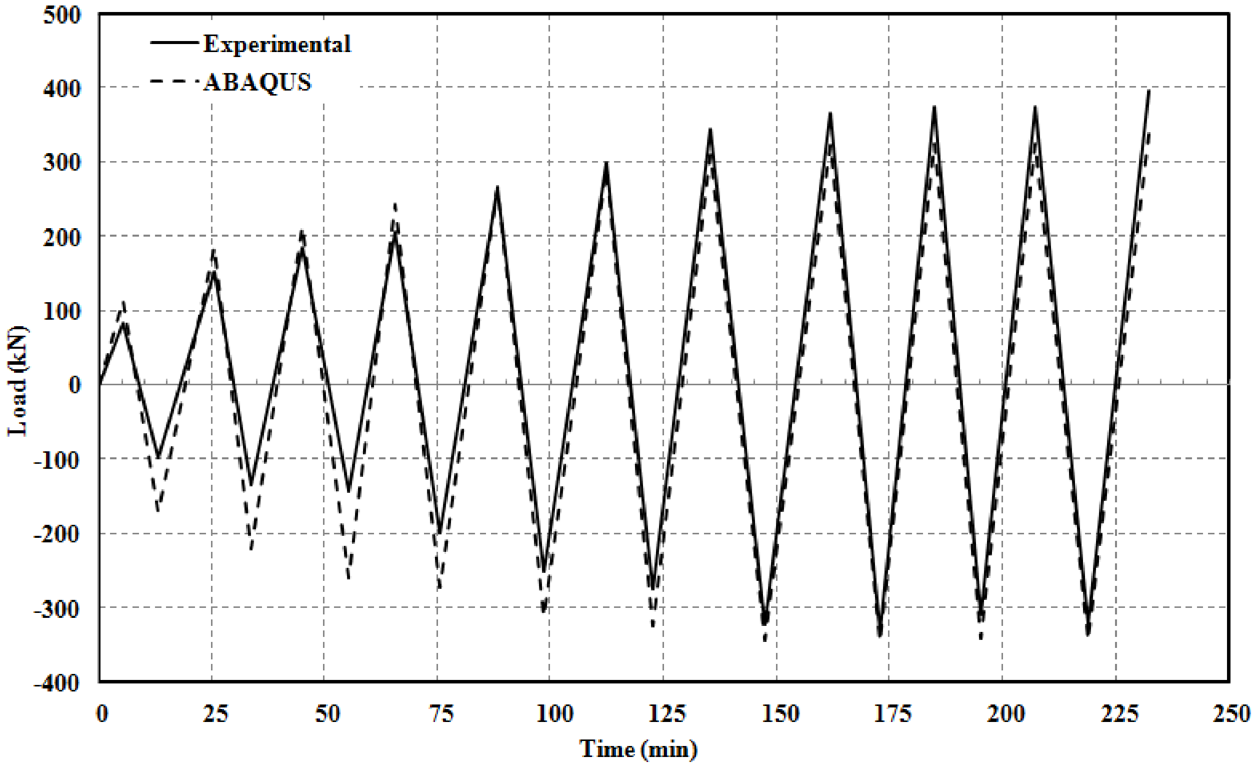

Fig. 5.6: Comparison of load vs. time plot

5.4 *HEAT TRANSFER ANALYSIS ON THE RC FRAME*

Heat transfer analysis, as the name suggests, it is a technique to numerically assess the amount of heat transferred between a fire, its source and different surfaces exposed in the compartment. Typically, a heat transfer analysis carried on a structure helps in studying the distribution of temperature in various structural elements during a fire event. This section presents an uncoupled heat transfer analysis conducted on the reinforced concrete frame modelled in section 5. The main aim was to obtain the temperature gradients and compare them with experimentally obtained temperature-time plots summarised in chapter 4. An assumption is made that the temperature distribution is not dependent on the stress or deformations in the reinforced concrete frame. The current section summarises the concepts of energy balance, boundary conditions, constitutive models, finite element discretization and time integration procedures used during uncoupled heat transfer analysis.

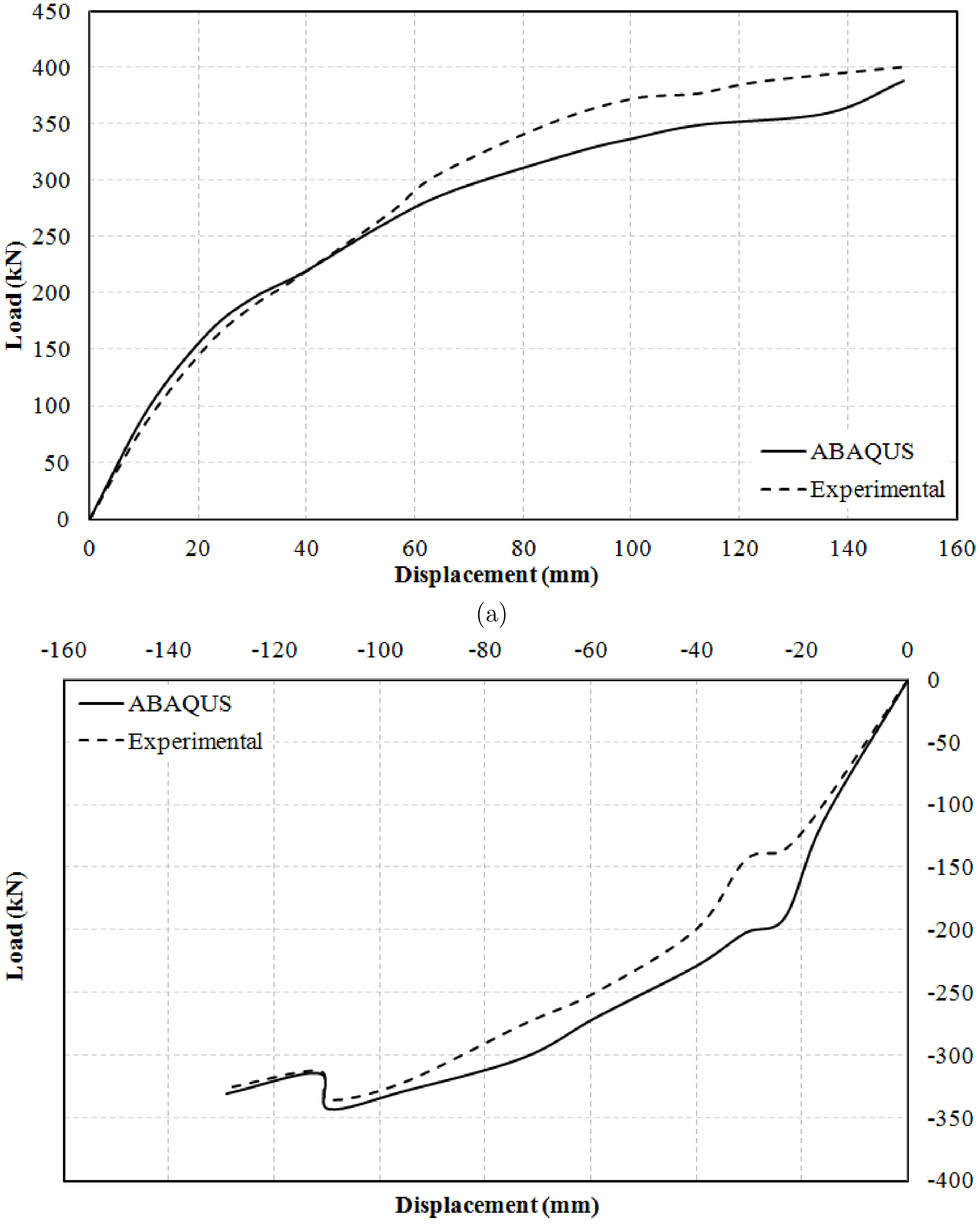

(a)

(b)

Fig. 5.7: Comparison of loading envelope (a) Push Cycle (b) Pull cycle

Time (min.)	**Load (kN) Experimental**	**Load (kN) ABAQUS**	**Inference ABAQUS**
0	0	0	*NA*
5	83	115	*Overestimates*
13	-98	-170	*Overestimates*
25	152	185	*Overestimates*
34	-134	-220	*Overestimates*
45	185	213	*Overestimates*
55	-141	-258	*Overestimates*
65	207	243	*Overestimates*
75	-198	-272	*Overestimates*
88	266	266	*Overestimates*
99	-249	-312	*Overestimates*
112	300	292	*Underestimates*
123	-273	-323	*Overestimates*
135	346	310	*Underestimates*
147	-320	-343	*Overestimates*
162	366	323	*Underestimates*
173	-333	-345	*Overestimates*
185	375	326	*Underestimates*
195	-309	-341	*Overestimates*
207	375	325	*Underestimates*
219	-322	-344	*Overestimates*
232	397	339	*Underestimates*

Tab. 5.3: Comparison of load values obtained in ABAQUS results with respect to experimental results *(+ indicates a push cycle and - indicates a pull cycle)*

5.4.0.3 Finite Element Formulation

A computational model for carrying out the heat transfer analysis has been presented in this section. The results from heat transfer analysis are used in predicting the temperature profile in various structural elements of the frame.

Fundamentally, heat transfer process occurs through three different modes: Conduction, Convection and Radiation. In conduction, heat transfer takes place either within a solid body or within two solid bodies which are in physical contact with each other by the virtue of temperature difference. Conduction is influenced by other modes of heat transfer at the boundary surfaces. Heat transfer is a transient phenomenon. It can be represented by a Fourier equation, relating the temperature T at each point of the continuum to the time t as shown in Equation 5.12.

$$\rho c \frac{\delta T}{\partial t} = \nabla[k \nabla T] + Q \tag{5.12}$$

Where,

$\rho \longrightarrow$ Density of solid in kg/m^3

$c \longrightarrow$ Specific heat of solid in $J/kg.\,°\mathrm{C}$

$Q \longrightarrow$ Time rate of heat generated per unit volume by hydration of cement paste in concrete within

the body (W/m^3)
Heat conduction equation is a partial differential equation (PDE). Solution to a PDE requires a set of non-linear or linear boundary and initial conditions, as required in time dependent problems. The boundary conditions are broadly classified into two types: Dirichlet boundary condition and Neumann boundary condition. In Dirichlet boundary condition, the temperature is prescribed along the boundary surface as given by Equation 5.13 whereas in Neumann boundary condition the derivatives of the temperature, the heat fluxes are prescribed over the boundary as shown in Equation 5.14.

$$T = T_0 \tag{5.13}$$

$$k\frac{\partial T}{\partial n} + q = 0 \tag{5.14}$$

Where,
$n \longrightarrow$ Unit normal vector to the surface
$q \longrightarrow$ Time rate of heat transferred between the environment and concrete surface per unit area, expressed in W/m^2
The outward heat flux q comprises of the components q_c, the loss of heat flux due to convection and q_r, the loss of heat flux due to radiation. Convection component is expressed in terms of compartment temperature, T_0 and convection heat transfer coefficient h_c as given by Equation 5.15.

$$q_c = h_c(T - T_0) \tag{5.15}$$

Equation 5.16 represents the thermal irradiation, q_r expressed as a simplified form of Stephen Boltzman's radiation law. q_r gives the heat transfer between the surface of concrete and its surroundings due to long wave radiation.

$$q_r = h_r(T - T_0) \qquad ; \qquad h_r = C_s\epsilon[(T + T^*)^4 - \alpha(T + T^*)^4] \tag{5.16}$$

Where,
$C_s \longrightarrow$ Stephen Boltzman's constant equal to $5.667 \times 10^{-8} W/m^2$ °C K^4
$\epsilon \longrightarrow$ Emissivity coefficient relating the radiation of the surface concrete surface (gray) to that of an ideal black body ($0 \leq \epsilon \leq 1$)
$T^* \longrightarrow$ Constant equal to 273 which is used to convert the temperature from degree Celsius °C to °CK
$\alpha \longrightarrow$ Emissivity coefficient given by Equation 5.17

$$\alpha = 1 - 0.261e^{[-7.776\times10^{-4}(T_0)^2]} \tag{5.17}$$

Enframing Equation 5.12 along with the appropriate boundary conditions gives a strong form solution. However, the finite element based solutions rely on weak formulation of the problem within the definite domain. To this end, Galerkin weighted residual principle has been employed, which assumes an approximate function $\tilde{T}$ for the unknown temperature variable at elemental level and yields to give Equation 5.18.

$$\int_{V^{(e)}} [N]^T \rho c \frac{\partial \tilde{T}}{\partial t} dV - \left(\int_{V^{(e)}} [N]^{\tilde{T}} \nabla[k\nabla\tilde{T}] + [N]^T Q \right) dV = 0 \tag{5.18}$$

A discretized approximation is usually taken as $C\,^{\circ}$C continuous in the scalar field variable $\tilde{T}$ and at elemental level is given in terms of elemental nodal degree of freedom as shown in Equation 5.19.

$$\tilde{T} = [N]\{T^e\} = [N_1 N_2 N_2 .....N_n]\{T^e\} \tag{5.19}$$

Using Green's theorem, Equation 5.18 can be decoupled into a domain and a boundary term as shown in Equation 5.20.

$$\rho c \int_{V^{(e)}} [N]^T \frac{\partial \tilde{T}}{\partial t} dV + \int_{V^{(e)}} [\nabla N]^T k \left[\nabla \tilde{T}\right] dV - \int_{V^{(e)}} [N]^T Q\, dV + \int_{S^{(e)}} [N]^T q\, dS = 0 \tag{5.20}$$

Equation 5.20, using Equation 3.15 can be written as shown in Equation 5.21.

$$[C^e]\left\{\dot{T}^e\right\} + [K^e]\{T^e\} = \{F^e\} \tag{5.21}$$

Where,
$[C^e] \longrightarrow$ The heat capacity matrix
$\left\{\dot{T}^e\right\} \longrightarrow$ The element conductivity matrix
$\{F^e\} \longrightarrow$ The thermal load vector

The matrix, $[C^e]$ and the vectors $\left\{\dot{T}^e\right\}$ and $\left\{\dot{T}^e\right\}$ may be obtained from equations 5.22, 5.23 and 5.24 respectively.

$$[C^e] = \rho c \int_{V^{(e)}} [N]^T [N]\, dV \tag{5.22}$$

$$[K^e] = \int_{V^{(e)}} [\nabla N]^T k\, [\nabla N]\, dV + (h_v + h_r) \int_{S^{(e)}} [N]^T [N]\, dS \tag{5.23}$$

$$\{F^e\} = \int_{V^{(e)}} [N]^T Q dV + (h_c + h_r) \int_{S^{(e)}} [N]^T T_0\, dS \tag{5.24}$$

Once the element characteristic matrices are established, element contributions will be identified. This provides an assembled matrix system for the structure so that the array of the global temperatures $\{T\}$ replaces the element arrays $\{T^e\}$ to give Equation 5.25.

$$[C]\left\{\dot{T}\right\} + [K]\{T\} = \{F\} \tag{5.25}$$

Where,
$[C] \longrightarrow$ Global heat capacity matrix
$[K] \longrightarrow$ Global heat conduction matrix
$\{F\} \longrightarrow$ Thermal load vector at the structural level
Equation 5.25 represents the spatially discretized finite element form of the transient heat conduction problem. A discretization in the time domain is carried out to arrive at the final set of algebraic equations as shown in Equation 5.26.

$$\{T\}_{n+1} = \{T\}_n + \Delta t \left[(1-\beta) \left\{ \dot{T} \right\}_n + \beta \left\{ \dot{T} \right\}_{n+1} \right] \tag{5.26}$$

Finally, an iterative expression is deduced as given in Equation 5.27.

$$\left(\frac{[C]}{\Delta t} + \beta [K] \right) \{T\} = \left(\frac{[C]}{\Delta t} + (\beta - 1) [K] \right) \{T\}_n + (1-\beta) \{F\}_n + \{F\}_{n+1} \tag{5.27}$$

Solution to Equation 5.27 provides time history of the temperature variable within the continuum. Considering the thermal properties from Eurocode.

5.4.0.4 Input Fire Idealization

Fire was simulated by defining the surface temperatures on the structural elements: beams, columns and slab of the modelled RC Frame. A rational approach was adopted to specify the surface temperatures based on experimentally obtained compartment temperatures. As explained in Chapter 4, fifteen mineral insulated thermocouples were positioned inside the compartment at three locations in plan, and at five different heights to measure the surface temperatures. The temperatures measured at each location were assigned to the surface of the member based in its proximity with respect to the thermocouple. The exposed surfaces of floor beams B1, B2 and B3 and roof beams B5, B6 and B7 in the ABAQUS model were partitioned into two zones whereas the floor beam B4 and the roof beam B8 were left un-partitioned, which corresponds to the location of three thermocouple trees in plan. The exposed surfaces of all the four columns, C1, C2, C3 and C4 were partitioned into five zones that corresponds to five depths of the thermocouples. Similarly, the slab was partitioned into three zones. The partitions fairly accurately simulated the compartment exposure conditions. Figures 5.8 (a), (b), (c) and (d) show the partitioned surfaces of various structural entities of the RC frame showing the labels of thermocouples, the history of which were assigned on to the surface.

As shown in Figure 5.8 (a), the columns C1 and C4, which were located close to the back wall of the fire compartment, shared an identical condition of exposure recorded by the thermocouple tree at location C in the compartment. The bottom most partition of the columns C1 and C4 was assigned the surface temperatures recorded by the thermocouple TMIC5. Four partitions above them were assigned the surface temperatures recorded by thermocouples TMIC4, TMIC3, TMIC2 and TMIC1 respectively. Column C2 and C3 were assigned the surface temperatures as obtained by the thermocouple trees positioned at Location A and B respectively. In the floor beam B1, the two partitions of exposed face were assigned the surface temperature recorded by the thermocouples

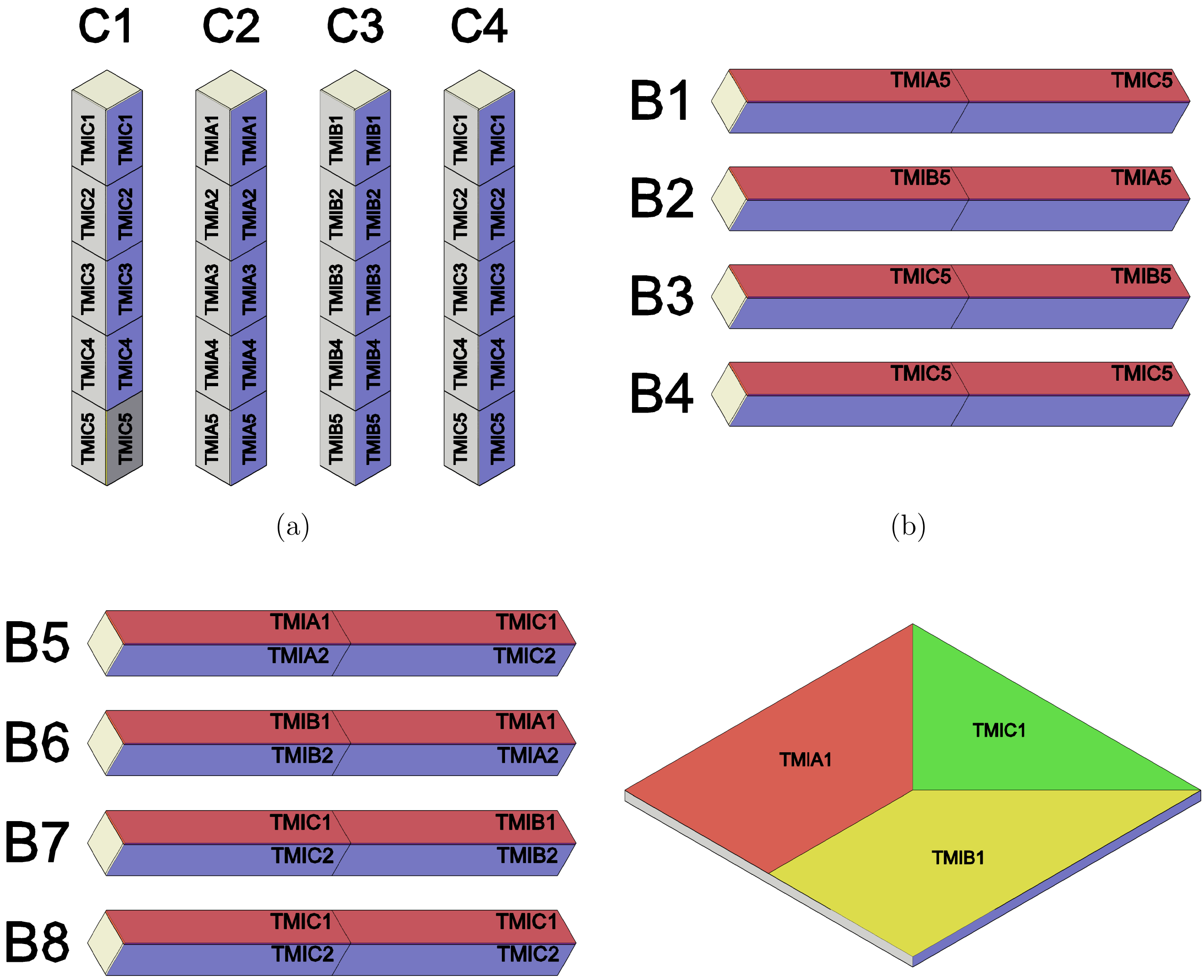

(a) (b)

(c) (d)

Fig. 5.8: Surface temperatures considered for heat transfer analysis (a) Columns (b) Floor beams (c) Roof beams (d) Slab

TMIA5 and TMIC5. Similarly, Beam B2 was assigned the surface temperatures from thermocouples TMIB5 and TMIA5, B3 from TMIC5 and TMIB5 and B4 from TMIC5 respectively. The surface temperature distribution for floor beams is shown in Figure 5.8 (b) Roof beams adopted a similar pattern of temperature allocation. However, since it had two exposed faces (soffit and side), the surface temperatures from the first layer of thermocouples (position 1) positioned at the topmost elevation in the compartment were assigned to the side face and the temperatures obtained by the layer below the topmost layer (position 2) were assigned to the soffit of the room beams, as shown in Figure 5.8 (c). The slab, as shown in Figure 5.8 (d) *(partitioned into three zones)*, was assigned the surface temperatures from thermocouples TMIA1, TMIB1 and TMIC1 recorded at the soffit inside the compartment.

5.4.0.5 Comparison of Thermal Profile of Different Structural Elements

The results obtained from the heat transfer analysis performed on the RC framed structure modelled using ABAQUS are being presented in this section. Nodal temperature histories extracted from specific locations have been compared with the experimental temperature - time curves. Broadly, it was observed that the numerically obtained results are in unison with the experimental results. However, the difference observed in the results may be attributed to a rational approach in defining the surface temperatures based on the actual temperature history obtained from the compartment during the experiment. Figures 5.9 to 5.36 show the comparison of the thermal profiles of different structural members: floor beams, roof beams and columns. The nodal location for extracting the temperature profiles were chosen to correspond to the location of thermocouples embedded in various structural elements of the full-scale RC frame tested under post-earthquake fire as given in the previous chapter. The various locations of the thermocouple may be obtained from Section 4, of Chapter 4.

Floor Beams

The temperature profiles for floor beams were generated by considering one side exposure to simulate the experimental condition where the top surface of the beam were exposed. Three locations along the length of the beam followed by three depths at each location were identified to extract temperature profiles. Nodal temperature at these prescribed locations were obtained and compared with the experimental results. Comparison of the temperature profiles obtained in beams B1, B2, B3 and B4 are shown in Figure 5.9 thru figure 5.12 respectively.

Figure 5.9 shows the comparison of temperature profiles obtained in the floor beam B1. Seven out of nine locations were compared with experimental plots. The numerically obtained temperature profiles on the Left and Mid-span sections of the beam B1 (Figures 5.9 (a)-(f)) under-predicted the temperature variation. Low peak temperatures were reported by the abaqus model. Two thermocouples on the surface, precisely on the left and mid-span section malfunctioned during fire and recorded no data. However, the temperature profiles obtained at the right section of beam B1 showed a closer match with experimental results. At depth D1, ABAQUS heat transfer analysis under-predicted the peak temperature by 27%. From Figure 5.9 (h) and (i), it is observed that the numerically obtained peak temperatures at depths D2 and D3 over-predicted the experimental result by 8% and 33% respectively. Figures 5.10 (a)-(i) show the comparison of temperature profiles of floor beam B2. Overall, in the inner-locations of the beam, the ABAQUS heat transfer analysis showed an under-prediction of results whereas near the surface *(left and mid-span section)*, an over-prediction of results was observed. The closest match obtained was 97% at the depth D2, in the left section of the beam. The temperature profiles for floor beam B3 are as shown in Figure 5.11 (a)-(i). A fairly good match of the temperature profiles are observed in beam B3. At location D3, in the left section, 96% match was registered in the peak temperature. The results exhibited a combination of an underprediction and overprediction of temperature profiles. The location close to exposed face (D3)and at the mid-point (D2) on all three sections (left/mid-span/right) slightly overpredicted the peak temperatures. Whereas, the values of peak temperature obtained from ABAQUS at location D1 shows a slight underprediction. However, on an average, 90% match of results was obtained in beam B3. Similar to beam B3, the temperature profiles in beam B4 (shown in Figure 5.12 (a)-(i)) exhibited a mixed prediction. Two of the three thermocouples mounted near the surface experienced the direct exposure to flame due to spalling. Due to this condition, they registered abnormally high temperatures. This was incomparable with the temperature profile obtained from ABAQUS. The temperature profiles at the midpoint location D2 at the mid-span and right sections showed a slight overprediction (14%) in comparison to the experimental results. The actual values of peak temperatures obtained in all four floor beams, their numerical counterparts and inference is given in Table 5.4.

Thermocouple Location	**Peak Temperature (Experimental)** °C	**Peak Temperature (ABAQUS HT)** °C	**Deviation** °C	**Comparison Inference**
TB1LD1	130	64	66	*Underpredicted*
TB1LD2	459	125	334	*Underpredicted*
TB1LD3	*0*	*329*	-	*No Result*
TB1MD1	320	75	245	*Underpredicted*
TB1MD2	464	145	318	*Underpredicted*
TB1MD3	*0*	*566*	-	*No Result*
TB1RD1	99	72	27	*Underpredicted*
TB1RD2	133	143	-11	*Overpredicted*
TB1RD3	299	398	-98	*Overpredicted*
TB2LD1	126	68	58	*Underpredicted*
TB2LD2	133	129	4	*Underpredicted*
TB2LD3	404	553	-149	*Overpredicted*
TB2MD1	153	66	86	*Underpredicted*
TB2MD2	159	125	34	*Underpredicted*
TB2MD3	355	464	-109	*Overpredicted*
TB2RD1	205	48	156	*Underpredicted*
TB2RD2	216	88	128	*Underpredicted*
TB2RD3	485	338	147	*Underpredicted*
TB3LD1	70	52	17	*Underpredicted*
TB3LD2	*9*	*98*	-	*No Result*
TB3LD3	270	260	10	*Underpredicted*
TB3MD1	82	63	19	*Underpredicted*
TB3MD2	109	118	-9	*Overpredicted*
TB3MD3	307	402	-95	*Overpredicted*
TB3RD1	73	65	8	*Underpredicted*
TB3RD2	91	126	-35	*Overpredicted*
TB3RD3	198	334	-136	*Overpredicted*
TB4LD1	*0*	*65*	-	*No Result*
TB4LD2	420	126	294	*Underpredicted*
TB4LD3	1154	534	619	*Underpredicted*
TB4MD1	81	505	-424	*Overpredicted*
TB4MD2	110	134	-24	*Overpredicted*
TB4MD3	924	505	419	*Underpredicted*
TB4RD1	74	58	16	*Underpredicted*
TB4RD2	101	109	-7	*Overpredicted*
TB4RD3	297	448	-152	*Overpredicted*

Tab. 5.4: Comparison of peak temperatures in the floor beams B1, B2, B3 and B4

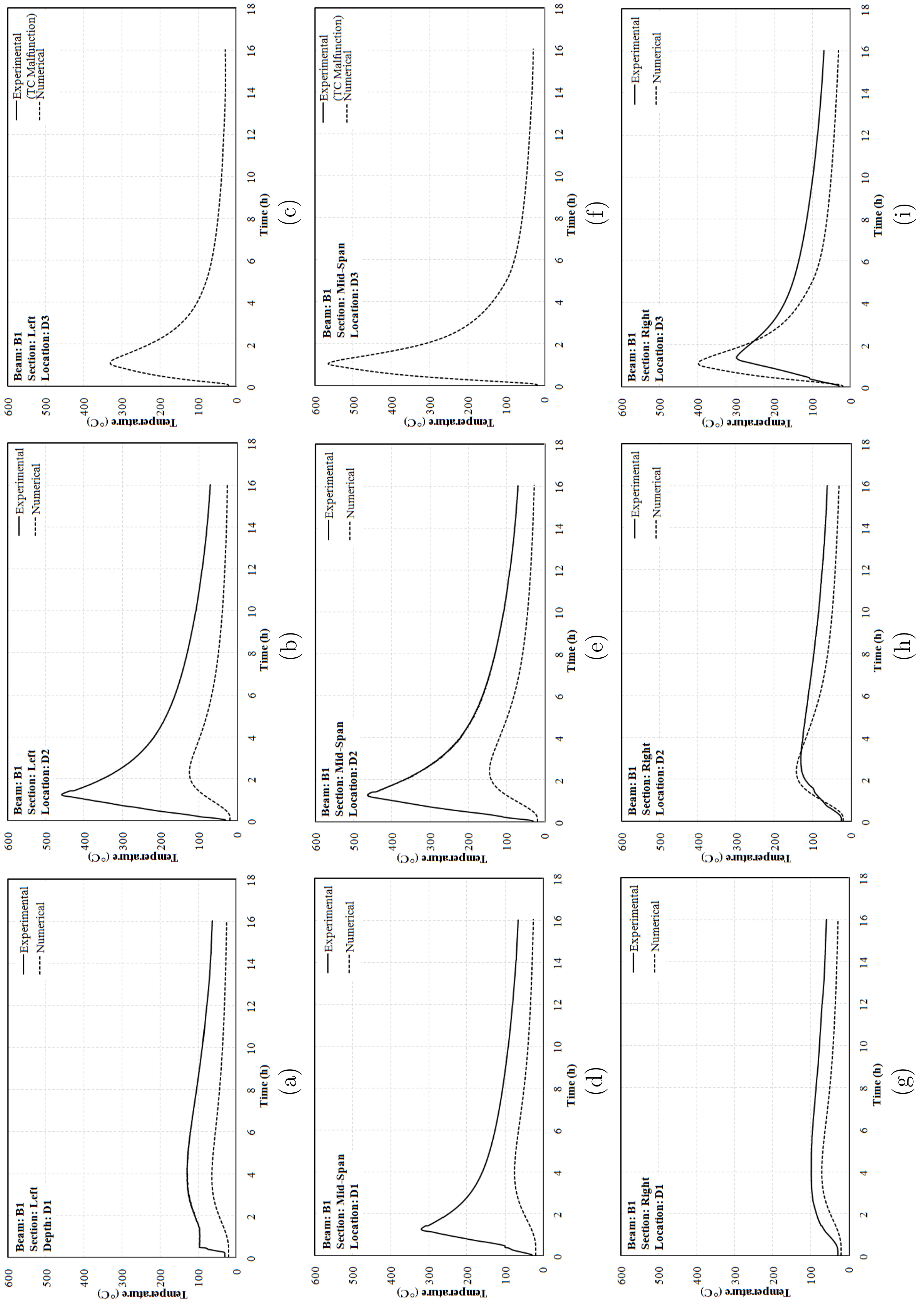

Fig. 5.9: Comparison of thermal profile for beam B1 (a) Left, D1 (b) Left, D2 (c) Left, D3 (d) Mid-Span, D1 (e) Mid-Span, D2 (f) Mid-Span, D3 (g) Right, D1 (h) Right, D2 (i) Right, D3

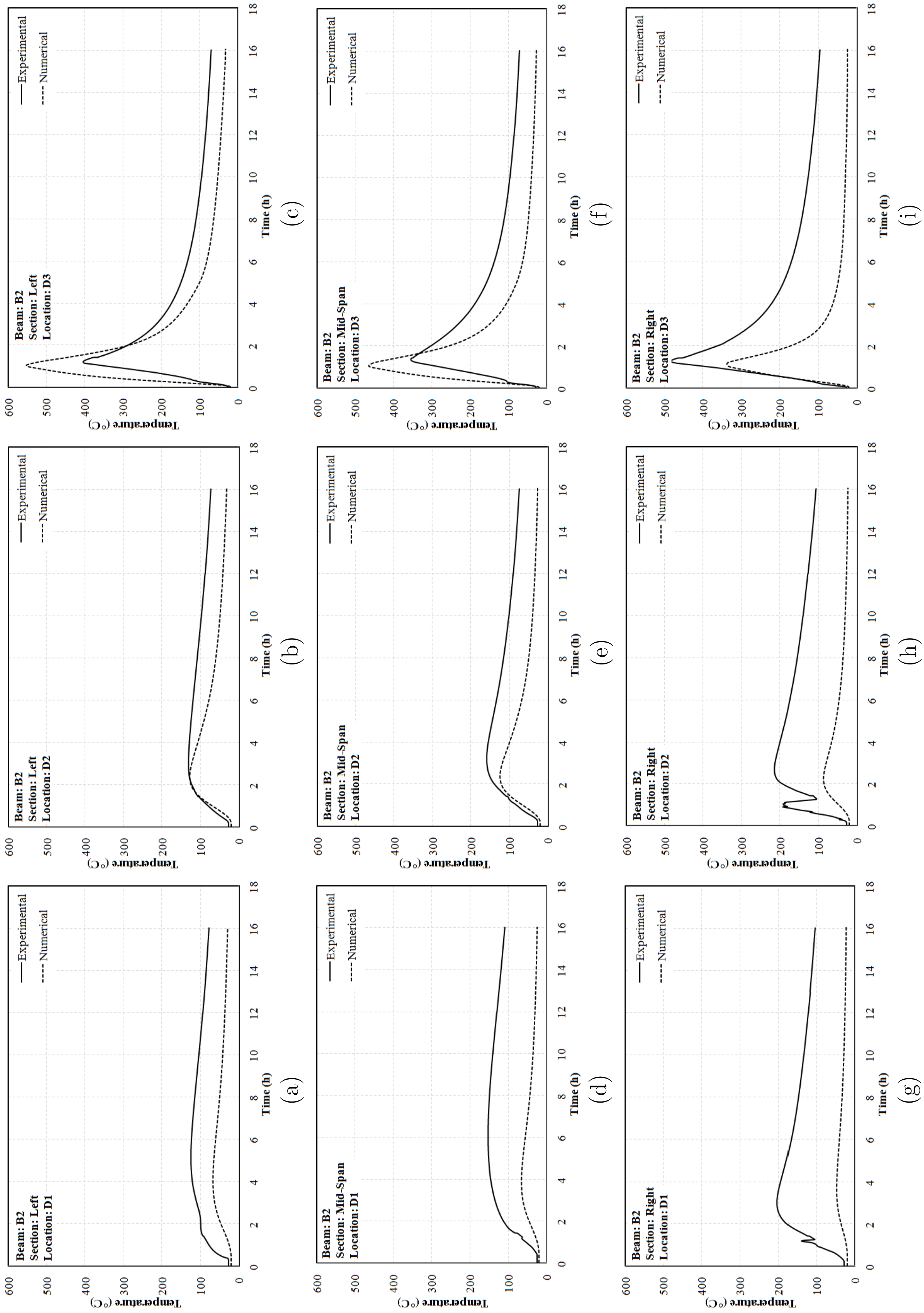

Fig. 5.10: Comparison of thermal profile for beam B2 (a) Left, D1 (b) Left, D2 (c) Left, D3 (d) Mid-Span, D1 (e) Mid-Span, D2 (f) Mid-Span, D3 (g) Right, D1 (h) Right, D2 (i) Right, D3

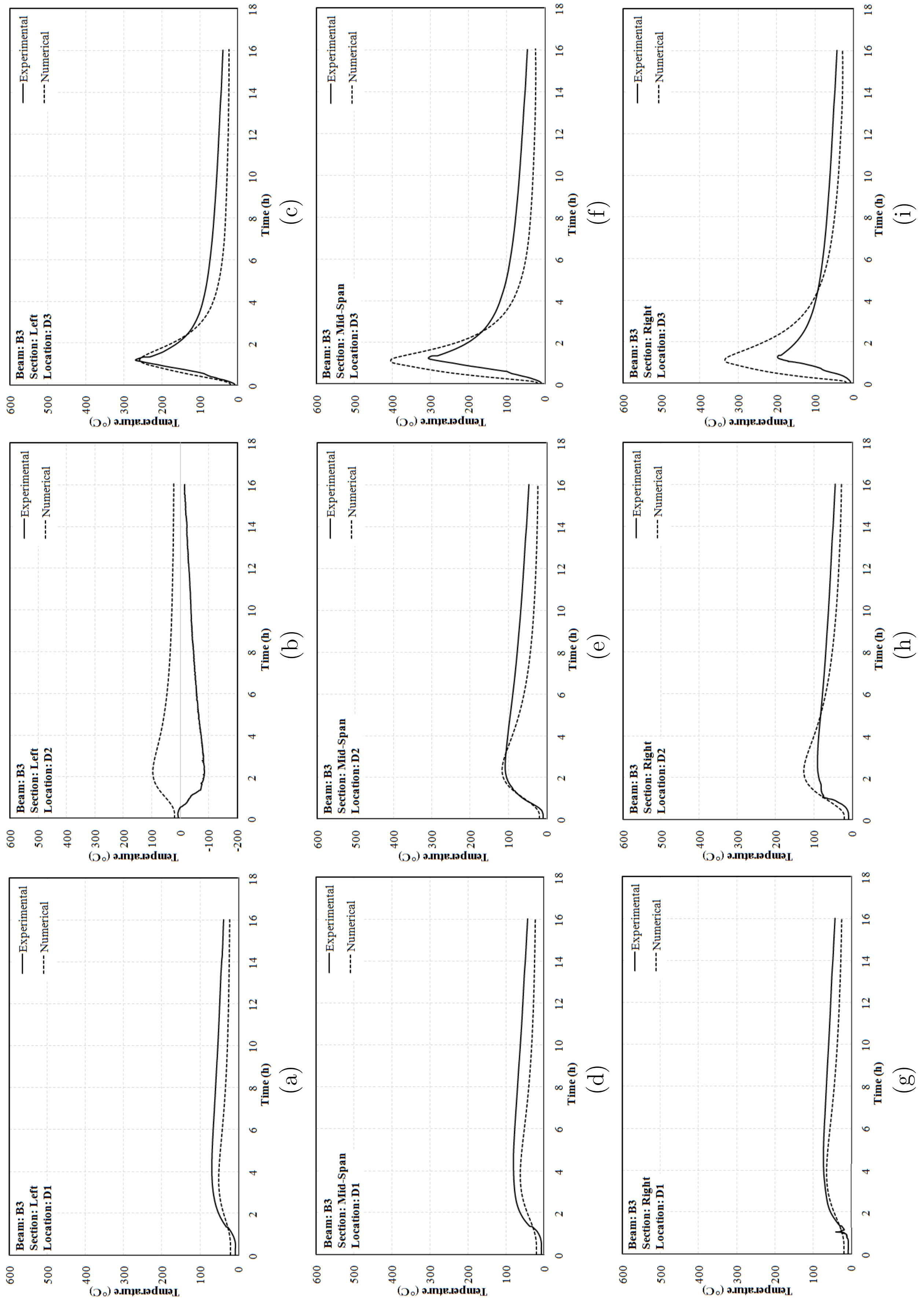

Fig. 5.11: Comparison of thermal profile for beam B3 (a) Left, D1 (b) Left, D2 (c) Left, D3 (d) Mid-Span, D1 (e) Mid-Span, D2 (f) Mid-Span, D3 (g) Right, D1 (h) Right, D2 (i) Right, D3

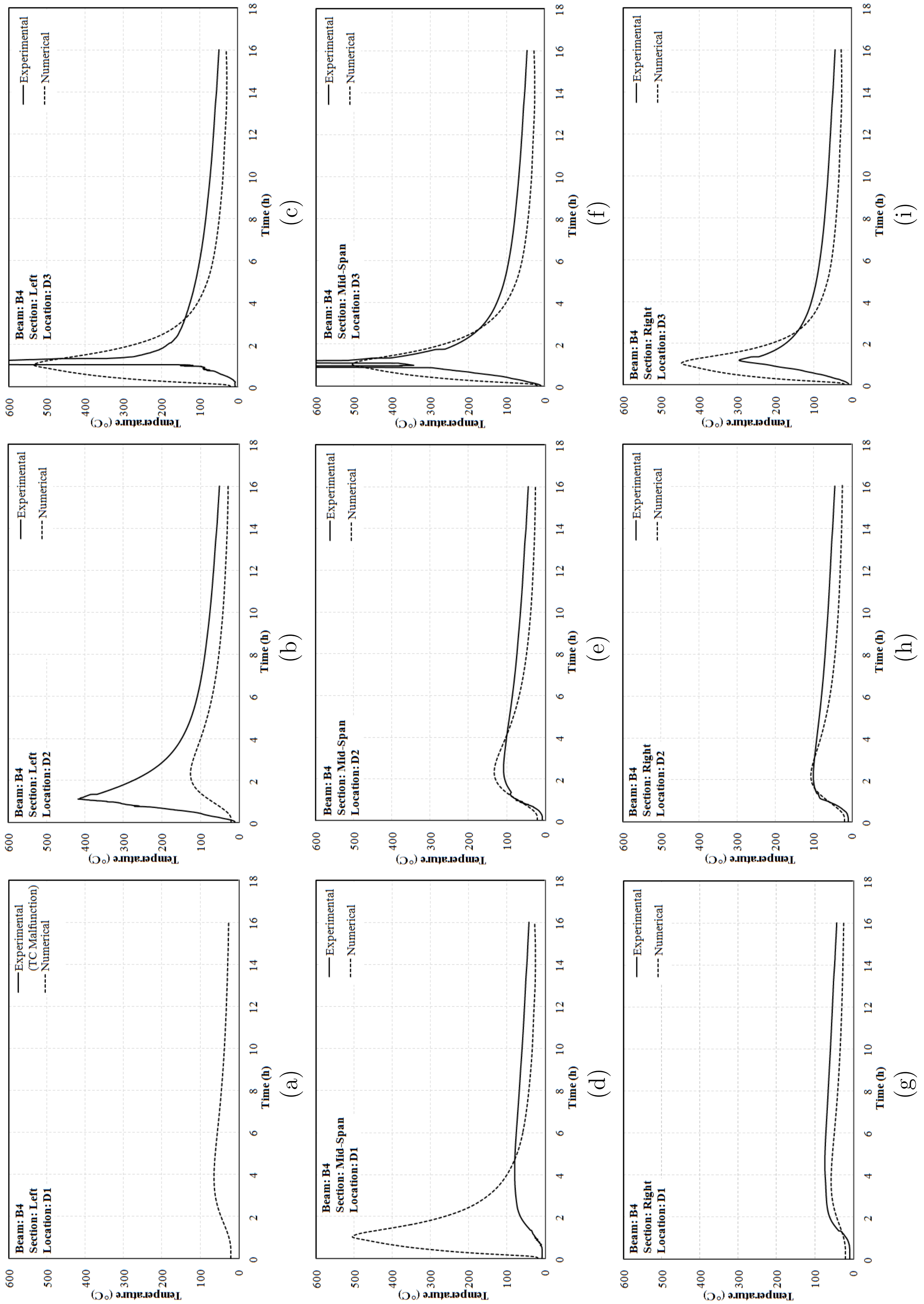

Fig. 5.12: Comparison of thermal profile for beam B4 (a) Left, D1 (b) Left, D2 (c) Left, D3 (d) Mid-Span, D1 (e) Mid-Span, D2 (f) Mid-Span, D3 (g) Right, D1 (h) Right, D2 (i) Right, D3

Roof Beams

All roof beams (B5, B6, B7 and B8) had two sides exposed to fire. The temperatures were recorded both along the width and across the depth of the beam by embedded thermocouples in the experimental frame sub-assemblage. In ABAQUS heat transfer analysis, the nodal temperature analogous to the thermocouple location were obtained and compared against the experimental results. Comparison of the temperature profiles obtained in beam B5 are shown in Figures 5.13 thru 5.24 respectively. Figure 5.13 (a)-(e) shows the comparison of temperature profiles for roof beam B5 at left section. The locations D3 and B2 were close to the exposed surface and have reported higher temperatures (489 °C and 556 °C). However, the ABAQUS values for peak temperature have shown a significant difference from experimental values (578 °C and 326 °C). The value of peak temperature at location D2, i.e., at the midpoint obtained from ABAQUS overpredicted the result by 65% and 59%. The value of peak temperatures at locations D1 and B1 showed a 89% and 96% match with experimental values respectively. Similarly, in beam B5 at mid-point section (shown in Figure 5.14 (a)-(e)), maximum temperatures were reported at locations B2 (308 °C) and D3 (436 °C), which were deviant from experimentally obtained values of peak temperatures (273 °C and 434 °C). At mid-point location (D2), the peak temperature obtained from ABAQUS was overestimated. At locations B1 and D1, close to the unexposed face, lower value of peak temperatures were obtained. However, the values were 21% low and 31% high than the experimentally obtained values respectively. Figure 5.15 (a)-(e) shows the temperature profiles at the right section of roof beam B5. It is observed that the value of peak temperatures obtained shows a mixed response. The locations B2 and D3, close to the exposed surface showed a maximum value of peak temperature in the member(415 °C and 410 °C). These values were 33% higher and 21% lower than the experimental values recorded. The value of peak temperature was found to be 59% higher than the experimental value. In locations B1 and D1, the values of peak temperature obtained by ABAQUS were underpredicted by 13% and 20% respectively. Figures 5.16 (a-e) to 5.18 (a-e) shows the comparison of temperature profiles for roof beam B6 at left, midspan and right sections respectively. The temperature profiles obtained for the left section of beam B6 highly overpredict the peak temperatures at different locations as shown in figure 5.16 (a)-(e). This is presumably due to the idealization of input fire in the compartment as opposed by the direction of actual fire. Figures 5.17 (a)-(i) shows the comparison of temperature profiles obtained in the mid-span section of beam B6. It is found that the ABAQUS underpredicts the value of peak temperatures. At locations B2 and D3 (Figures 5.17 (b) and (e)), the deviant behaviour is attributed to the inconsistency of experimentally obtained values of peak temperature due to spalling of cover concrete exposing the thermocouple to direct fire. Moreover, the temperature profiles in the right section of beam B6 overpredicts the peak temperatures, which is evident from Figures 5.18 (a)-(e). However, at location B2, the experimental value superseded the ABAQUS-obtained value due to cover concrete spalling. Table 5.5 shows the comparison of peak temperature values obtained using abaqus with the peak temperature values recorded by thermocouples in the experiment for roof beams B5 and B6.

Thermocouple Location	**Peak Temperature (Experimental)** °C	**Peak Temperature (ABAQUS HT)** °C	**Deviation** °C	**Comparison Inference**
TB5LB1	122	115	7	*Underpredicted*
TB5LB2	578	489	89	*Underpredicted*
TB5LD1	113	101	12	*Underpredicted*
TB5LD2	144	243	-99	*Overpredicted*
TB5LD3	326	556	-230	*Overpredicted*
TB5MB1	119	93	26	*Underpredicted*
TB5MB2	273	436	-164	*Overpredicted*
TB5MD1	113	156	-42	*Overpredicted*
TB5MD2	143	192	-49	*Overpredicted*
TB5MD3	434	308	126	*Underpredicted*
TB5RB1	151	131	20	*Underpredicted*
TB5RB2	310	415	-105	*Overpredicted*
TB5RD1	140	113	28	*Underpredicted*
TB5RD2	168	267	-100	*Overpredicted*
TB5RD3	521	410	111	*Underpredicted*
TB6LB1	0	128	-128	*Overpredicted*
TB6LB2	92	448	-356	*Overpredicted*
TB6LD1	86	112	-26	*Overpredicted*
TB6LD2	115	263	-148	*Overpredicted*
TB6LD3	276	432	-156	*Overpredicted*
TB6MB1	289	149	140	*Underpredicted*
TB6MB2	1287	457	830	*Underpredicted*
TB6MD1	*0*	*131*	*-131*	*No Result*
TB6MD2	119	291	-171	*Overpredicted*
TB6MD3	1255	374	880	*Underpredicted*
TB6RB1	32	124	-92	*Overpredicted*
TB6RB2	722	420	302	*Underpredicted*
TB6RD1	116	178	-62	*Overpredicted*
TB6RD2	89	252	-163	*Overpredicted*
TB6RD3	262	416	-154	*Overpredicted*

Tab. 5.5: Comparison of peak temperatures in the roof beams B5 and B6

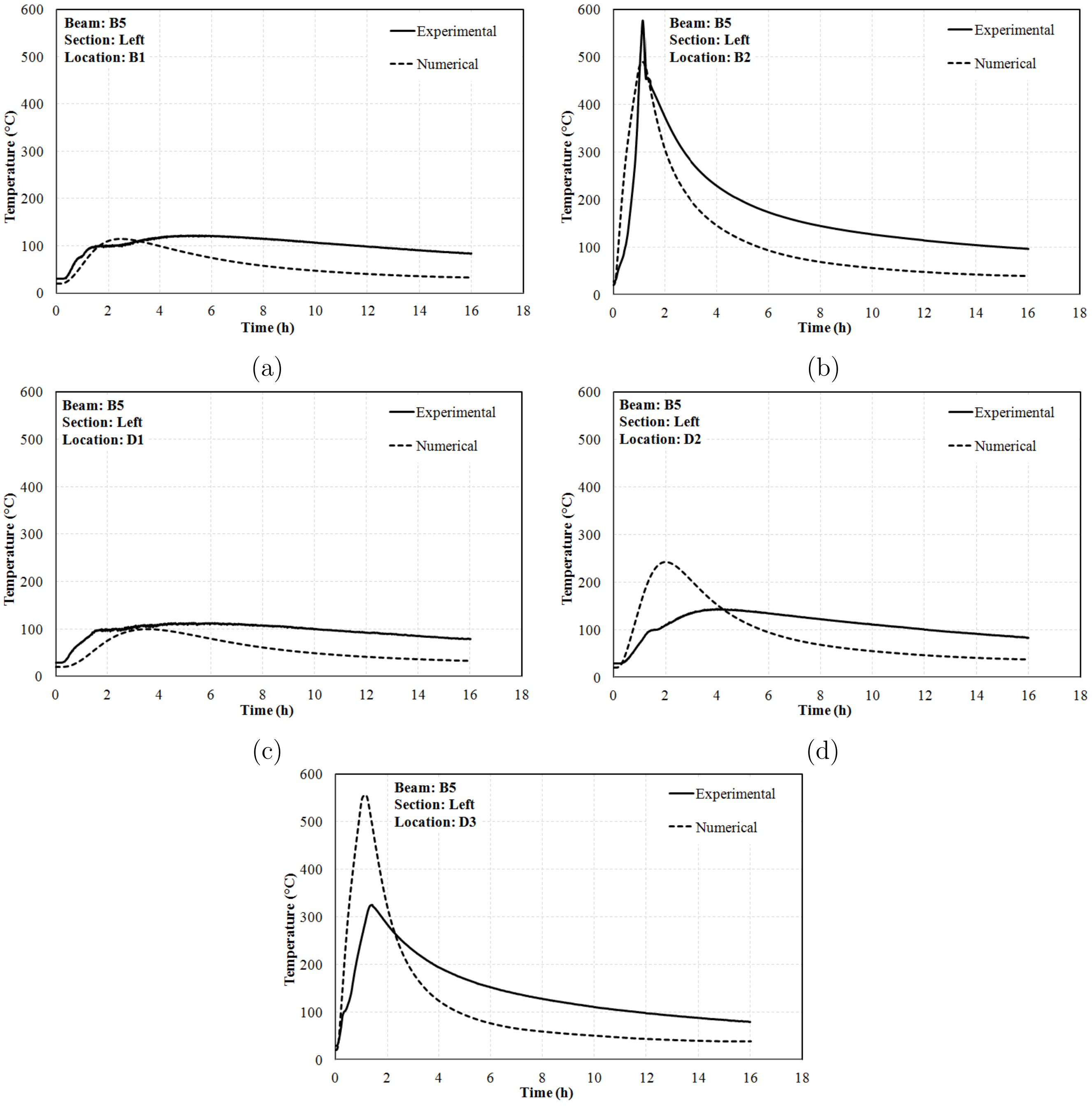

(a) (b) (c) (d) (e)

Fig. 5.13: Comparison of thermal profile for beam B5 (a) Left, B1 (b) Left, B2 (c) Left, D1 (d) Left, D2 (e) Left, D3

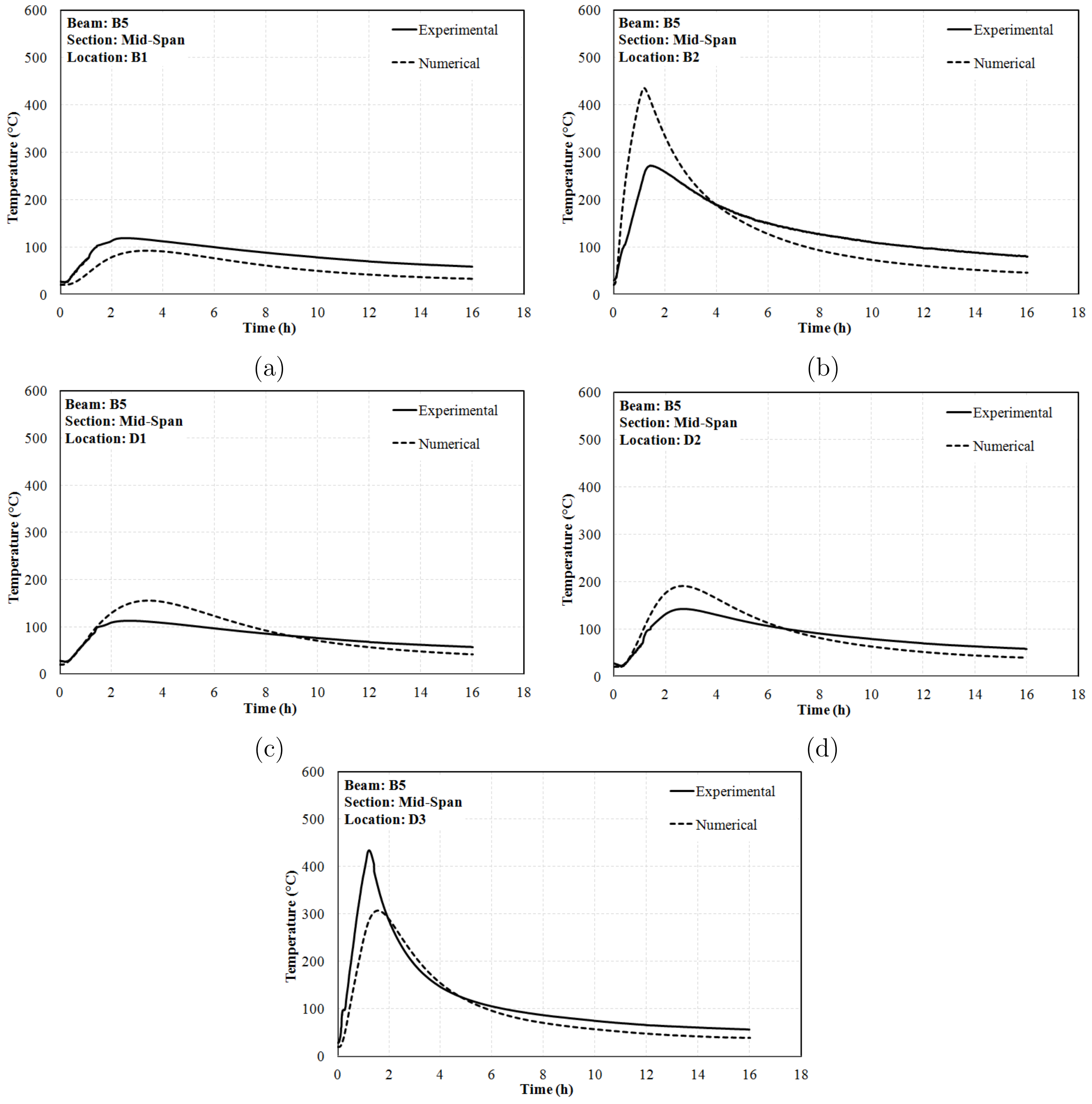

(a)

(b)

(c)

(d)

(e)

Fig. 5.14: Comparison of thermal profile for beam B5 (a) Mid-Span, B1 (b) Mid-Span, B2 (c) Mid-Span, D1 (d) Mid-Span, D2 (e) Mid-Span, D3

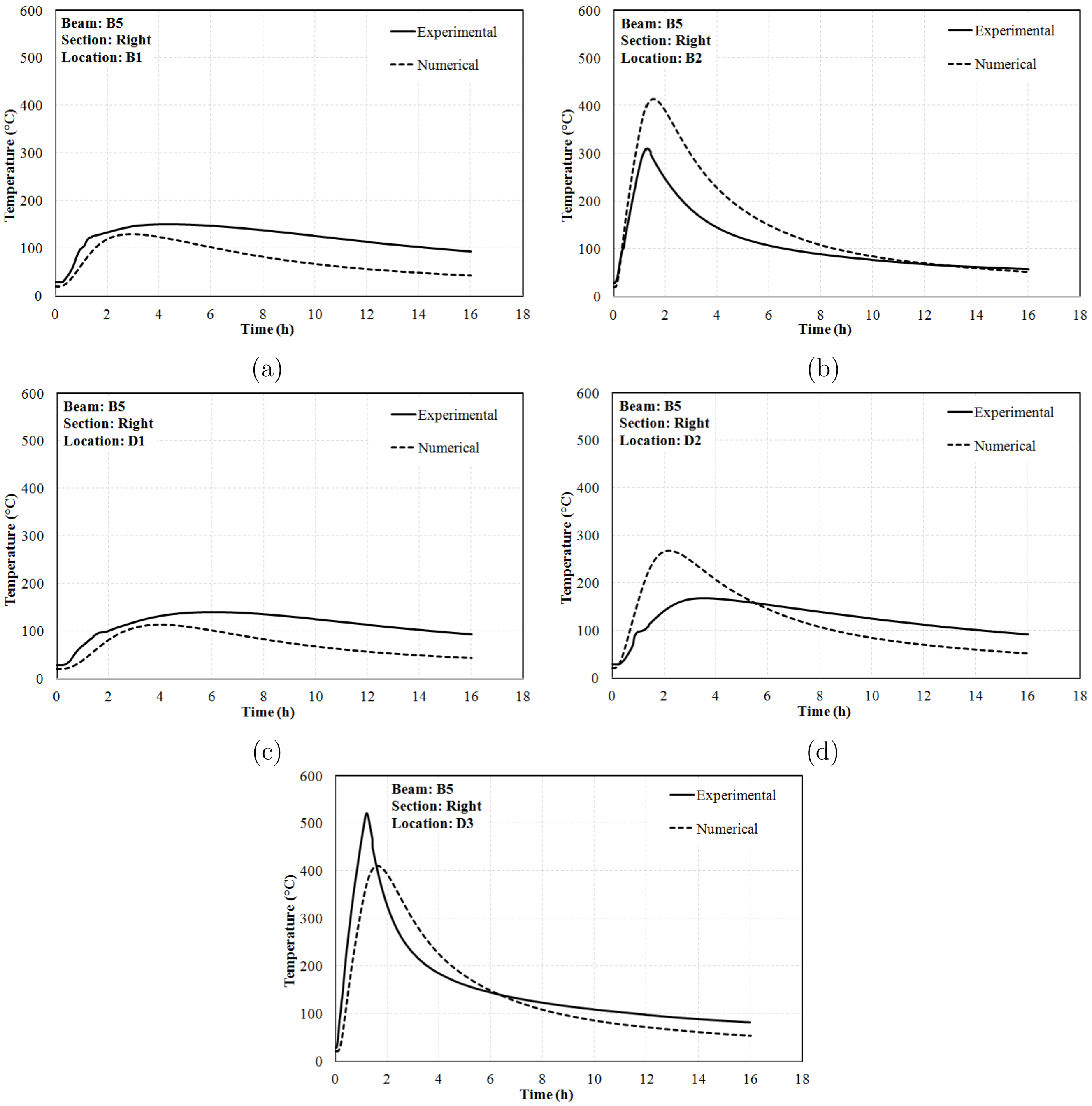

(a)

(b)

(c)

(d)

(e)

Fig. 5.15: Comparison of thermal profile for beam B5 (a) Right, B1 (b) Right, B2 (c) Right, D1 (d) Right, D2 (e) Right, D3

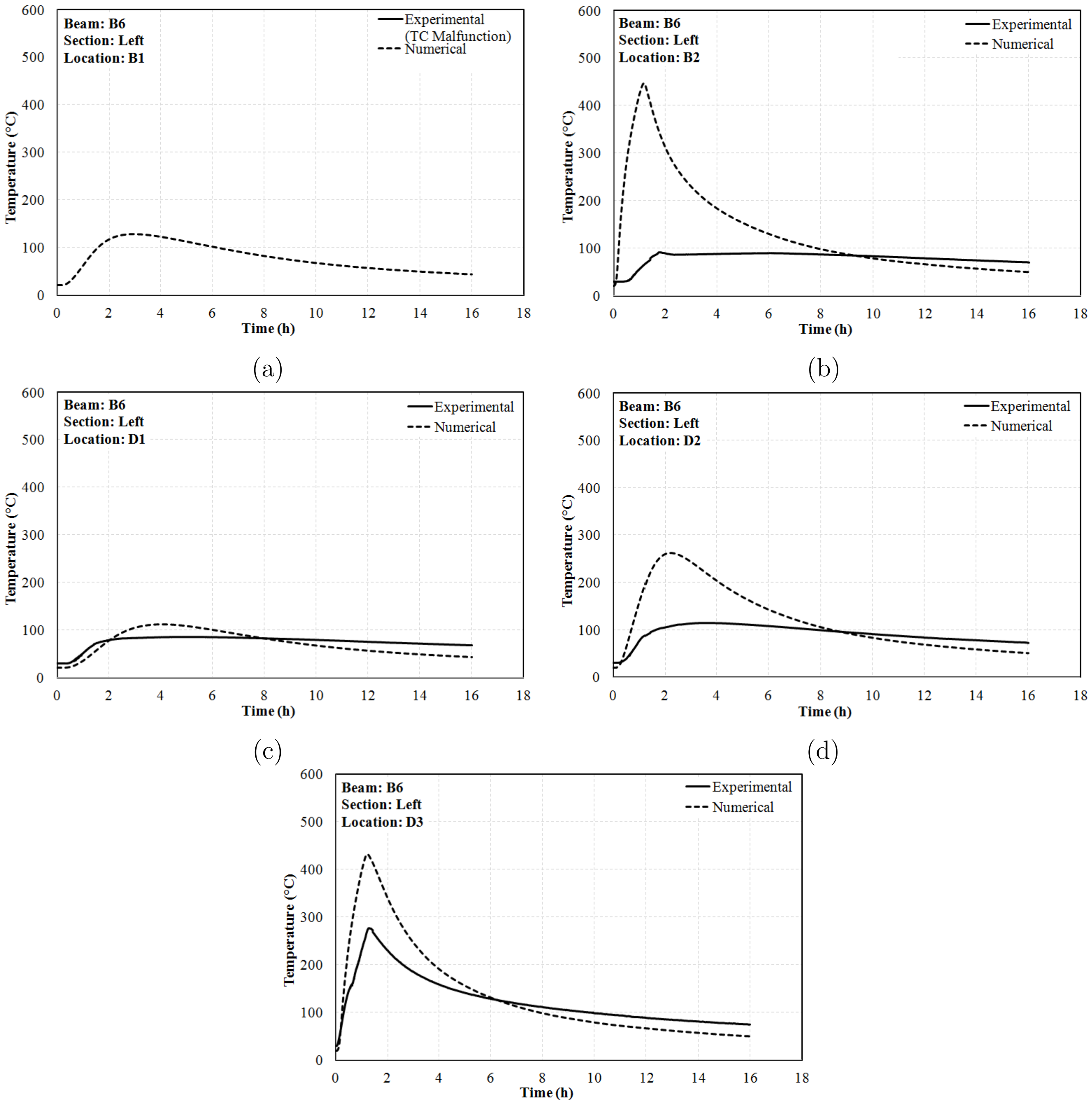

(a) (b) (c) (d) (e)

Fig. 5.16: Comparison of thermal profile for beam B6 (a) Left, B1 (b) Left, B2 (c) Left, D1 (d) Left, D2 (e) Left, D3

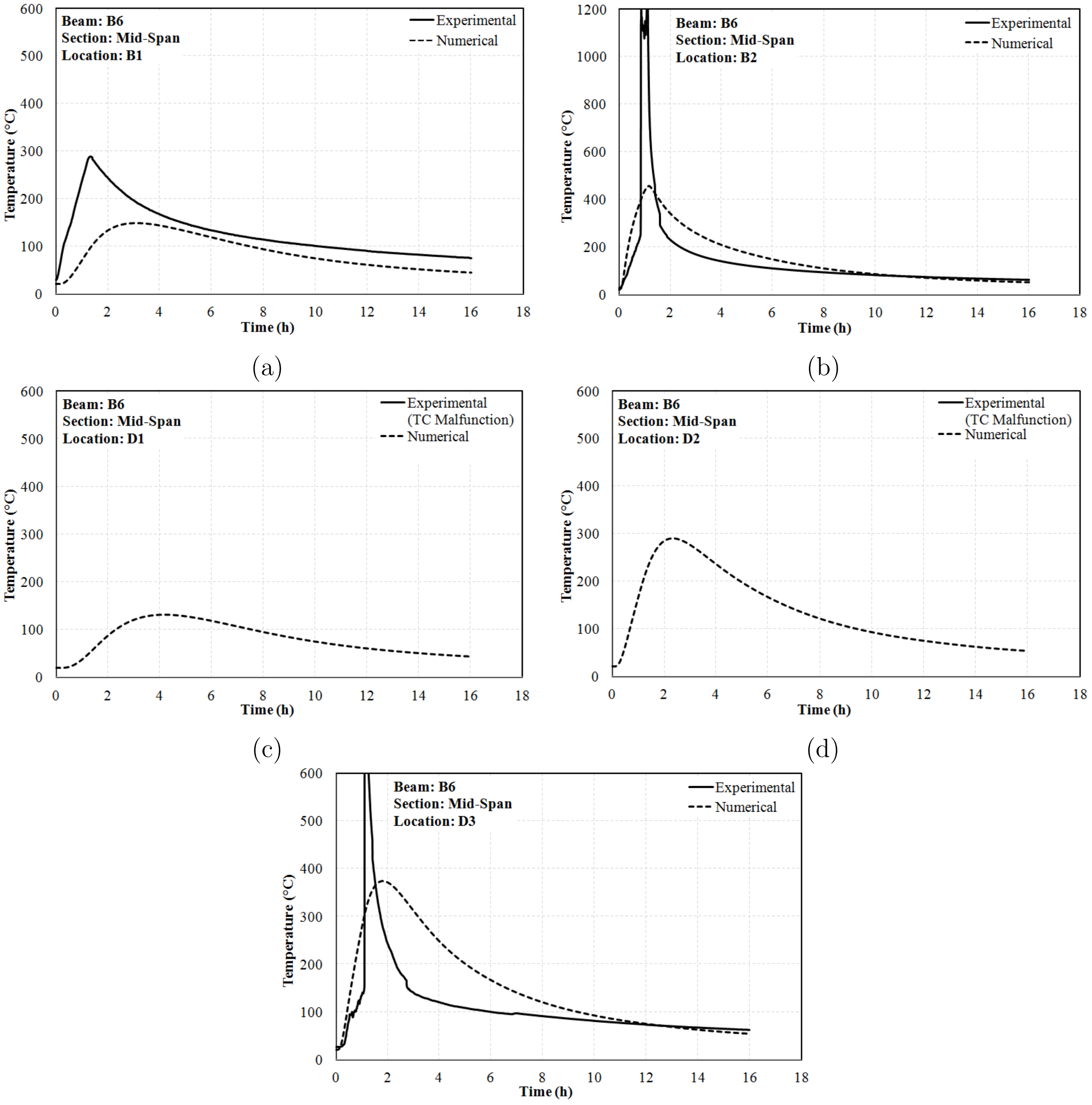

(a) (b) (c) (d) (e)

Fig. 5.17: Comparison of thermal profile for beam B6 (a) Mid-Span, B1 (b) Mid-Span, B2 (c) Mid-Span, D1 (d) Mid-Span, D2 (e) Mid-Span, D3

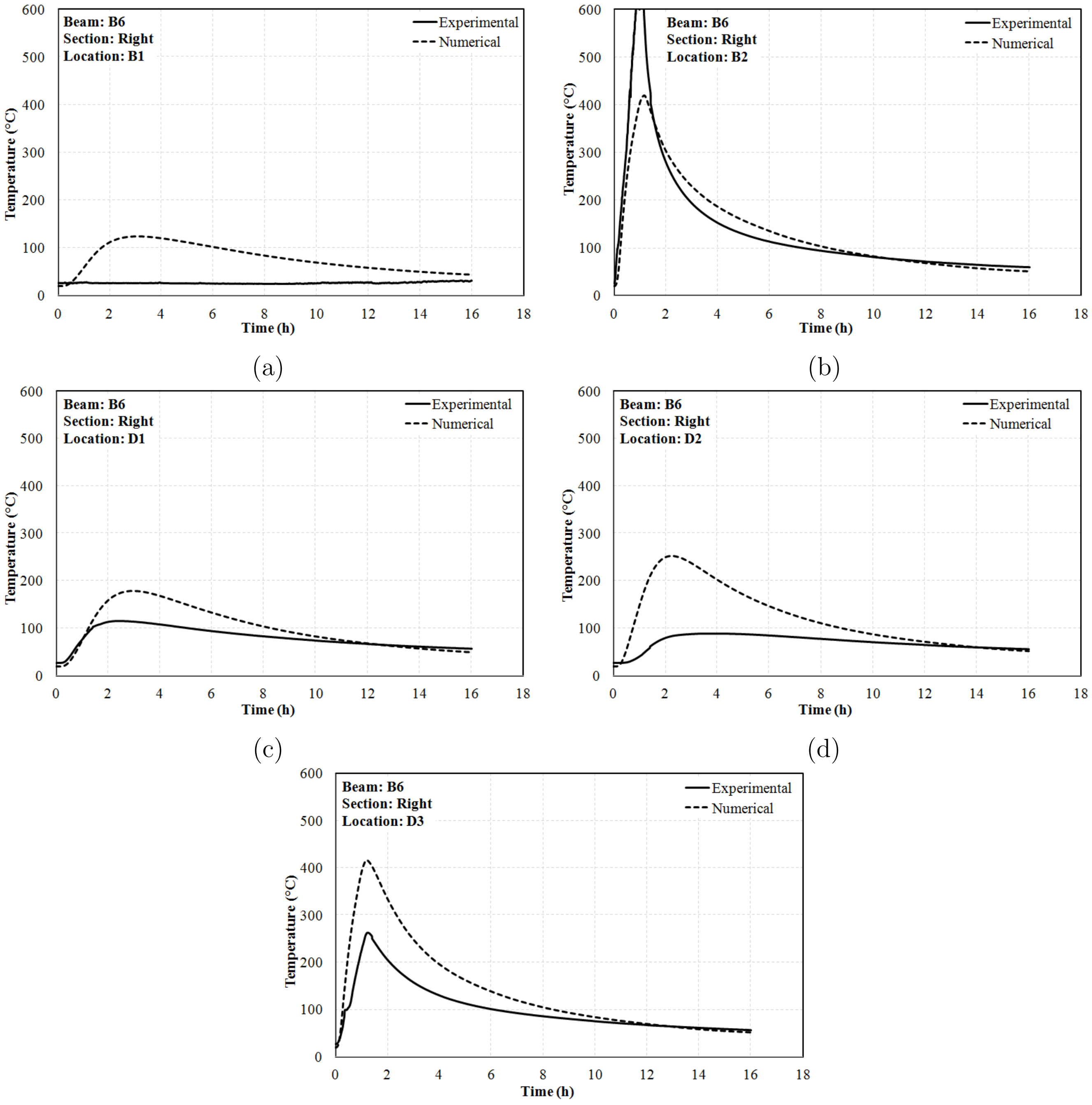

(a) (b) (c) (d) (e)

Fig. 5.18: Comparison of thermal profile for beam B6 (a) Right, B1 (b) Right, B2 (c) Right, D1 (d) Right, D2 (e) Right, D3

Figures 5.19, 5.20 and 5.21 show the comparison of the temperature profiles for roof beam B7 at left, mid-span and right sections respectively. In the right section, a good match of results was obtained at locations B1, B2 and D1, where an average deviation of 6% was observed. However, at locations D2 and D3, the ABAQUS heat transfer analysis seemed to overpredict the value of peak temperatures. At mid-span section, the temperature histories obtained were as shown in Figure 5.20 (a)-(i). It is observed that the ABAQUS-obtained temperature profiles have registered a very good match with experimental results. Maximum temperatures obtained in the heat transfer analysis were at locations B2 (444 °C) and D3 (519 °C). They were close to the experimentally obtained values of 468 °C and 519 °C. The temperature profiles for beam B7 at right section exhibited a mixed response in comparison with experimental values. The values were underpredicted at locations B1 and B2, sightly overpredicted at Location D1, 27% higher than experimental value at D2 and the closest (97%) and highest, with a value of 536 °C at D3.

In case of roof beam B8, ABAQUS heat transfer analysis slightly underpredicted the value of peak temperatures at different locations as observed in Figures 5.22, 5.23 and 5.24. At left section, a closer match was observed at Figure 5.22 (c) and Figure 5.22 (d), where the value of peak stress was 22% lower and 20% higher than the experimentally obtained values. At locations B1 and D3, the values were quite underpredicted. Figure 5.23 (a)-(e) shows the comparison of temperature profiles for mid-span section of beam B8. It is observed that a close match of peak temperature value (267 °C) is obtained at mid-point of this section. At the right section, a fairly good match of 88% is obtained at the locations B2 and D3, which were close to the exposed surface. Also, a peak temperature value of 97 °C was obtained using ABAQUS in comparison with the thermocouple value of 107 °C at location D1, which was close to the unexposed face of the beam. The value of peak temperatures obtained at different locations in the roof beams B7 and B8 are as given in Table 5.6.

Thermocouple Location	**Peak Temperature (Experimental)** °C	**Peak Temperature (ABAQUS HT)** °C	**Deviation** °C	**Comparison Inference**
TB7LB1	116	126	-9	*Overpredicted*
TB7LB2	298	299	0	*Overpredicted*
TB7LD1	99	110	-11	*Overpredicted*
TB7LD2	114	255	-140	*Overpredicted*
TB7LD3	234	387	-154	*Overpredicted*
TB7MB1	*0*	*163*	-	*No Result*
TB7MB2	468	444	24	*Underpredicted*
TB7MD1	148	149	-1	*Overpredicted*
TB7MD2	230	283	-53	*Overpredicted*
TB7MD3	519	519	0	*Underpredicted*
TB7RB1	194	114	80	*Underpredicted*
TB7RB2	614	368	247	*Underpredicted*
TB7RD1	112	116	-4	*Overpredicted*
TB7RD2	189	241	-51	*Overpredicted*
TB7RD3	553	536	17	*Underpredicted*
TB8LB1	261	113	149	*Underpredicted*
TB8LB2	*0*	*420*	-	*No Result*
TB8LD1	124	97	28	*Underpredicted*
TB8LD2	199	239	-40	*Overpredicted*
TB8LD3	600	426	175	*Underpredicted*
TB8MB1	337	131	206	*Underpredicted*
TB8MB2	622	386	236	*Underpredicted*
TB8MD1	159	114	45	*Underpredicted*
TB8MD2	263	267	-4	*Overpredicted*
TB8MD3	*0*	*352*	-	*No Result*
TB8RB1	324	112	211	*Underpredicted*
TB8RB2	479	421	59	*Underpredicted*
TB8RD1	107	97	9	*Underpredicted*
TB8RD2	179	238	-59	*Overpredicted*
TB8RD3	473	415	59	*Underpredicted*

Tab. 5.6: Comparison of peak temperatures in the roof beams B7 and B8

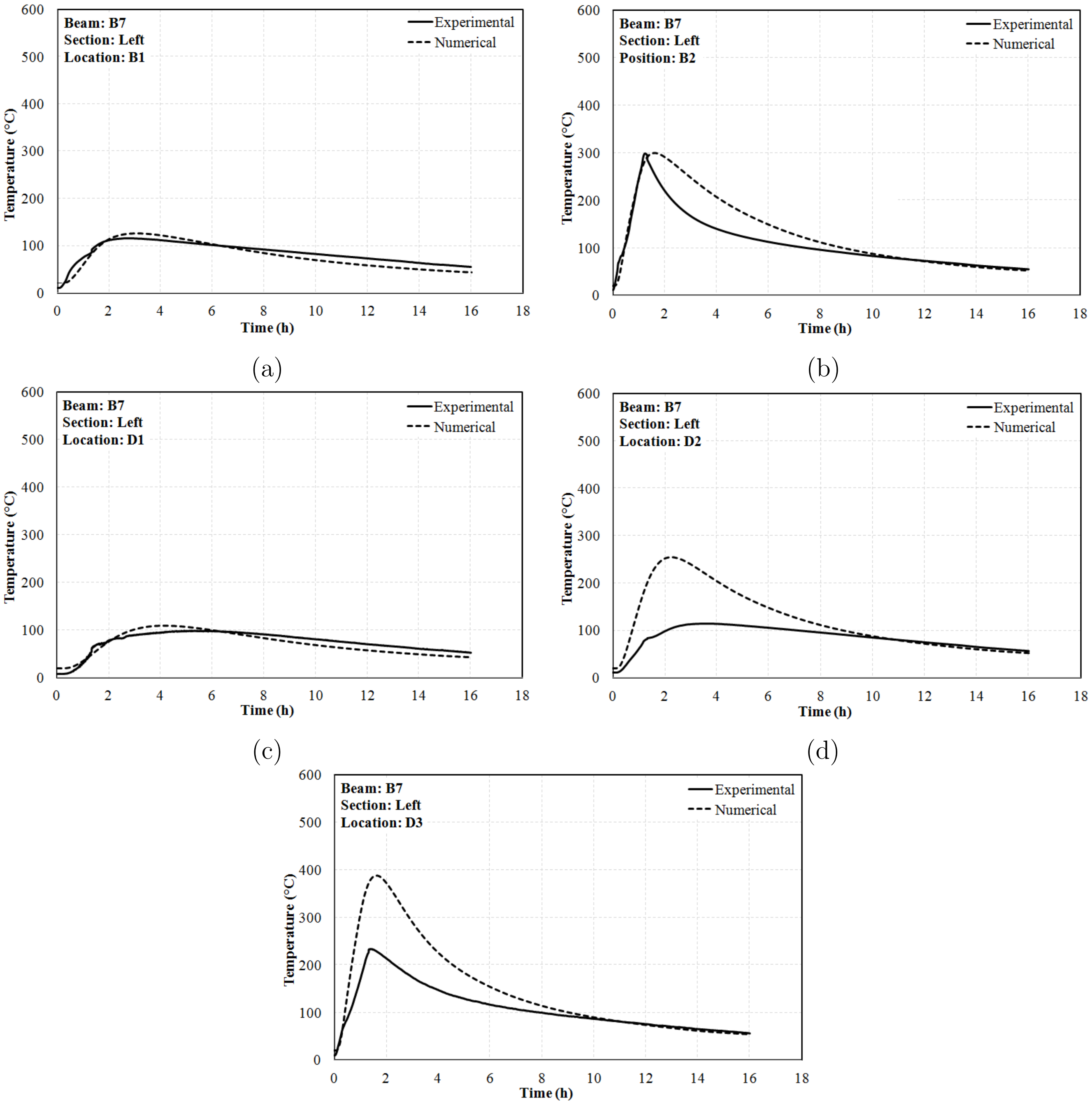

(a) (b)

(c) (d)

(e)

Fig. 5.19: Comparison of thermal profile for beam B7 (a) Left, B1 (b) Left, B2 (c) Left, D1 (d) Left, D2 (e) Left, D3

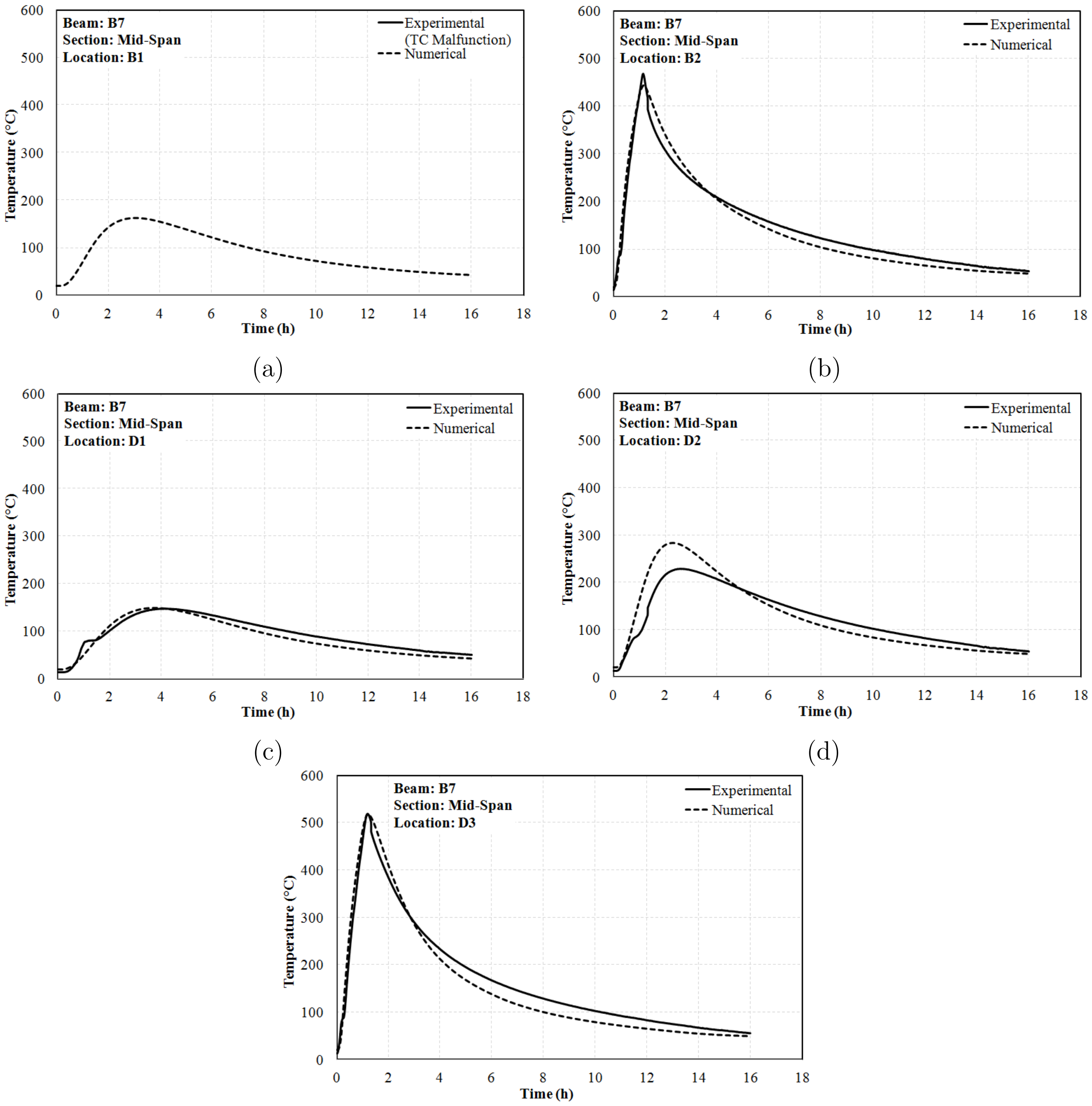

(a) (b) (c) (d) (e)

Fig. 5.20: Comparison of thermal profile for beam B7 (a) Mid-Span, B1 (b) Mid-Span, B2 (c) Mid-Span, D1 (d) Mid-Span, D2 (e) Mid-Span, D3

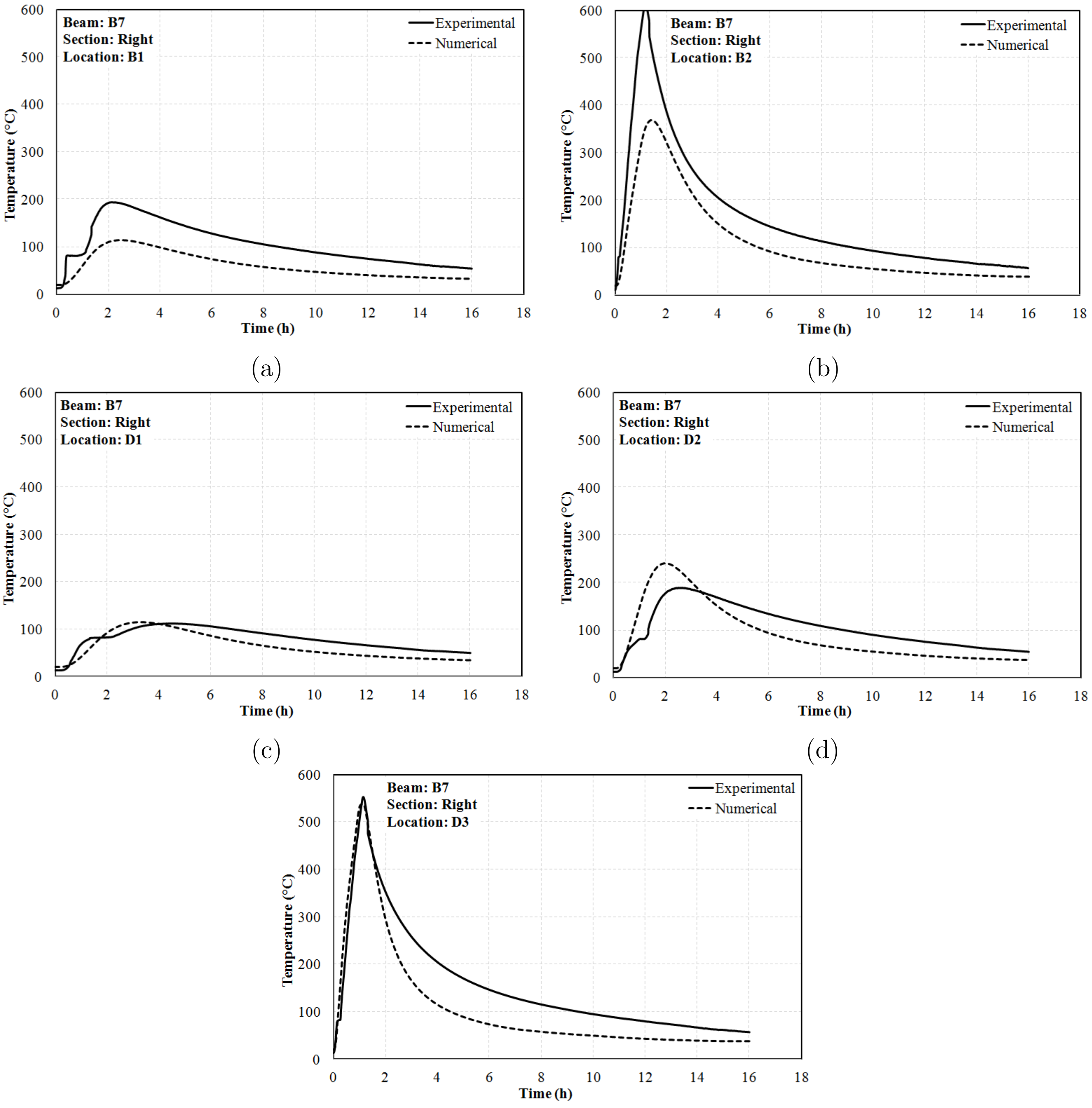

(a)

(b)

(c)

(d)

(e)

Fig. 5.21: Comparison of thermal profile for beam B7 (a) Right, B1 (b) Right, B2 (c) Right, D1 (d) Right, D2 (e) Right, D3

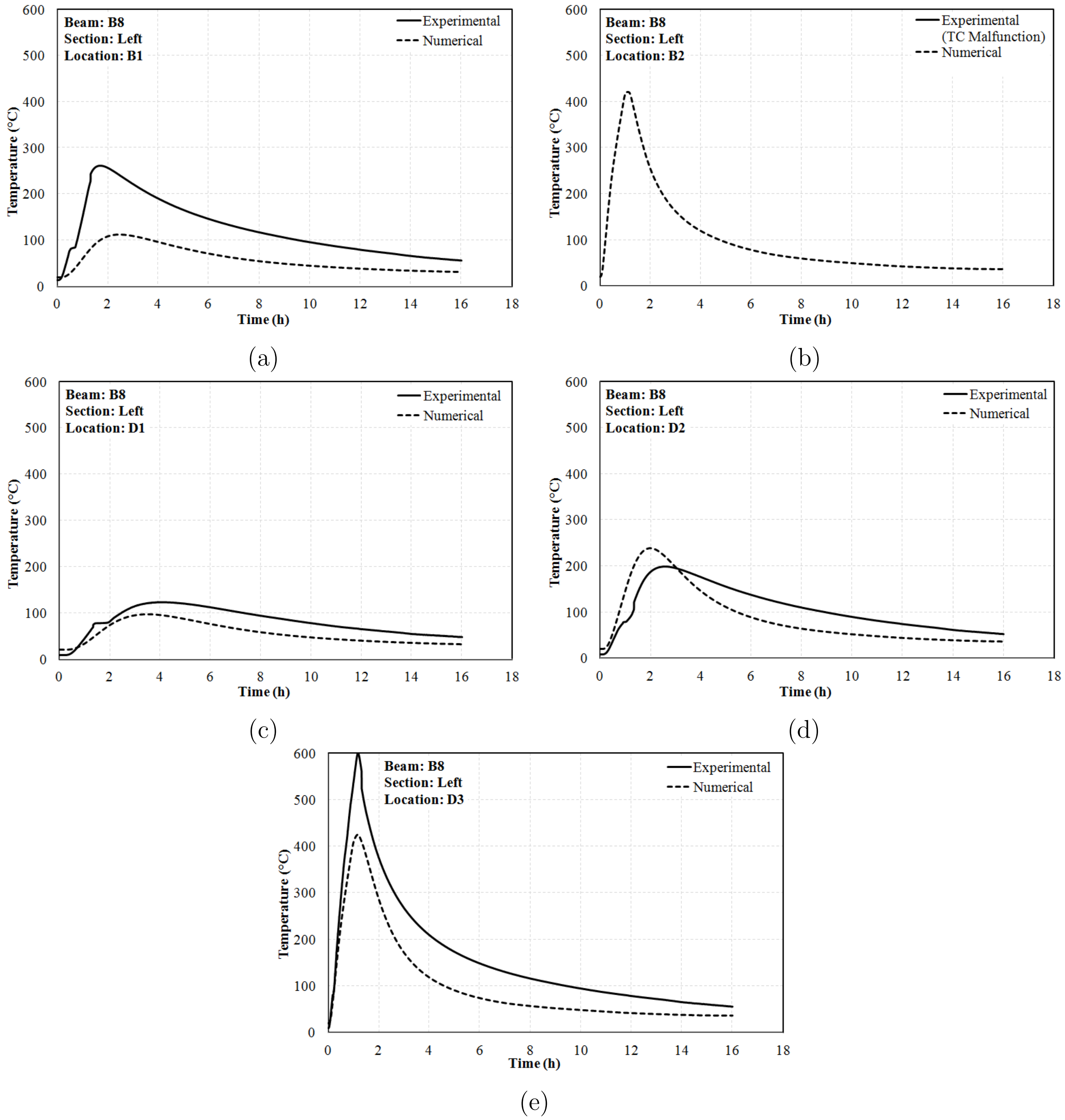

Fig. 5.22: Comparison of thermal profile for beam B8 (a) Left, B1 (b) Left, B2 (c) Left, D1 (d) Left, D2 (e) Left, D3

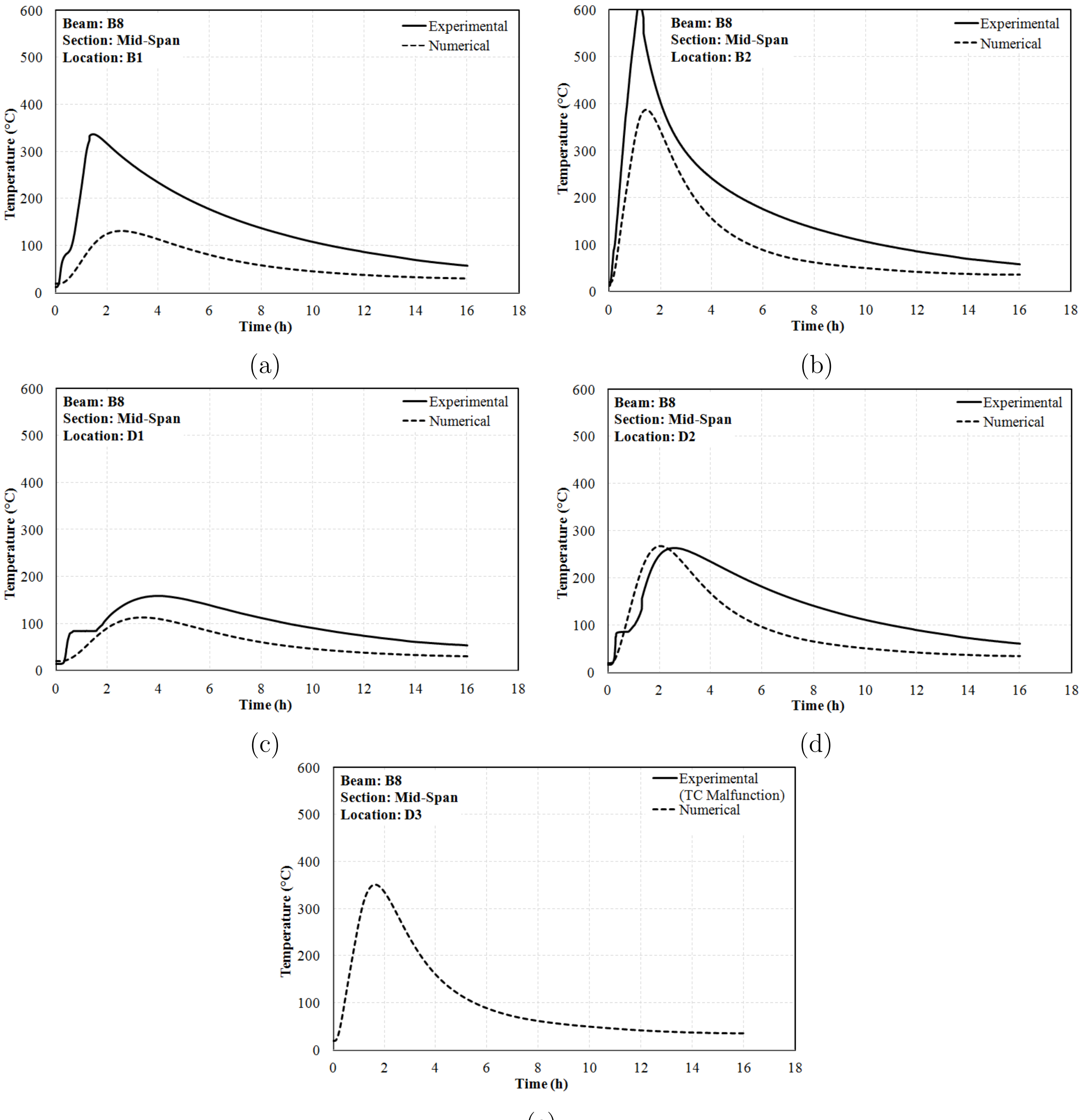

(a) (b) (c) (d) (e)

Fig. 5.23: Comparison of thermal profile for beam B8 (a) Mid-Span, B1 (b) Mid-Span, B2 (c) Mid-Span, D1 (d) Mid-Span, D2 (e) Mid-Span, D3

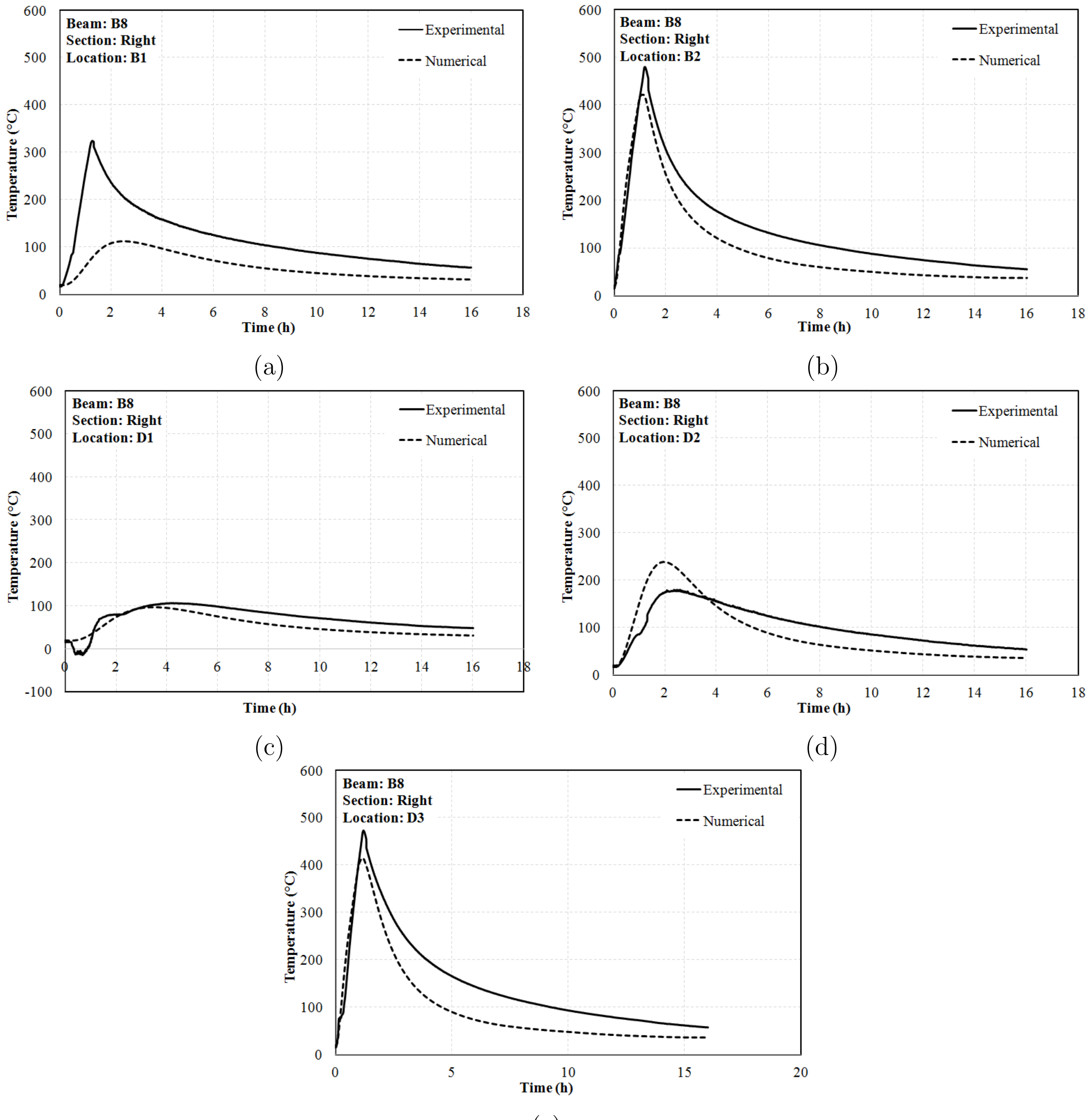

(a) (b) (c) (d) (e)

Fig. 5.24: Comparison of thermal profile for beam B8 (a) Right, B1 (b) Right, B2 (c) Right, D1 (d) Right, D2 (e) Right, D3

Columns

Comparison of the temperature profiles obtained in columns C1, C2, C3 and C4 are shown in Figure 5.25 thru Figure 5.36 respectively. Each columns consisted of three sections (Bottom/Mid-Height/Top), across which temperature profiles were compared at five different locations where the thermocouple values were recorded during the experiment.

Figures 5.25, 5.26 and 5.27 shows the comparison of temperature profiles at left, mid-span and right sections respectively. A maximum peak temperature value of 382 °C was predicted by ABAQUS heat transfer analysis at location L2 against an experimental value of 382 °C. At locations P1 and P2, ABAQUS obtained values of peak temperature showed a match of 98% and 82% respectively. At locations L1 and P3, ABAQUS underpredicted the peak temperature values as seen in Figures 5.25 (a) and (e). Figure 5.26 (a)-(e) shows the comparison of temperature profiles obtained at the mid-height section of column C1. The profiles obtained shows a mixed response. At locations L1 and L2, along the loading direction, the peak temperature was underpredicted by ABAQUS. At locations P1, P2 and P3, the peak temperature was slightly overpredicted by ABAQUS heat transfer analysis. It is evident from Figures 5.27 (a)-(e) that the peak temperatures were mostly underestimated by ABAQUS heat transfer analysis at locations L1, P1, P2 and P3. However at location P2, the peak temperature was overpredicted by 10% as seen in Figure 5.27 (b).

Figure 5.28 to 5.30 shows the comparison of temperature profiles obtained by ABAQUS heat transfer analysis in column C2 at different locations (bottom/mid-height/top). As shown in Figure 5.28 (a)-(e), ABAQUS underpredicted the peak temperatures and hence the temperature profiles at locations L1, L2, P1, P3 and P3 respectively. A closest match of peak temperature (95%) was registered at location L2, which was close to the exposed surface. At the mid-height section, a mixed response was predicted by ABAQUS as seen in Figures 5.29 (a)-(e). The value of peak temperature was overpredicted at L1 and P2 whereas it was underpredicted at locations L2, P1 and P3. However, the maximum peak temperature (366 °C) was registered at location L2 in comparison with the experimentally obtained value of 396 °C, showing a match of 92%. From Figures 5.30 (a)-(e), it is observed that a fairly good match of temperature profiles has been obtained. An average match of 84% was obtained at locations L1 and L2. At location P3, the predicted peak temperature was found to be 310 °C as opposed to the experimentally obtained value of 307 °C. At mid-point location P2, the peak temperature was overpredicted by 24%. The values of peak temperatures obtained by ABAQUS heat transfer analysis and their and their comparison can be interpreted from Table 5.7.

Thermocouple Location	**Peak Temperature (Experimental)** °C	**Peak Temperature (ABAQUS HT)** °C	**Deviation** °C	**Comparison Inference**
TC1BL1	128	75	53	*Underpredicted*
TC1BL2	382	382	-1	*Overpredicted*
TC1BP1	92	90	2	*Underpredicted*
TC1BP2	145	118	27	*Underpredicted*
TC1BP3	404	159	245	*Underpredicted*
TC1ML1	179	141	38	*Underpredicted*
TC1ML2	388	257	130	*Underpredicted*
TC1MP1	83	110	-26	*Overpredicted*
TC1MP2	98	172	-74	*Overpredicted*
TC1MP3	236	257	-21	*Overpredicted*
TC1TL1	121	100	21	*Underpredicted*
TC1TL2	435	481	-46	*Overpredicted*
TC1TP1	217	101	116	*Underpredicted*
TC1TP2	423	151	272	*Underpredicted*
TC1TP3	618	485	133	*Underpredicted*
TC2BL1	184	123	62	*Underpredicted*
TC2BL2	298	283	15	*Underpredicted*
TC2BP1	144	106	38	*Underpredicted*
TC2BP2	289	129	160	*Underpredicted*
TC2BP3	633	283	351	*Underpredicted*
TC2ML1	83	111	-29	*Overpredicted*
TC2ML2	396	366	31	*Underpredicted*
TC2MP1	149	111	37	*Underpredicted*
TC2MP2	148	201	-53	*Overpredicted*
TC2MP3	397	309	88	*Underpredicted*
TC2TL1	137	100	37	*Underpredicted*
TC2TL2	429	380	49	*Underpredicted*
TC2TP1	201	116	84	*Underpredicted*
TC2TP2	136	170	-34	*Overpredicted*
TC2TP3	307	310	-3	*Overpredicted*

Tab. 5.7: Comparison of peak temperatures in the columns C1 and C2

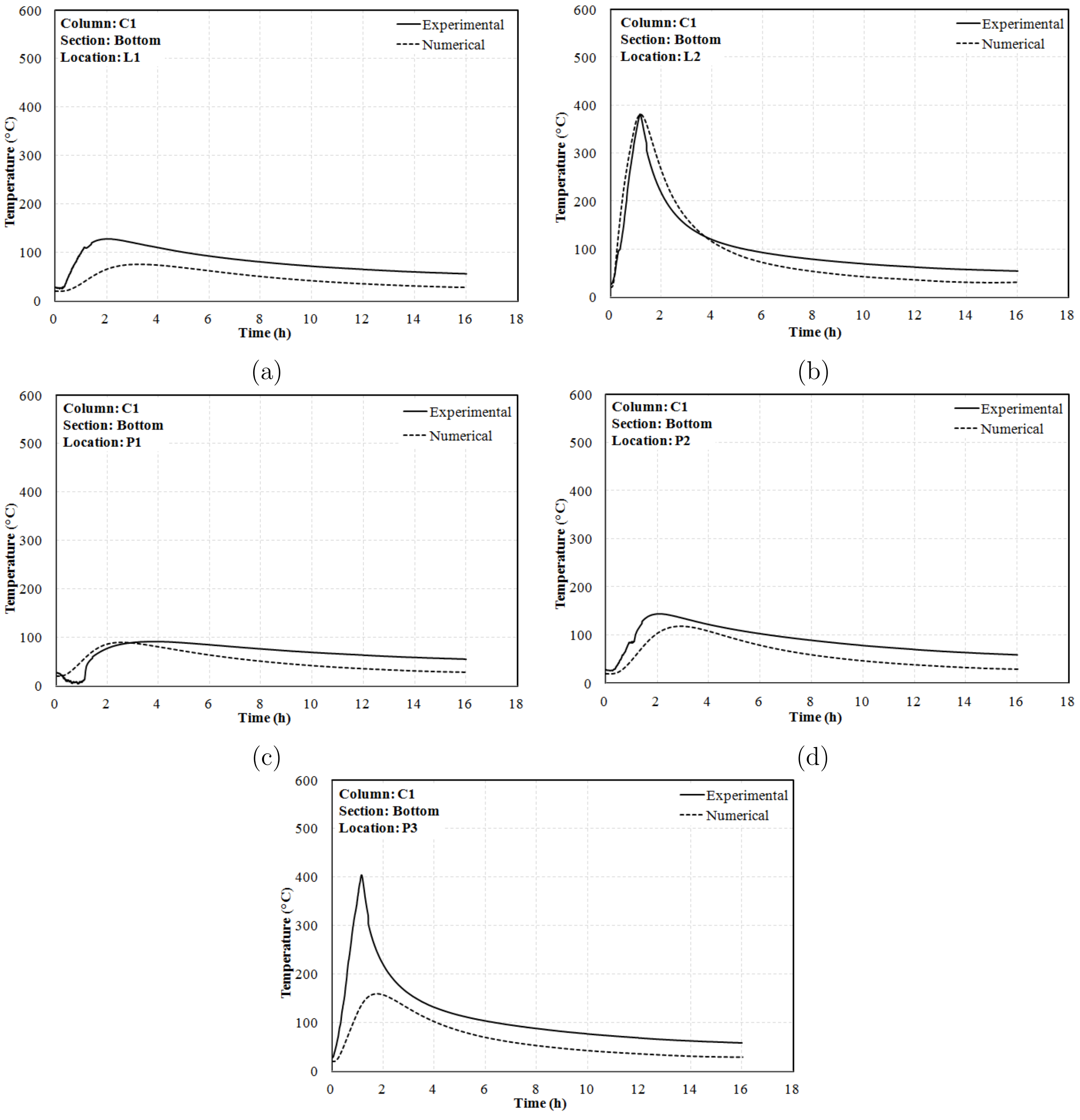
(a)

(b)

(c)

(d)

(e)

Fig. 5.25: Comparison of thermal profile for column C1 (a) Bottom, L1 (b) Bottom, L2 (c) Bottom, P1 (d) Bottom, P2 (e) Bottom, P3

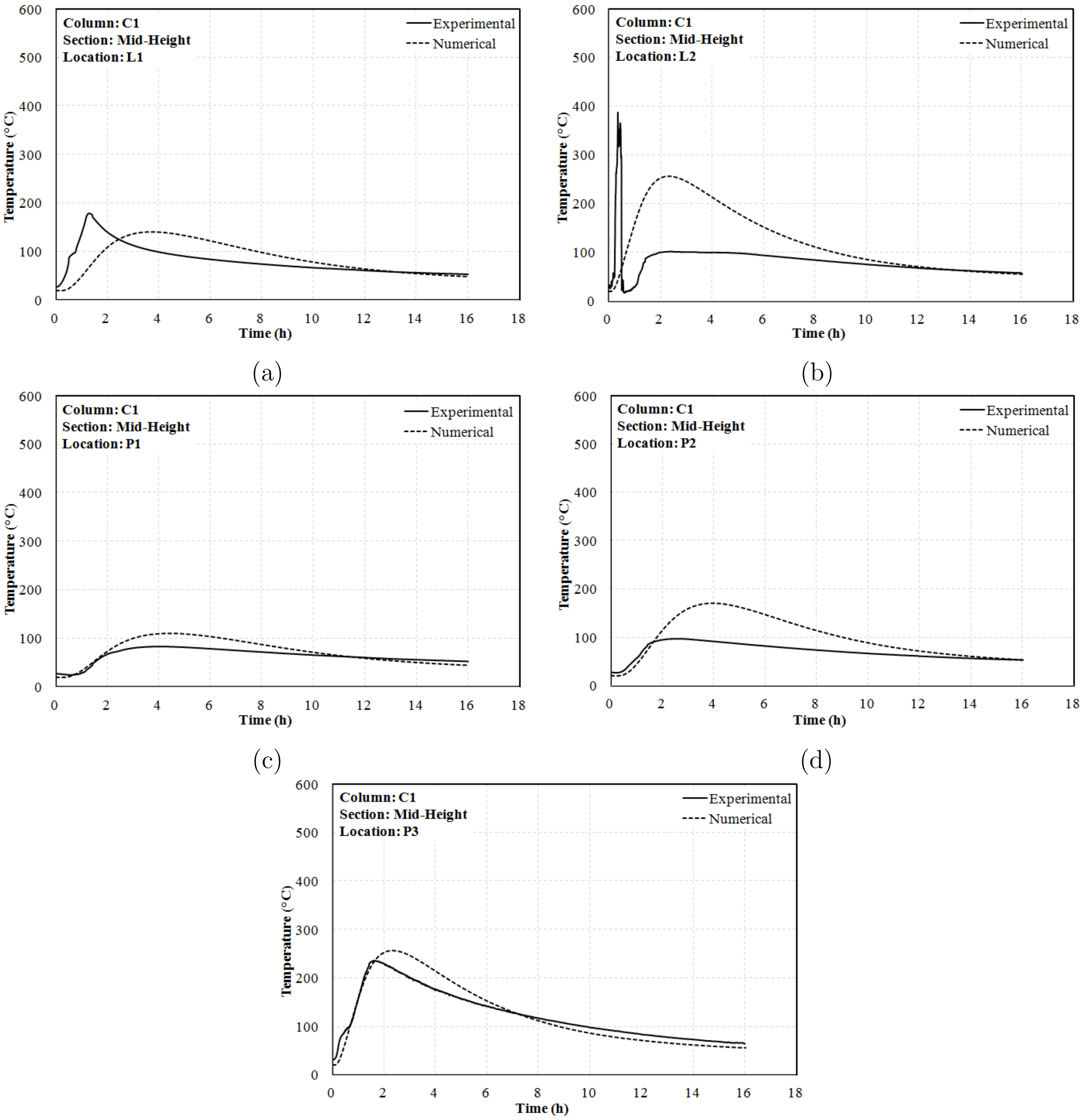

(a) (b)

(c) (d)

(e)

Fig. 5.26: Comparison of thermal profile for column C1 (a) Mid-Height, L1 (b) Mid-Height, L2 (c) Mid-Height, P1 (d) Mid-Height, P2 (e) Mid-Height, P3

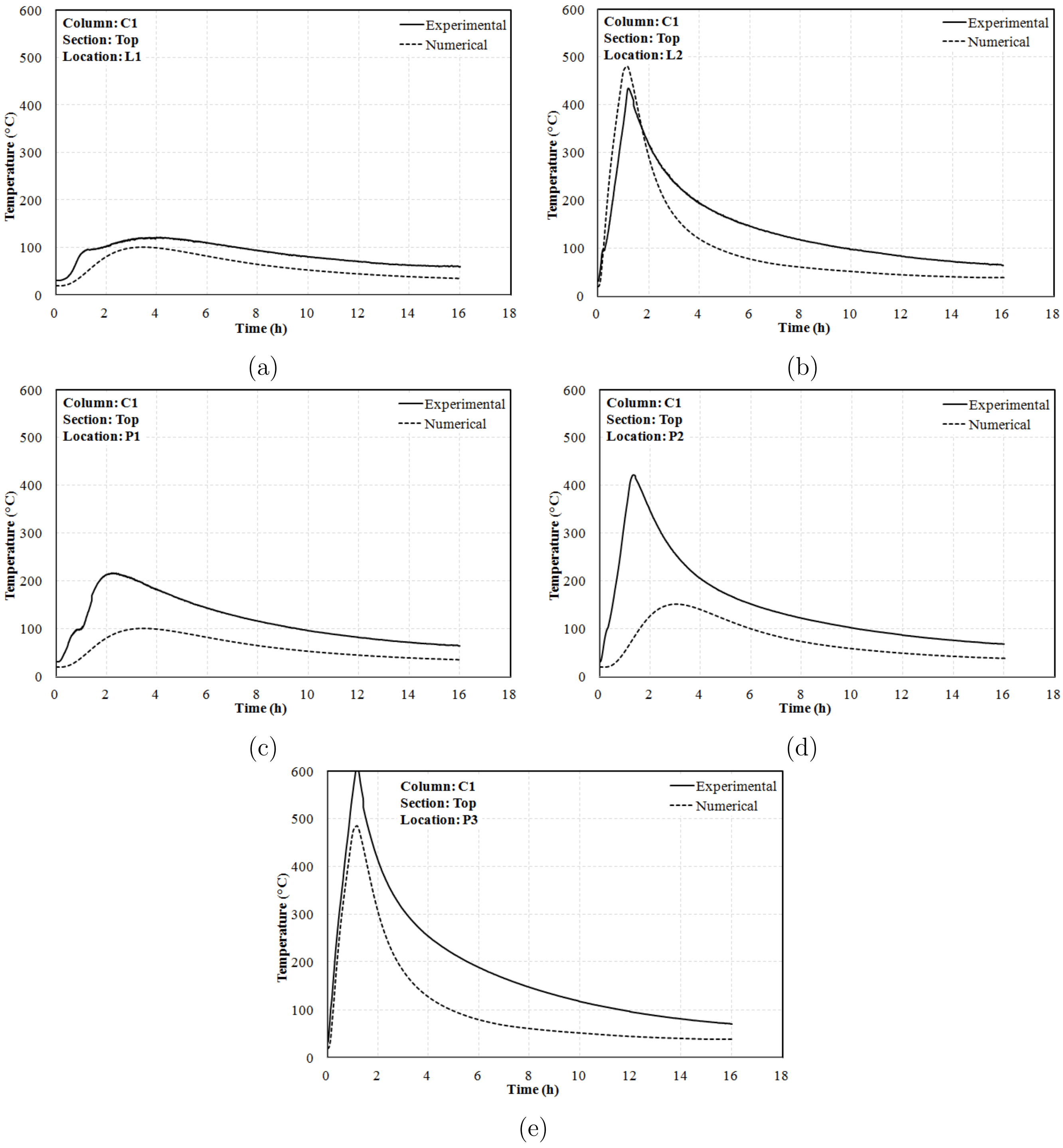

(a) (b) (c) (d) (e)

Fig. 5.27: Comparison of thermal profile for column C1 (a) Top, L1 (b) Top, L2 (c) Top, P1 (d) Top, P2 (e) Top, P3

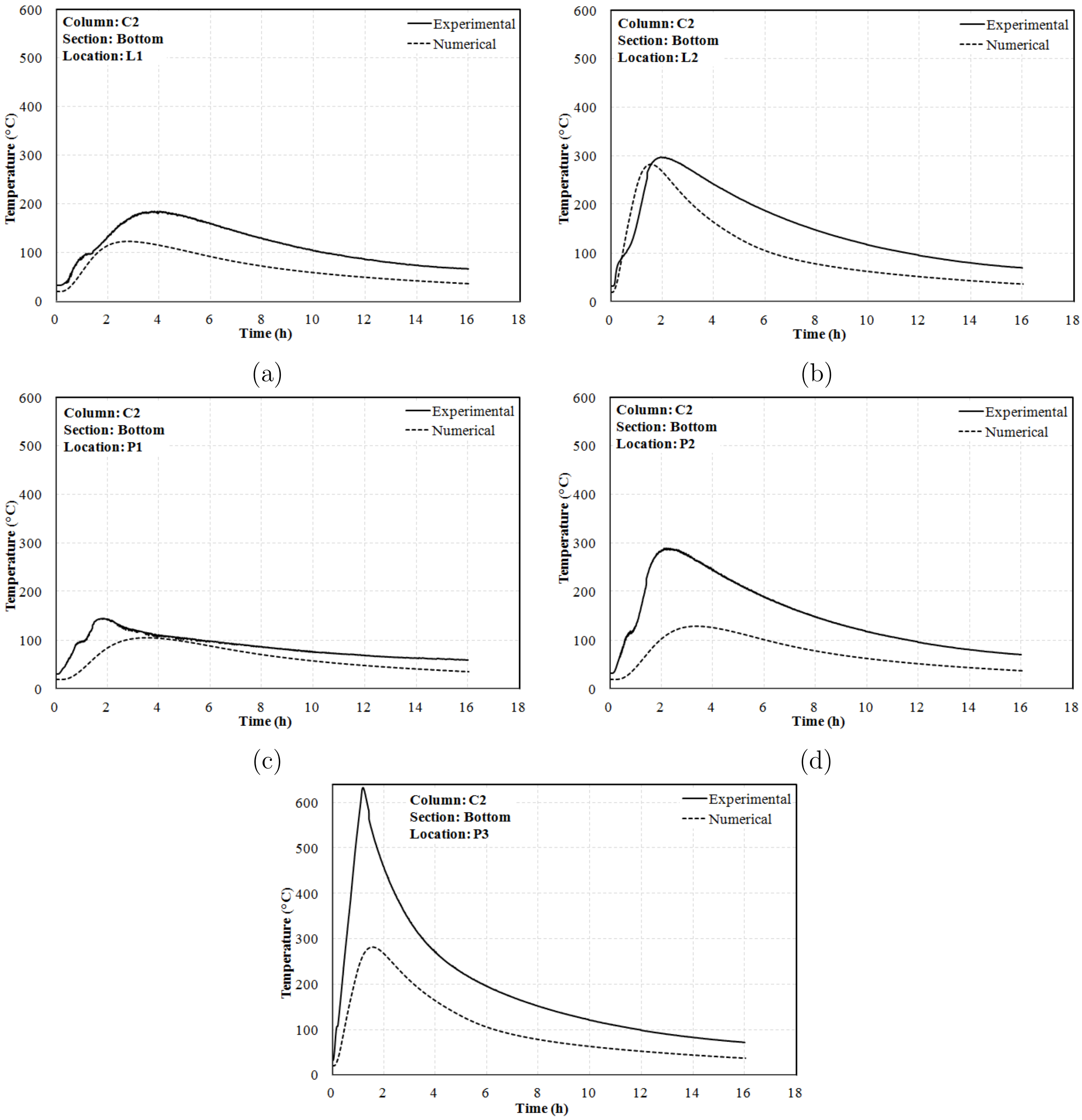

(a)

(b)

(c)

(d)

(e)

Fig. 5.28: Comparison of thermal profile for column C2 (a) Bottom, L1 (b) Bottom, L2 (c) Bottom, P1 (d) Bottom, P2 (e) Bottom, P3

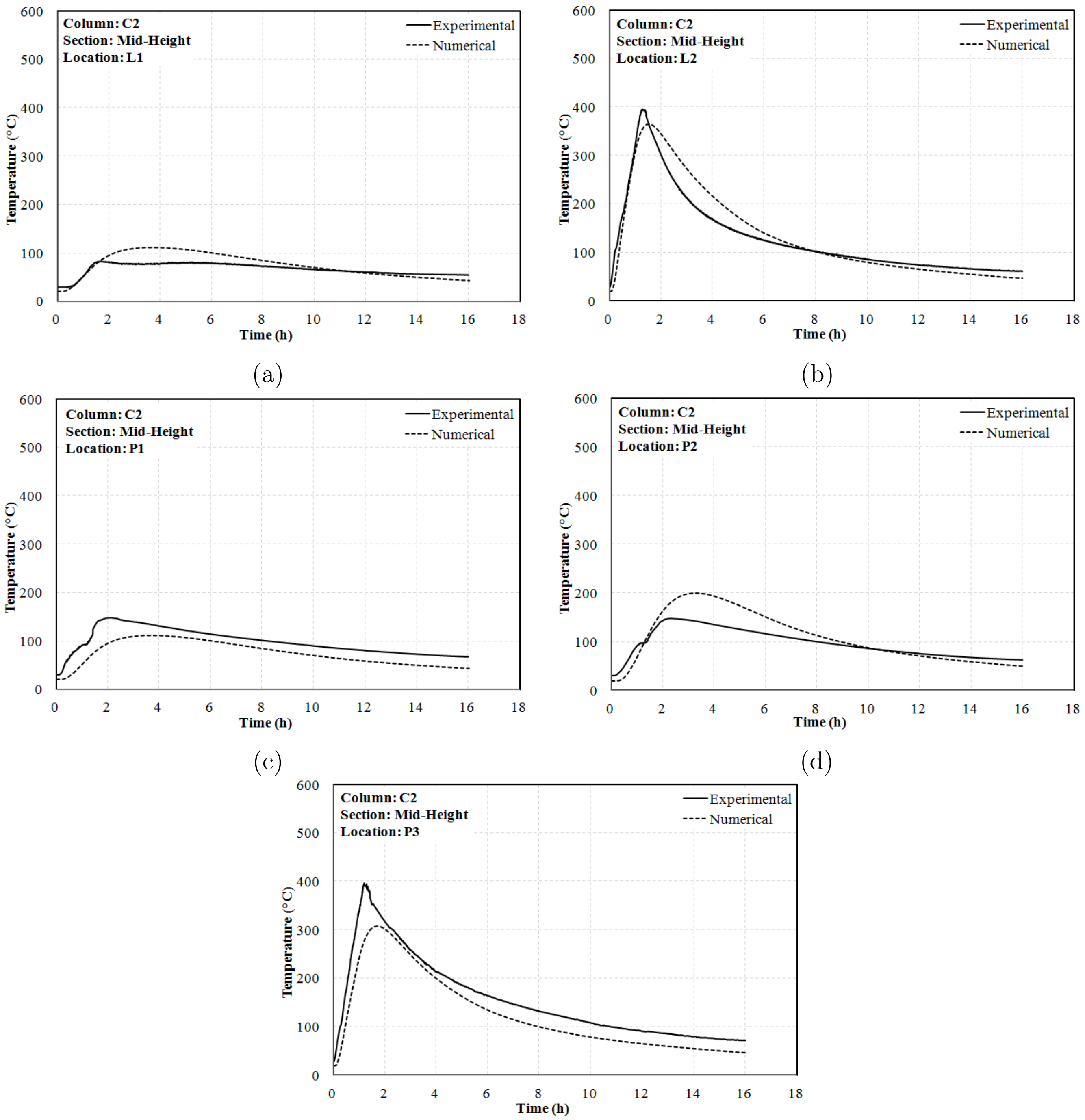

(a) (b) (c) (d) (e)

Fig. 5.29: Comparison of thermal profile for column C2 (a) Mid-Height, L1 (b) Mid-Height, L2 (c) Mid-Height, P1 (d) Mid-Height, P2 (e) Mid-Height, P3

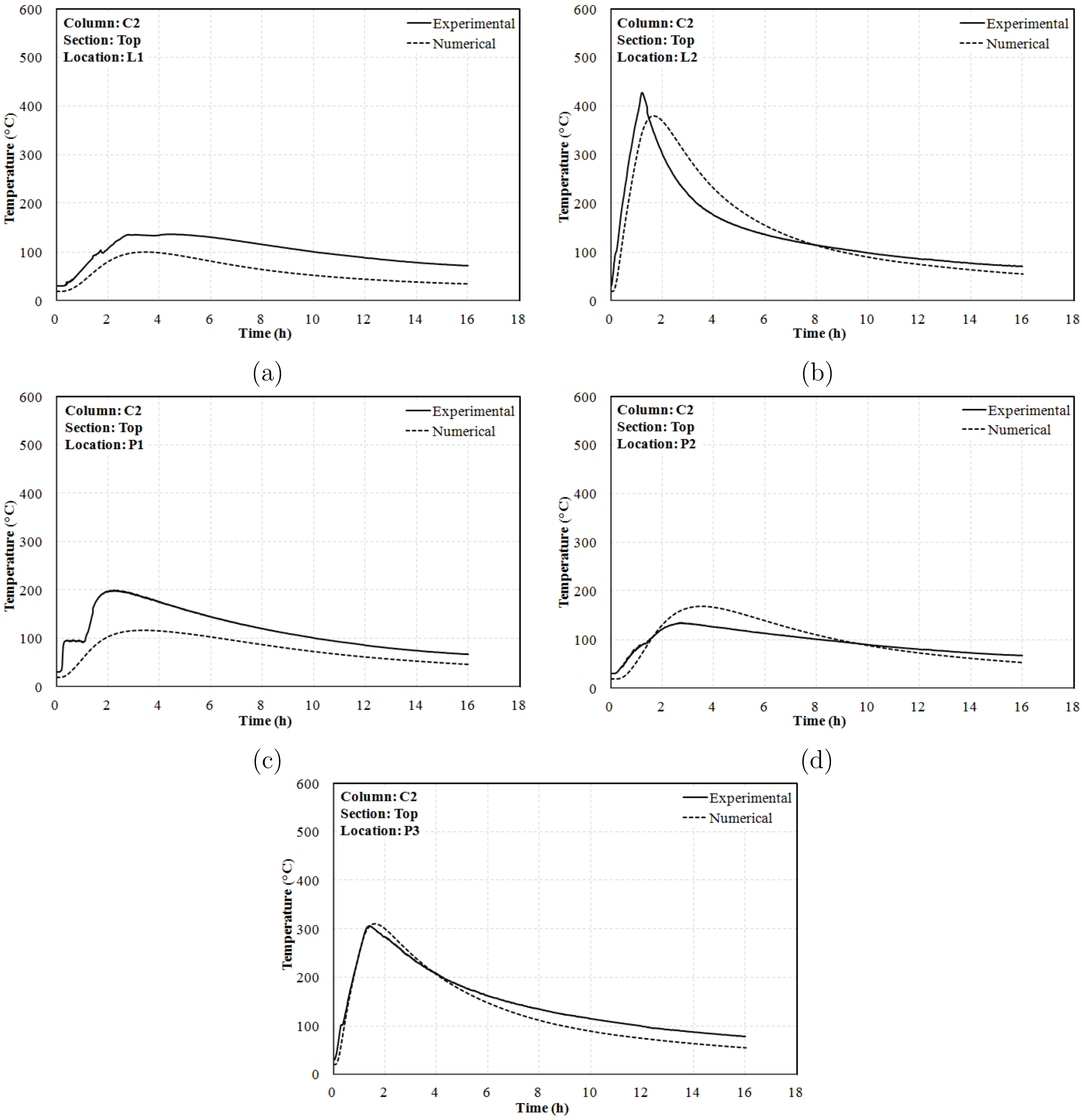

(a)

(b)

(c)

(d)

(e)

Fig. 5.30: Comparison of thermal profile for column C2 (a) Top, L1 (b) Top, L2 (c) Top, P1 (d) Top, P2 (e) Top, P3

Figures 5.31 to 5.36 show the comparison of temperature profiles obtained by ABAQUS heat transfer analysis with experimentally recorded temperature profiles for column C3 and C4. The temperature profiles were obtained at five locations at two sections near the supports and one section at mid-height of the column. In column C3, the temperature profiles showed a mixed response. At the bottom section, ABAQUS slightly under predicted the temperature profiles as seen in Figure 5.31 (a)-(e). However an average match of 85% was obtained in the peak stress values. A maximum peak temperature of 167 °C and 170 °C was predicted at locations L2 and D3, against the experimentally-obtained peak temperatures of 197 °C and 215 °C. Figure 5.32 (a)-(e) shows the comparison of the temperature profiles at mid-height section. It is observed that the temperature profiles were slightly overpredicted (25%) at location L1 and underpredicted (30%) at location L2. However, at locations P1, P2 and P3, an average match of 94% in the peak stress was observed. Unlike the results of the left and mid-height section, the temperature profiles at the top section is found to be overpredicted by ABAQUS heat transfer analysis as shown in Figure 4.44 (a)-(e). A close match (27% higher) was obtained at locations L1 and P2.

The comparison of temperature profiles at three sections: bottom, mid-height and top of column C4 are as shown in figures 5.34, 5.35 and 5.36 respectively. It is observed that ABAQUS heat transfer analysis slightly underpredicted the temperature profiles at the bottom section as shown in Figures 5.34 (a)-(e). An average match of 89% was noticed in the peak temperatures. Maximum peak temperature of 236 °C was obtained by ABAQUS at locations L2 and B3 against the experimental values of 274 °C and 377 °C respectively. At the mid-height location, a slight underprediction of temperature profiles with an average match of 77% was observed (at locations L1, P1 and P3). At location L2, no experimental value was recorded during the experiment, whereas at location P2, a perfect match of result was observed, however with a slight overprediction of 3%. Furthermore, the comparison plots obtained are as shown in Figure 5.35 (a)-(e) respectively. Finally at the top section, a decent match of temperature profiles was registered as seen in Figure 5.36 (a)-(e). ABAQUS heat transfer analysis was found to slightly overpredict the results. The maximum values of peak temperatures obtained at locations L2 (485 °C) and P3 (484 °C) against an experimental value of 404 °C and 439 °C. The values of peak temperature obtained in ABAQUS heat transfer analysis, their experimental counterpart and inferences may however be obtained from Table 5.8.

Thermocouple Location	**Peak Temperature (Experimental)** °C	**Peak Temperature (ABAQUS HT)** °C	**Deviation** °C	**Comparison Inference**
TC3BL1	86	72	14	*Underpredicted*
TC3BL2	197	167	30	*Underpredicted*
TC3BP1	89	69	20	*Underpredicted*
TC3BP2	106	113	-7	*Overpredicted*
TC3BP3	215	160	55	*Underpredicted*
TC3ML1	93	116	-23	*Overpredicted*
TC3ML2	467	326	142	*Underpredicted*
TC3MP1	111	102	10	*Underpredicted*
TC3MP2	159	158	1	*Underpredicted*
TC3MP3	360	326	34	*Underpredicted*
TC3TL1	88	113	-25	*Overpredicted*
TC3TL2	134	215	-80	*Overpredicted*
TC3TP1	44	114	-70	*Overpredicted*
TC3TP2	101	127	-26	*Overpredicted*
TC3TP3	160	214	-54	*Overpredicted*
TC4BL1	102	97	6	*Underpredicted*
TC4BL2	274	236	38	*Underpredicted*
TC4BP1	99	97	2	*Underpredicted*
TC4BP2	123	117	6	*Underpredicted*
TC4BP3	337	236	101	*Underpredicted*
TC4ML1	143	110	33	*Underpredicted*
TC4ML2	*0*	*357*	-	*No Result*
TC4MP1	135	110	25	*Underpredicted*
TC4MP2	165	172	-7	*Overpredicted*
TC4MP3	516	367	148	*Underpredicted*
TC4TL1	99	100	-1	*Overpredicted*
TC4TL2	404	485	-81	*Overpredicted*
TC4TP1	118	103	15	*Underpredicted*
TC4TP2	135	135	1	*Underpredicted*
TC4TP3	439	484	-45	*Overpredicted*

Tab. 5.8: Comparison of peak temperatures in the columns C3 and C4

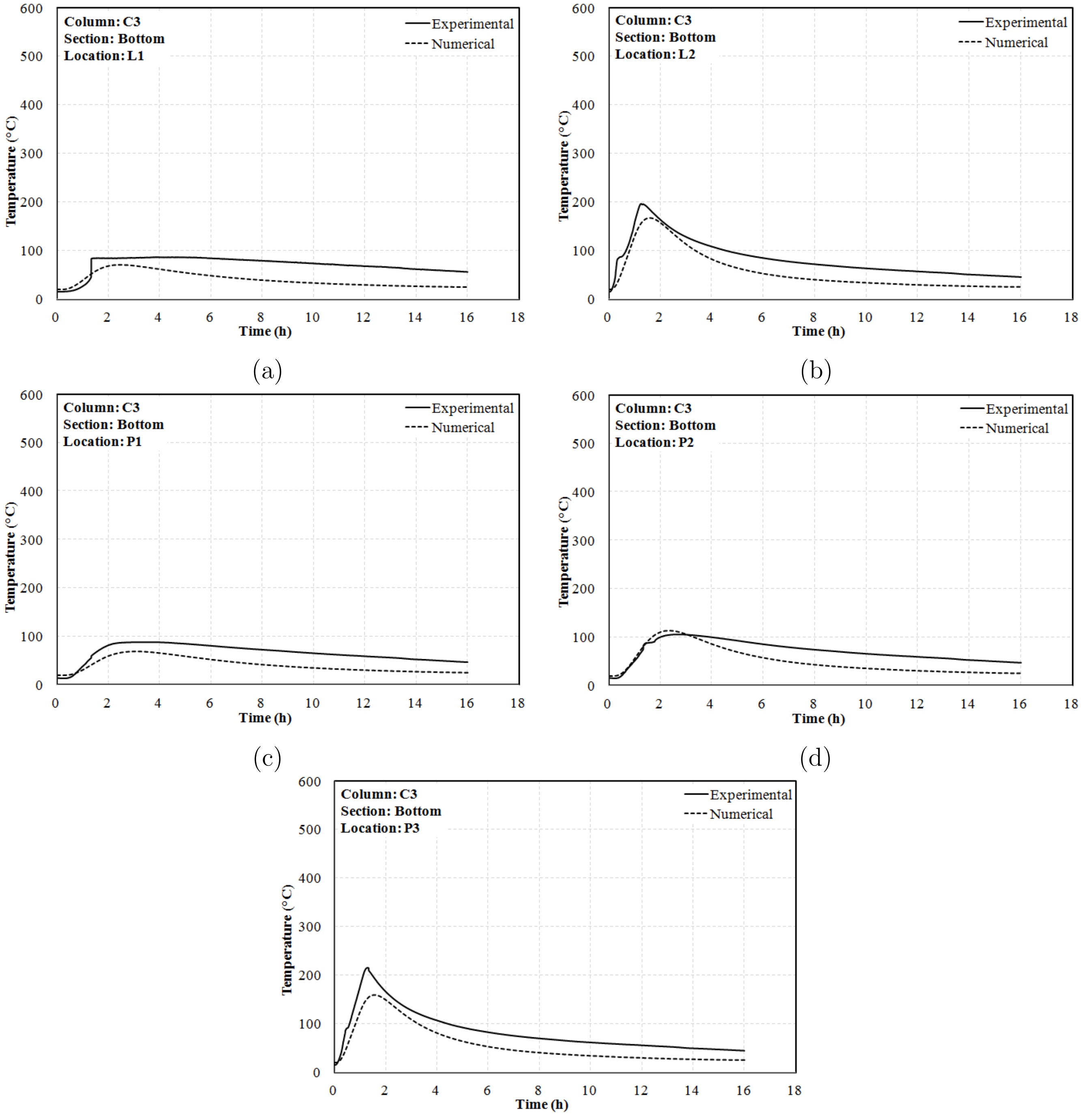

(a)

(b)

(c)

(d)

(e)

Fig. 5.31: Comparison of thermal profile for column C3 (a) Bottom, L1 (b) Bottom, L2 (c) Bottom, P1 (d) Bottom, P2 (e) Bottom, P3

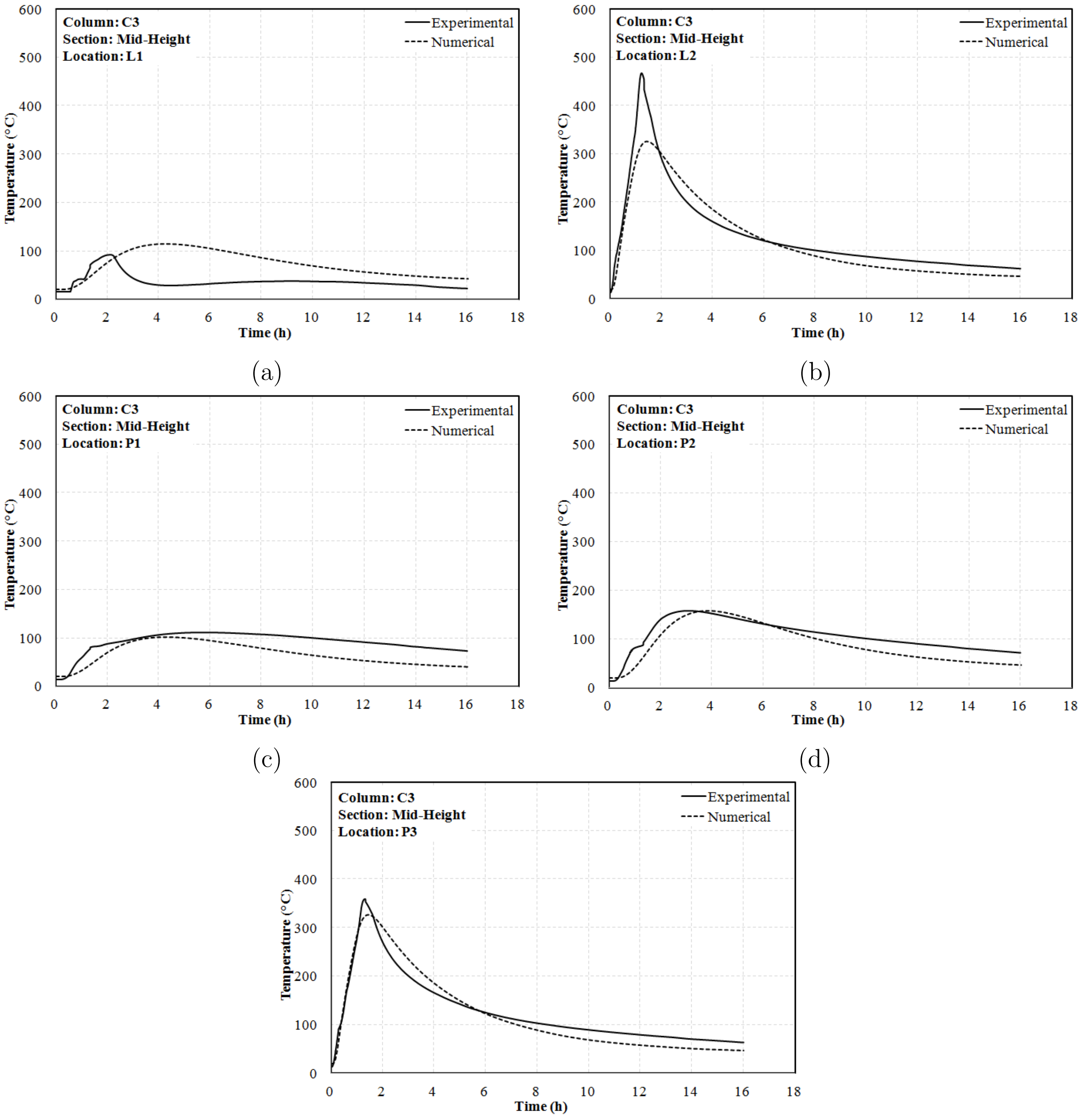

(a)

(b)

(c)

(d)

(e)

Fig. 5.32: Comparison of thermal profile for column C3 (a) Mid-Height, L1 (b) Mid-Height, L2 (c) Mid-Height, P1 (d) Mid-Height, P2 (e) Mid-Height, P3

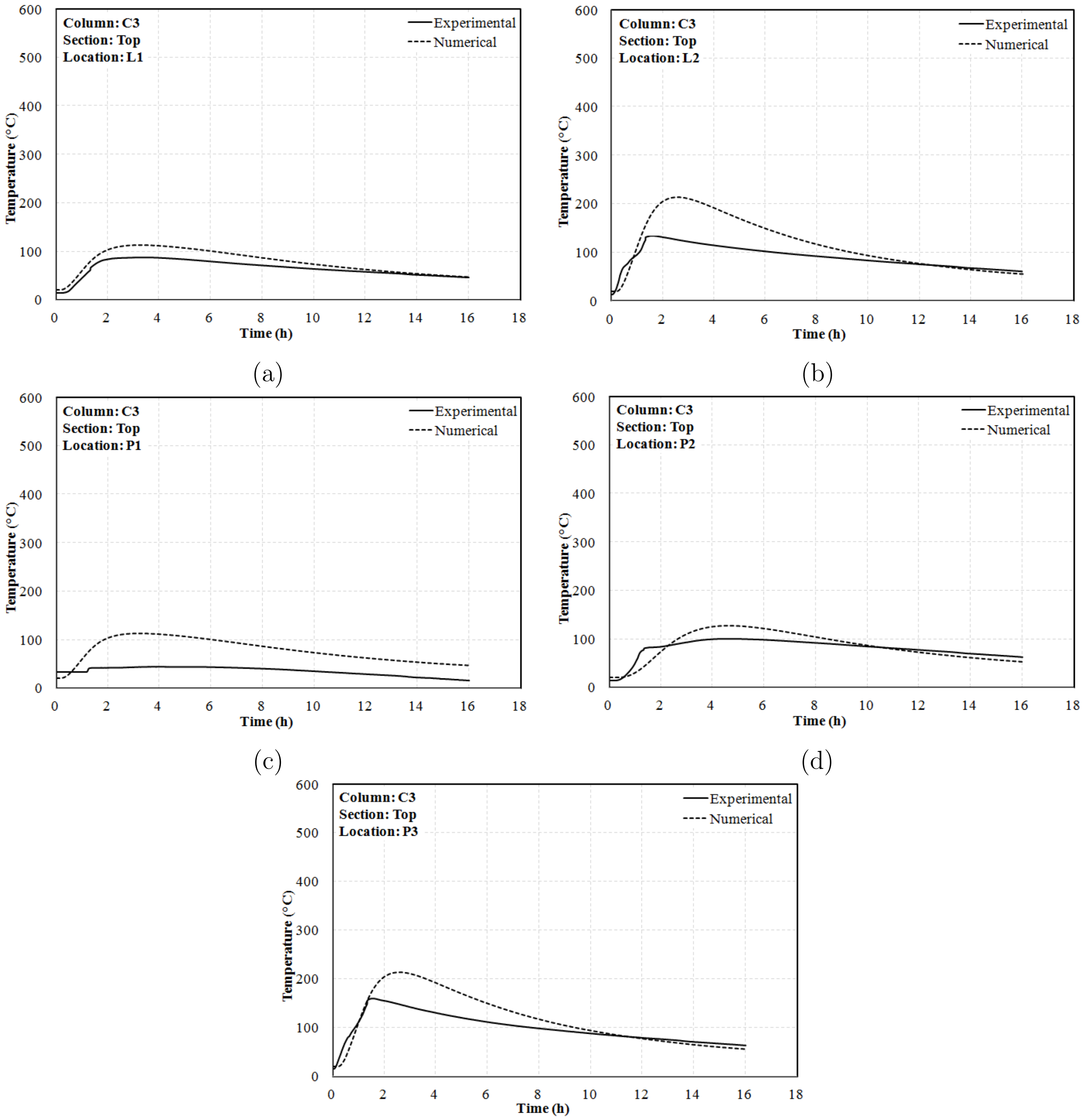

(a) (b) (c) (d) (e)

Fig. 5.33: Comparison of thermal profile for column C3 (a) Top, L1 (b) Top, L2 (c) Top, P1 (d) Top, P2 (e) Top, P3

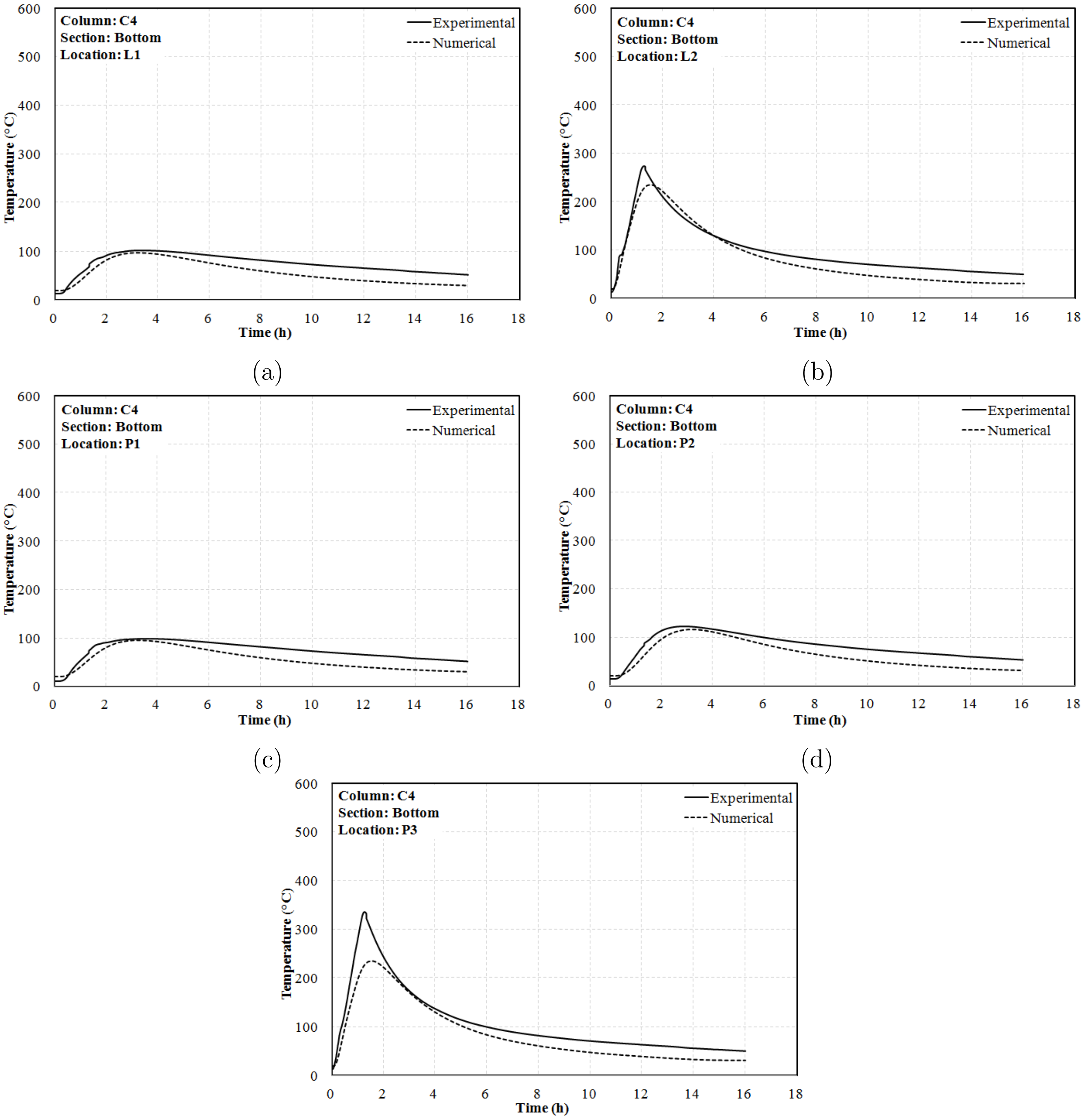

(a)

(b)

(c)

(d)

(e)

Fig. 5.34: Comparison of thermal profile for column C4 (a) Bottom, L1 (b) Bottom, L2 (c) Bottom, P1 (d) Bottom, P2 (e) Bottom, P3

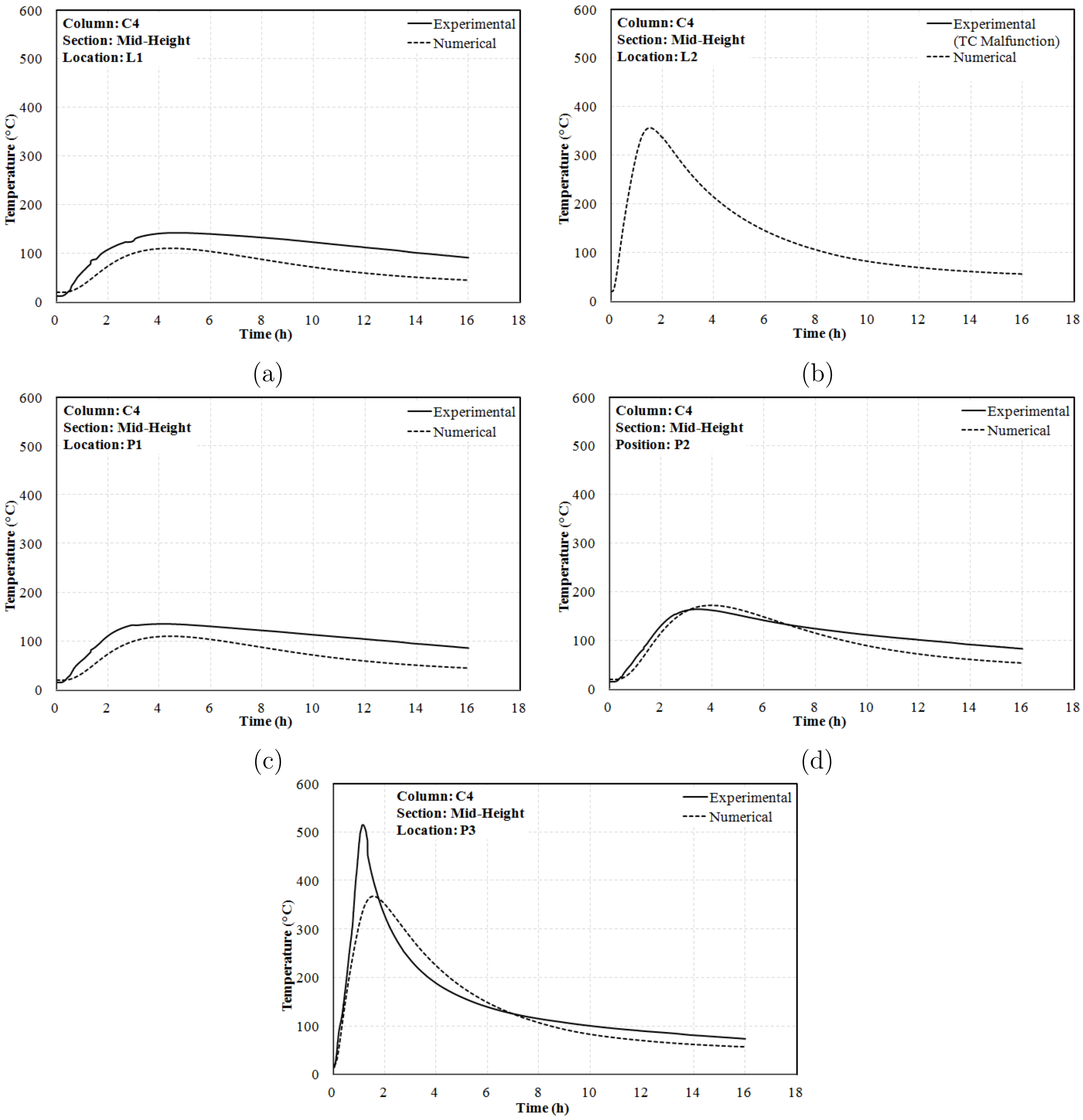

(a) (b) (c) (d) (e)

Fig. 5.35: Comparison of thermal profile for column C4 (a) Mid-Height, L1 (b) Mid-Height, L2 (c) Mid-Height, P1 (d) Mid-Height, P2 (e) Mid-Height, P3

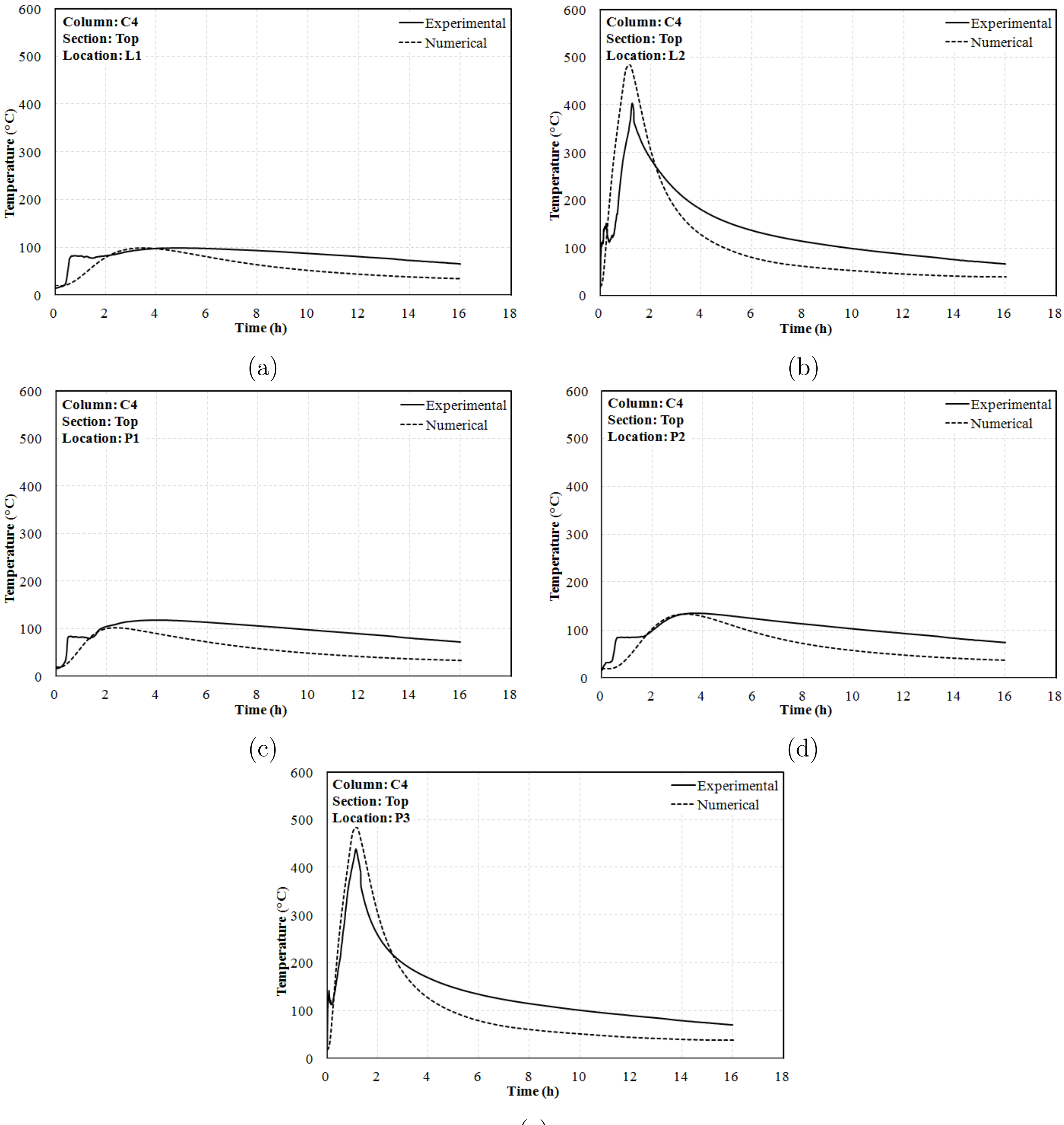

(a) (b) (c) (d) (e)

Fig. 5.36: Comparison of thermal profile for column C4 (a) Top, L1 (b) Top, L2 (c) Top, P1 (d) Top, P2 (e) Top, P3

5.5 *THERMAL STRESS ANALYSIS*

Thermal stress analysis constitutes the response of the reinforced concrete frame to the combined effects of loading and fire. Thermal stress analysis helps to reckon the behaviour of the RC frame loaded with gravity loads and exposed to fire. The main outputs obtained from the normal stress analysis holds good also for thermal stress analysis, however, with the effect of temperature. In the present study, the behaviour of the frame was monitored by studying the vertical displacement on various points of the roof slab throughout the analysis.

5.5.1 *Material Constitutive Models for Thermal Stress Analysis*

The constitutive models used for the constituent materials of the RC frame, i.e., concrete and steel were chosen from Eurocode 2 [34]. The Eurocode model for concrete proposed values of strength that have been developed for steady and transient state, however the creep effects are not explicitly considered. Figure 5.37 shows the mathematical model given by Eurocode for concrete under compression at elevated temperatures. The values for the main parameters of the stress-strain relationships of normal weight concrete with silicious and calcarious aggregates is shown in Table 5.9. The tensile strength of the concrete is governed by the coefficient $k_{c,t}(\theta)$.

$$f_{ck,t}\left(\theta\right) = k_{c,t}\left(\theta\right) f_{ck,t}$$

Where,

$f_{ck,t} \longrightarrow$ Characteristic tensile strength at ambient temperature, and,

$$\begin{aligned} k_{c,t}\left(\theta\right) &= 1.0 & for \quad 20\,^{\circ}\mathrm{C} \leq \theta \leq 100\,^{\circ}\mathrm{C} \\ k_{c,t}\left(\theta\right) &= 1.0 - 1.0\left(\theta - 100\right)/500 & for \quad 100\,^{\circ}\mathrm{C} < \theta \leq 600\,^{\circ}\mathrm{C} \end{aligned}$$

The constitutive model for reinforcing steel is also considered from Eurocode 2 [34], which is explained in detail in Chapter 2.

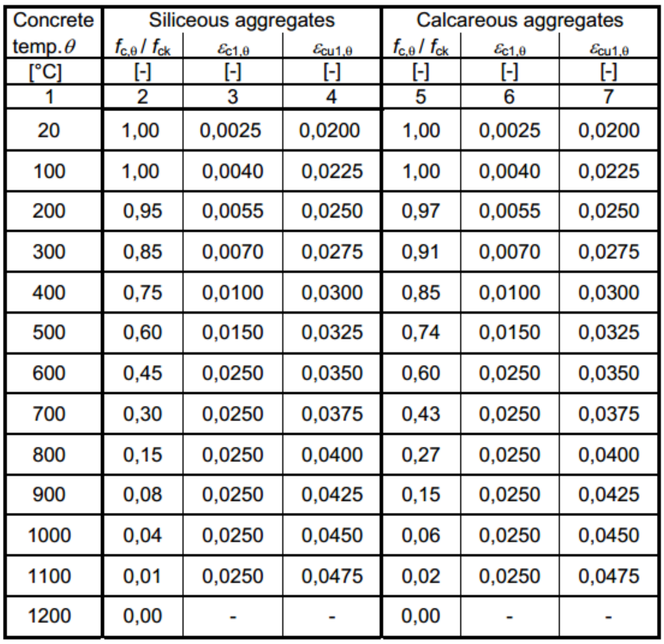

Concrete temp. θ [°C]	Siliceous aggregates $f_{c,\theta}/f_{ck}$ [-]	$\varepsilon_{c1,\theta}$ [-]	$\varepsilon_{cu1,\theta}$ [-]	Calcareous aggregates $f_{c,\theta}/f_{ck}$ [-]	$\varepsilon_{c1,\theta}$ [-]	$\varepsilon_{cu1,\theta}$ [-]
1	2	3	4	5	6	7
20	1,00	0,0025	0,0200	1,00	0,0025	0,0200
100	1,00	0,0040	0,0225	1,00	0,0040	0,0225
200	0,95	0,0055	0,0250	0,97	0,0055	0,0250
300	0,85	0,0070	0,0275	0,91	0,0070	0,0275
400	0,75	0,0100	0,0300	0,85	0,0100	0,0300
500	0,60	0,0150	0,0325	0,74	0,0150	0,0325
600	0,45	0,0250	0,0350	0,60	0,0250	0,0350
700	0,30	0,0250	0,0375	0,43	0,0250	0,0375
800	0,15	0,0250	0,0400	0,27	0,0250	0,0400
900	0,08	0,0250	0,0425	0,15	0,0250	0,0425
1000	0,04	0,0250	0,0450	0,06	0,0250	0,0450
1100	0,01	0,0250	0,0475	0,02	0,0250	0,0475
1200	0,00	-	-	0,00	-	-

Tab. 5.9: Values for the stress-strain relationships of normal weight concrete at elevated temperatures

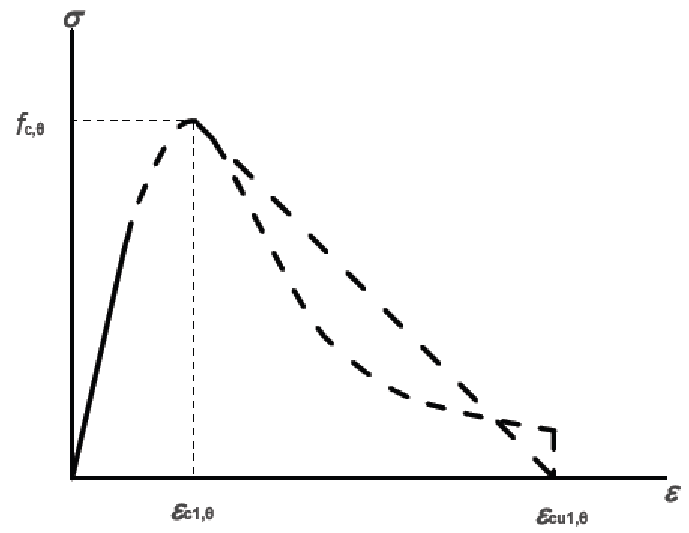

Range	Stress $\sigma(\theta)$
$\varepsilon \le \varepsilon_{c1,\theta}$	$\frac{3\varepsilon f_{c,\theta}}{\varepsilon_{c1,\theta}\left(2+\left(\frac{\varepsilon}{\varepsilon_{c1,\theta}}\right)^{3}\right)}$
$\varepsilon_{c1(\theta)} < \varepsilon \le \varepsilon_{cu1,\theta}$	**For numerical purposes a descending branch should be adopted. Linear or non-linear models are permitted.**

Fig. 5.37: Mathematical model for concrete at elevated temperature *(from Eurocode 2 [34])*

5.5.2 Results of Thermal Stress Analysis

The results obtained in the thermal stress analysis in terms of slab vertical deflections is presented in this section. Fiugres 5.38 thru 5.42 shows a comparison of vertical displacements obtained in the slab at various locations *(near columns and at the centre)*. The general trend of results suggest a downward deflection of the slab from the onset of fire upto about 45 - 60 *minutes*. After an hour of fire, the deflections tend to recover and reach the minimum in about 120 - 180 *minutes*. Thereafter, a slight upward deflection is observed in most of the locations, especially in the cooling phase. The behaviour is well acknowledged by the ABAQUS results. Although, it is observed from the figures that the numerically obtained values underpredict the displacements. Figures 5.38, 5.39, 5.40 and 5.41 shows the comparison of numerically obtained displacements against the experimental displacements obtained at locations VLVDT1, VLVDT2, VLVDT3 and VLVDT4 respectively. A maximum displacement of 19 *mm* is predicted by ABAQUS thermal stress analysis at the center of the slab as shown in Figure 5.42. However, the experimental result at this point remained unavailable due to malfunctioning of the LVDT at high temperatures. The peak vertical displacements obtained by ABAQUS at locations VLVDT1, VLVDT2, VLVDT3 and VLVDT4 registered a match of 78%, 71%, 89% and 72% respectively with experimental results. From the results, it can be inferred that the numerical behaviour was stiff for the material models considered. This may be attributed to the models ignoring the effect of damage caused during pushover analysis.

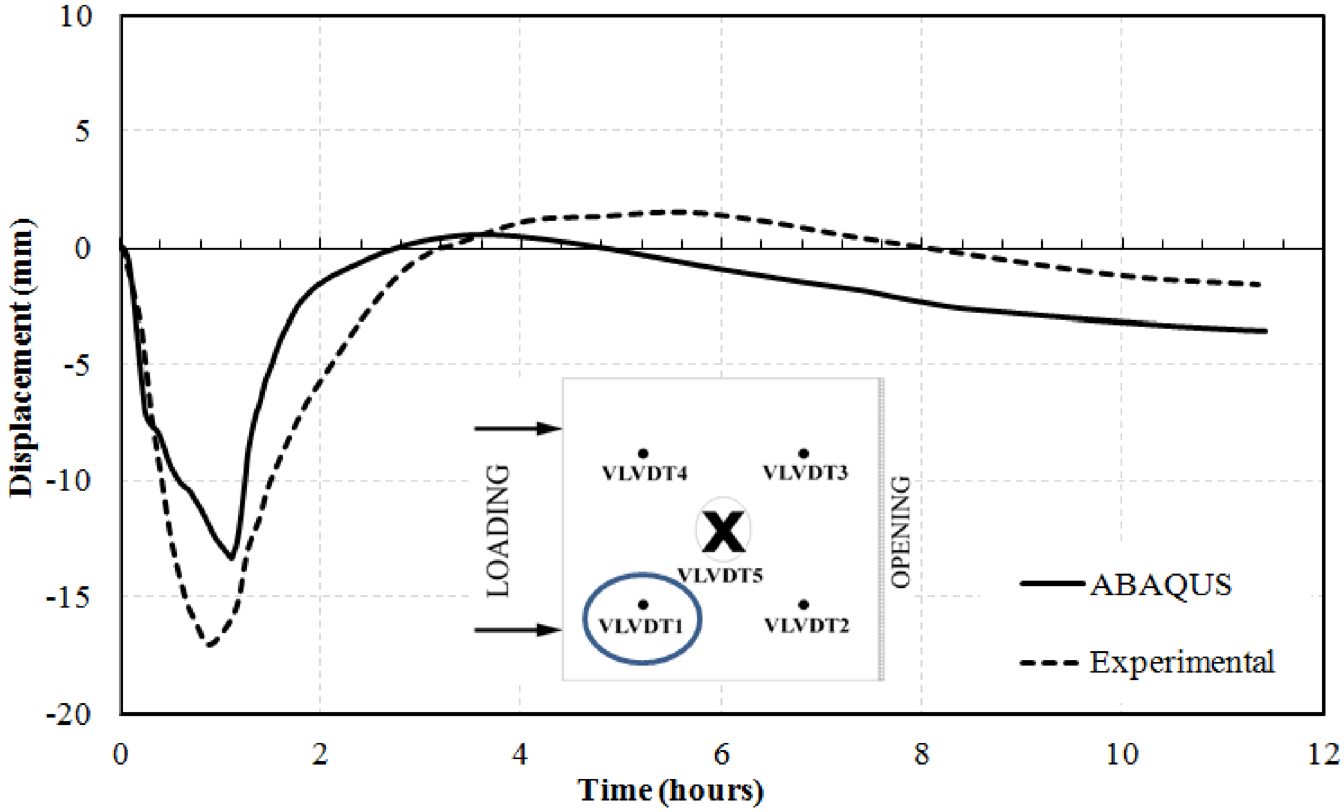

Fig. 5.38: Comparison of vertical displacement for VLVDT1

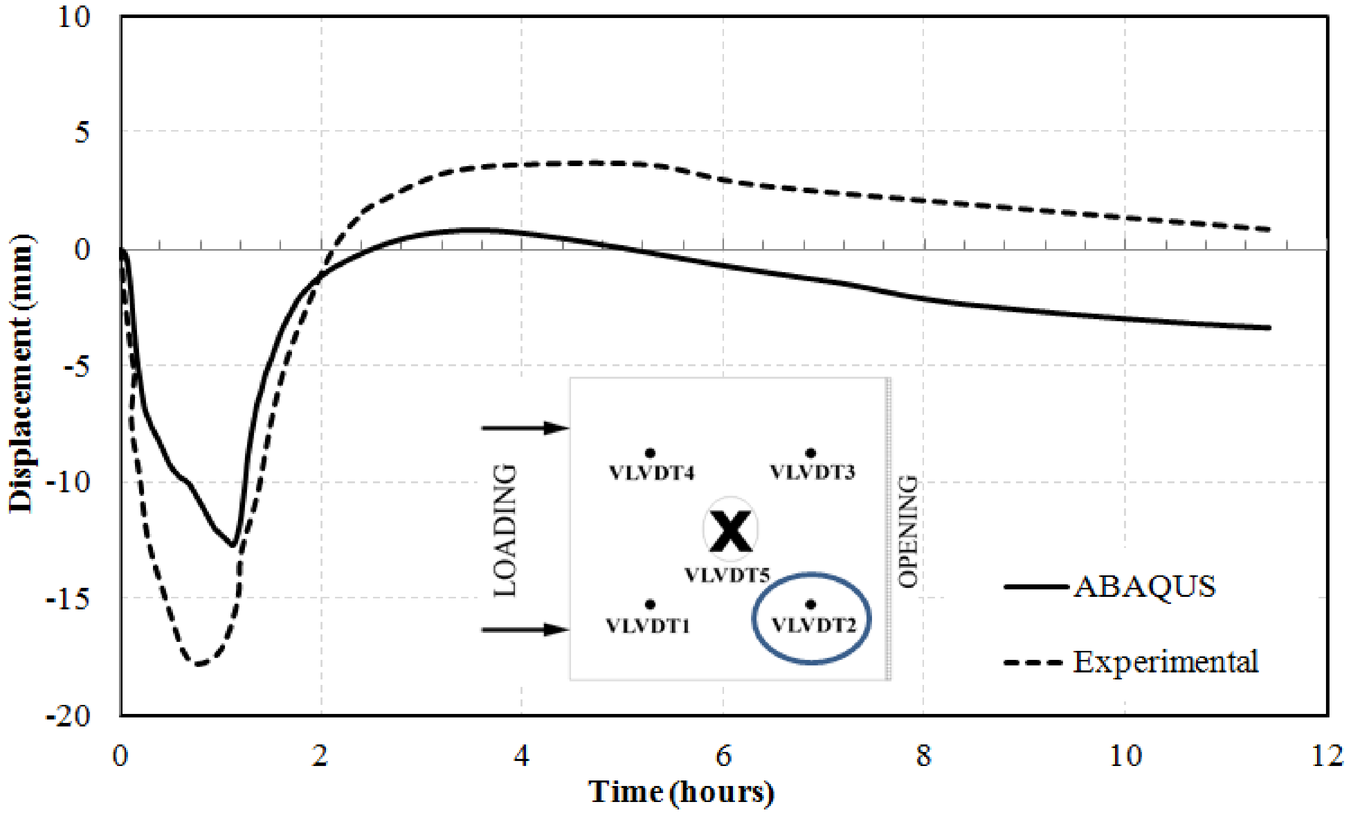

Fig. 5.39: Comparison of vertical displacement for VLVDT2

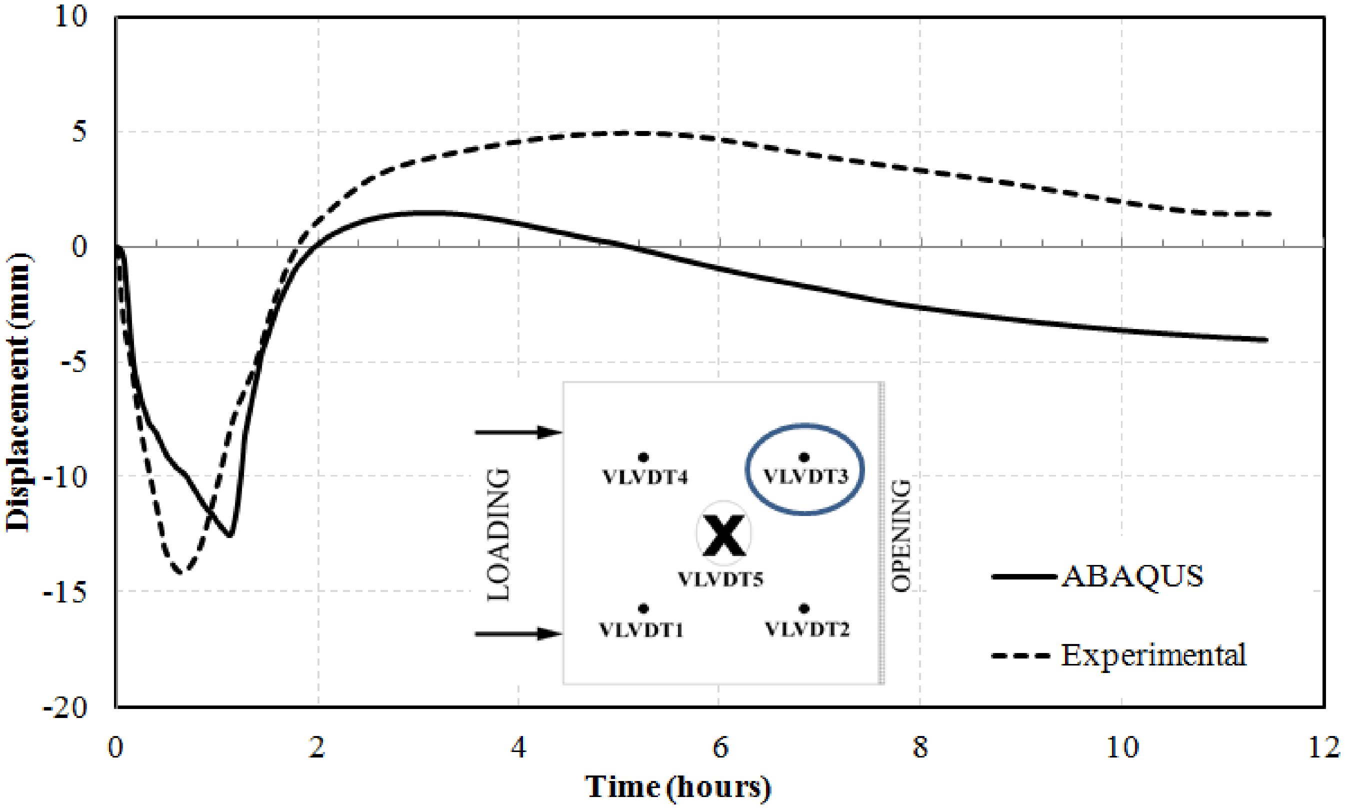

Fig. 5.40: Comparison of vertical displacement for VLVDT3

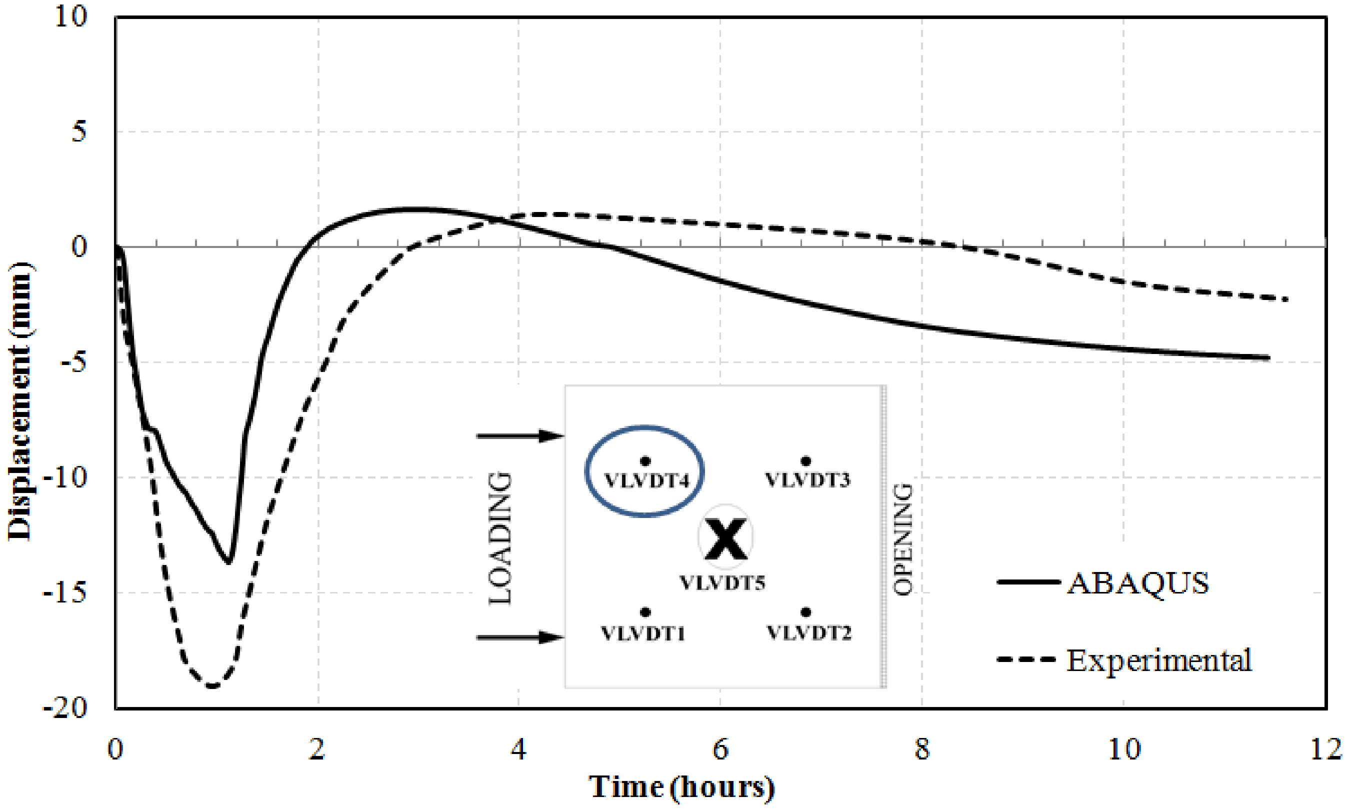

Fig. 5.41: Comparison of vertical displacement for VLVDT4

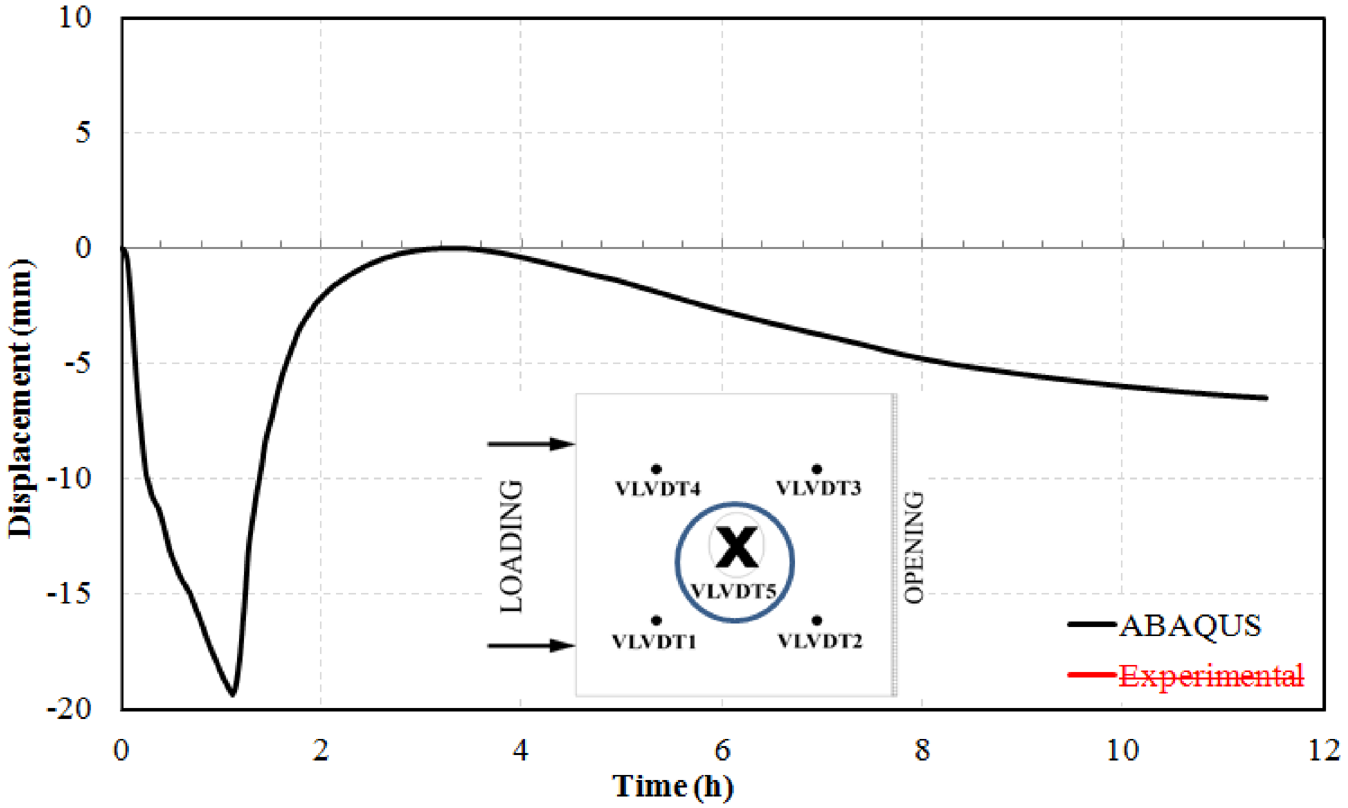

Fig. 5.42: Comparison of vertical displacement for VLVDT5

5.6 *RESIDUAL TEST ON FIRE DAMAGED FRAME*

After performing the simulations on the modelled reinforced concrete frame, it was given a monotonic push loading upto a displacement of 200 mm to simulate the residual capacity test. For carrying out this test, the constitutive models for concrete considered was as per the model proposed by Sharma et. al. [77]. Sharma et al. modified the concrete model proposed by Carreira and Chu [25] to account for temperature variation in the assessment of residual strength of confined concrete exposed to elevated temperatures. The residual stress-strain curves for steel reinforcement used in the analysis were obtained from Topcu and Karakurt [83].

In the experiment, the frame was pushed to its maximum capacity, without releasing the load. This registered an ultimate displacement of 190 mm at a load of 328 kN. Whereas, the simulation predicted a load of 347 kN at an equivalent displacement. Figure 5.43 shows a comparison of residual capacity results obtained in experimental study as well as ABAQUS. As observed from the figure, ABAQUS overestimates the residual capacity of the damaged frame initially. This trend, which a difference of 15% to 20%, continues upto about 145 mm displacement. Thereafter, ABAQUS is observed to underestimate the predicted load value upto a displacement of $\sim$ 185 mm. However, at a max. displacement of 190 mm, a minor difference (6%) in results may be observed in the predicted load value against the experimental value. Overall, a variation in predicted result and a stiff initial behaviour has been exhibited by the ABAQUS Model. This fact may be attributed to the constitutive models for the constituent materials; concrete and steel, which did not take into account, the damage *(especially mechanical)* in the assessment of the residual properties.

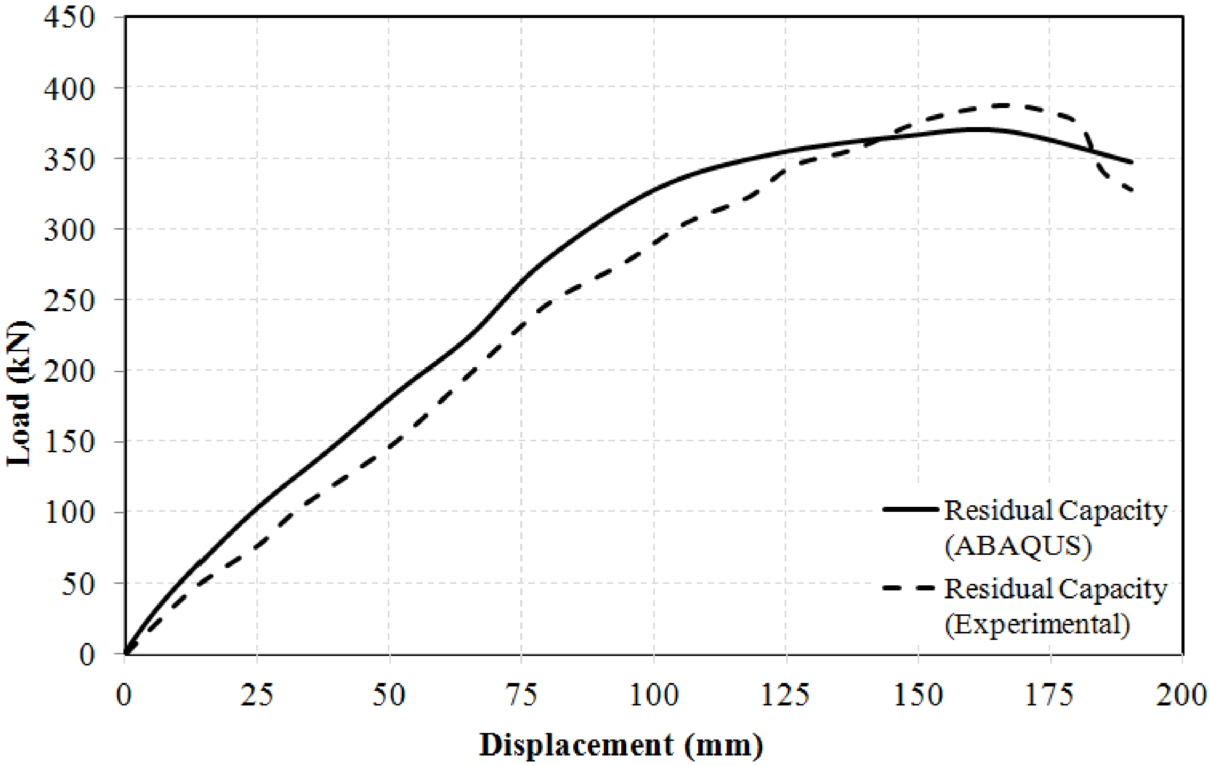

Fig. 5.43: Comparison of residual capacity plots

5.7 CONCLUDING REMARKS

This chapter summarizes the numerical work achieved in connection with the experimental work carried out in the previous chapter (Chapter 4). The frame, modelled in ABAQUS, was simulated for the three stages of test: earthquake loading *(pushover)*, fire and residual capacity. The predicted results obtained by simulating the reinforced concrete frame model were widely compared with the experimental results from Chapter 4. A few rational approaches were used in modelling, assigning material properties and carrying out the analysis, which brought about significant changes in the results obtained in the simulation. In the earthquake load simulation or pushover analysis, ABAQUS analysis overestimated the results. Higher values of loads were obtained in the initial cycles, which diminished and left a marginal difference between the values in the higher cycles. In the numerical heat transfer analysis, temperature profiles at different sections of the structural elements were obtained in response to assigned compartment fire data distributed to various members as surface temperatures. A low percentage of match was obtained against the experimental results. However, an identical trend is seen in the temperature variations and at certain locations, a highly satisfactory match *($>$ 90%)* has been observed. The vertical deflections registered in the roof slab during the heat transfer at various locations, similar to those instrumented with LVDTs in the experiment were also compared and a satisfactory trend has been observed. Results from the thermal stress analysis show an average of 78% match in the numerically obtained results of slab vertical displacements, against the experimental values. In the simulation of residual capacity test, the frame was imparted a final monotonic displacement of 200 mm and the load envelope obtained against the displacement exhibited a $15-20\%$ overprediction in the simulated results in comparison with experimentally obtained load-displacement envelope. The deviation in results may be generalized to several possibilities, few of which include a rational modelling approach, empirical yet similar material properties, absence of damage in the material models, approximate distribution of surface temperatures based on compartment fire, assumed symmetric behaviour of the frame ruling out the local effects exhibited in the experiment, architecture of the software framework, importantly solution algorithms and their appropriate usage. However, as a scope of future work, author suggests that it is imperative to model and discretize the structure more robustly to surpass the many imperfections obtained in the results.

Conclusions and Scope for Further Research

6

6.1 CONCLUSIONS

Chapter 6 presents a brief overview of the present research work. A panoptic study of structures subjected to post-earthquake fire was undertaken with four principal objectives:

1. Evaluation of the response of steel reinforcement bars with and without pre-load at elevated temperatures.
2. Evaluation of the response of undamaged and damaged confined concrete at elevated temperatures.
3. Structural response of a full-scale reinforced concrete frame under simulated post-earthquake fire.
4. Numerical simulation of reinforced concrete frame subjected to post-earthquake fire.

These objectives were addressed by carrying out three unique experimental studies followed by a brief analytical work. A novel set of results obtained and the key findings/observations of the research have been enumerated as follows:

1. Contemporary steel reinforcing bars manufactured to cater the earthquake resistance, $fe500$ and $fe500D$ TMT EQR, were successfully tested at elevated temperatures. The uniqueness of the work was reflected from testing the pre-loaded rebars at elevated temperatures.

2. Degradation in strength of fe500 and fe500D TMT EQR steel rebars at elevated temperatures was evident from the tests conducted. The behaviour resembled the findings of other researchers in the literature. 8 mm, 10 mm, 16 mm and 20 mm diameter reinforcing bars with no pre-load exhibited a brittle mode of failure under elevated temperature upto 250 °C. At 500 °C, the mode of failure was in transition from brittle to ductile. However, at 750 °C, the mode of failure was purely ductile. Unlike steel rebars without pre-load, pre-loaded steel rebars exhibited brittle mode of failure only at 250 °C. Beyond this temperature, the behaviour of rebars changed from brittle to ductile. For a target temperature of 750 °C, the pre-loaded rebar failed in tension before reaching the target temperature.

3. An elaborate study on behaviour of peak stress of steel rebars without pre-load reports a degradation of 3%, 31% and 88% for rebars exposed to 250 °C, 500 °C and 750 °C respectively. Whereas, for pre-loaded rebars, the reduction in peak stress was determined as 0% *(due to marginal gain in strength)*, 32% and 100% *(rebar failed before the target temperature was achieved)* at 250 °C, 500 °C and 750 °C.

4. Mechanical properties of undamaged and damaged confined concrete specimens subjected to elevated temperatures were successfully investigated by conducting elaborate tests on specimens of two different levels of confinement. The importance of the test may be attributed to the study of damaged confined concrete, since the constitutive model developed aids numerical analysis of the damaged reinforced concrete structures in fire. Current research benefits the performance based design practice. Three pre-defined levels of damage induced to the specimens in the 'damaged' category well-simulated the damage conditions as caused by the earthquakes.

5. The fundamental mechanical properties such as peak stress, modulus of elasticity, strain at peak stress and ultimate strain were considered as the attributes of interest. Effect of damage and the effect of confinement on damaged concrete were considered as the significant findings of the study. The specimen behaviour and failure modes observed have been explicitly discussed.

6. Peak stress of confined concrete decreases with an increase in temperature in the specimens under undamaged category. Whereas, a damage induced prior to heating, further degrades them. In case of damaged confined concrete specimens, an average further degradation of peak stress of 14%, 5% and 2% was observed at 250 °C, 500 °C and 750 °C respectively in concrete with closer confinement*(42 mm)*. Similarly, at concrete with wider confinement *(68 mm)*, an average further degradation of peak stress of 17%, 13% and 5% was observed at 250 °C, 500 °C and 750 °C respectively. Results also indicate that the effect of damage was significant at lower temperatures than at higher temperatures.

7. Similarly, in confined concrete with a damage induced prior to heating, shows a further degradation in modulus of elasticity. Results show further degradation of modulus of elasticity of 37%, 28% and 2% was observed at 250 °C, 500 °C and 750 °C respectively in concrete with closer confinement *(42 mm)*. However, at concrete with wider confinement *(42 mm)*, an average further degradation of modulus of elasticity of 17%, 9% and 11% was observed at 250 °C, 500 °C and 750 °C respectively. These facts indicate that damaged concrete is more vulnerable in case of fire accidents in reinforced concrete structures. It is supported by the evidence of the current study that the effect of confinement is greatly reduced at a temperature of 750 °C, which is normally attained in case of building fires.

8. Theoretical stress-strain relationship developed by Youssef & Moftah [90] by inclusion of temperature dependent material properties in well-accepted Mander's confined concrete stress-strain model [60] has successfully been compared against the experimental results obtained for undamaged confined concrete. The results were in conformity with the proposed theoretical model, upto a temperature of 500 °C, registering an average match of 97%for closer confinement and 88% for wider confinement. However, at 750 °C, the theoretical model was found to underpredict the results.

9. Contemporary construction of high rise buildings require the usage of high strength concrete due to its advantage in catering to a higher load carrying capacity. As it has been reported by various researchers, high strength concrete is susceptible to explosive spalling during fire. In fire accidents on reinforced concrete structures, cover spalling leads to direct exposure of confining reinforcement to fire. This in turn weakens the performance of the structure by rapid reduction in confining effect.

10. Full-scale test on reinforced concrete frame under simulated earthquake followed by fire loading was successfully accomplished. The test comprised of three stages:
    - Simulated earthquake loading achieved by a push-pull loading.
    - Exposure of frame to one-hour compartment fire.
    - Assessment of residual capacity of the earthquake and fire damaged RC frame by uni-directional push loading.
11. Novel set of test results were obtained, which adds on to generate a large database of temperatures, temperature induced displacements, force and strains in structural elements such as beam, column, slab and the RC frame as a single entity. The database is beneficial to the researchers in structural engineering community working on numerical simulation.
12. Key results obtained in the test are as follows:
    - The maximum lateral displacement imparted to the frame in simulated earthquake loading test was 150 *mm* in each direction applied gradually in eleven cycles as stated earlier.
    - Eleven push-pull cycles of displacement yielded an in-elastic lateral displacement of 19 *mm*.
    - A maximum lateral load of 400.87 *kN* was applied to achieve the target displacement.
    - The RC frame survived the simulated earthquake loading with visible cracks of widths 0.1 *mm* to 2.4 *mm* and minor concrete cover spalling. Distress mapping was done after each push-pull cycle.
    - The frame was then exposed to a one hour compartment fire, which reported a maximum temperature of 1370 °C inside the compartment.

- Flashover was achieved within 10 to 15 minutes after the fire ignition, which initiated concrete spalling in beams and columns.
- Maximum temperature in various structural elements were recorded within 10 to 15 minutes after one hour and are enumerated as follows.

  Floor Beam (Top Face): 307 °C at 73 *minutes*
  Roof Beam (Soffit): 614 °C at 70 *minutes*
  Roof Beam (Side Face): 553 °C at 69 *minutes*
  Column (Inner Face): 618 °C at 69 *minutes*
  Column (Side Face): 435 °C at 72 *minutes*
  Roof Slab (Soffit): 534 °C at 70 *minutes*
- The damage caused in the fire was primarily governed by the propagation of hot air currents generated post-flashover. The fire plume traversed the corners of all the four columns completely spalling the cover concrete and leaving the main reinforcement exposed to fire.

- Concrete cover spalling during and after the fire, thermal micro-cracking, deterioration of concrete and loss of bond between rebar and concrete were some of the predominant damaged observed in structural elements exposed to fire.

- Post-earthquake fire exercise declares the frame visibly intact without collapse after the residual test. However, the frame experiences a great loss of strength and stiffness. The state of concrete and partially burned steel rebars pronounce the retrofitting task either unacceptable or extremely challenging since the structure loses its health to a greater extent than most of the deficient structures that can be put to use upon retrofitting.

A collective inference can be established based on scaled laboratory tests on confined concrete and full-scale test on RC frame under post-earthquake fire as follows.

13. A successful attempt has been made to numerically simulate the behaviour of the RC test frame under sequentially applied actual loading comprising of: Quasi-static cyclic pushover loading, this followed by one hour compartment fire, still further followed by a monotonic pushover analysis for residual capacity. This included numerical nonlinear pushover analysis, heat transfer analysis followed by thermal stress analysis and finally, a monotonic pushover loading to assess its residual capacity. The numerical work was carried out using the commercial finite element and CAE software suite ABAQUS version 6.8.

14. Numerical simulation of cyclic pushover analysis resulted in overpredicting the load values, however the trend was observed in the initial cycles corresponding to the applied push-pull cyclic displacements.

15. Numerical heat transfer analysis was satisfactorily achieved by a rational input of experimentally obtained compartment temperatures at different locations idealized as element surface temperatures distributed over exposed faces of beams, columns and slab. A modest, nevertheless fairly accurate match was obtained in analytically predicted and experimentally measured element temperature distribution across various sections of the structural elements.

16. Thermal stress analysis on the earthquake damaged concrete frame, was conducted by considering the residual state of stress from pushover analysis and then giving input temperatures from heat transfer analysis at different instants. The behaviour of the frame was reckoned by qualitatively studying the slab deflection profile at different locations. An average match of 78% was obtained in the maximum downward deflection during fire at different locations. The deviation in the results can be attributed to an undamaged constitutive material models used in thermal stress analysis.

17. Residual capacity of the RC frame subject to pushover analysis and thermal stress analysis was re-analysed for assessment of numerical residual capacity. In this attempt, the final state of stress from thermal analysis was input to the frame in addition to residual mechanical properties for steel and concrete. ABAQUS was found to overestimate $(15-20\%)$ the residual capacity of the damaged frame initially, upto about 145 mm displacement. Thereafter, ABAQUS marginally underestimates the predicted load value upto a displacement of ~ 185 mm. However, at a max. displacement of 190 mm, a minor (6%) overprediction in results may be observed against the experimental value.

6.2 SCOPE FOR FURTHER RESEARCH

With a rigorous experimental work accomplished in the domain of fire following earthquake, author outlines the following prognostic ventures that can elucidate the domain further as follows.

1. Displacement controlled tests on pre-loaded rebars considering more damage levels is beneficial in further conducting a sensitivity analysis to generate accurate constitutive models. There is also a need to develop more robust instrumentation to facilitate direct measurement of strains on bars at elevated temperatures in the furnace.

2. After conducting the tests on steel reinforcing bars and confined concrete separately, further tests are recommended to study the behaviour of bond-slip of rebars in concrete at elevated temperatures.

3. Assessment of the mechanical properties of rebar and concrete specimens may be extended to more frequent temperature ranges to closely study their effect under sustained loads to incorporate effect of creep on residual strength and mechanical properties.

4. A robust material model for reinforcing bars and confined concrete can be proposed utilizing the test results which is very helpful in generating user-defined stress-strain relationship in finite element and design computer packages.

5. An attempt was made to measure the confinement strains to estimate the confining pressures, which apparently failed due to debonding / melting of strain gauges at elevated temperatures. Measurement of confining pressures and lateral displacement would prove advantageous in analysing the variation in Poisson's ratio of confined concrete.

6. Finite element analysis of the reinforced concrete frame for fire following earthquake is a complex task that involves variable set of material properties and constitutive material models at each stage. The attempt to carry out the finite element analysis on the RC frame in the present study does not consider the apt constitutive models in all the three stages due to unavailability of material models for concrete and steel in a pre-loaded / damaged state. In an effort to reckon the behaviour of damaged concrete and pre-loaded steel rebars, empirical relationships have been proposed by the author in chapters 3 and 2. With the help of further rigorous testing and investigations, robust material constitutive models in the damaged state may be proposed. These damaged constitutive models, when used in appropriate stages of numerical analysis, may help in enhancing the accuracy of results obtained in the numerical simulation to have better match with test results.

References

[1] Ali, F., and Nadjai, A. Fire resistance of high strength concrete columns subjected to moderate axial restraint. *Journal of Applied Fire Science 18*, 1 (2008), 79–103.

[2] Ali, F., Nadjai, A., and Abu-Tair, A. Explosive spalling of normal strength concrete slabs subjected to severe fire. *Materials and Structures 44*, 5 (2011), 943–956.

[3] Ali, F., Nadjai, A., and Choi, S. An experimental and numerical study on the behavior of high strength concrete columns in fire subjected to high restraint. *Journal of Structural Fire Engineering 1*, 1 (2010), 1–16.

[4] Anderberg, Y. Analytical fire engineering design of reinforced roncrete structures based on real fire conditions. In *Proceedings of the FIB Congress, Part 1* (London, 1978), pp. 112–121.

[5] Anderberg, Y., and Thelanderson, S. *Stress and deformation characteristics of concrete at high temperatures: 2, Bullitin 54*. Lund Institute of Technology, Swedan, Lund, Swedan, 1976.

[6] Arioz, O. Effects of elevated temperatures on properties of concrete. *Fire Safety Journal 42*, 8 (2007), 516–522.

[7] Armer, G. S. . T., and O'Dell, T. *Fire, static, and dynamic tests of building structures: Proceedings of the second cardington conference, Cardington, England, 12-14 March 1996*. E & FN Spon, 1997.

[8] Aslani, F., and Bastami, M. Constitutive relationships for normal- and high-strength concrete at elevated temperatures. *ACI Materials Journal 108*, 4 (2011), 355–364.

[9] ASTM. Standard test methods for fire tests of building construction and materials. Standard ASTM E119-95a, American Society for Testing Materials, Pennsylvania, USA, 1995.

[10] Bastami, M., and Aslani, F. Preloaded high-temperature constitutive models and relationships for concrete. *Civil Engineering 17*, 1 (2010), 11–25.

[11] Bayrak, O., and Sheikh, S. A. High-strength concrete columns under simulated earthquake loading. *ACI Structural journal 94*, 6 (1997).

[12] BIS. Code of practice for design loads (other than earthquake) for buildings and structures: Part 2: Imposed loads. Indian Standard Code IS875):1987, Bureau of Indian Standards, New Delhi, India, 2003.

[13] BIS. Code of practice for design loads (other than earthquake)for buildings and structures Part 1: Dead loads - unit weights of building material and stored materials (incorporating is:1911-1967). Indian Standard Code IS875(Part 1):1987, Bureau of Indian Standards, New Delhi, India, 2003.

[14] BIS. Ductile detailing of reinforced concrete structures subjected to seismic forces - code of practice. Indian Standard Code I13920:1993, Bureau of Indian Standards, New Delhi, India, 2003.

[15] BIS. Plain and reinforced concrete code of practice (fourth edition). Indian Standard Code IS456:2000, Bureau of Indian Standards, New Delhi, India, 2005.

[16] BIS. Criteria for earthquake resistant design of structures - Part 1 : General provisions and buildings (fifth revision). Indian Standard Code IS1893(Part 1):2002, Bureau of Indian Standards, New Delhi, India, 2007.

[17] Bisby, L., and Stratford, T. Design for fire of concrete elements strengthened or reinforced with fibre-reinforced polymer: State-of-the-art and opportunities from performance-based approaches. *Canadian Journal of Civil Engineering 40*, 11 (2013), 1034–1043.

[18] Bisby, L. A., Chen, J. F., Li, S. Q., Stratford, T. J., Cueva, N., and Crossling, K. Strengthening fire-damaged concrete by confinement with fibre-reinforced polymer wraps. *Engineering Structures 33*, 12 (2011), 3381–3391.

[19] Botting, R. The impact of post-earthquake fire on the built urban environment. masters thesis, University of Canterbury, Canterbury, New Zealand, 1998.

[20] BSI. Fire tests on building materials and structures - Part 20: Method for determination of the fire resistance of elements of construction. Standard 20, British Standard Institution, UK, 1987.

[21] BSI. Fire tests on building materials and structures - Part 21: Methods for determination of the fire resistance of load bearing elements of construction. Standard 21, British Standard Institution, UK, 1987.

[22] BSI. Fire tests on building materials and structures - Part 22: Methods for determination of the fire resistance of non- load bearing elements of construction. Standard 22, British Standard Institution, UK, 1987.

[23] BSI. Fire tests on building materials and structures - Part 23: Methods for determination of the contribution of components to the fire resistance of a structure. Standard 23, British Standard Institution, UK, 1987.

[24] Buchanan, A. H. *Structural design for fire safety.* Wiley, 2001.

[25] Carreira, D. J., and Chu, K.-H. Stress-strain relationship for plain concrete in compression. *ACI Journal proceedings 82*, 6 (1985).

[26] Chang, Y. F., Chen, Y. H., Sheu, M. S., and Yao, G. C. Residual stressstrain relationship for concrete after exposure to high temperatures. *Cement and Concrete Research 36*, 10 (2006), 1999–2005.

[27] Chen, W. F., and Scawthorn, C. *Earthquake Engineering Handbook.* New directions in civil engineering. CRC Press, Boca Raton, FL, 2003.

[28] Cousins, W. J., Dowrick, D. J., and Sritharan, S. Fire following earthquake. In *Proceedings of Institution of fire engineers conference, New Plymouth, August* (1991), Institution of Fire Engineers.

[29] Drysdale, D. *An introduction to fire dynamics.* John Wiley & Sons, 2011.

[30] ECCS. European recommendations for the design of steel structures exposed to the standard fire. Tech. rep., European Convention for Constructional Steel, Brussels, 1981.

[31] Elghazouli, A., and Izzuddin, B. Failure of lightly reinforced concrete members under fire. ii: Parametric studies and design considerations. *Journal of Structural Engineering 130*, 1 (2004), 18–31.

[32] Elghazouli, A. Y., Cashel, K. A., and Izzuddin, B. A. Experimental evaluation of the mechanical properties of steel reinforcement at elevated temperature. *Fire Safety Journal 44*, 6 (2009), 909–919.

[33] European Committee for Standardization, . *Eurocode 1: Actions on structures Part 1-2: General actions Actions on structures exposed to fire.* No. EN 1991-1-2 in Forschung Strassenbau und Strassenverkehrstechnik. CEN, Brussels, 2002.

[34] European Committee for Standardization, . *Eurocode 2: Design of concrete structures - Part 1-2: General rules - Structural fire design.* No. EN 1992-1-2 in Forschung Strassenbau und Strassenverkehrstechnik. CEN, Brussels, 2005.

[35] European Committee for Standardization, . *Eurocode 4 - Design of composite steel and concrete structures - Part 1-2: General rules - Structural fire design.* No. EN 1994-1-2 in Forschung Strassenbau und Strassenverkehrstechnik. CEN, Brussels, 2005.

[36] FEMA. Prestandard and commentary for the seismic rehabilitation of buildings: Fema-356. Tech. rep., Federal Emergency Management Agency, Washington DC, 2000.

[37] Gales, J., Bisby, L. A., and Gillie, M. Unbonded post tensioned concrete slabs in fire: Part 1 - Experimental response of unbonded tendons under transient localized heating. *Journal of Structural Fire Engineering 2*, 3 (2011), 139–154.

[38] Hertz, K. D. Reinforcement data for fire safety design. *Magazine of Concrete Research 56*, 8 (Jan. 2004), 453–459.

[39] Hibbitt. *ABAQUS theory manual (version 6.10).* Hibbitt, Karlsson and Sorenson Inc., Providence, RI, 2010.

[40] Hult, J. A. H. *Creep in engineering structures.* Blaisdell Pub. Co., 1996.

[41] ISO. Fire resistance tests-element of building construction. Standard ISO 834:1975, International Organization for Standardization, Geneva, Switzerland, 1975.

[42] Izzuddin, B., and Elghazouli, A. Failure of lightly reinforced concrete members under fire. i: Analytical modeling. *Journal of Structural Engineering 130*, 1 (2004), 3–17.

[43] Jowsey, A., Torero, J. L., Usmani, A., Lane, B., and Lamont, S. Determination of fire induced collapse mechanisms of multi-storey steel framed structures. In *Proc. of the 4th European Conference on Steel and Composite Structures* (Maastricht, The Netherlands, 2005).

[44] Kamath, P., and Suresh, N. Fire hazards due to earthquakes. In *Proceedings of the international conference on earthquake engineering* (Thanjavur, 2006), J. Venkataramana, Ed., SASTRA.

[45] Kawagoe, K. Fire behaviour in rooms. Report 27, Building Research Institute, Ministry of Construction, Tokyo, Japan, 1958.

[46] Khennane, A., and Baker, G. Uniaxial model for concrete under variable temperature and stress. *Journal of Engineering Mechanics 119*, 8 (1993), 1507–1525.

[47] Khezr Zadeh, H., and Mofid, M. Interpretation of tensile softening in concrete, using fractal geometry. *Scientia Iranica 15*, 1 (2008), 8–15.

[48] Kodur, V. K. R., Dwaikat, M., and Fike, R. High-temperature properties of concrete for fire resistance modeling of structures. *Journal of Materials in Civil Engineering 22*, 5 (2010), 423.

[49] Kodur, V. K. R., and Dwaikat, M. M. S. Effect of high temperature creep on the fire response of restrained steel beams. *Materials and Structures 43*, 10 (2010), 1327–1341.

[50] Kodur, V. K. R., Dwaikat, M. M. S., and Dwaikat, M. B. High-temperature properties of concrete for fire resistance modeling of structures. *ACI Materials Journal 105*, 5 (2008), 517.

[51] Kodur, V. K. R., Garlock, M., and Iwankiw, N. Structures in fire: State-of-the-Art, research and training needs. *Fire Technology 48*, 4 (2012), 825–839.

[52] Lamont, S., Lane, B., Flint, G., and Usmani, A. Behavior of structures in fire and real design - A case study. *Journal of Fire Protection Engineering 16*, 1 (2006), 5–35.

[53] Lamont, S., Lane, B., Jowsey, A., Torerro, J., Usmani, A., and Flint, G. Innovative structural engineering for tall buildings in fire. *Structural Engineering International: Journal of the International Association for Bridge and Structural Engineering (IABSE) 16*, 2 (2006), 142–147.

[54] Lee, J., and Fenves, G. Plastic damage model for cyclic loading of concrete structures. *Journal of Engineering Mechanics 124*, 8 (1998), 892–900.

[55] Lie, T. T. *Structural fire protection, manuals and reports on engineering practice.* No. 78 in ASCE Manual. ASCE, New York, NY, 1992.

[56] Lubliner, J., Oliver, J., Oller, S., and Onate, E. A plastic-damage model for concrete. *International Journal of Solids and Structures 25* (1989), 299–326.

[57] Magnusson, S. E., and Thelandersson, S. Temperature-time curves of the complete process of fire development - Theoretical study of wood fuel fires in enclosed spaces. *Acta Polytechnica Scandinavia - Civil Engineering and Building Construction 91*, 65 (1970), 1.

[58] Malhotra, H. L. The effect of temperature on the compressive strength of concrete. *Magazine of Concrete Research 8*, 23 (1956), 1–95.

[59] Malhotra, H. L. *Design of fire-resisting structures.* Surrey University Press, 1982.

[60] Mander, J. B., Priestley, M. J. N., and Park, R. Theoretical stress-strain model for confined concrete. *Journal of Structural Engineering 114*, 8 (1989), 1804–1826.

[61] Naus, D. J. *The effect of elevated temperature on concrete materials and structures - A literature review.* US Nuclear Regulatory Commission, Washington, DC, 2006.

[62] Nishiyama, M. Mechanical properties of concrete and reinforcement state-of-the-art report on hsc and hss in Japan. *Journal Of Advanced Concrete Technology 7*, 2 (2009), 157–182.

[63] Omer, E., Izzuddin, B. A., and Elghazouli, A. Y. Simplified method for failure assessment of composite slabs subject to fire. *IABSE Symposium Report 90*, 7 (2005), 39–46.

[64] Omer, E., Izzuddin, B. A., and Elghazouli, A. Y. Failure assessment of simply supported floor slabs under elevated temperature. *Structural Engineering International 16*, 2 (2006), 148–155.

[65] Paultre, P., and Legeron, F. Confinement reinforcement design for reinforced concrete columns. *Journal of Structural Engineering 134*, 5 (2008), 738–749.

[66] Phan, L. T. *Fire performance of high-strength concrete: A report of the state-of-the-art.* National Institute of the Standards and Technology, Gaitherburg, MD, 1996.

[67] Phan, L. T., and Carino, N. Review of mechanical properties of hsc at elevated temperature. *Journal of Materials in Civil Engineering 10*, 1 (1998), 58–65.

[68] Phan, L. T., and Carino, N. J. Code provisions for high strength concrete strength-temperature relationship at elevated temperatures. *Materials and Structures 36*, 2 (2003), 91–98.

[69] Purkiss, J. A. *Fire safety engineering design of structures.* Butterworth-Heinemann, 1996.

[70] Rini, D., and Lamont, S. Performance based structural fire engineering for modern building design. In *Proceedings of the 2008 Structures Congress - Structures Congress 2008: Crossing the Borders* (2008), vol. 314.

[71] Robertson, J. N., and Mehaffey, J. Accounting for fire following earthquakes in the development of performance based building design codes. *Bulletin of the New Zealand Society for Earthquake Engineering 33*, 3 (2000).

[72] Rollason, E. C. *Metallurgy for engineers.* Edward Arnold, 1961.

[73] SAA. Fire resistance test of elements of structure. Standard AS1530.4-1990, Standards Association of Australia, Australia, 1990.

[74] Schneider, U. *Properties of Materials at High Temperatures: Concrete.* Gesamthochschul-Bibliothek, 1985.

[75] Sharma, U. K., Bhargava, P., Singh, B., Singh, Y., Kumar, V., Kamath, P., Usmani, A., Torero, J., Gillie, M., Pankaj, P., May, I., and Zhang, J. Full-scale testing of a damaged reinforced concrete frame in fire. *Proceedings of the ICE - Structures and Buildings 165*, 7 (2012), 335–346.

[76] Sharma, U. K., Singh, B., Bhargava, P., Singh, Y., Kamath, P., and Usmani, A. Testing of full-scale RC frame under simulated fire following earthquake. In *Proc. of the 7th International Conference on Structures in Fire* (Zurich, 2012), M. Fontana, A. Frangi, and M. Knobloch, Eds.

[77] Sharma, U. K., Zaidi, K. A., and Bhandari, N. M. Residual compressive stress-strain relationship for concrete subjected to elevated temperatures. *Journal of Structural Fire Engineering 3*, 4 (2012), 327–350.

[78] Sheikh, S. A., and Khoury, S. S. A performance-based approach for the design of confining steel in tied columns. *ACI Structural Journal 94*, 4 (1997).

[79] Sheikh, S. A., Shah, D. V., and Khoury, S. S. Confinement of high-strength concrete columns. *ACI Structural Journal 91*, 1 (1994).

[80] Sheikh, S. A., and Toklucu, M. T. Reinforced concrete columns confined by circular spirals and hoops. *ACI Structural Journal 90*, 5 (1993).

[81] Takeuchi, M., Hiramoto, M., Kumagai, N., Yamazaki, N., Kodaira, A., and Sugiyama, K. Material properties of concrete and steel bars at elevated temperatures. *Nuclear Engineering and Design 12* (1993), 133–138.

[82] Thomas, P. H., and Heselden, A. J. M. *Fully-developed Fires in Single Compartments: A Co-operative Research Programme of the Conseil International Du Bâtiment.* Building Research Establishment, Fire Research Station, 1972.

[83] Topcu, I. B., and Karakurt, C. Properties of reinforced concrete steel rebars exposed to high temperatures. *Research Letters in Materials Science 2008* (2008), 1–4.

[84] Twilt, L. Strength and deformation properties of steel at elevated temperatures: Some practical implications. *Fire Safety Journal 13*, 1 (1988), 9–15.

[85] Usmani, A. S. Research prioroties for maintaining structural fire resistance after seismic damage. In *Proc. of The 14th World Conference on Earthquake Engineering* (Beijing, China, 2008).

[86] Wellington Lifeline Group, . *Fire following earthquake: Identifying key issues for New Zealand, Report on a project undertaken for the New Zealand fire service contestable research fund.* Fire Research Report. New Zealand Fire Service Commission, Wellington, NZ, 2002.

[87] William, K., Xi, Y., Lee, K., and Kim, B. *The effect of elevated temperature on concrete materials and structures: A literature review.* Oak Ridge National Laboratory, US Nuclear Regulatory Commission, Boulder, CO, 2006.

[88] William, K., Xi, Y., Lee, K., and Kim, B. Thermal response of reinforced concrete structures in nuclear power plants. Tech. Rep. 02, University of Colorado, Boulder, CO, 2009.

[89] Wu, B., Ma, Z., and Ou, J. Experimental research on deformation and constitutive relationship of concrete under axial loading and high temperature. *Journal of Building Structures 20*, 05 (1999), 42.

[90] Youssef, M. A., and Moftah, M. General stressstrain relationship for concrete at elevated temperatures. *Engineering Structures 29*, 10 (2007), 2618–2634.

LIST OF PUBLICATIONS (INTERNATIONAL CONFERENCE / JOURNAL)

[1] P. Kamath, P. Bhargava, U.K. Sharma, N.M. Bhandari, and A. Usmani. Mechanical properties of undamaged and damaged steel rebars at elevated temperatures. *Journal of Structural Fire Engineering*, 5(3), 2014. (in press).

[2] U.K. Sharma, V. Kumar, B. Singh, P. Bhargava, Y. Singh, P. Kamath, A. Usmani, J. Torero, M. Gillie, and P. Pankaj. Testing of full-scale rc frame under simulated fire following earthquake. *Journal of Structural Fire Engineering*, 5(3), 2014. (in press).

[3] P. Kamath, P. Bhargava, N.M. Bhandari, and U.K. Sharma. Effect of pre-damage on confined concrete at eleveted temperatures. In *Proceedings of the 8th International Conference on Structures in Fire, (SiF'14), 11 - 13 June*, Tongji University, Shanghai, China, 2014. (Accepted for Oral Presentation).

[4] P. Kamath, P. Bhargava, N.M. Bhandari, U.K. Sharma, and V. Kumar. Behaviour of earthquake damaged rc structures in fire. In *Proceedings of the 4th International Workshop on Performance, Protection and Strengthening of Structures under Extreme Loading, (Protect 2013), 26 - 27 August*, pages 1–70, Mysore, India, 2013. (Special Publication of Indian Concrete Journal).

[5] P. Kamath, U.K. Sharma, P. Bhargava, N.M. Bhandari, B. Singh, V. Kumar, A. Usmani, and M. Gillie. Structural response of reinforced concrete frame under simulated earthquake and fire. *Engineering Structures (Elsevier)*, 2014. (communicated, March 2013; Status: under review).

[6] V. Kumar, U.K. Sharma, B. Singh, P. Bhargava, Y. Singh, P. Kamath, A. Usmani, J. Torero, M. Gillie, and P. Pankaj. Behaviour of full-scale reinforced concrete frame under post-earthquake fire. *Fire Safety Journal (Elsevier)*, 2014. (communicated, August 2012; Status: under review).

[7] P. Kamath, P. Bhargava, U.K. Sharma, N.M. Bhandari, and A. Usmani. Mechanical properties of undamaged and damaged steel rebars at elevated temperatures. In *Proceedings of the 7th International Conference on Structures in Fire, (SiF'12), 6 - 8 June*, pages 729 – 736, Zurich, Switzerland, 2012.